EUROPEAN CENTRE FOR MEDIUM RANGE WEATHER FORECASTS

TECHNICAL REPORT NO. 1

****

SEPTEMBER

1976

****

***

*

A CASE STUDY OF A 10 DAY PREDICTION

BY

K. Arpe, L.Bengtsson, A. Hollingsworth and Z. Janjić

EUROPEAN CENTRE FOR MEDIUM RANGE WEATHER FORECASTS

Fitzwilliam House

Skimped Hill

BRACKNELL,BERKS.

UNITED KINGDOM

C O N T E N T S

A B S T R A C T

For a preliminary study in developing a global model for medium range weather forecasts, a case study of 10-day prediction with three general circulation models has been carried out. The forecasts have been compared with observations of the northern hemisphere

(i) by a synoptic presentation of 1000 mb and 500 mb-level maps, which is supported by a spectral decomposition presented by Hovmöller's trough-ridge-diagrams,

(ii) by conventional verification scores, i.e. RMS-errors and correlation coefficients,

(iii) by verification of energetics consisting of kinetic and available potential energy in the wavenumber domain and the transfer between their zonal and eddy modes.

The large scale changes in the developments of cyclones and anticyclones were surprisingly well predicted. It could be seen that the horizontal and vertical resolutions of the models are decisive factors in the quality of the forecasts. These and other differences in quality of the models were hardly represented by the RMS-error or correlation coefficients, so they should not be used unassisted. The energetics seem to be very sensitive for verification purposes and proved best in showing the influence of the vertical resolution on the forecast.

1. Introduction

As a preliminary study in the development of a global model for medium range weather forecasting at the European Centre for Medium Range Weather Forecasts (ECMWF) a case study of three global 10-day predictions has been carried out.

The numerical models used in the investigation have been provided by the Geophysical Fluid Dynamics Laboratory, NOAA, and the Department of Meteorology, UCLA.

Three 10-day integrations have been produced, one with the UCLA model and two with the GFDL model. The experiments with the GFDL model were done with 2 different horizontal resolutions: N24 - 24 latitudinal grid intervals between each pole and the equator and 96 longitudinal grid intervals around the earth between ± 26° latitude, with a decreasing number of longitudinal grid intervals poleward of ± 26° latitude (an average grid distance of about 420 km); and the N48 - 48 latitudinal grid intervals between each pole and the equator and 192 longitudinal grid intervals around the earth between ± 26° latitude, with a decreasing number of longitudinal grid intervals poleward of ± 26° latitude (an average grid distance of about 210 km). The version of the UCLA model that was used has 22½ latitudinal grid intervals between each pole and the equator and 72 longitudinal grid intervals around the earth in all latitudes (an average grid distance of about 450 km). We shall call this the UCLA-N22 model. The experiments were based on real data from 1 March 1965 00Z; the data set obtained from GFDL. This case has been studied frequently by the GFDL group (MIYAKODA et al, 1970, 1971, 1974). Sections 2 and 3 of this report contain a brief description of the models used and necessary references.

The problem of making numerical atmospheric predictions for periods beyond 4 - 5 days differs substantially from that of 2 - 3 day forecasting. From the physical point of view we may characterise a medium range forecast as a forecast where the initial disturbances have lost their individual structure. However, we still hope to predict the developments of atmospheric state as is done in short range forecasting, which means that the model must be able to predict the dissipation and decay of the initial disturbances and the creation of new ones.

The models used in this study have been mainly designed for simulation studies of the general circulation of the atmosphere. However, the potential of using general circulation models for medium range forecasting has been explored by MIYAKODA et al (1972) where twelve two-week forecasts were carried out with the 1967 version of the GFDL model. Another six cases of two-week numerical prediction experiments have also been reported by DRUYAN et al (1975), who used the model developed at the Goddard Institute for Space Studies (GISS), by SOMERVILLE et al (1974), for which an earlier version of the UCLA model (ARAKAWA,1972) was the prototype.

Bulk RMS-error, correlation coefficients or similar measures averaged over large areas indicate that forecasts of 10 days to 2 weeks apparently are on the fringe of predictability. However, bulk verification quantities are not very appropriate measures of forecast quality, in particular when the errors are large. Daily comparisons carried out during 1972 and 1973 at the Swedish and Finnish Meteorological Institutes between RMS-error and subjective verification of 24-hour forecasts for northern Europe for different operational models indicated that these two methods were very slightly correlated, if correlated at all.

For extended integrations simple verification measures can be even more misleading. The variance of atmospheric flow consists of a quasi-stationary part and of a transient part. At middle and high latitudes the transient part dominates and a major part of the energy of the atmosphere can be found in the travelling waves. For forecasts longer than 3 to 4 days, there is little hope of predicting the exact timing of individual cyclones. They will be out of phase and consequently they will contain large RMS-errors when verified against corresponding observations. In fact, a trivial statistical forecast or excessively smoothed forecasts may show higher scores.

Section 4 of this report contains a presentation of results as well as a number of computed quantities chosen as verification parameters. In order to simplify the interpretation of the results we have stratified the verification in four spectral domains - zonal flow, wavenumbers 1-3, 4-9 and 10-20.

An investigation of the influence of arithmetic precision on this 10-day forecast is contained in a report to be published (BAEDE and HOLLINGSWORTH, 1976).

2. Summary of the main features of the GFDL Model

For an extensive description of the GFDL model we refer to MANABE, HOLLOWAY and SPELMAN (1974) and to MIYAKODA (1974).

2.1 Horizontal Grid

The horizontal grid is a modified KURIHARA grid with resolution N24 or N48. The grid spacing in the north south is $\Delta\theta = \Pi/2N$ where N = 24 or 48. There are 2N-1 rows of boxes, all of width $\Delta\theta$ except for the rows nearest the pole which are of width 3/2 $\Delta\theta$. There is a row of boxes on the equator. The box boundaries are at $\pm$ (k-$\frac{1}{2}$) $\Delta\theta$, k=1,2.....N-1. The six rows of boxes closest to each pole have 36 boxes in both resolutions. The seven rows of boxes on and closest to the equator have 96 boxes in the N24 resolution and 192 boxes in the N48 resolution. Between the polar rows and the equatorial rows each row has four more boxes than its poleward neighbour. As a consequence the four main meridians, 0, 90°E, 180°E, 270°E are box boundaries at all latitudes.

2.2 Vertical Grid

The vertical coordinate is the coordinate defined by $\sigma = p/p^*$ where p is pressure and p^* surface pressure. The coordinate levels are specified by $\sigma_k = \delta_k^2(3 - 2\delta_k)$, $\delta_k = (2k-1)/18$, k = 1,2,.....9. This is a 9-level model with two levels in the stratosphere and seven levels in the troposphere (three of which are in the planetary boundary layer).

2.3 Finite difference scheme

The finite difference scheme is of second order accuracy in space and time. It is a centred scheme and is energy conserving. The equations are written in flux form so that the box method can be used to maintain energy conservation.The Euler-backward scheme is used for the first twelve hours, after that a leap frog scheme is used except for every 53rd time step when a forward time step is used to prevent the separation of solutions. The time step is 200 seconds in the GFDL-N48 model and 360 seconds in the GFDL-N24 model.

2.4 Radiation

The radiation calculation is done once every twelve hours and is based on climatologically specified

(i) absorber distribution (H_2O, CO_2, O_3),
(ii) sea surface temperature for open ocean and sea ice,
(iii) zonal mean cloudiness,
(iv) ice-limit over ocean
and (v) zonal mean cloud absorptivity, reflectivity and height.

The absorptivities for the solar absorption calculation and the emissivities for the long wave calculation are based on laboratory measurements. Pressure and temperature effects are taken into account by appropriate scalings.

There is no diurnal variation of incident solar radiation.

2.5 Dry Convection

Dry convective instability, when it occurs, is taken into account by adjusting the temperature profile so that it is neutral while preserving the column integral of the potential plus internal energy.

2.6 Moist Convection

The conditions for the onset of moist convection are

$$h > h_c \text{ and } -\frac{\partial T}{\partial p} > \Gamma_c \qquad (2.1)$$

where h is relative humidity, h_c is a critical relative humidity (taken as 0.8) and Γ_c is the moist adiabat defined by von Bezold's equation. If these conditions are satisfied it is assumed that free moist convection is sufficiently intense to make the partial equivalent potential temperature θ_{ep} and the relative humidity uniform in the convection layer i.e.

$$\frac{\partial}{\partial p}\,\theta_{ep} = 0, \qquad h = h_c \qquad (2.2)$$

where $\theta_{ep} = \theta \exp \frac{Lr_c}{c_p T}$

and $r_c = \frac{0.622(h_c . e_s\,(T))}{p-(h_c . e_s\,(T))}$ where the notation is standard.

In addition it is assumed that the total energy in a column is unaltered by the process of moist convection.

2.7 Surface Fluxes

The sea surface temperature is specified from climatology. Over land the surface temperature is specified by a budget calculation taking account of the net radiation at the surface and the surface fluxes of heat and moisture, using the assumption that the land has zero heat capacity. The fluxes are calculated using bulk formulae. The drag coefficient is 0.002.

2.8 Vertical Diffusion

Momentum and humidity are diffused vertically using a mixing length formulation in which the mixing length decreases linearly to zero at z = 2.5 km. There is no explicit vertical diffusion of temperature. This role is taken by the convective schemes.

2.9 Horizontal Diffusion

The horizontal diffusion is a non-linear diffusion scheme formulated by SMAGORINSKY (1963). The diffusion of momentum temperature and humidity is done on pressure surfaces rather than on sigma surfaces to prevent spurious changes of these quantities near mountains.

2.10 Mountains

The topography of the earth's surface, in smoothed form, is used as the lower boundary condition in the integration of the hydrostatic equation.

2.11 Hydrology

The treatment of the ground hydrology is quite elaborate. Account is taken of rainfall, evaporation, snow accumulation, snow melt and run-off. Further details may be found in MANABE, HOLLOWAY and SPELMAN (1974).

2.12 Initial Data

The initial data for these experiments were provided by GFDL. They consisted of analysed fields for the historical variables for 1 March 1965 00z. Poleward of 15^{o} the fields are balanced using the non-linear balance equation. For details of the data analyses and initialisation see MIYAKODA, SADLER and HEMBREE(1974). For the run with the UCLA model the data on the GFDL tapes were interpolated to the UCLA grid using linear interpolation in the vertical and horizontal. The surface pressure was reduced to UCLA orography in a straightforward manner using the GFDL surface temperature. Prognostic variables peculiar to the UCLA model (boundary layer depth, soil moisture, snow cover, etc.) were initialised using UCLA-model-generated data for the same time of year.

3. The version of UCLA general circulation model used at ECMWF

Since a comprehensive model description is given elsewhere (ARAKAWA and MINTZ, 1974) we shall here only review the basic features of the model, mainly following the introductory part of the model descriptions referred to above.

3.1 Variables of the model

The primary prognostic variables of the atmospheric general circulation model are horizontal velocity, temperature and surface pressure, governed respectively by the horizontal momentum equation, the thermodynamic energy equation and the surface pressure tendency equation. With appropriate boundary conditions, these equations form a closed system for an atmosphere that is adiabatic and frictionless.

The secondary prognostic variables are water vapour, ground temperature, ground water storage and mass of snow on the ground. The most important of these secondary prognostic variables, necessary to calculate the heating, is water vapour, which is governed by the continuity equation for water vapour.

Since the source and sink terms in the continuity equation for water vapour and in the thermodynamic energy equation greatly depend on sub-grid scale cumulus convection, the model has a parameterised penetrative cumulus convection, which interacts with a parameterised planetary boundary layer.
The planetary boundary layer depth and the magnitudes of the temperature discontinuity and moisture discontinuity at the top of the boundary layer are prognostic variables.

The ground temperature, ground water storage and mass of snow on the ground are also taken as prognostic variables, governed by the energy and water budget equations for the ground. This is done because there can be a large diurnal heat storage in the ground; because the available water stored in the ground can be a significant source of water vapour for the atmosphere; and because snow lying on the ground can have a large influence on the surface albedo as well as be a significant water vapour source.
Although these variables define the state of the uppermost lithosphere, they are included in the model.

3.2 Physical processes

In the horizontal momentum equation, the source and sink term consists of :

(i) frictional drag at the surface of the earth;

(ii) sub-grid scale vertical eddy flux of horizontal momentum within the planetary boundary layer

and (iii) sub-grid scale vertical eddy flux of horizontal momentum within the free atmosphere.

The sub-grid scale vertical flux of horizontal momentum, in the free atmosphere, takes place only through the entrainment and detrainment of horizontal momentum by the parameterised cumulus cloud ensembles.

In the thermodynamic equation, the source and sink term consists of :

(i) solar and infrared radiational heating, with a diurnal variation (hour-angle dependence) of the incident solar radiation;

(ii) sensible heat flux across the earth's surface, with a sub-grid scale vertical eddy flux of heat and release of heat of condensation within the planetary boundary layer;

(iii) a sub-grid scale vertical eddy flux of sensible heat and release of heat of condensation by the parameterised cumulus convection in the free atmosphere

and (iv) the latent heat of large-scale condensation and lower level evaporation of the falling raindrops.

In the continuity equation of water vapour, the source and sink term consists of :

(i) evaporation at the earth's surface, with a sub-grid scale vertical eddy flux of water vapour within the planetary boundary layer;

(ii) sub-grid scale vertical eddy flux of water vapour and condensation sink by the parameterised cumulus convection in the free atmosphere

and (iii) large-scale condensation and evaporation of the falling raindrops.

Sub-grid scale lateral eddy diffusion is by a non-linear scheme formulated by SMAGORINSKY (1963).

3.3 Principles of mathematical modelling in the UCLA model

In long-term numerical integrations there is no "true" solution in the deterministic sense, and long-term integrations (including long-range numerical weather predictions from observed initial states) can only predict the statistical properties of the atmosphere. In a long-term integration we must, therefore, be concerned with the accuracy of the statistical properties of the solution. Therefore, in the UCLA-model (ARAKAWA and LAMB, 1976), as the grid size approaches zero, the finite difference solution is required to approach a solution having the same basic statistical properties as the true solution. In order to achieve this the finite difference scheme of the model is designed to maintain many of the integral constraints of the continuous atmosphere such as

(i) the conservation of total mass,

(ii) the conservation of total kinetic energy during the inertial processes,

(iii) the conservation of enstrophy during vorticity advection by the non-divergent part of the horizontal velocity,

(iv) the conservation of total energy during adiabatic and non-dissipative processes

and (v) the conservations of the total entropy and total potential enthalpy during adiabatic processes.

In addition, the finite difference scheme maintains the feature of the continuous atmosphere; only when there is a non-horizontal boundary surface can there be any acceleration of the circulation of the vertically integrated atmosphere by the pressure gradient force.

The purpose of maintaining the conservation of enstrophy and kinetic energy in the horizontal advection is to maintain the statistical properties of non-divergent horizontal flow. This does not only prevent non-linear computational instability, but it maintains the integral constraint on the kinetic energy exchange between motions of different scales.

The other integral constraints which are maintained by the finite difference scheme of the UCLA model are not included for the purpose of preventing computational cascade, and, therefore they do not directly increase the overall accuracy of the statistics of the solution. But the maintenance of the other integral constraints should lead to less systematic error, in terms of the generation, conversion and dissipation of the energy, entropy, angular momentum and vorticity; and, therefore, in a statistical sense, they should make the discrete model more analogous to the continuous atmosphere.

It is further assumed that the energy propagation in physical space, as well as in spectral space, should be properly simulated. In particular, the energy propagation by dispersive inertia - gravity waves, excited by a local breakdown of the quasi-geostrophic balance, is important in order to restore the quasi-geostrophic adjustment. It is believed that unless the geostrophic adjustment can operate properly, nothing is gained by maintaining the integral constraints on the quasi-geostrophic motion. Therefore, special attention is paid to the choice of distribution of dependent variables over grid points which provides the best simulation of dispersive properties of gravity-inertia waves.

3.5 Coordinate system, resolution and time differencing

The horizontal coordinates are longitude and latitude. In the version of the model that was used for the present study, the grid size is 5^{o} of longitude and 4^{o} of latitude. This means $22\frac{1}{2}$ grid intervals between each pole and the equator, and we therefore refer to it as the UCLA-N22 model. To avoid an extremely small finite difference time step because the meridians converge toward the poles, a longitudinal averaging is done of selected terms in the prognostic equations. Near the poles, Fourier filtering is used instead of longitudinal averaging.

The horizontal distribution of variables over grid points is the following:

h	u	h	u	h
v		v		v
h	u	h	u	h
v		v		v
h	u	h	u	h

The vertical coordinate used in the model is a combination of the σ-coordinate for the lower part of the atmosphere, and the pressure coordinate for the upper part of the atmosphere. The version of the UCLA model that we have used is a 6-level model, with one level in the stratosphere and five in the troposphere.

The time step is 6 minutes. A splitting technique is used to introduce sink and source terms for which the time step is 30 minutes. The leap frog time differencing scheme is used, except for the time step immediately following introduction of the sink and source terms, when an Euler-backward scheme is used to prevent the separation of solutions. This use of an Euler-backward time scheme also has the effect of selectively damping high frequency modes.

4. Results

4.1 Methods of presentation and verification

This section presents the result of three different prediction experiments, one with the UCLA model, described in section 3; and two with the GFDL model, one with each of the grid sizes, described in section 2.

In view of the difficulties in summarising the results from these integrations in a few bulk parameters, we have chosen to present the forecast experiments in a very comprehensive way. The first part will consist of a synoptic presentation of the daily 1000 mb and 500 mb charts, the second part of conventional verification parameters, and the third part of the verification of the kinetic energy and available potential energy as well as the transfer between them.

In carrying out these comparisons all data has been converted into a common format consisting of zonal Fourier coefficients of temperature, geopotential and geostrophic horizontal winds. The verification has been done against the NMC's operational analyses and only analyses north of 20^{o}N have been used.

It was decided to limit the investigation to the geostrophic part of the wind field in order to be consistent with the verifying analyses. This may cause an additional smoothing of the predicted wind data which may lead to a loss of energy for the high wave components.

Another limiting factor in arriving at an accurate comparison is the problem of vertical interpolation. The standard levels between 1000 mb and 200 mb have been used for the verification and the predicted data, available at the sigma levels of the model, have been interpolated to these pressure levels. Slightly different programs for interpolation from sigma levels to pressure levels have been used for the two

different models, which may possibly imply differences over mountainous regions.

Interpolation as well as differences between initialised data and analysed fields create initial deviations. As can be seen from the subsequent diagrams these differences are mainly confined to the wind fields and can mainly be noticed in the kinetic energy of the higher wave numbers.

As a general principle the data has been stratified into four different spectral domains; zonal flow, wave numbers 1 to 3, 4 to 9, and 10 to 20. This separation has been recommended by the JOC WGNE (1975) . In that way , the separate RMS scores will more adequately reveal the skill in portraying the quasi-stationary or slowly moving long waves, the more rapidly moving baroclinic waves, and the shorter waves of marginal resolutions.

This stratification also roughly corresponds to the wave length domains in which different physical effects, different data densities, and different numerical resolutions would be expected to be most clearly seen and, therefore, has both practical and scientific justification.

To present a general view of these wave number groups, Fig. 4.1.1 shows the spectral distribution of mean amplitudes of geopotential height of the 500 mb level for the predicted last five days It can be seen that the long waves contain the largest amplitudes and that the forecasts underestimate the amplitude of wave number two in particular. Also considerable amplitudes are contained in the medium wave lengths, wave numbers 4 to 9, while the short waves are characterised by relatively small amplitudes.

4.2 Synoptic comparison

The case study which has been investigated is a northern hemisphere late winter situation, initially characterised by a marked meridional flow, as can be seen in Fig. 4.2.1. In the middle and high latitudes, two cyclones over Europe and the Pacific and two anticyclones over the western Atlantic and over Siberia dominate the patterns at 1000 mb and 500 mb. Another cyclone over the United States at 1000 mb which is connected with a trough at 500 mb, will become important later. At 500 mb the polar and subtropic fronts can easily be recognised as two belts with stronger height gradients. The 5230 m and 5680 m lines can be taken as coarse guide lines for the polar and subtropic fronts respectively. Over the Pacific both fronts are too close together to be separated.

During the course of the next 5 days this meridional flow is gradually transformed into a more zonal type of circulation. This is connected with a vanishing of the blocking anticyclone over the western Atlantic, a weakening of the Siberian anticyclone, and the development of a cut-off low over America.

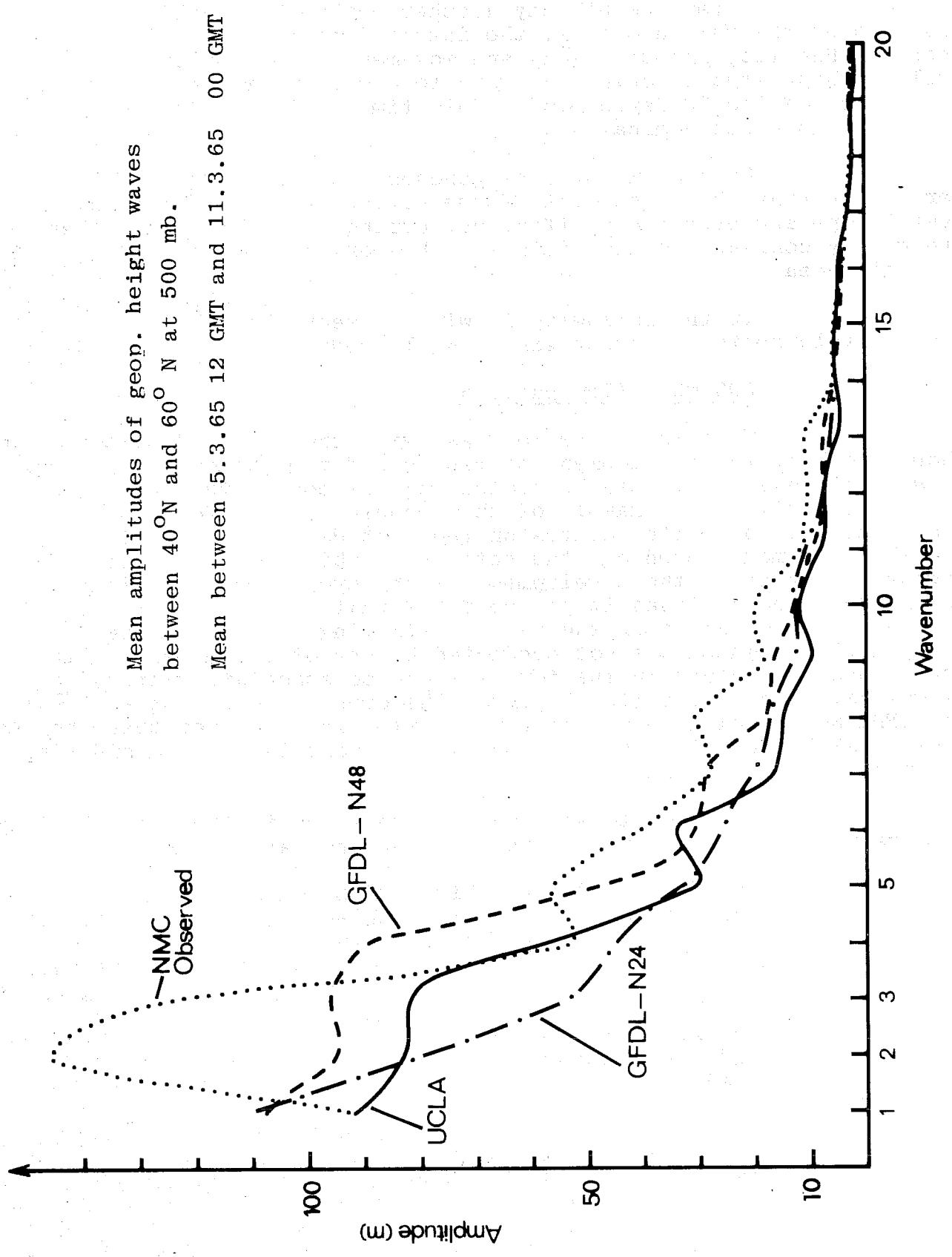
Mean amplitudes of geop. height waves
between 40°N and 60° N at 500 mb.
Mean between 5.3.65 12 GMT and 11.3.65 00 GMT
NMC
Observed
GFDL–N48
UCLA
GFDL–N24
Amplitude (m)
100
50
10
1
2
3
5
10
15
20
Wavenumber

Fig. 4.1.1.

After the 6th day another outbreak of cold air masses over the United States, the intensification of a ridge over the Pacific, and the decay and movement of the European cyclone change the circulation again to a more meridional flow by the end of the 10 day period. This time it is wave number 3 instead of 2 which dominates.

Several major cyclogeneses take place during the period. During the first part of the period they are mainly found over Europe and over the Pacific, but during the latter part they are mainly confined to East Asia, North America, and the Norwegian Sea.

In the following it will be seen that these large scale developments are surprisingly well predicted.

500 mb - flow pattern

To compare the forecast with the observed pattern, one should look at the development of ridges and troughs over a period of several days, as it can be misleading to compare the pattern at only one time. An example of this problem can be found over the west coast of the United States on the 10th day (Fig. 4.2.11). The GFDL-N48 model predicts the pattern on this day very well. However, looking at the development of the cyclone over California on the observed analyses it can be found that it originates from an outbreak of cold air over the Pacific starting on the 3rd day (Fig. 4.2.4), which was not predicted by any of the models. The corresponding cyclone in the forecast can be associated with an outbreak of cold air over the United States. Therefore, one cannot say that the GFDL-N48 model made a better prediction in this area than the other models, although this could be concluded if one is only considering the maps of the 10th day.

In order to show some differences in the quality of the different models, four interesting developments are described:

1.) Up to the 2nd day (Fig. 4.2.3) an anticyclone lies south of Greenland. The UCLA-N22 model predicts its position correctly but is wrong in the prediction of its height. In contrast, the GFDL-N48 model is correct in its prediction of height, but predicts a big shift to the west. The GFDL-N24 model is wrong in both predictions - it shows the wrong position of the GFDL-N48 model and the wrong height of the UCLA-N22 model prediction.

2.) A ridge over Siberia, which moves slowly to the east at the beginning of the forecast period is predicted well by the GFDL-N48 model until the 3rd day. The UCLA-N22 model predicts its position correctly but is wrong in the prediction of the intensity. The forecast by the GFDL-N24 model is slightly worse than that by the UCLA-N22 model.

3.) A ridge along the west coast of the United States with a cold outbreak ahead, which is moving to the east over the continent on the 4th day (Fig. 4.2.5) is predicted

by the UCLA-N22 model correctly in position but far too weak in its intensity. The GFDL models fail totally at this point.

4.) The UCLA-N22 forecast shows an anticyclone or ridge over the north pole almost daily. This feature is neither observed nor predicted by the other models.

Summing up, it can be said that the UCLA-N22 model predicts the positions of ridges and troughs in general somewhat better than the GFDL-N48 model; THE GFDL-N48 model, however, is better in predicting their intensities. The GFDL-N48 model constantly provides better forecasts than the GFDL-N24 model.

1000 mb - flow pattern

Since the circulation at 1000 mb and 500 mb is strongly coupled, it may be expected that the large scale features are predicted as well at 1000 mb as the previously shown 500 mb forecast. However, the 1000 mb-flow also has smaller scale cyclones and anticyclones, so it is worthwhile giving some examples of cyclonic and anticyclonic development at this level:

1.) A cyclone near Newfoundland is predicted quite well in position and depth by all models up to the 4th day (Fig. 4.2.15). Then it starts to move to the NE in the models, although it is observed to remain stationary for an additional day. From that day on the discrepancies are larger.

2.) At the beginning of the forecast period, an extensive low pressure region can be found over Europe (Fig. 4.2.1). The development is predicted very well by all models up to the 3rd day (Fig. 4.2.14). However, over southern Europe an anticyclone displaces the cyclone in the forecasts, which was not observed until two days later. So on the 6th day (Fig. 4.2.17) the forecasts look quite accurate again.

3.) Asia is covered by an extensive stationary anticyclone. All the models predict this feature quite well for the first 4 days (Fig. 4.2.15). Even the newly developed anticyclone advancing from the Black Sea is well predicted. The Asian anticyclone weakens after the 5th day. This weakening starts earlier in the forecasts. In the GFDL-N24 model the anticyclone breaks down into a disordered pattern after the 5th day.

4.) On the 3rd day (Fig. 4.2.14), a cyclone that develops near Japan joins the main cyclone over the Pacific on the 6th day. The trend of this development is forecast by all models, but the GFDL-models predict the cyclogenesis one day before it is actually observed. This cyclone gains its maximum intensity on the 6th day (Fig. 4.2.17). The very low values in the centre are only predicted by the GFDL-N48 model.

Summing up, it can be said that the gross features of the 1000 mb level are predicted quite well by the models for at least four days. No clear-cut differences in the performances of the three models can be found because it is sometimes difficult to follow the continuity of the cyclones or anticyclones and different interpretations are possible. When the 1000 mb flow patterns are not evident at 500 mb, it is due to the domination of different horizontal scales at the two levels. When looking at the same scales, as will be done below by using spectral decomposition, greater similarities at both levels are found.

Spectral decomposition

To compare the positions of the forecast troughs and ridges with the observed ones, the positions of the lowest and highest pressure were determined, at several standard levels and several latitudes . These positions were plotted in longitude-time diagrams (Hovmöller diagrams). The contributions of three wave number groups(1-3 4-9, 10-20), were considered separately. The observed positions of troughs and ridges (NMC) are repeated in each figure as thin solid and dotted lines, respectively, for the three comparative groups so that a comparison can easily be made. Lines for ridges are plotted,if a relative maximum is found in the zonal direction and its value is higher than the zonal mean. An equivalent plot is made for the troughs. No distinction between intense and weak troughs and ridges can be made in these figures and this is a disadvantage of this representation . The same type of diagrams are made for the temperature fields.

Only a few selected levels and latitudes can be considered here and cases with interesting features were chosen.

Figure 4.2.22 shows the ridges and troughs of geopotential height at 50°N and 500 mb for the long waves with zonal wave numbers 1-3. It can easily be seen that all three forecasts predict the positions of these long waves very well. Only the GFDL-N24 model shows a wrong forecast of the ridge at about 75°E. It is a considerable disadvantage that these figures show only the positions of the ridges and troughs and not their intensities. Going into more detail at this stage, the observations show that this ridge, starting at about 75°E, splits after 4 days into an almost stationary one, which is dominating, and a westward moving one,which appears two days later in the figure at about 360°. Since the GFDL-N24

model predicts only the westward moving branch the prediction appears to be unrealistically poor in this type of presentation. The other models predict both branches of this ridge.

Figure 4.2.22 is almost identical with the contours for 1000 mb and for temperature at 500 mb, so that those need not be shown. But at 60°N at the 1000 mb level it is quite different and is therefore shown in figure 4.2.23. The observations show strong variations in wave propagation that is not always predicted. In particular the eastward propagation after about 1½ days over Europe and the western Atlantic is not predicted by any of the models. The eastward propagation of the ridge starting at about 100°E is predicted poorly by the GFDL-N24 model, but is well predicted by the other two models.

Figure 4.2.24 shows the behaviour of the temperature maxima and minima of the long waves at the 850 mb level at 50°N. Again it can be seen that the GFDL-N24 model gives a very bad prediction at about 45°E and that the UCLA-N22 and GFDL-N48 models make good predictions. From 300° to 360° E it can be seen that the maxima (ridges) are not well predicted after the first few days, but then with the UCLA-N22 and GFDL-N48 models the quality of the forecasts improves again and is excellent by the 10th day; a feature which could already be observed by looking at the maps.

At 40°N and 500 mb the temperature forecast of the long waves (Fig. 4.2.25) by the GFDL-N24 model shows some very unrealistic fast moving waves while the two other models predict these waves very well. These fast moving waves, wrongly predicted by the GFDL-N24 model, have only small amplitudes.

For the medium wave numbers (4-9), which are essentially baroclinic waves, the agreement is not as good as for the long waves. Nevertheless the results are encouraging.
Figure 4.2.26 shows the geopotential height at 500 mb and 40°N. The UCLA-N22 forecast is particularly good for the first 5 or 6 days and it even predicts correctly the change in propagation velocity over America after 3 days.
The GFDL-N24 forecasts show considerable disagreement with the observations, especially over North America.

The predictions of the phases of the medium scale waves at the 1000 mb level (Fig. 4.2.27) are poor. Ridges were forecast between 270° and 360° for the 10th day where troughs were observed, and vice versa. For the first three days, however, the forecasts are good.

For the group of short waves (10-20) only one diagram is shown (Fig. 4.2.28), since one cannot expect that the positions of these short waves will be well predicted. It is, however, encouraging to see that the general propagation velocity of these waves is predicted well both by the UCLA-N22 model and by the GFDL-N48 model, even though in the UCLA model wave number 10 is represented by only 7 grid intervals and wave number 20 by only 3.5 grid intervals. In the GFDL-N48 model, at 45° latitude, wave number 10 is represented by 11 grid intervals and wave number 20 by 5.5 grid intervals.

Summing up, it can be said that the large scale features were forecast very well. The Hovmöller diagrams are a good tool for verification purposes. Only figures showing differences between forecasts and observations were chosen. As a consequence the agreement between the forecasts and the observations is better than is represented overall by these figures.

The daily maps and the Hovmöller diagrams show very clearly that forecasts provide useful information for at least 5 days.

4.3 Conventional verification scores

RMS-error

One of the most frequently used scores for verification is the RMS-error. Since the data are expanded in zonal Fourier series, the RMS-error may be expressed in the following form :

$$RMS(N_1,N_2)=\sqrt{\frac{1}{\int_{\varphi_1}^{\varphi_2}\int_{\psi_1}^{\psi_2}\cos\varphi\,d\psi\,d\varphi}\int_{\varphi_1}^{\varphi_2}\int_{\psi_1}^{\psi_2}\cos\varphi\sum_{N=N_1}^{N_2}\frac{\delta^N}{2}\left[\left(\phi^c_{Obs}(N)-\phi^c_F(N)\right)^2+\left(\phi^s_{Obs}(N)-\phi^s_F(N)\right)^2\right]d\psi\,d\varphi} \qquad (4.1)$$

$\phi_{obs}(N)$ observed values

$\phi_F(N)$ forecast values

$\phi^c(N)$ cosine coefficient of Fourier series

$\phi^S(N)$ sine coefficient of Fourier series

$\delta^N = 1$ if $N \neq 0$
$= 2$ if $N = 0$

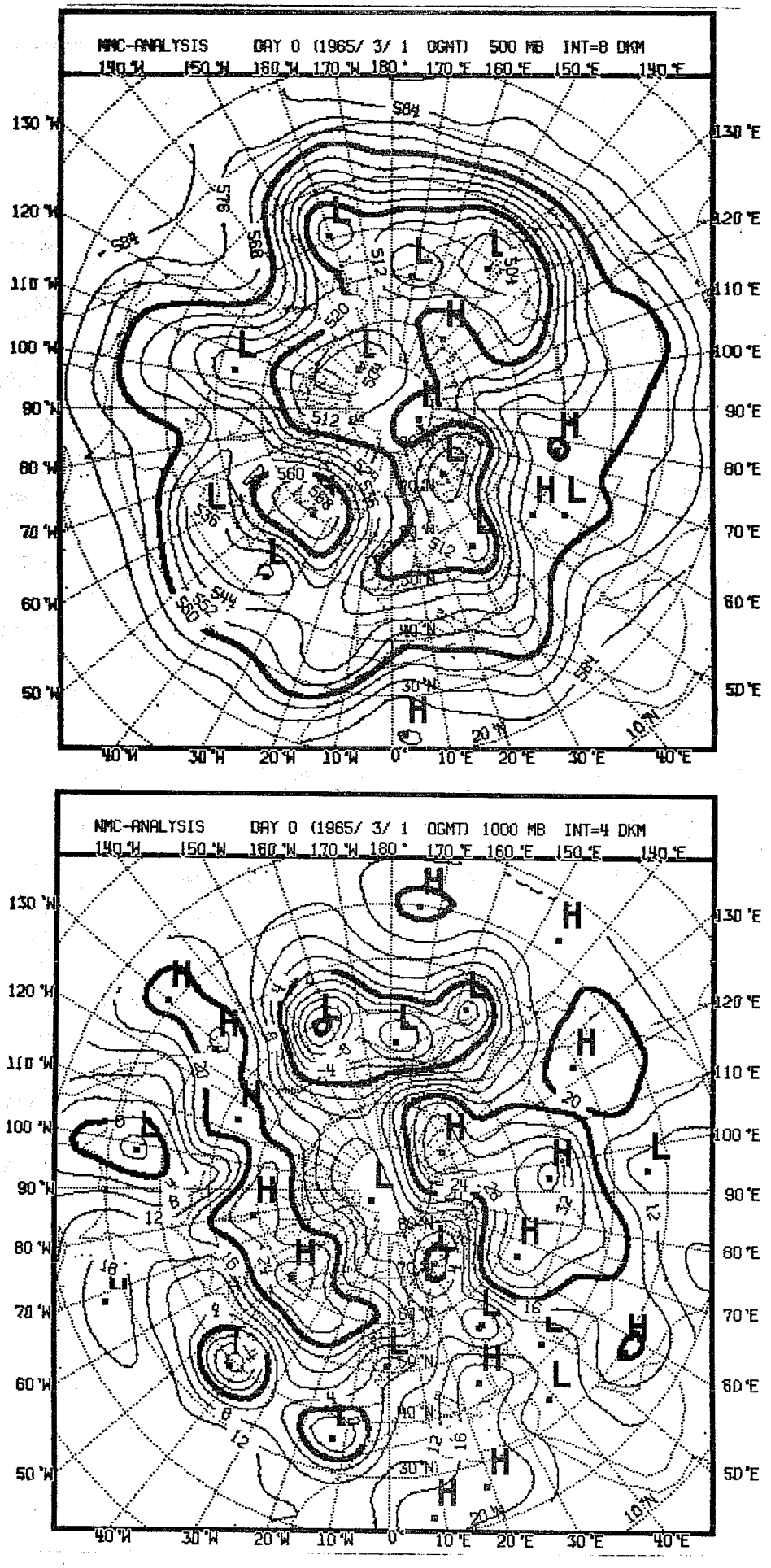

Fig. 4.2.1 :Observed maps of 1000 mb (bottom) and 500 mb (top) geopotential height.

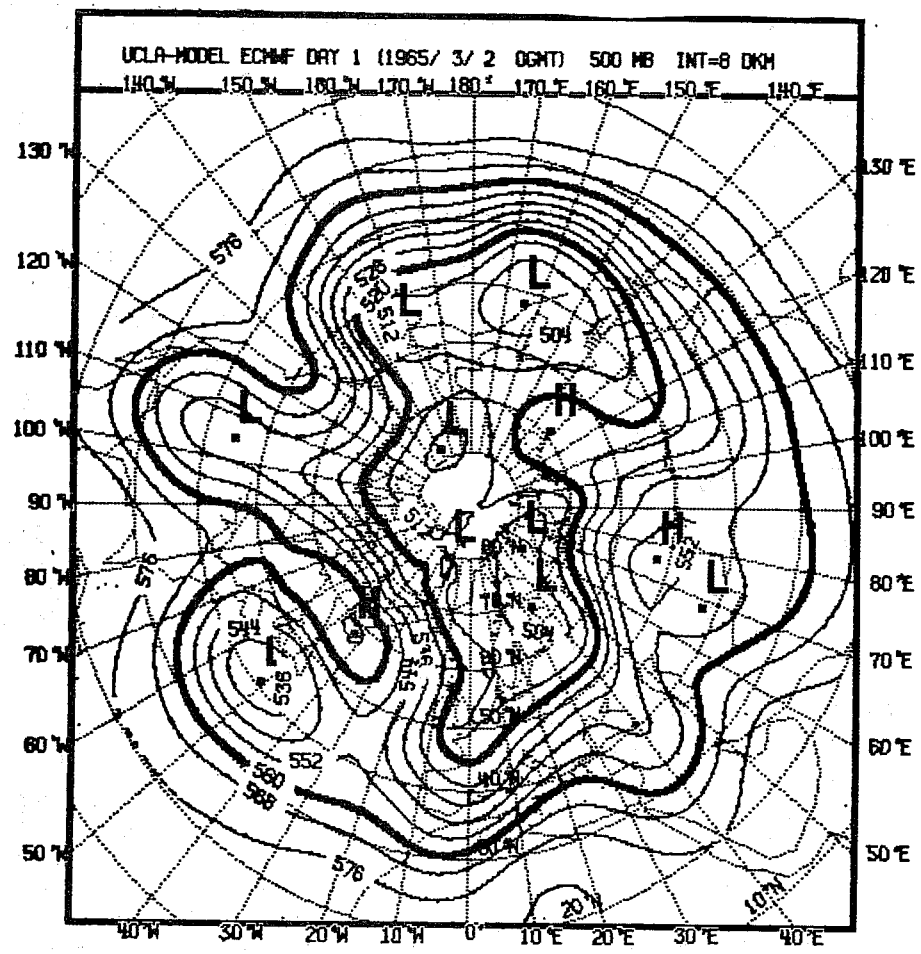
UCLA-MODEL ECMWF DAY 1 (1965/ 3/ 2 0GMT) 500 MB INT=8 DKM
140°W 150°W 160°W 170°W 180° 170°E 160°E 150°E 140°E
130°N 120°N 110°N 100°N 90°N 80°N 70°N 60°N 50°N
130°E 120°E 110°E 100°E 90°E 80°E 70°E 60°E 50°E
40°W 30°W 20°W 10°W 0° 10°E 20°E 30°E 40°E
576
568
560
552
544
536
528
520
512
504
496
488
480
H
L

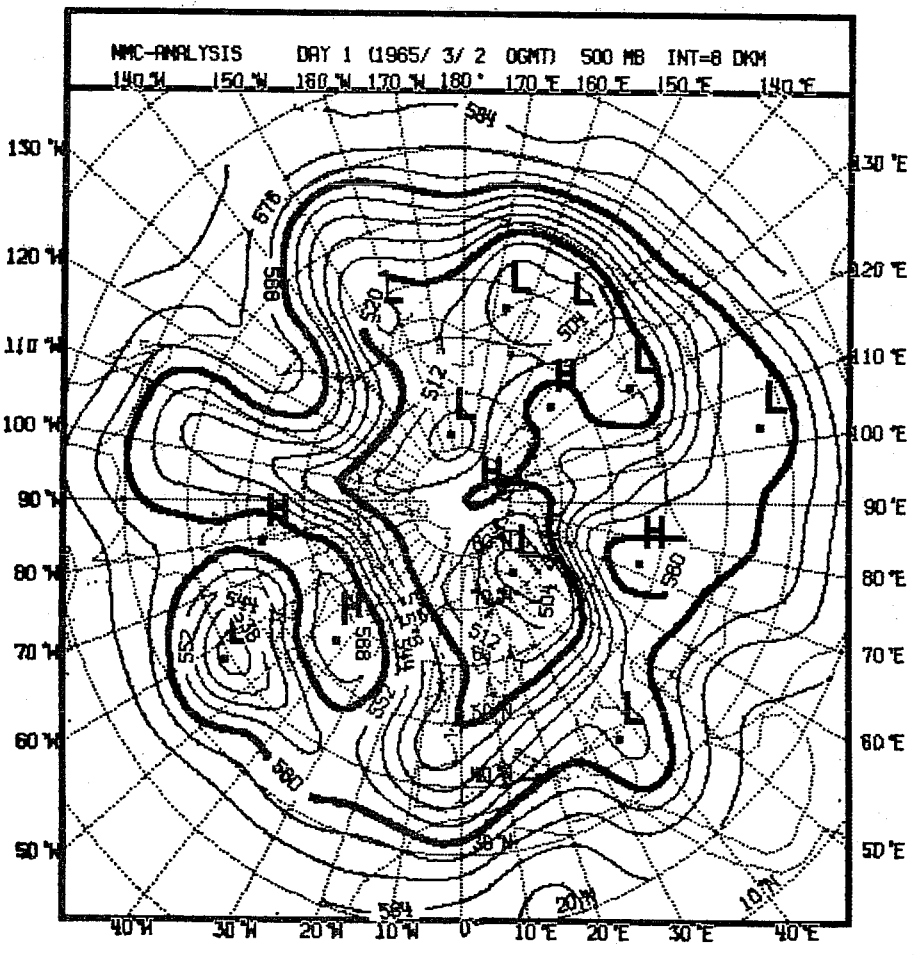
NMC-ANALYSIS DAY 1 (1965/ 3/ 2 0GMT) 500 MB INT=8 DKM
140°W 150°W 160°W 170°W 180° 170°E 160°E 150°E 140°E
130°N 120°N 110°N 100°N 90°N 80°N 70°N 60°N 50°N
130°E 120°E 110°E 100°E 90°E 80°E 70°E 60°E 50°E
40°W 30°W 20°W 10°W 0° 10°E 20°E 30°E 40°E
584
576
568
560
552
544
536
528
520
512
504
496
488
480
H
L

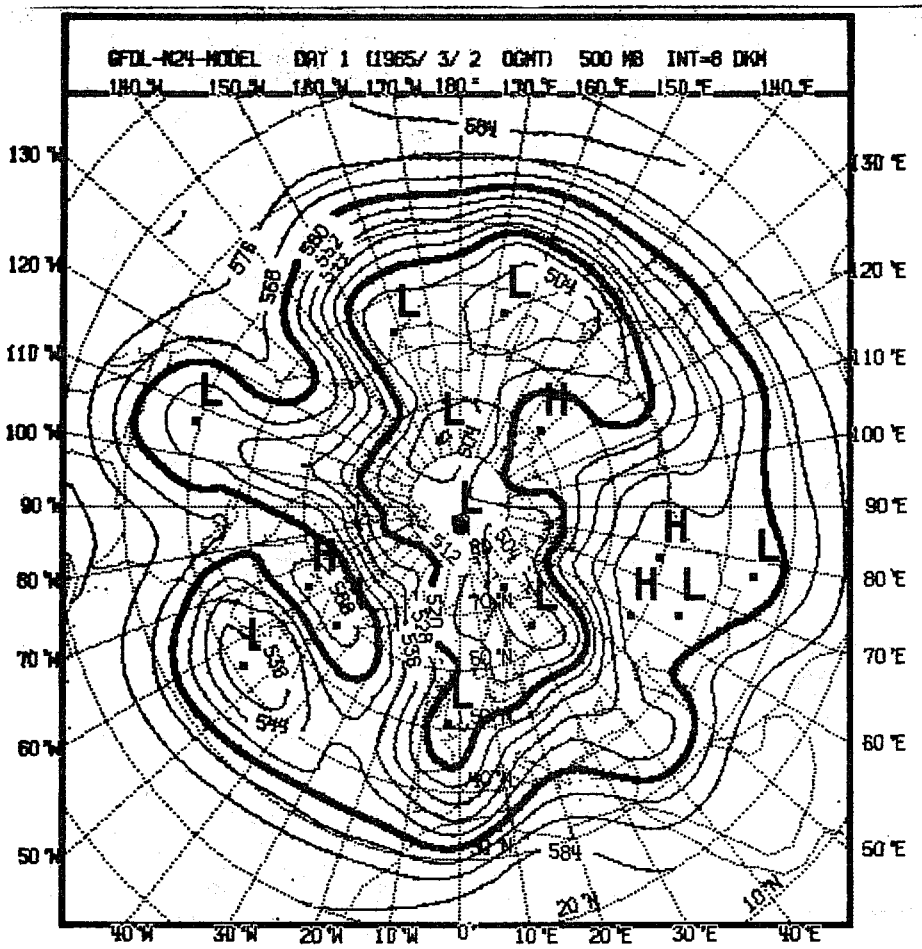

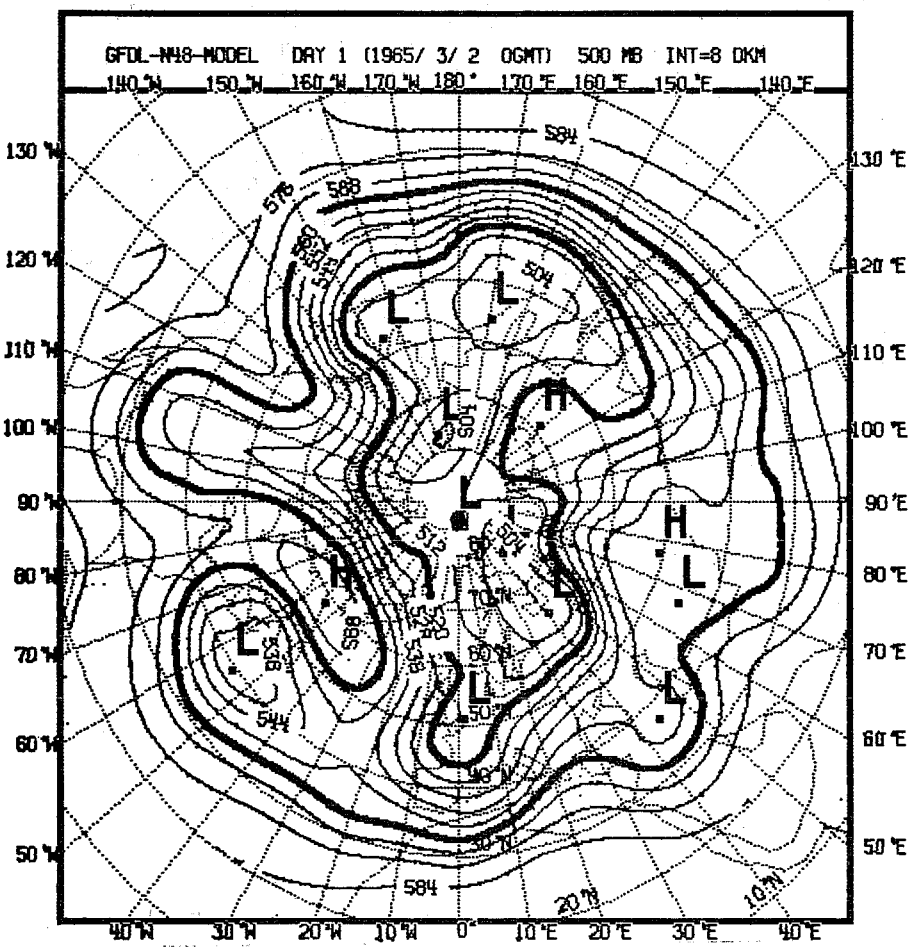

Fig. 4.2.2 :Observed (bottom left) and predicted maps of 500 mb geopotential height, day 1

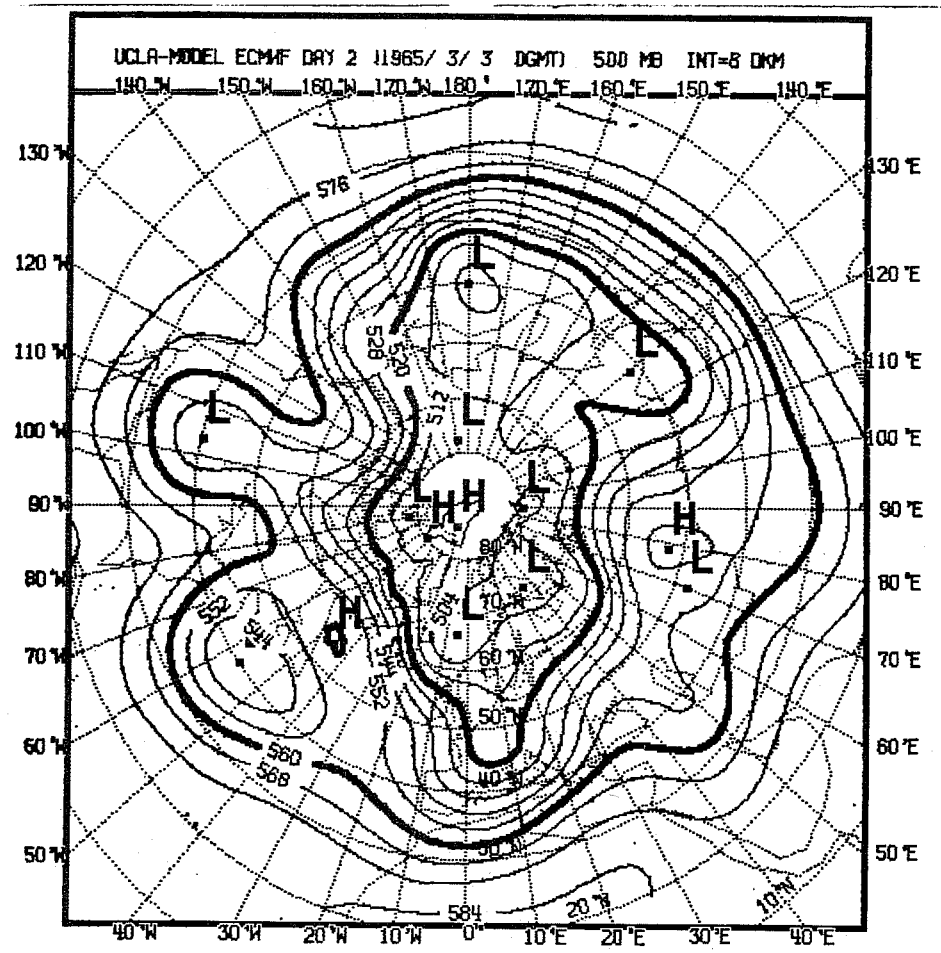
UCLA-MODEL ECMWF DAY 2 (1965/ 3/ 3 0GMT) 500 MB INT=8 DKM
140 °W 150 °W 160 °W 170 °W 180 ° 170 °E 160 °E 150 °E 140 °E
130 °W 120 °W 110 °W 100 °W 90 °W 80 °W 70 °W 60 °W 50 °W
130 °E 120 °E 110 °E 100 °E 90 °E 80 °E 70 °E 60 °E 50 °E
40 °W 30 °W 20 °W 10 °W 0° 10 °E 20 °E 30 °E 40 °E
576
528
520
512
552
544
560
568
584
80 °N
70 °N
60 °N
50 °N
40 °N
30 °N
20 °N
10 °N

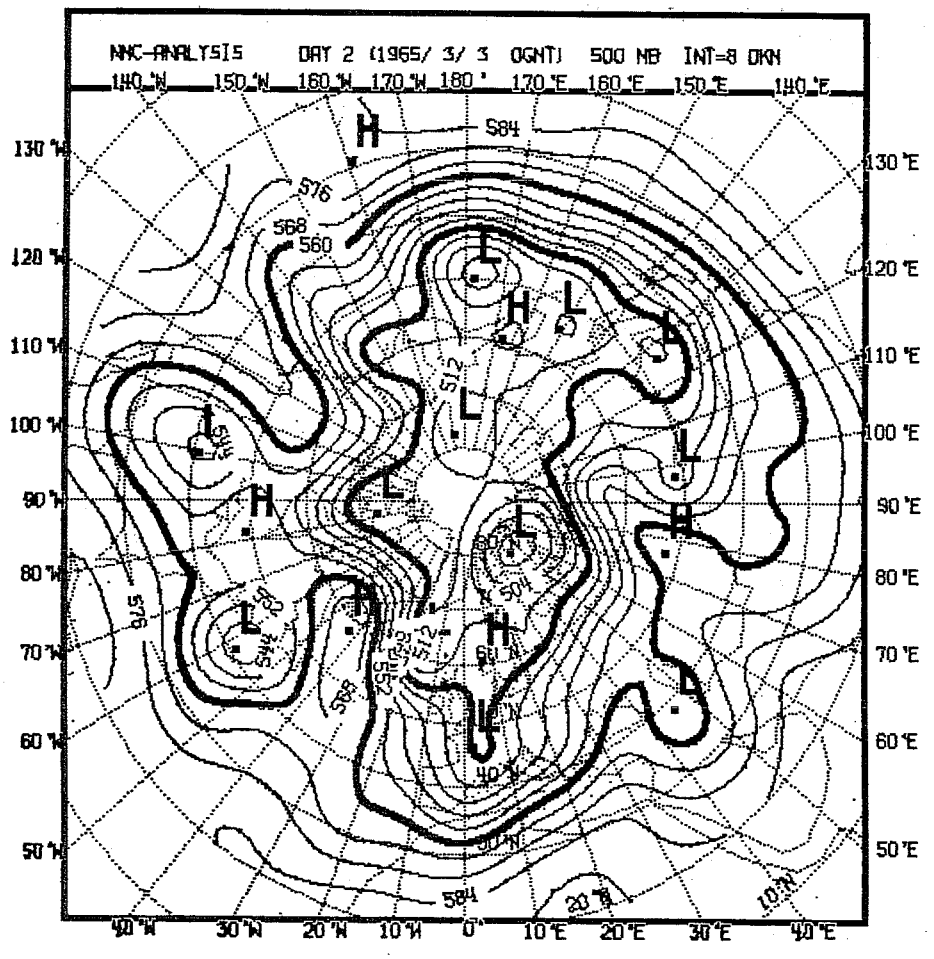
NMC-ANALYSIS DAY 2 (1965/ 3/ 3 0GMT) 500 MB INT=8 DKM
140 °W 150 °W 160 °W 170 °W 180 ° 170 °E 160 °E 150 °E 140 °E
130 °W 120 °W 110 °W 100 °W 90 °W 80 °W 70 °W 60 °W 50 °W
130 °E 120 °E 110 °E 100 °E 90 °E 80 °E 70 °E 60 °E 50 °E
40 °W 30 °W 20 °W 10 °W 0° 10 °E 20 °E 30 °E 40 °E
584
576
568
560
512
504
496
488
80 °N
70 °N
60 °N
50 °N
40 °N
30 °N
20 °N
10 °N

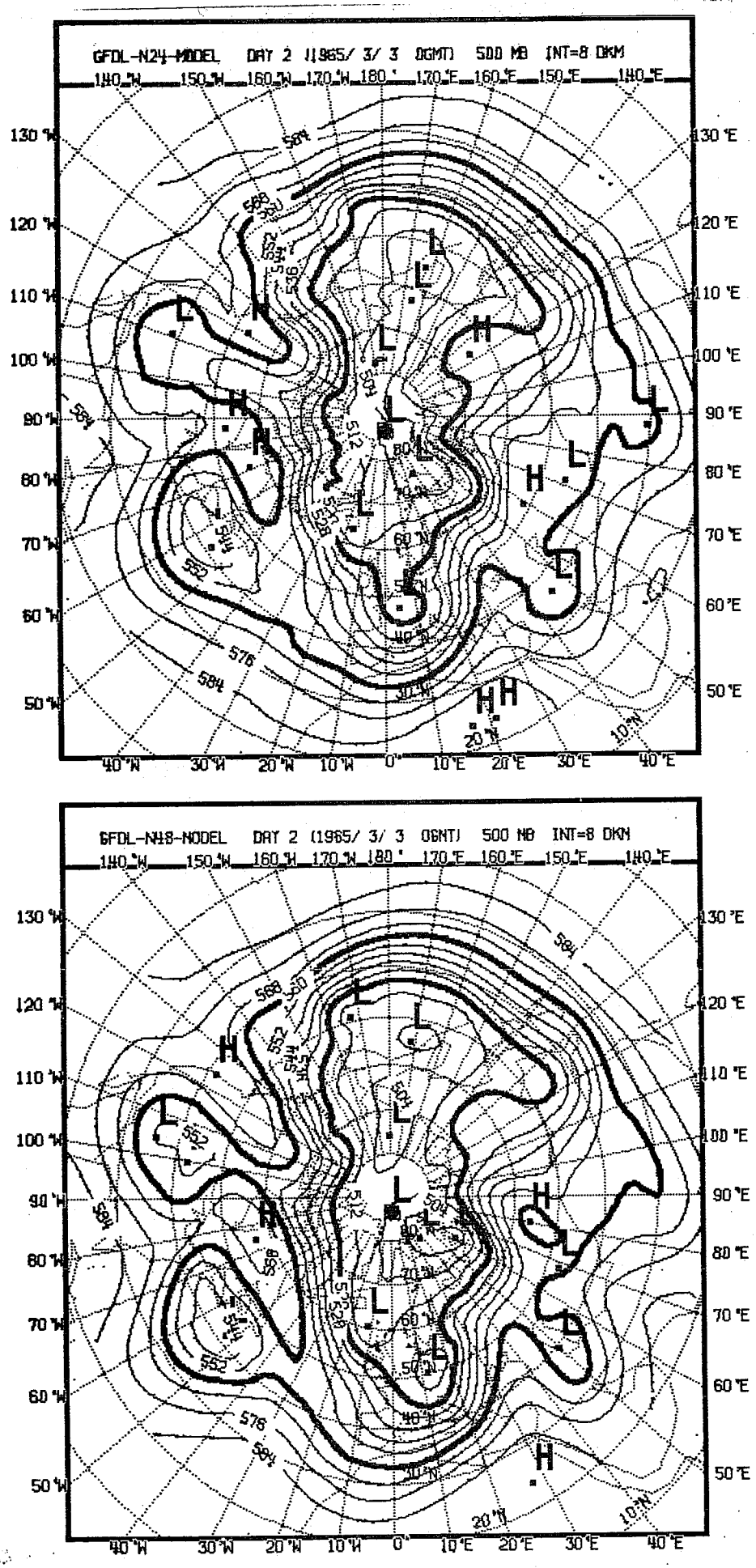

Fig. 4.2.3 :Observed (bottom left) and predicted maps of 500 mb geopotential height, day 2.

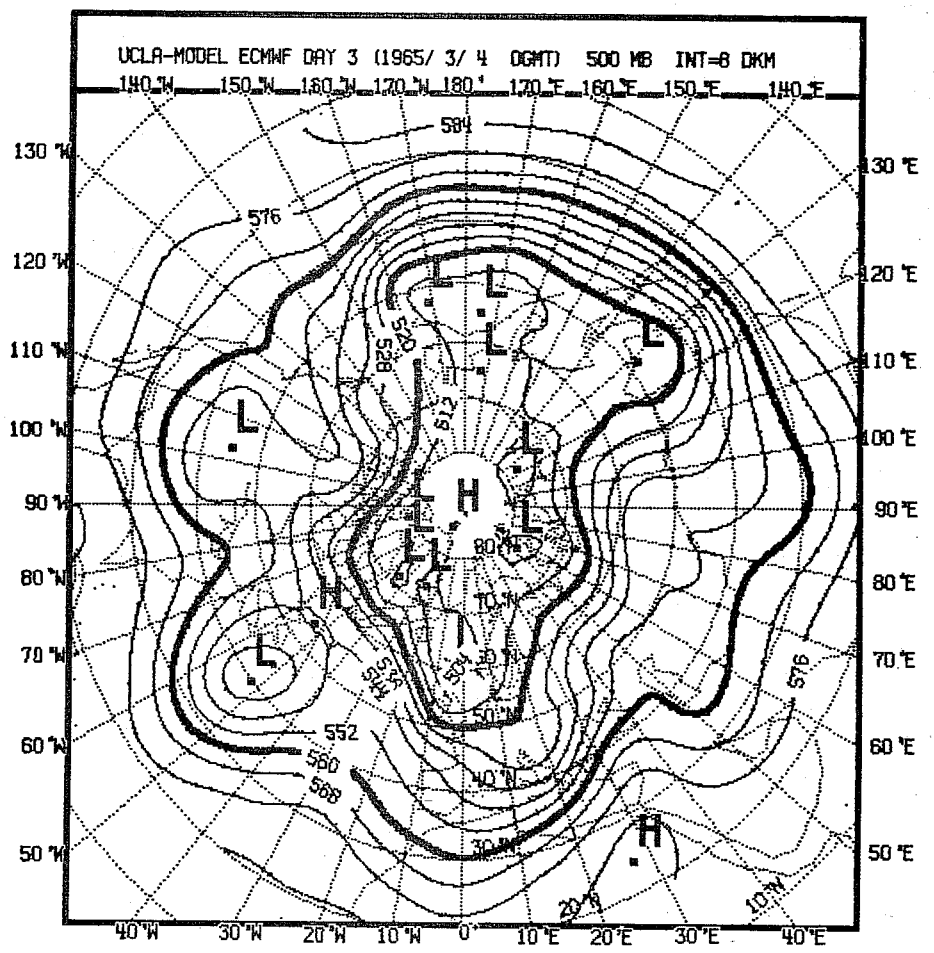
UCLA-MODEL ECMWF DAY 3 (1965/ 3/ 4 0GMT) 500 MB INT=8 DKM
140°W 150°W 160°W 170°W 180° 170°E 160°E 150°E 140°E
130°W 120°W 110°W 100°W 90°W 80°W 70°W 60°W 50°W
130°E 120°E 110°E 100°E 90°E 80°E 70°E 60°E 50°E
40°W 30°W 20°W 10°W 0° 10°E 20°E 30°E 40°E
584
576
568
560
552
544
536
528
520
512
504
496
488
80°N
70°N
60°N
50°N
40°N
30°N
20°N
10°N

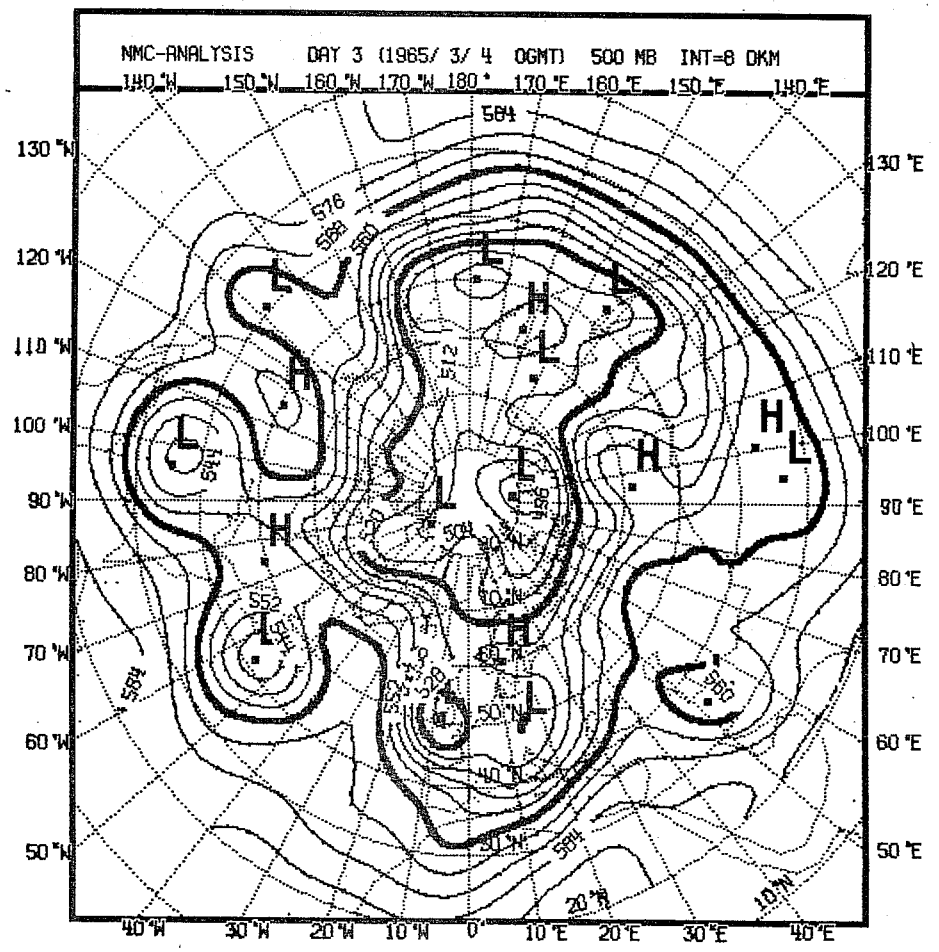
NMC-ANALYSIS DAY 3 (1965/ 3/ 4 0GMT) 500 MB INT=8 DKM
140°W 150°W 160°W 170°W 180° 170°E 160°E 150°E 140°E
130°W 120°W 110°W 100°W 90°W 80°W 70°W 60°W 50°W
130°E 120°E 110°E 100°E 90°E 80°E 70°E 60°E 50°E
40°W 30°W 20°W 10°W 0° 10°E 20°E 30°E 40°E
584
576
568
560
552
544
536
528
520
512
504
496
488
80°N
70°N
60°N
50°N
40°N
30°N
20°N
10°N

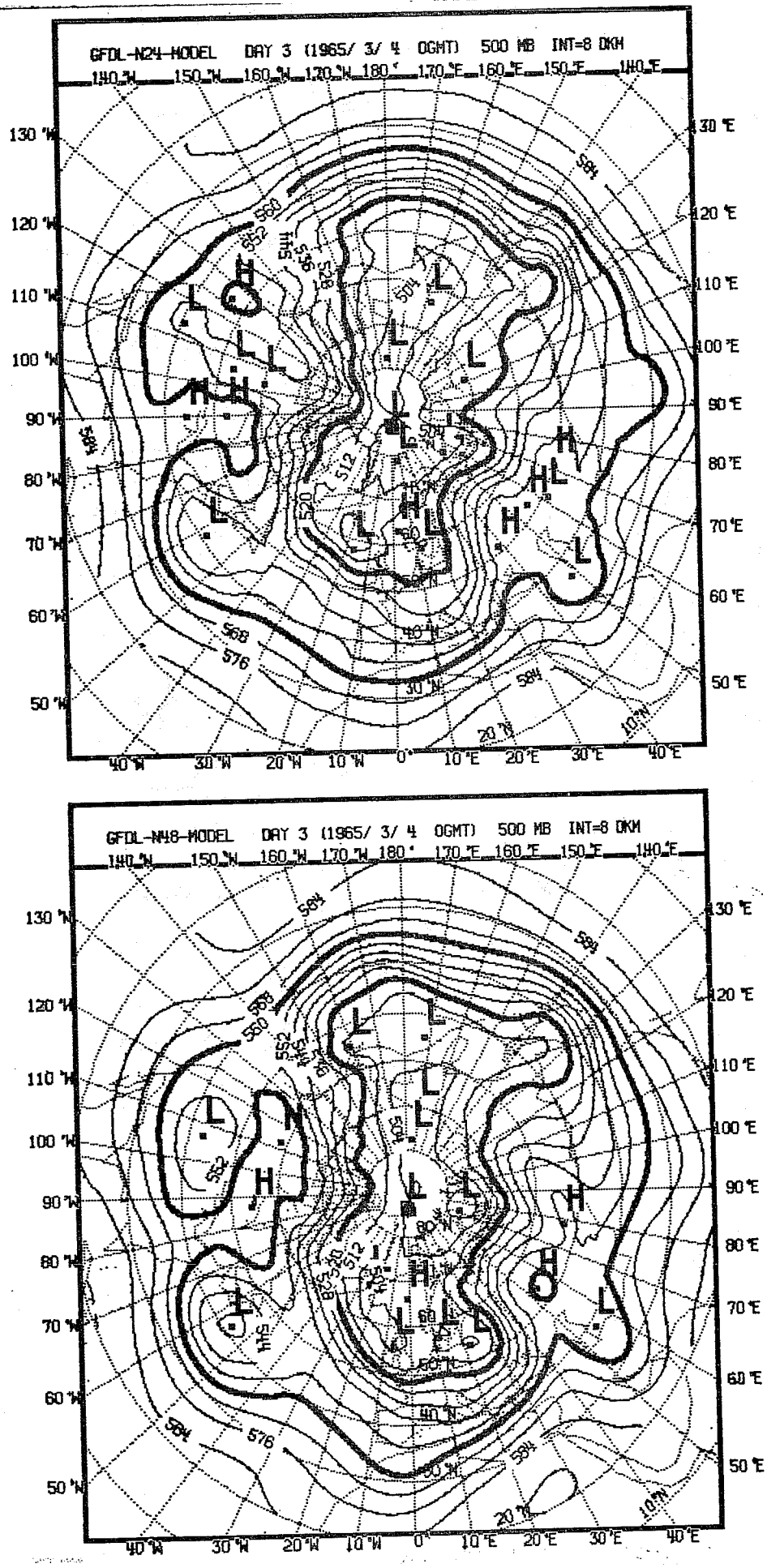

Fig. 4.2.4 :Observed (bottom left) and predicted maps of 500 mb geopotential height, day 3.

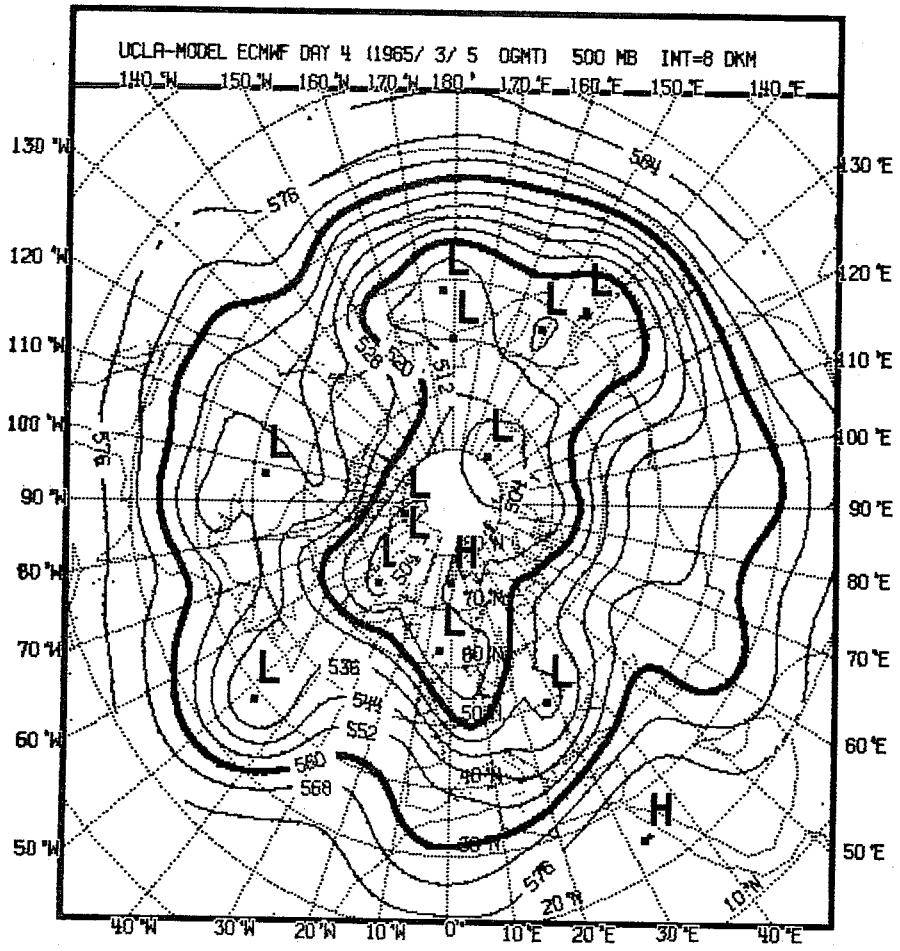
UCLA-MODEL ECMWF DAY 4 (1965/ 3/ 5 0GMT) 500 MB INT=8 DKM
140 °W 150 °W 160 °W 170 °W 180 ° 170 °E 160 °E 150 °E 140 °E
130 °W 120 °W 110 °W 100 °W 90 °W 80 °W 70 °W 60 °W 50 °W
130 °E 120 °E 110 °E 100 °E 90 °E 80 °E 70 °E 60 °E 50 °E
40 °W 30 °W 20 °W 10 °W 0 ° 10 °E 20 °E 30 °E 40 °E
584
576
568
560
552
544
536
528
520
512
504
496
488
70 °N
60 °N
50 °N
40 °N
30 °N
20 °N
10 °N

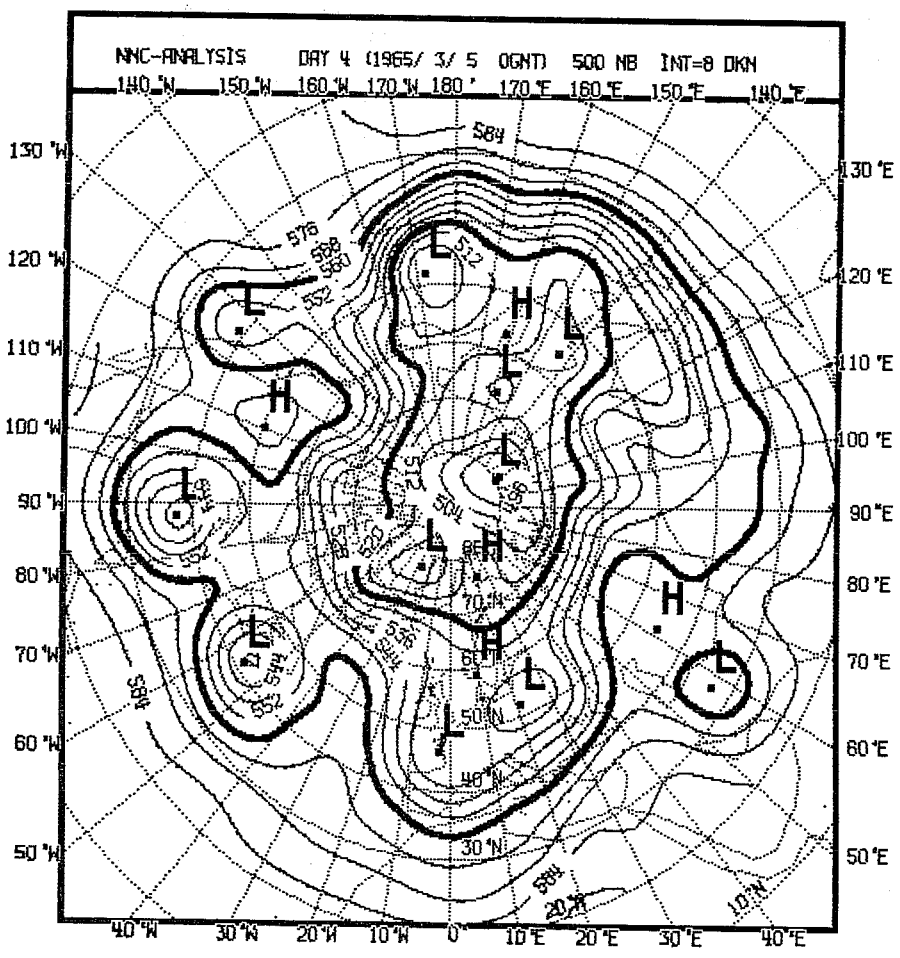
NMC-ANALYSIS DAY 4 (1965/ 3/ 5 0GMT) 500 MB INT=8 DKM
140 °W 150 °W 160 °W 170 °W 180 ° 170 °E 160 °E 150 °E 140 °E
130 °W 120 °W 110 °W 100 °W 90 °W 80 °W 70 °W 60 °W 50 °W
130 °E 120 °E 110 °E 100 °E 90 °E 80 °E 70 °E 60 °E 50 °E
40 °W 30 °W 20 °W 10 °W 0 ° 10 °E 20 °E 30 °E 40 °E
584
576
568
560
552
544
536
528
520
512
504
496
488
480
70 °N
60 °N
50 °N
40 °N
30 °N
20 °N
10 °N

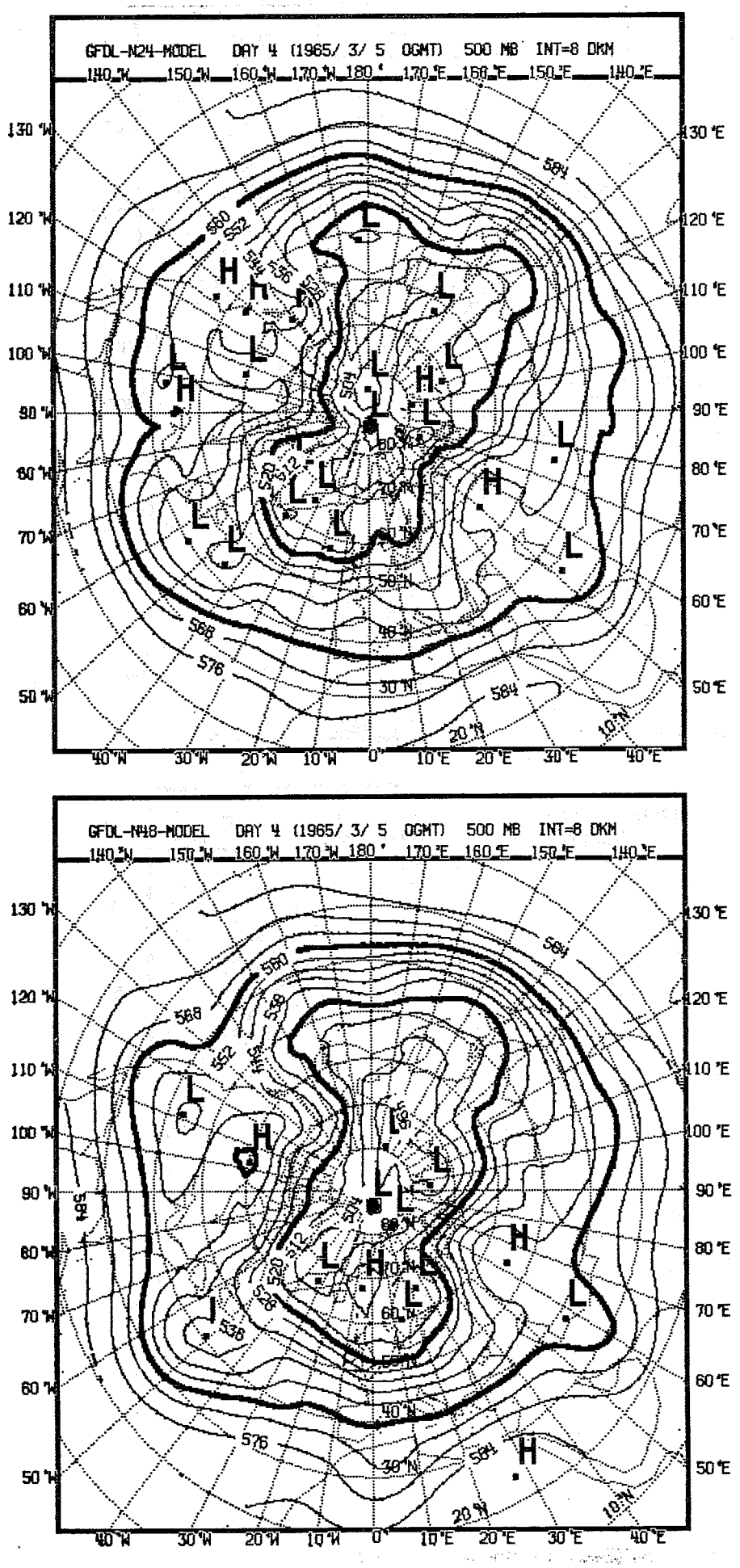

Fig. 4.2.5 :Observed (bottom left) and predicted maps of 500 mb geopotential height, day 4.

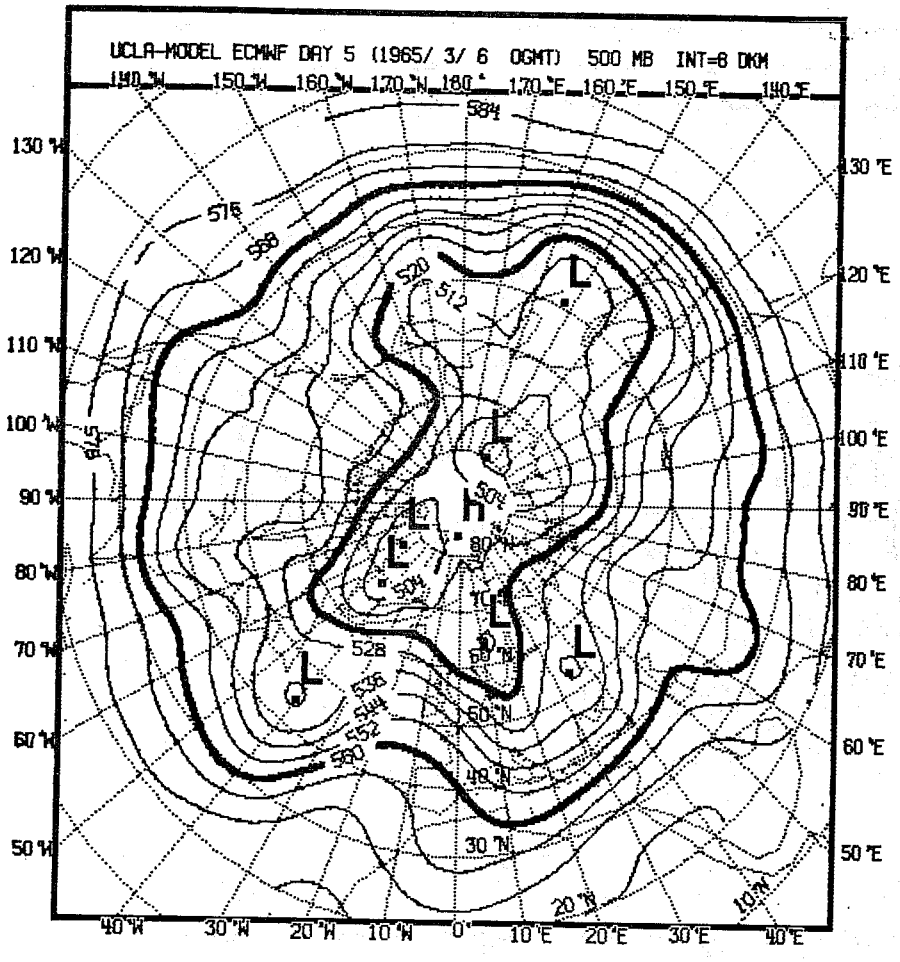
UCLA-MODEL ECMWF DAY 5 (1965/ 3/ 6 0GMT) 500 MB INT=8 DKM
140 °W 150 °W 160 °W 170 °W 180 ° 170 °E 160 °E 150 °E 140 °E
130 °W 120 °W 110 °W 100 °W 90 °W 80 °W 70 °W 60 °W 50 °W
130 °E 120 °E 110 °E 100 °E 90 °E 80 °E 70 °E 60 °E 50 °E
40 °W 30 °W 20 °W 10 °W 0 ° 10 °E 20 °E 30 °E 40 °E
80 °N 70 °N 60 °N 50 °N 40 °N 30 °N 20 °N 10 °N
584
576
568
560
552
544
536
528
520
512
504
496
488
480
H
L

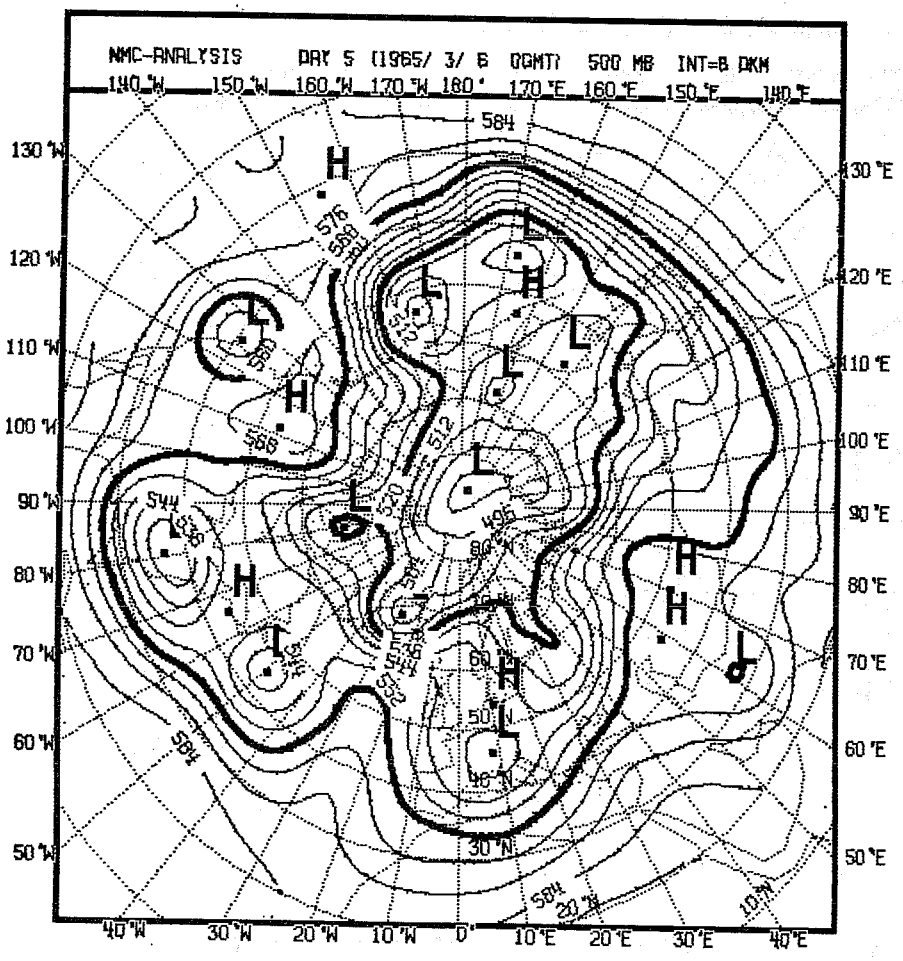
NMC-ANALYSIS DAY 5 (1965/ 3/ 6 0GMT) 500 MB INT=8 DKM
140 °W 150 °W 160 °W 170 °W 180 ° 170 °E 160 °E 150 °E 140 °E
130 °W 120 °W 110 °W 100 °W 90 °W 80 °W 70 °W 60 °W 50 °W
130 °E 120 °E 110 °E 100 °E 90 °E 80 °E 70 °E 60 °E 50 °E
40 °W 30 °W 20 °W 10 °W 0 ° 10 °E 20 °E 30 °E 40 °E
80 °N 70 °N 60 °N 50 °N 40 °N 30 °N 20 °N 10 °N
584
576
568
560
552
544
536
528
520
512
504
496
488
480
H
L

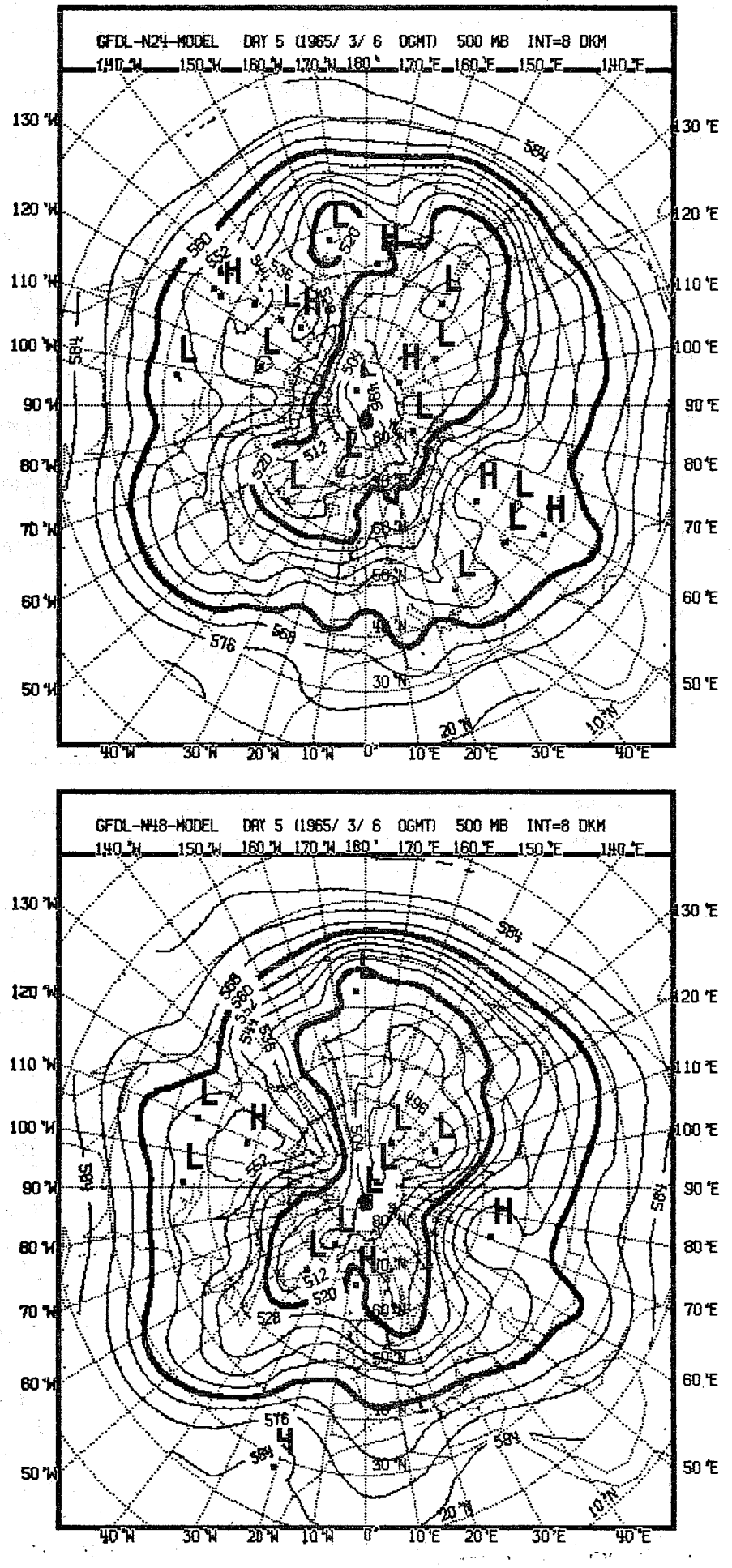

Fig. 4.2.6: Observed (bottom left) and predicted maps of 500 mb geopotential height, day 5.

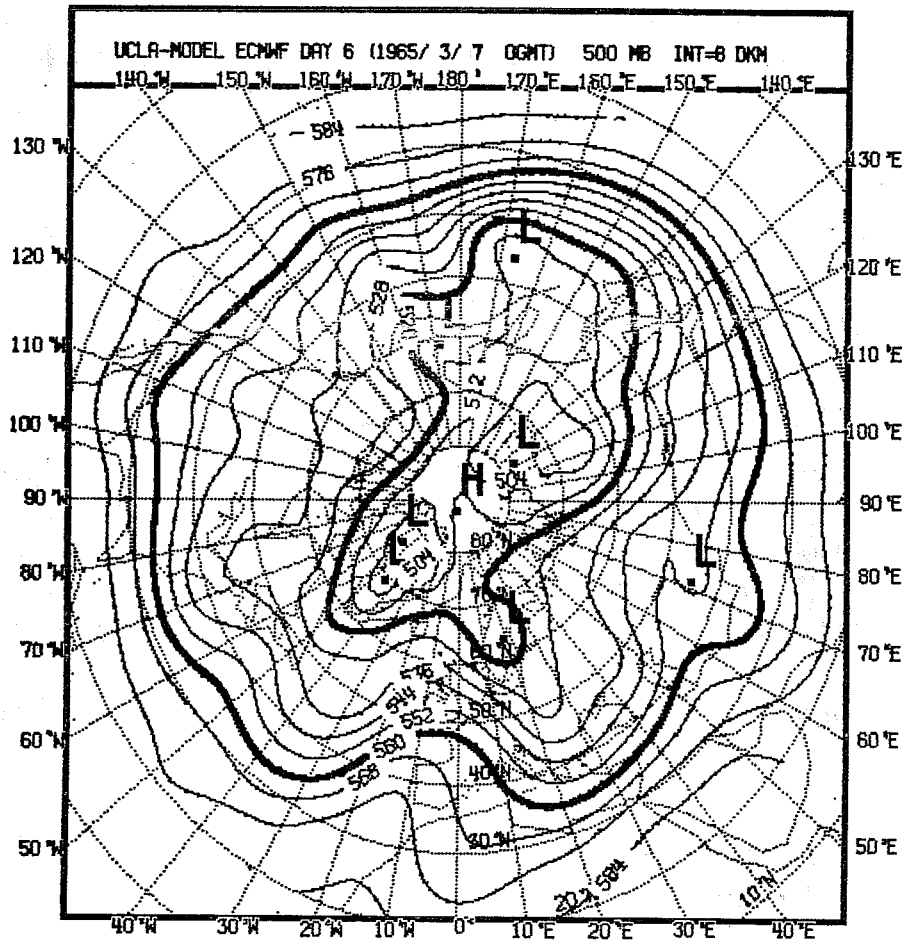
UCLA-MODEL ECMWF DAY 6 (1965/ 3/ 7 0GMT) 500 MB INT=8 DKM
140°W 150°W 160°W 170°W 180° 170°E 160°E 150°E 140°E
130°W 120°W 110°W 100°W 90°W 80°W 70°W 60°W 50°W
130°E 120°E 110°E 100°E 90°E 80°E 70°E 60°E 50°E
40°W 30°W 20°W 10°W 0° 10°E 20°E 30°E 40°E
584
576
568
560
552
544
536
528
520
512
504
496
488
480
60°N
50°N
40°N
30°N
20°N
10°N
H
L

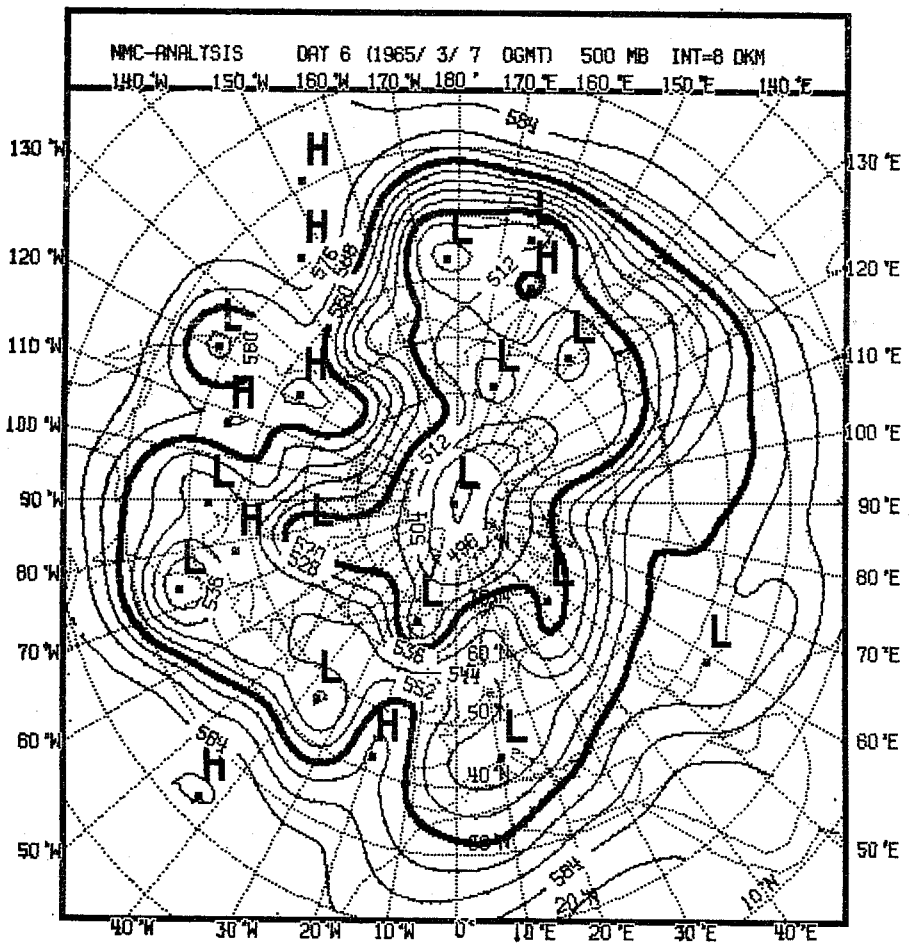
NMC-ANALYSIS DAY 6 (1965/ 3/ 7 0GMT) 500 MB INT=8 DKM
140°W 150°W 160°W 170°W 180° 170°E 160°E 150°E 140°E
130°W 120°W 110°W 100°W 90°W 80°W 70°W 60°W 50°W
130°E 120°E 110°E 100°E 90°E 80°E 70°E 60°E 50°E
40°W 30°W 20°W 10°W 0° 10°E 20°E 30°E 40°E
584
576
568
560
552
544
536
528
520
512
504
496
488
480
60°N
50°N
40°N
30°N
20°N
10°N
H
L

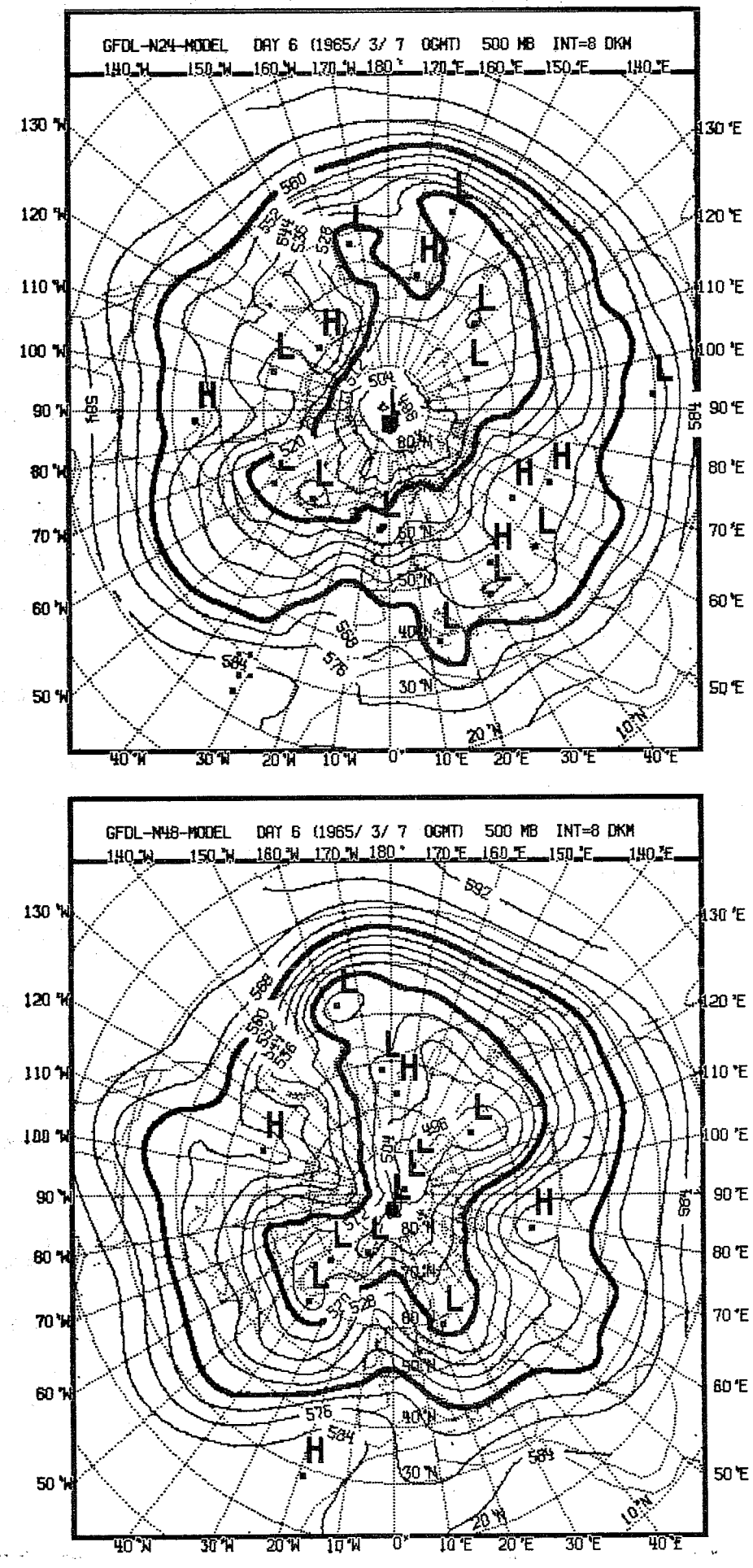

Fig. 4.2.7: Observed (bottom left) and predicted maps o
500 mb geopotential height, day 6.

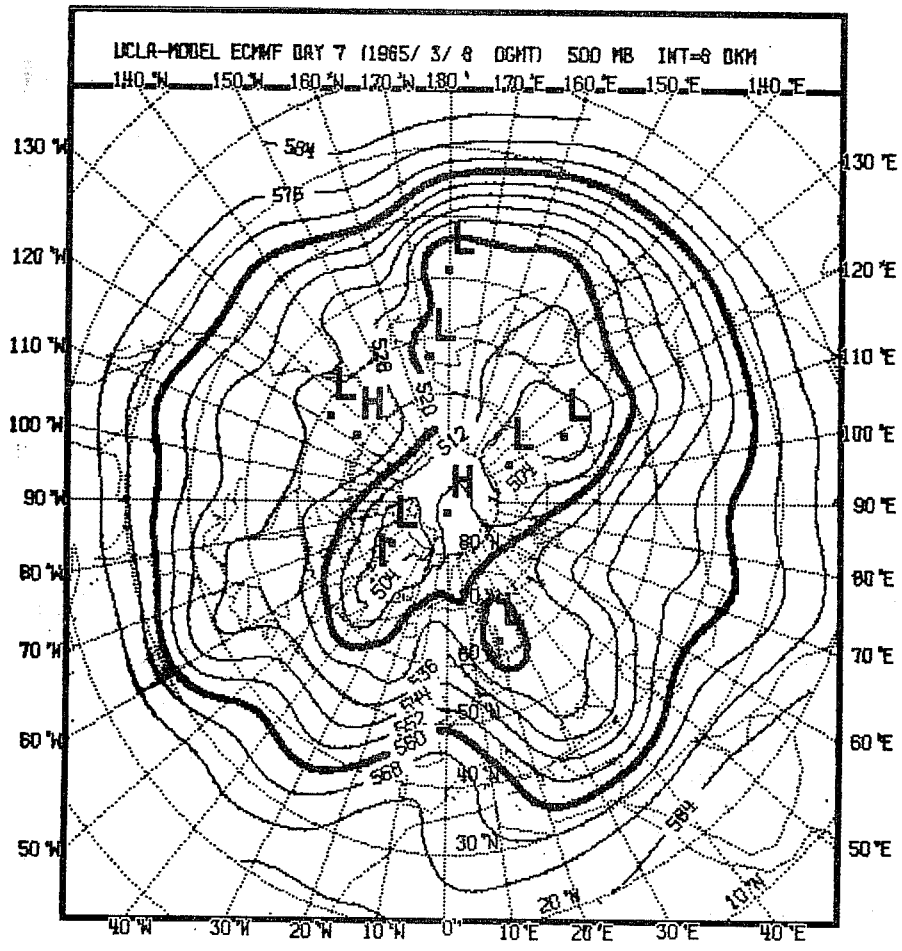
UCLA-MODEL ECMWF DAY 7 (1965/ 3/ 8 0GMT) 500 MB INT=8 DKM
140 °W 150 °W 160 °W 170 °W 180 ° 170 °E 160 °E 150 °E 140 °E
130 °W 120 °W 110 °W 100 °W 90 °W 80 °W 70 °W 60 °W 50 °W
130 °E 120 °E 110 °E 100 °E 90 °E 80 °E 70 °E 60 °E 50 °E
40 °W 30 °W 20 °W 10 °W 0° 10 °E 20 °E 30 °E 40 °E
584
576
568
560
552
544
536
528
520
512
504
496
488
480
30 °N
20 °N
10 °N

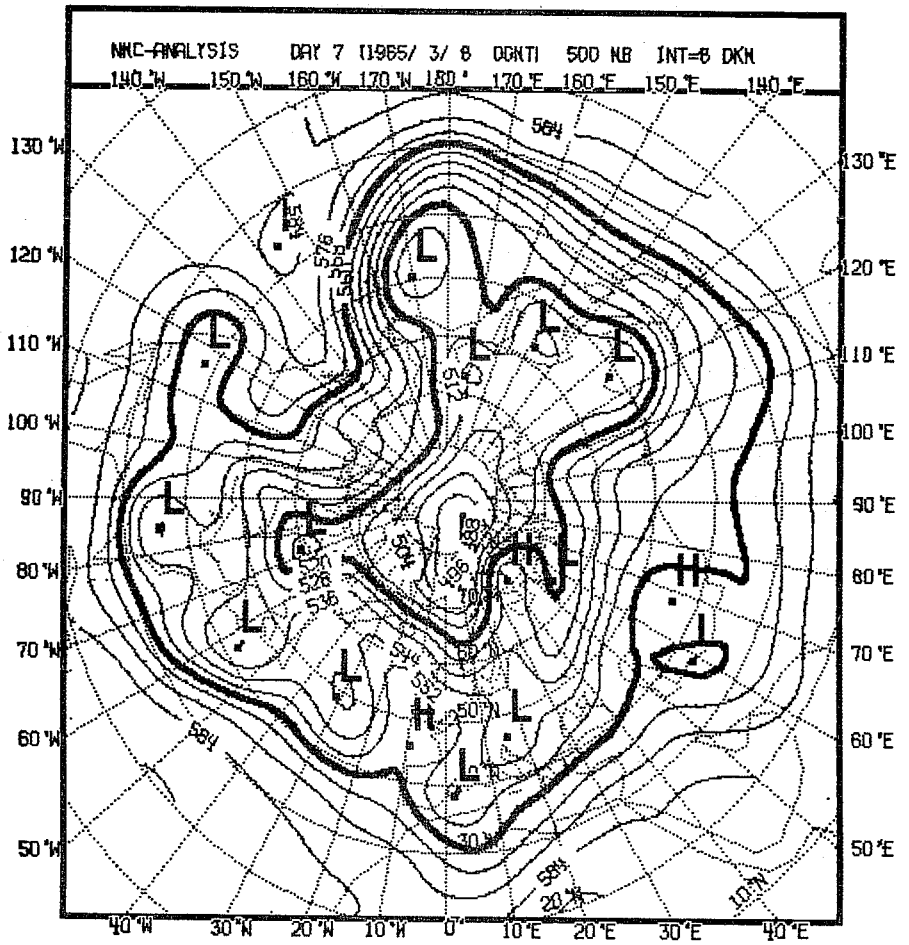
NMC-ANALYSIS DAY 7 (1965/ 3/ 8 0GMT) 500 MB INT=8 DKM
140 °W 150 °W 160 °W 170 °W 180 ° 170 °E 160 °E 150 °E 140 °E
130 °W 120 °W 110 °W 100 °W 90 °W 80 °W 70 °W 60 °W 50 °W
130 °E 120 °E 110 °E 100 °E 90 °E 80 °E 70 °E 60 °E 50 °E
40 °W 30 °W 20 °W 10 °W 0° 10 °E 20 °E 30 °E 40 °E
584
576
568
560
552
544
536
528
520
512
504
496
488
480
30 °N
20 °N
10 °N

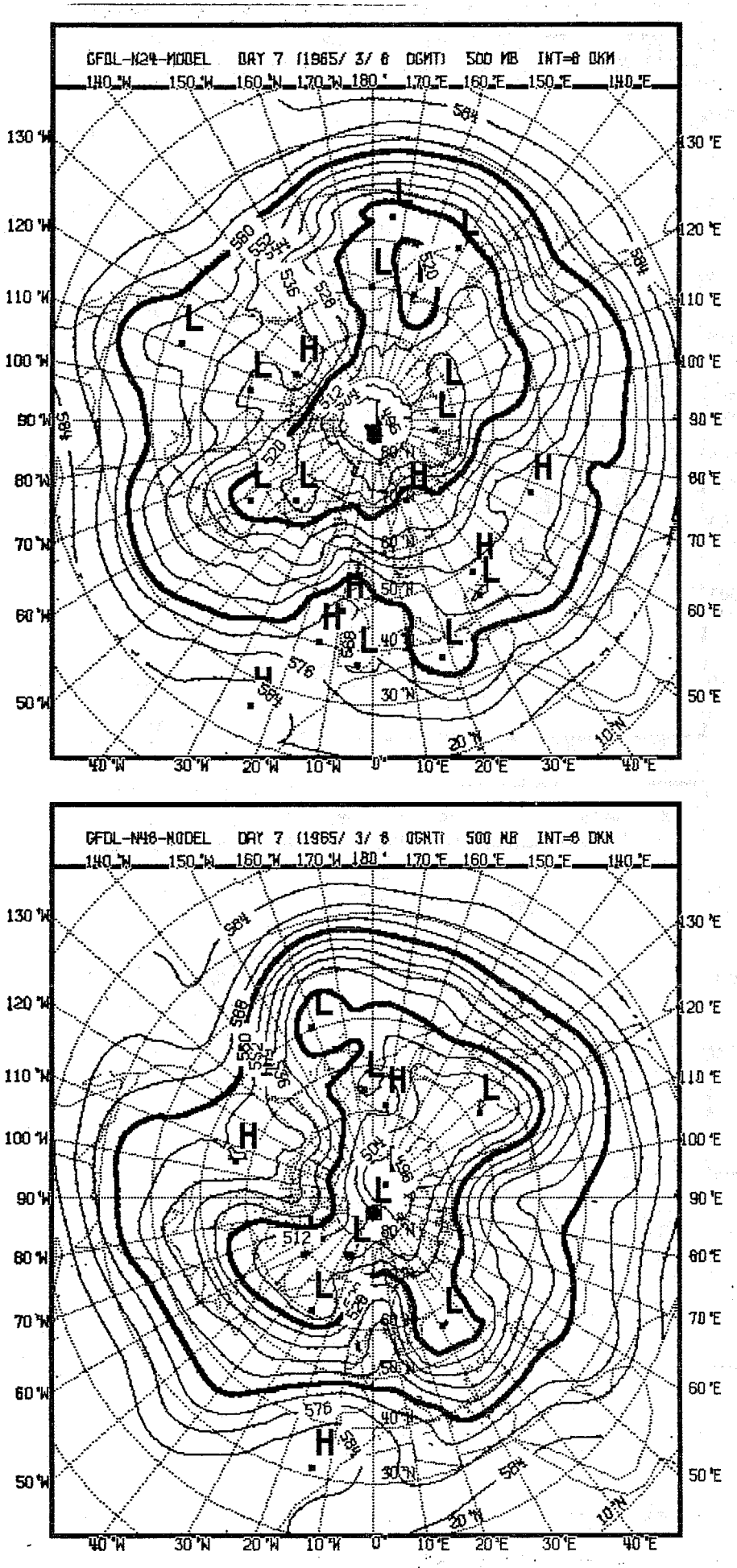

Fig. 4.2.8: Observed (bottom left) and predicted maps of 500 mb geopotential height, day 7.

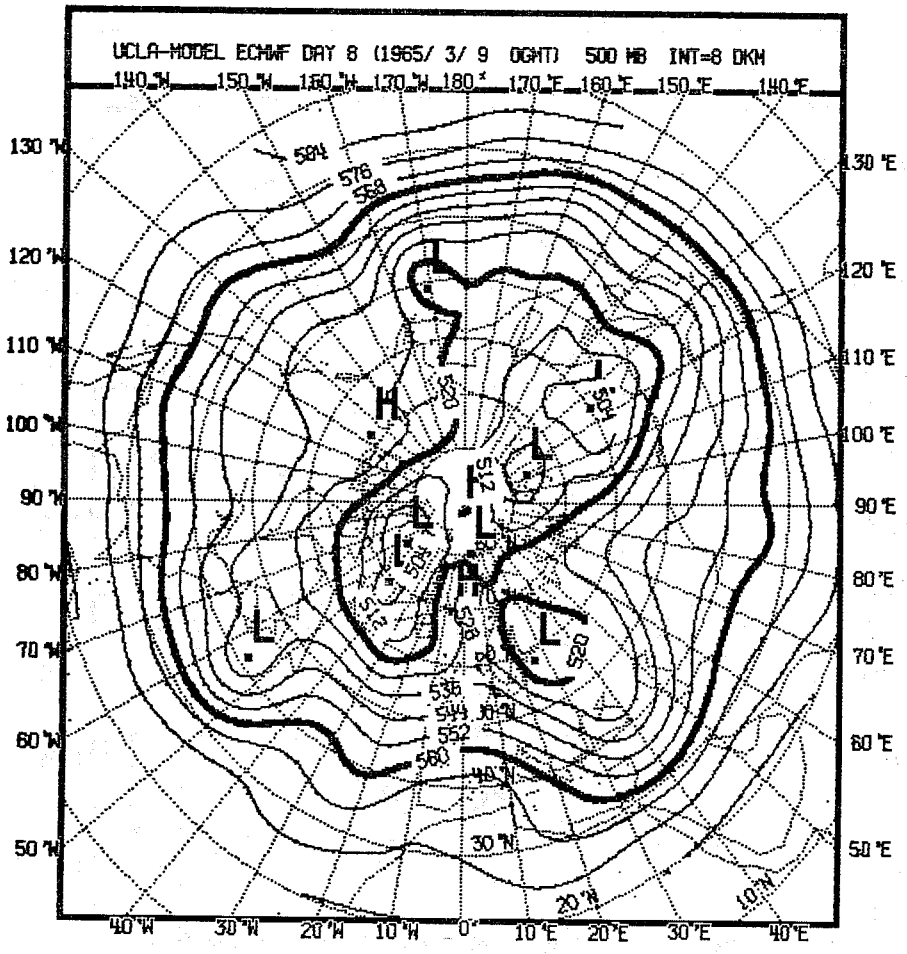
UCLA-MODEL ECMWF DAY 8 (1965/ 3/ 9 0GMT) 500 MB INT=8 DKM
140°W 150°W 160°W 170°W 180° 170°E 160°E 150°E 140°E
130°W 120°W 110°W 100°W 90°W 80°W 70°W 60°W 50°W
130°E 120°E 110°E 100°E 90°E 80°E 70°E 60°E 50°E
40°W 30°W 20°W 10°W 0° 10°E 20°E 30°E 40°E
584
576
568
520
512
528
536
544
552
560
70°N
60°N
40°N
30°N
20°N
10°N
H
L

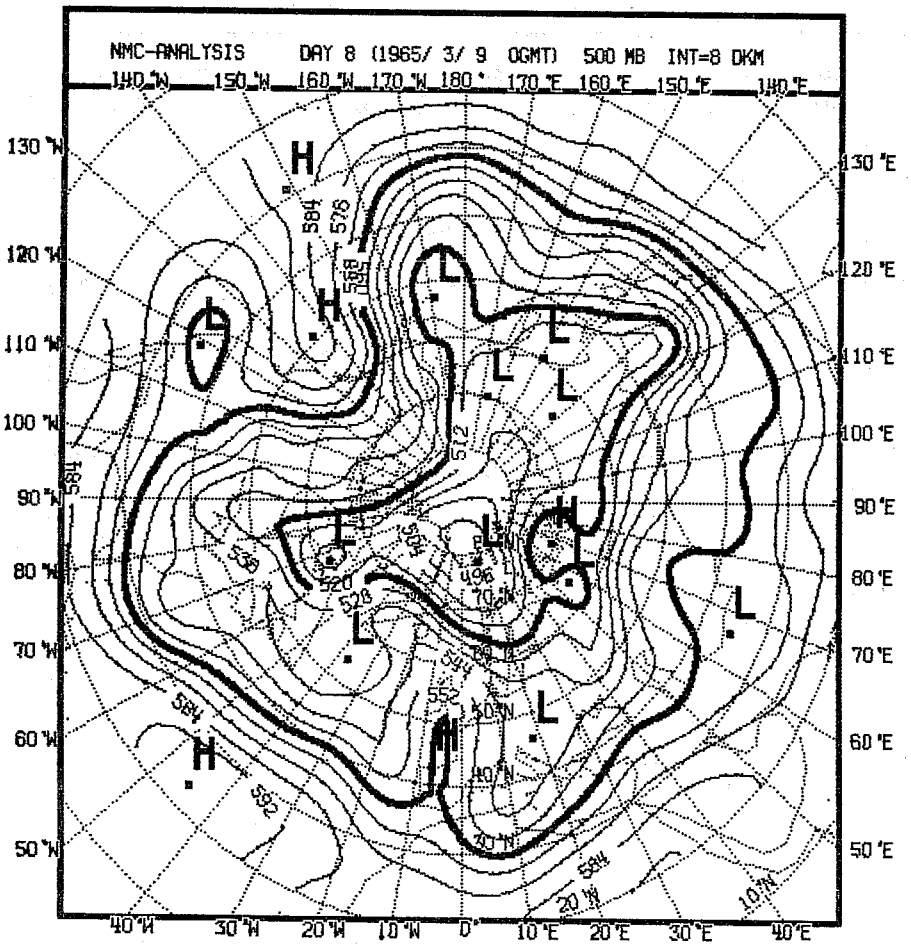
NMC-ANALYSIS DAY 8 (1965/ 3/ 9 0GMT) 500 MB INT=8 DKM
140°W 150°W 160°W 170°W 180° 170°E 160°E 150°E 140°E
130°W 120°W 110°W 100°W 90°W 80°W 70°W 60°W 50°W
130°E 120°E 110°E 100°E 90°E 80°E 70°E 60°E 50°E
40°W 30°W 20°W 10°W 0° 10°E 20°E 30°E 40°E
584
576
568
512
520
528
496
70°N
60°N
40°N
20°N
10°N
H
L

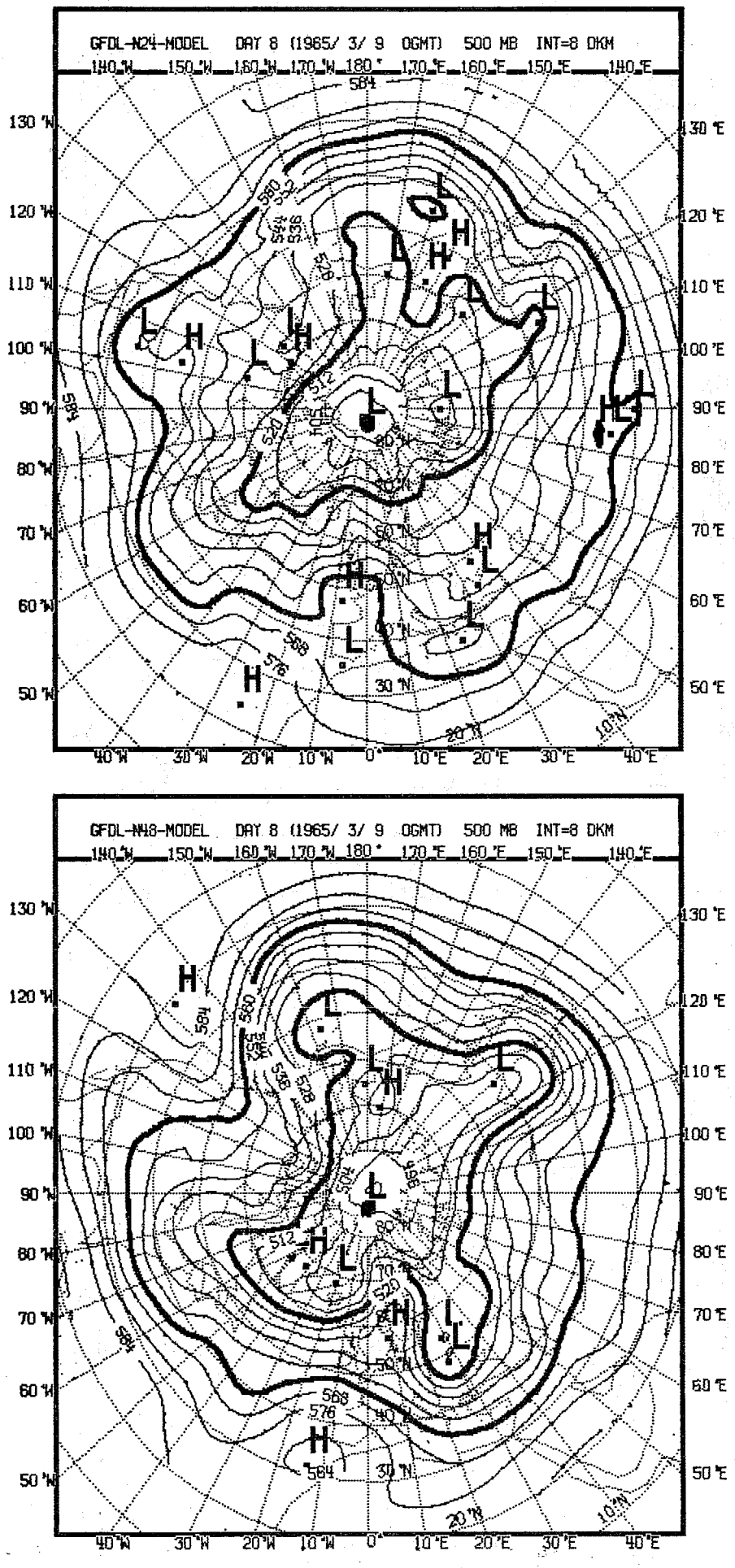

Fig.4.2.9: Observed (bottom left) and predicted maps of 500 mb geopotential height, day 8.

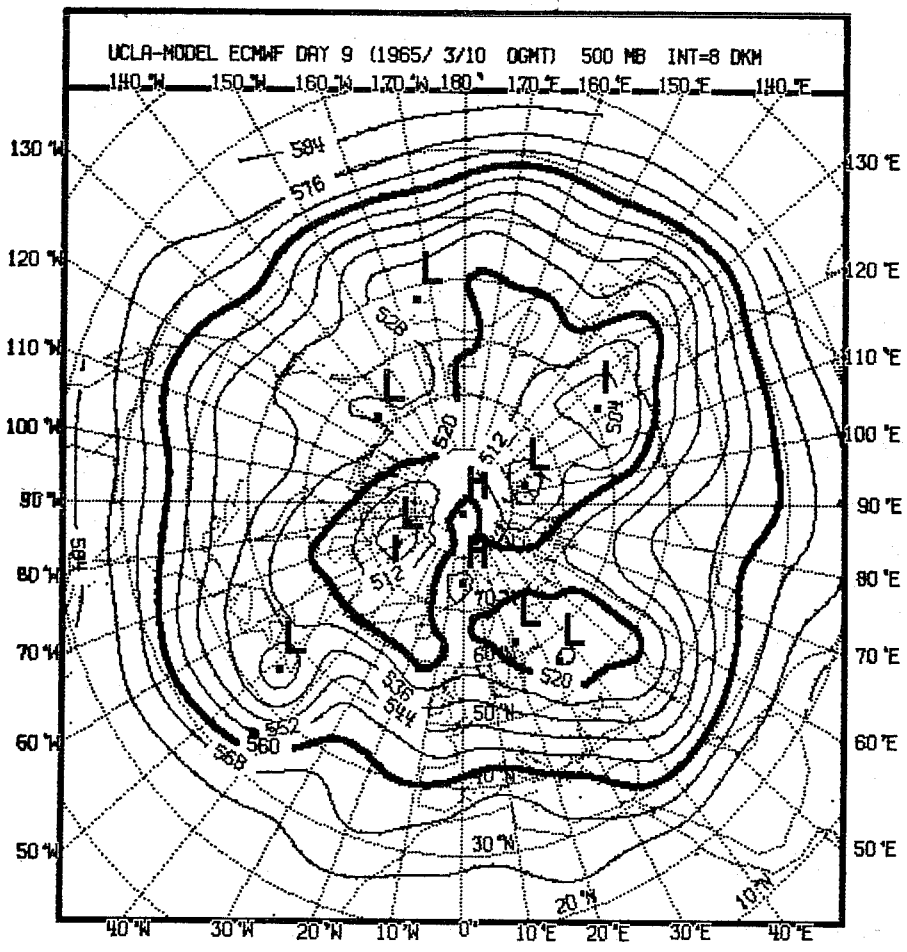
UCLA-MODEL ECMWF DAY 9 (1965/ 3/10 0GMT) 500 MB INT=8 DKM
140 °W 150 °W 160 °W 170 °W 180 ° 170 °E 160 °E 150 °E 140 °E
130 °W 120 °W 110 °W 100 °W 90 °W 80 °W 70 °W 60 °W 50 °W
130 °E 120 °E 110 °E 100 °E 90 °E 80 °E 70 °E 60 °E 50 °E
584 576 568 560 552 544 536 528 520 512 504 496 488
50 °N 40 °N 30 °N 20 °N 10 °N
40 °W 30 °W 20 °W 10 °W 0° 10 °E 20 °E 30 °E 40 °E

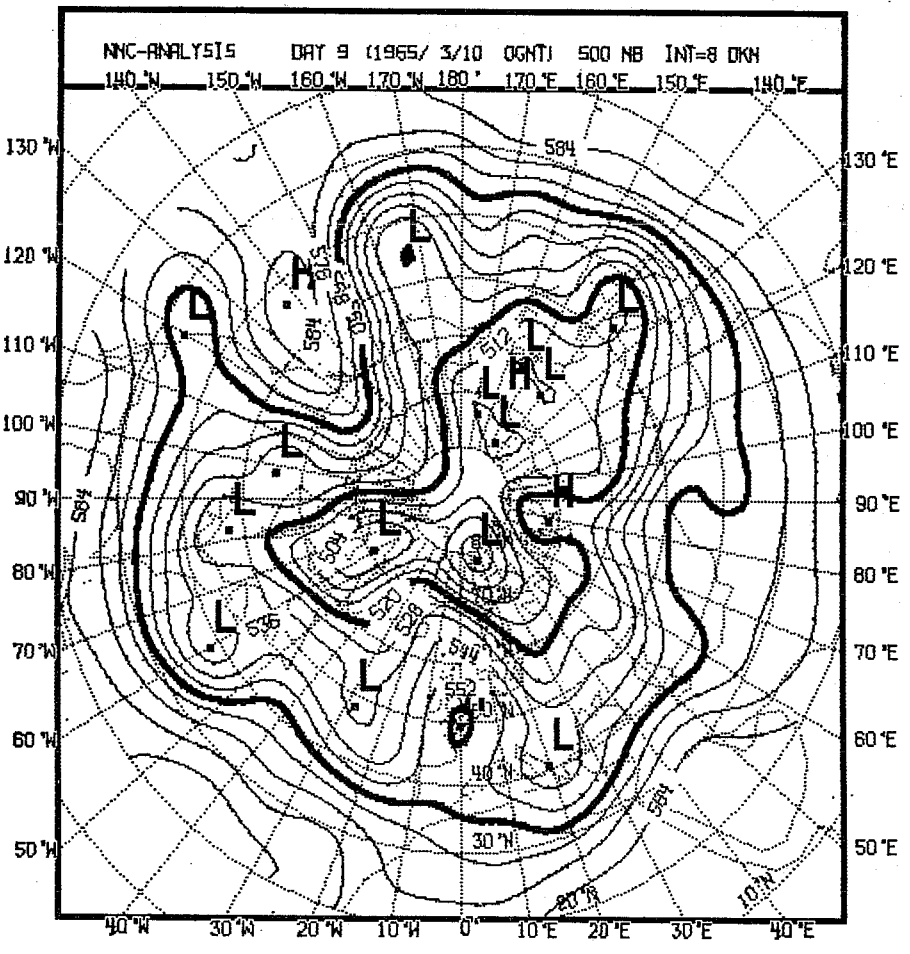
NMC-ANALYSIS DAY 9 (1965/ 3/10 0GMT) 500 MB INT=8 DKM
140 °W 150 °W 160 °W 170 °W 180 ° 170 °E 160 °E 150 °E 140 °E
130 °W 120 °W 110 °W 100 °W 90 °W 80 °W 70 °W 60 °W 50 °W
130 °E 120 °E 110 °E 100 °E 90 °E 80 °E 70 °E 60 °E 50 °E
584 576 568 560 552 544 536 528 520 512 504 496 488
50 °N 40 °N 30 °N 20 °N 10 °N
40 °W 30 °W 20 °W 10 °W 0° 10 °E 20 °E 30 °E 40 °E

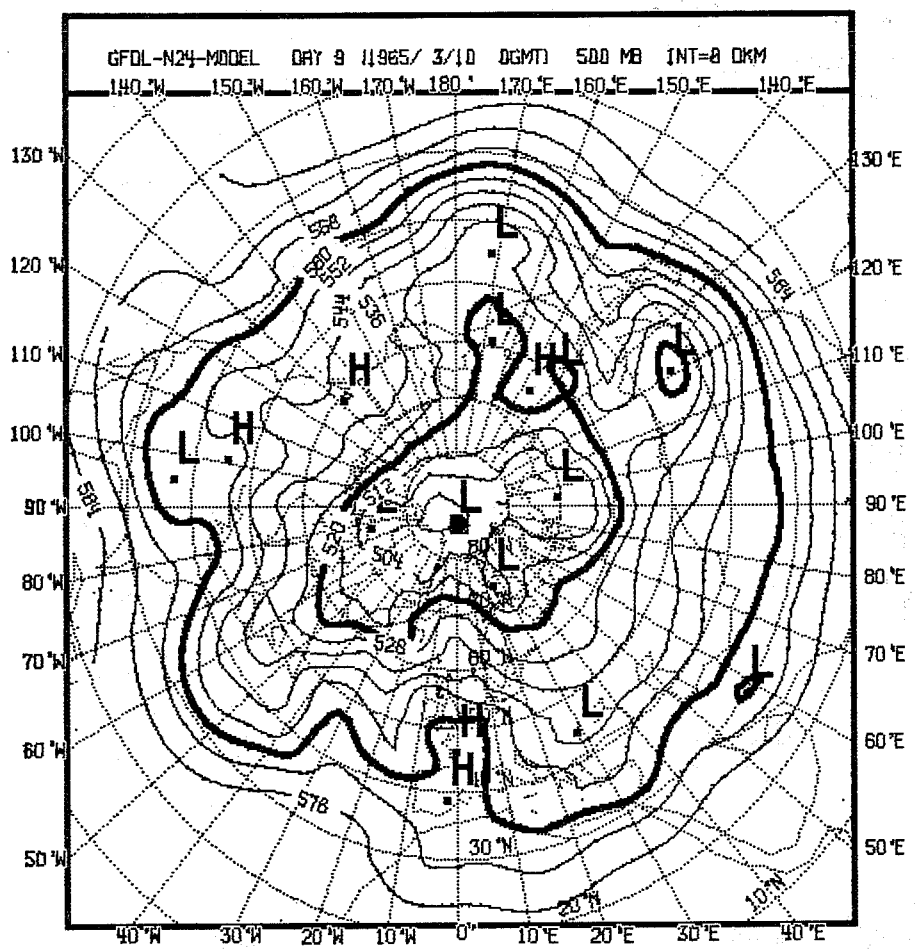

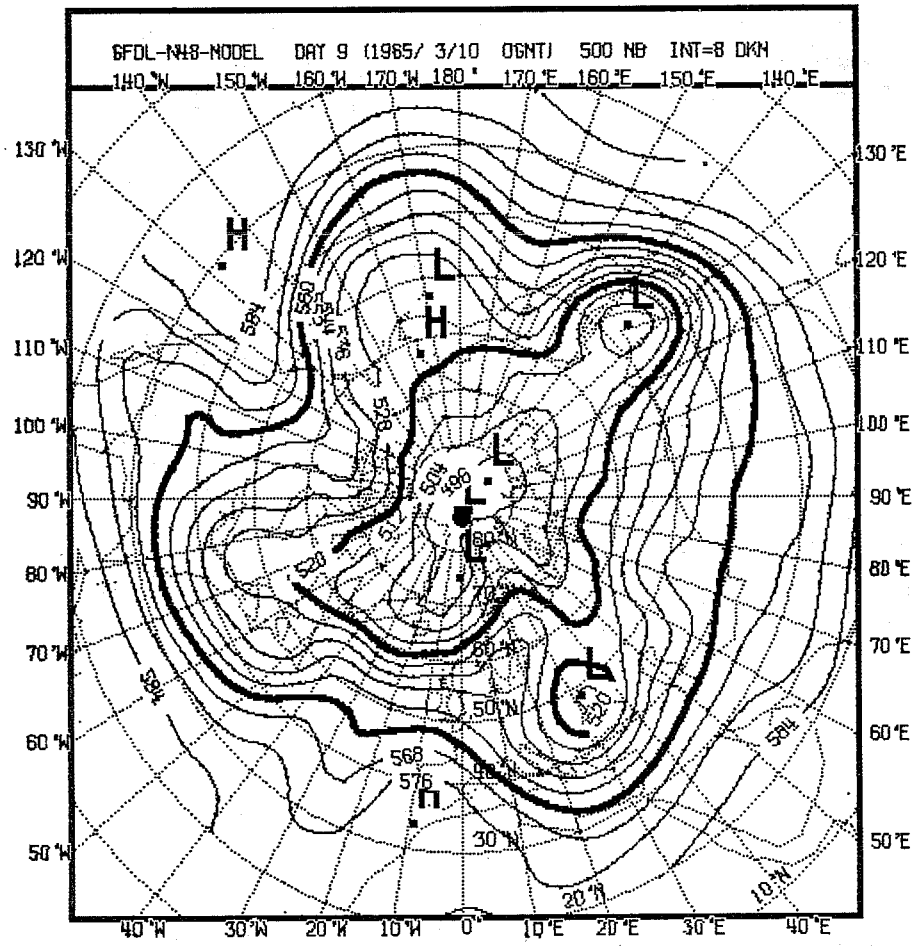

Fig. 4.2.10: Observed (bottom left) and predicted maps of 500 mb geopotential height, day 9.

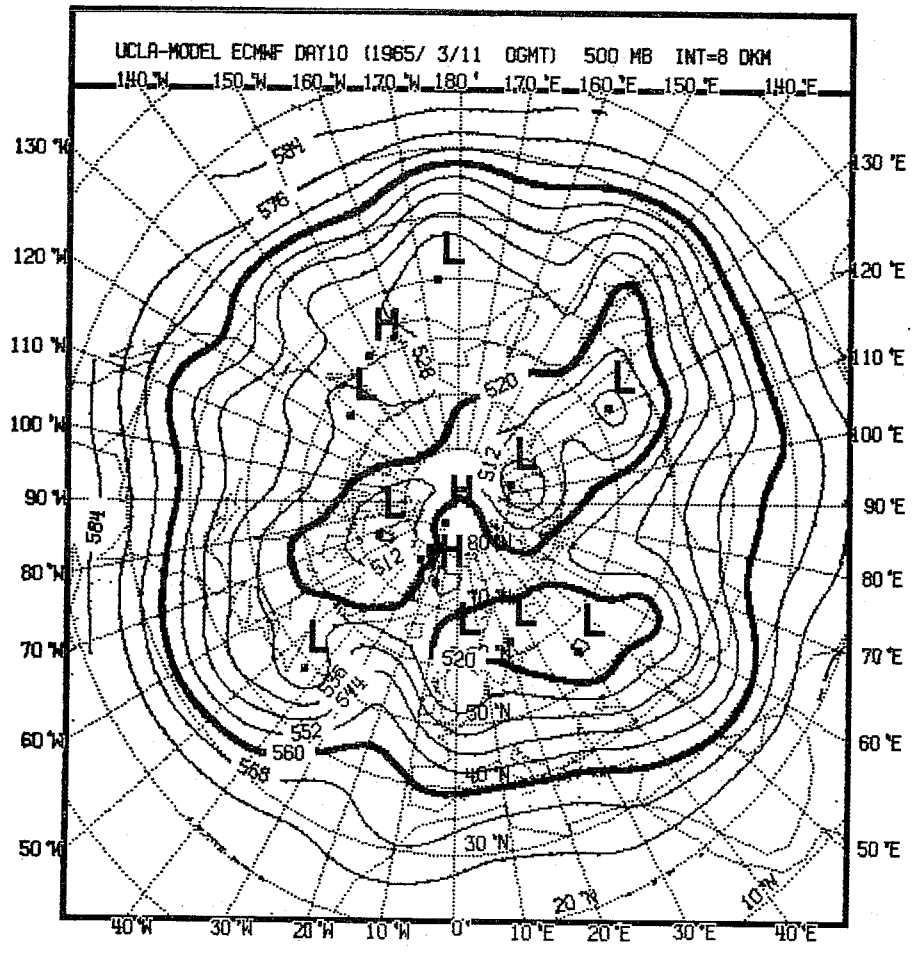
UCLA-MODEL ECMWF DAY10 (1965/ 3/11 0GMT) 500 MB INT=8 DKM
140 °W 150 °W 160 °W 170 °W 180 ° 170 °E 160 °E 150 °E 140 °E
130 °W 120 °W 110 °W 100 °W 90 °W 80 °W 70 °W 60 °W 50 °W
130 °E 120 °E 110 °E 100 °E 90 °E 80 °E 70 °E 60 °E 50 °E
40 °W 30 °W 20 °W 10 °W 0° 10 °E 20 °E 30 °E 40 °E
584
576
568
552
560
536
544
528
520
512
80 °N
70 °N
60 °N
40 °N
30 °N
20 °N
10 °N

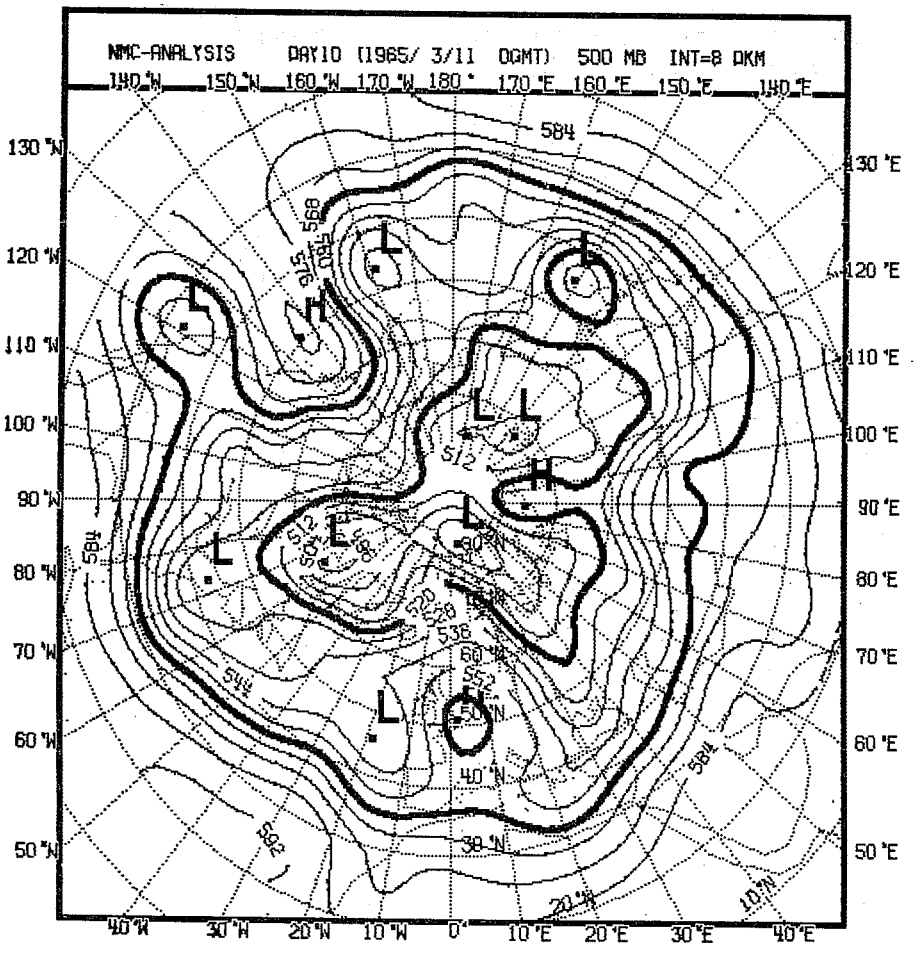
NMC-ANALYSIS DAY10 (1965/ 3/11 0GMT) 500 MB INT=8 DKM
140 °W 150 °W 160 °W 170 °W 180 ° 170 °E 160 °E 150 °E 140 °E
130 °W 120 °W 110 °W 100 °W 90 °W 80 °W 70 °W 60 °W 50 °W
130 °E 120 °E 110 °E 100 °E 90 °E 80 °E 70 °E 60 °E 50 °E
40 °W 30 °W 20 °W 10 °W 0° 10 °E 20 °E 30 °E 40 °E
584
576
568
560
552
544
536
528
520
512
592
80 °N
70 °N
60 °N
50 °N
40 °N
30 °N
20 °N
10 °N

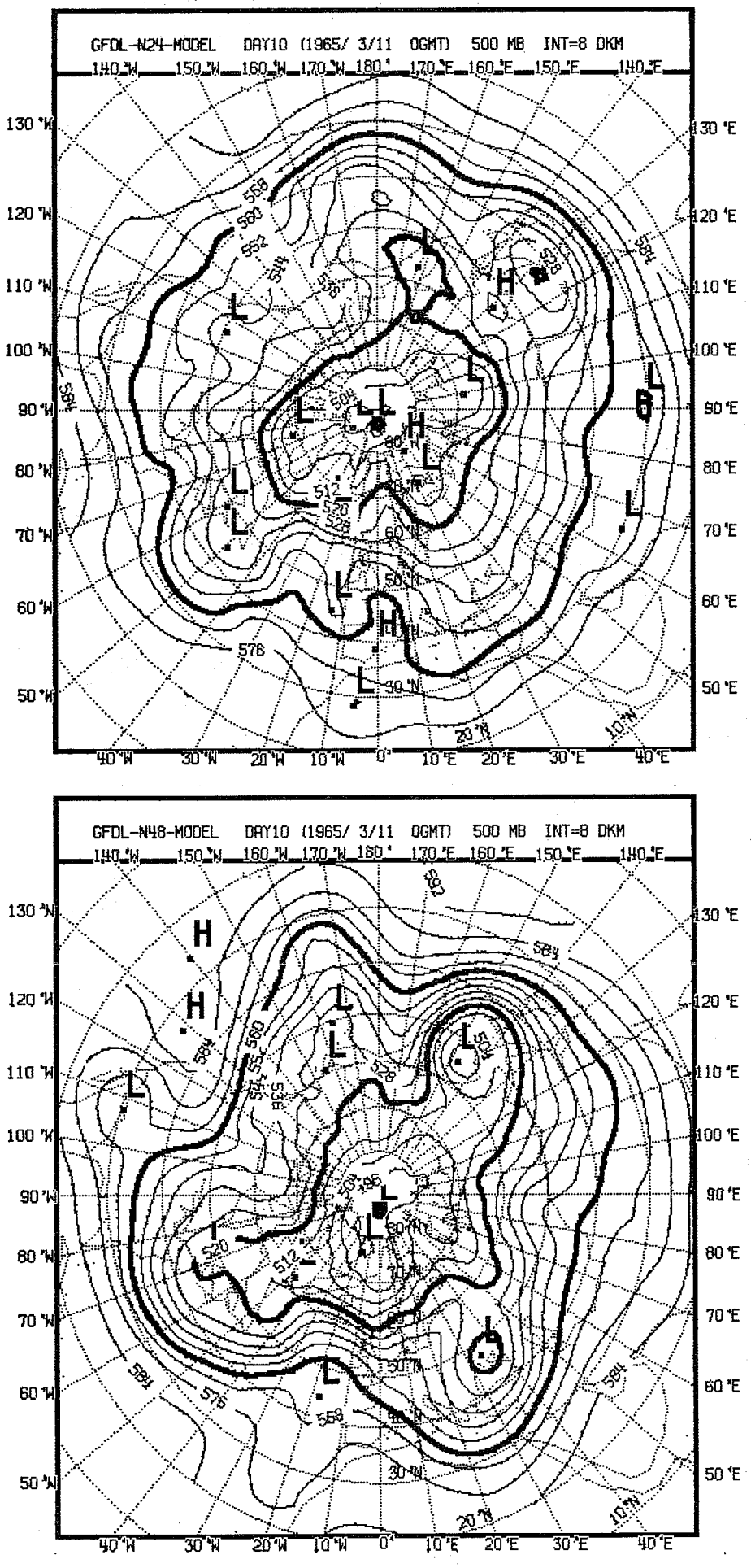

Fig. 4.2.11: Observed (bottom left) and predicted maps of 500 mb geopotential height, day 10.

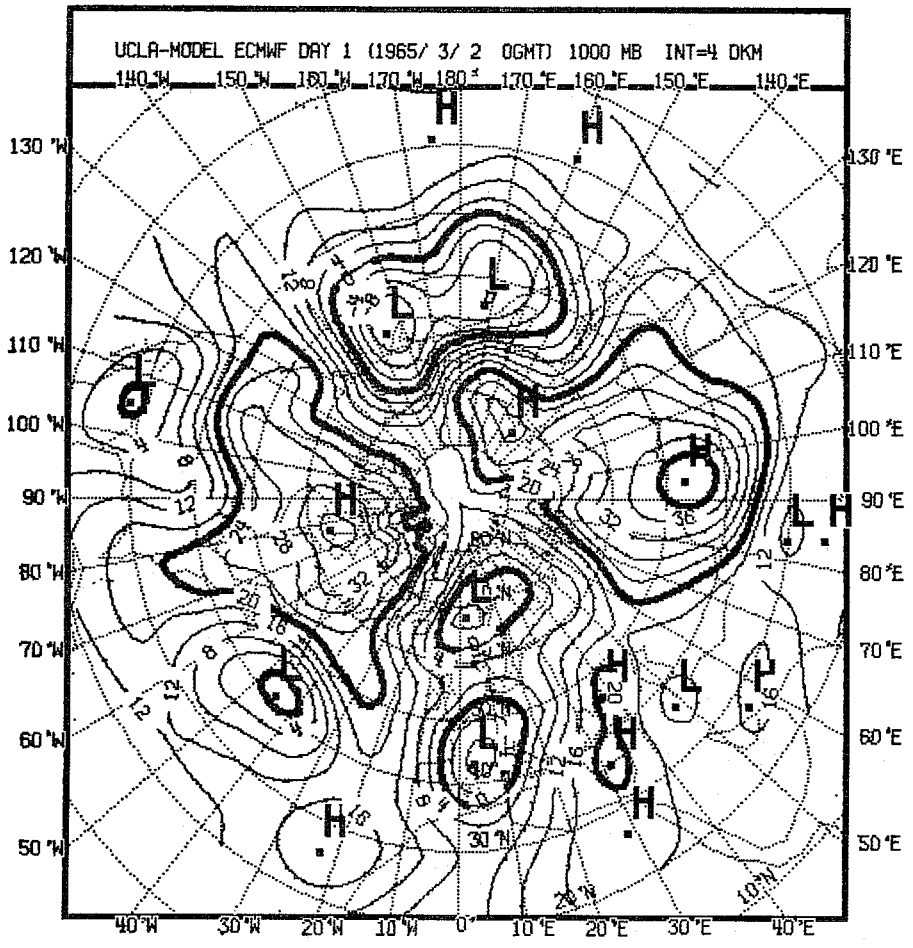
UCLA-MODEL ECMWF DAY 1 (1965/ 3/ 2 0GMT) 1000 MB INT=4 DKM
140°W 150°W 160°W 170°W 180° 170°E 160°E 150°E 140°E
130°W 120°W 110°W 100°W 90°W 80°W 70°W 60°W 50°W
130°E 120°E 110°E 100°E 90°E 80°E 70°E 60°E 50°E
40°W 30°W 20°W 10°W 0° 10°E 20°E 30°E 40°E

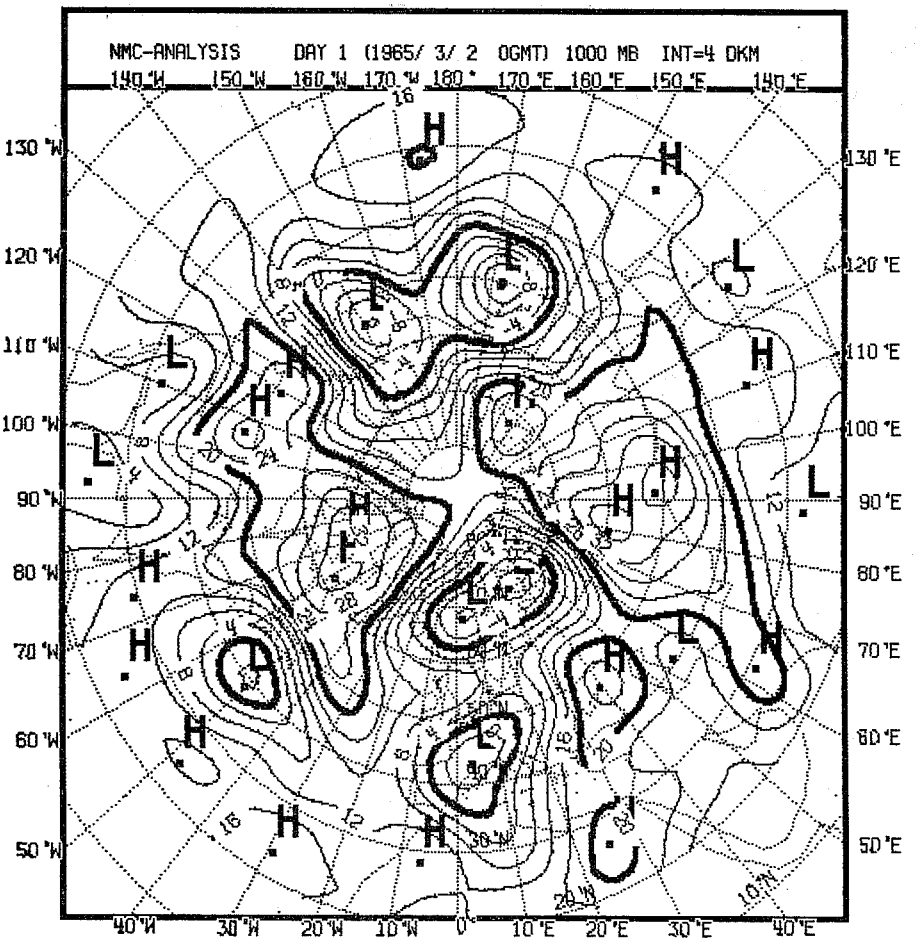
NMC-ANALYSIS DAY 1 (1965/ 3/ 2 0GMT) 1000 MB INT=4 DKM
140°W 150°W 160°W 170°W 180° 170°E 160°E 150°E 140°E
130°W 120°W 110°W 100°W 90°W 80°W 70°W 60°W 50°W
130°E 120°E 110°E 100°E 90°E 80°E 70°E 60°E 50°E
40°W 30°W 20°W 10°W 0° 10°E 20°E 30°E 40°E

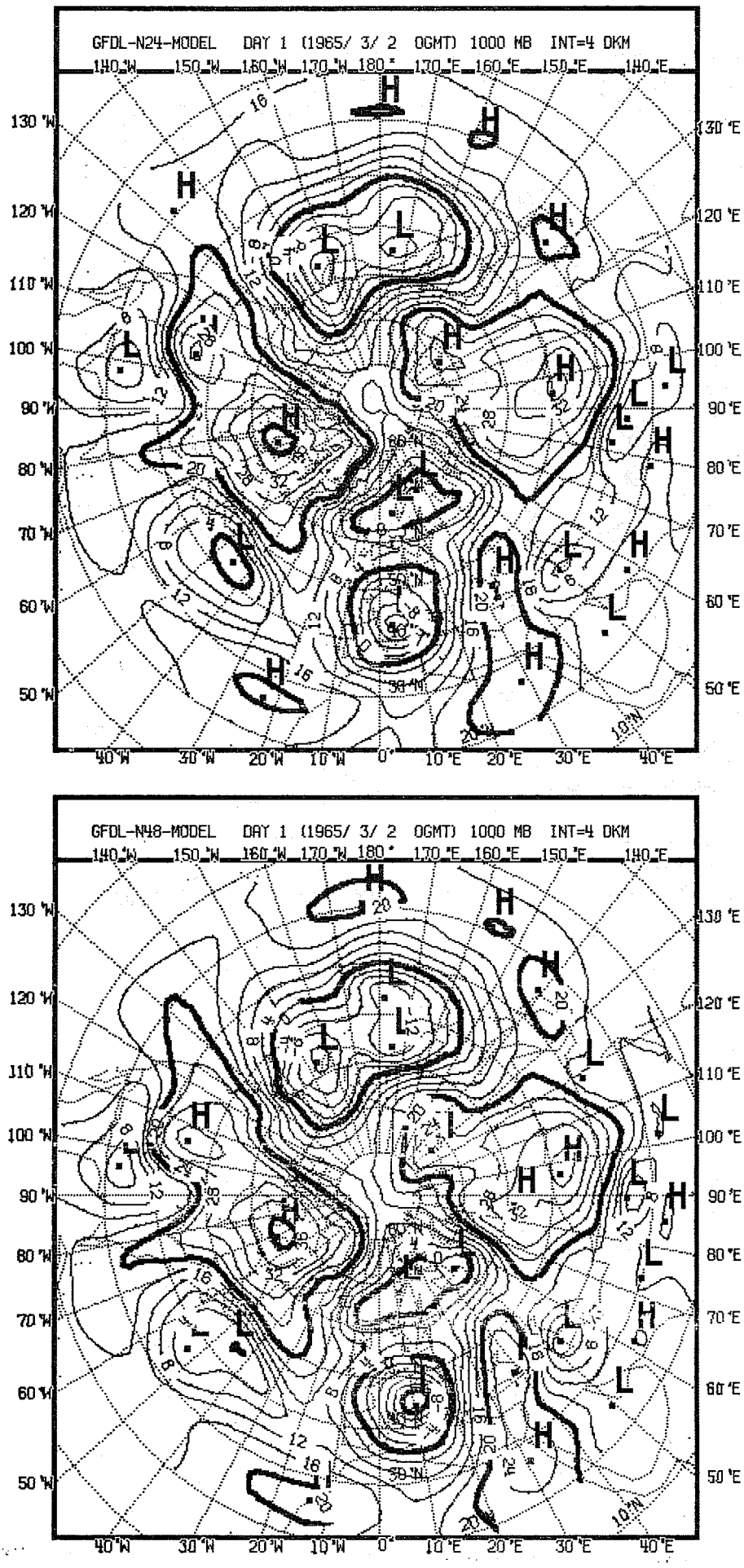

Fig. 4.2.12: Observed (bottom left) and predicted maps of 1000 mb geopotential height, day 1.

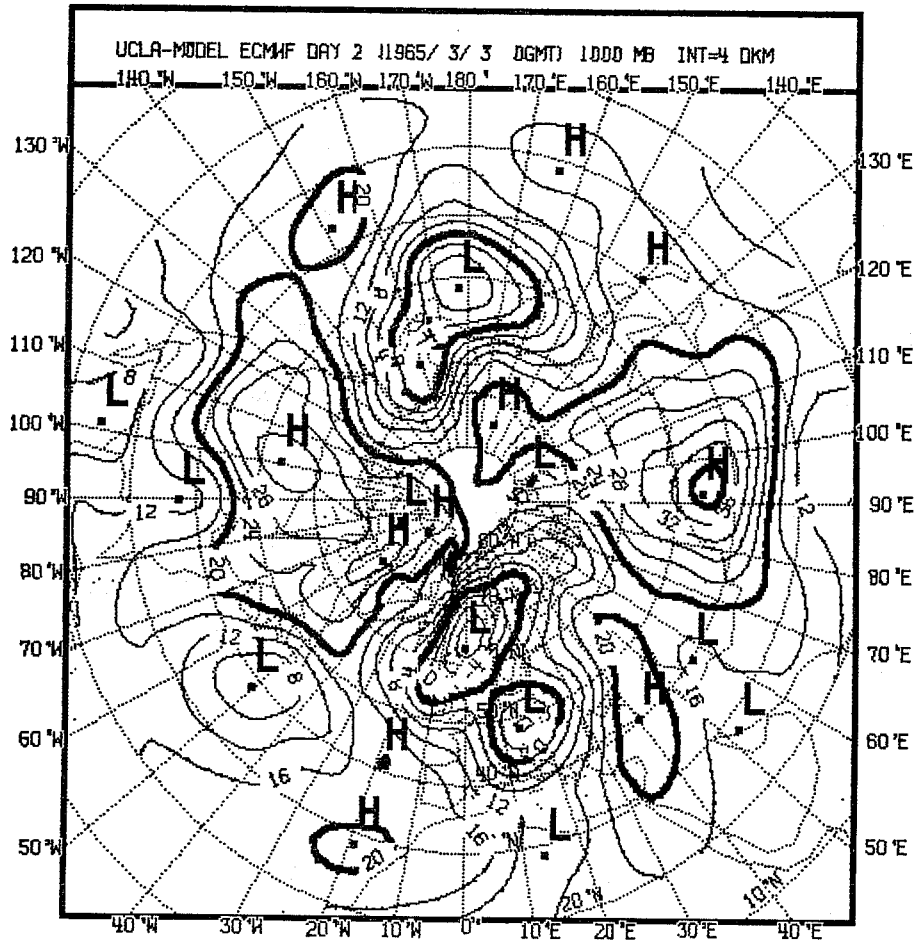
UCLA-MODEL ECMWF DAY 2 (1965/ 3/ 3 0GMT) 1000 MB INT=4 DKM
140 °W 150 °W 160 °W 170 °W 180 ° 170 °E 160 °E 150 °E 140 °E
130 °W 120 °W 110 °W 100 °W 90 °W 80 °W 70 °W 60 °W 50 °W
130 °E 120 °E 110 °E 100 °E 90 °E 80 °E 70 °E 60 °E 50 °E
40 °W 30 °W 20 °W 10 °W 0° 10 °E 20 °E 30 °E 40 °E

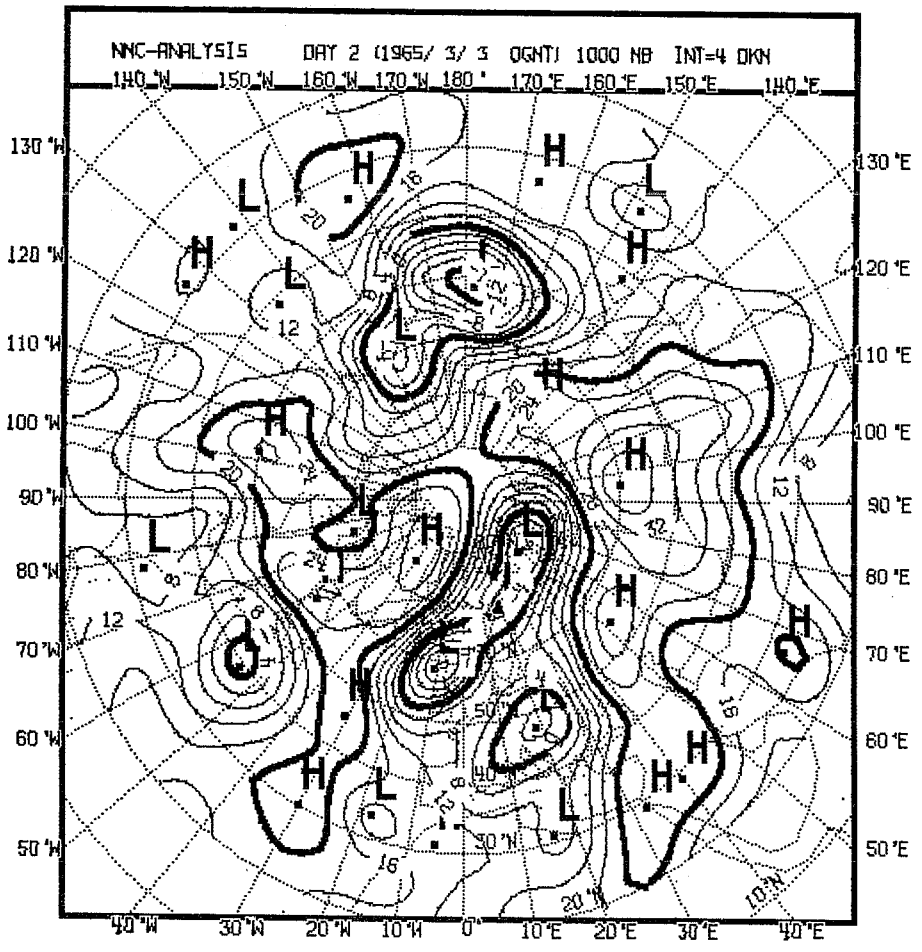
NMC-ANALYSIS DAY 2 (1965/ 3/ 3 0GMT) 1000 MB INT=4 DKM
140 °W 150 °W 160 °W 170 °W 180 ° 170 °E 160 °E 150 °E 140 °E
130 °W 120 °W 110 °W 100 °W 90 °W 80 °W 70 °W 60 °W 50 °W
130 °E 120 °E 110 °E 100 °E 90 °E 80 °E 70 °E 60 °E 50 °E
40 °W 30 °W 20 °W 10 °W 0° 10 °E 20 °E 30 °E 40 °E

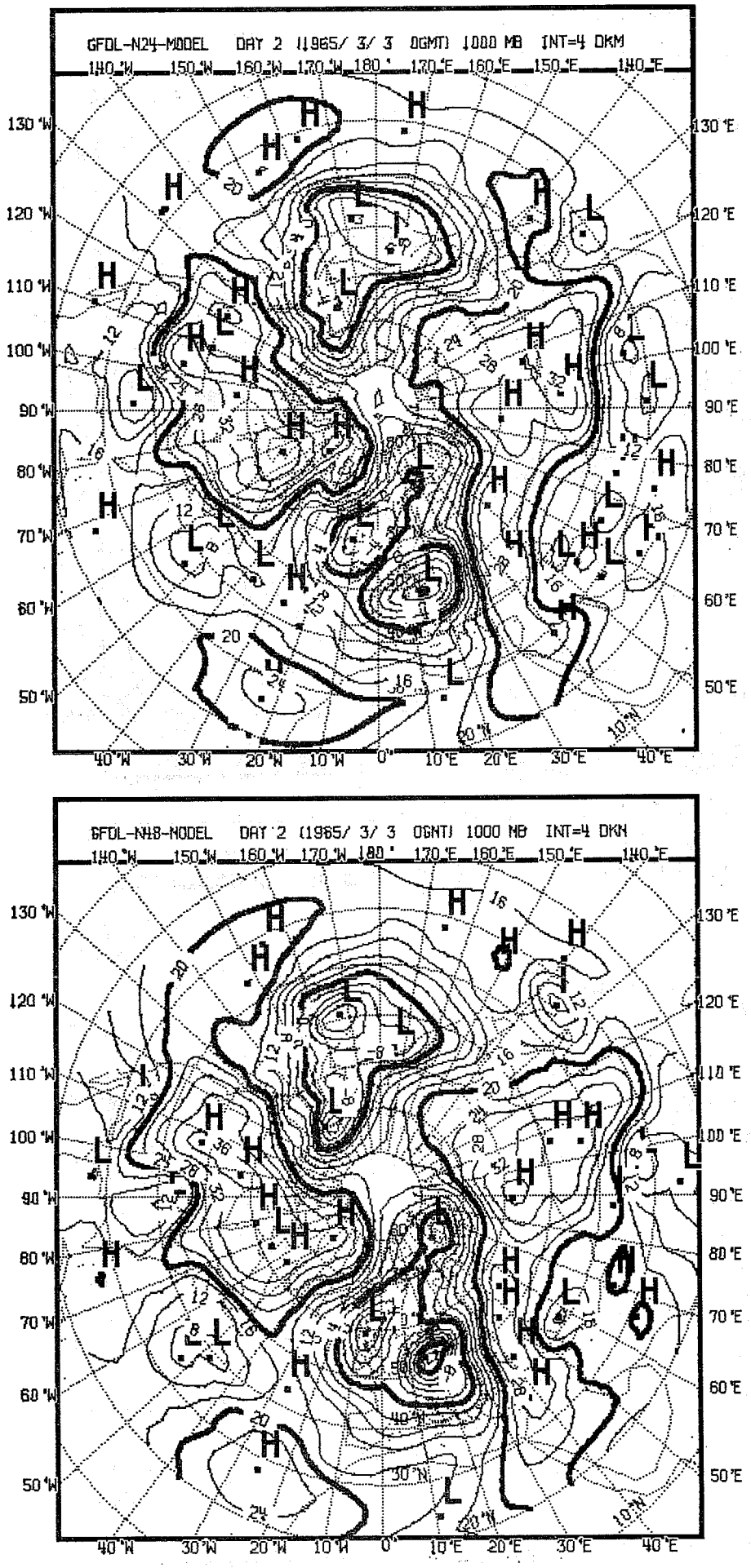

Fig. 4.2.13:Observed (bottom left) and predicted maps of 1000 mb geopotential height, day 2.

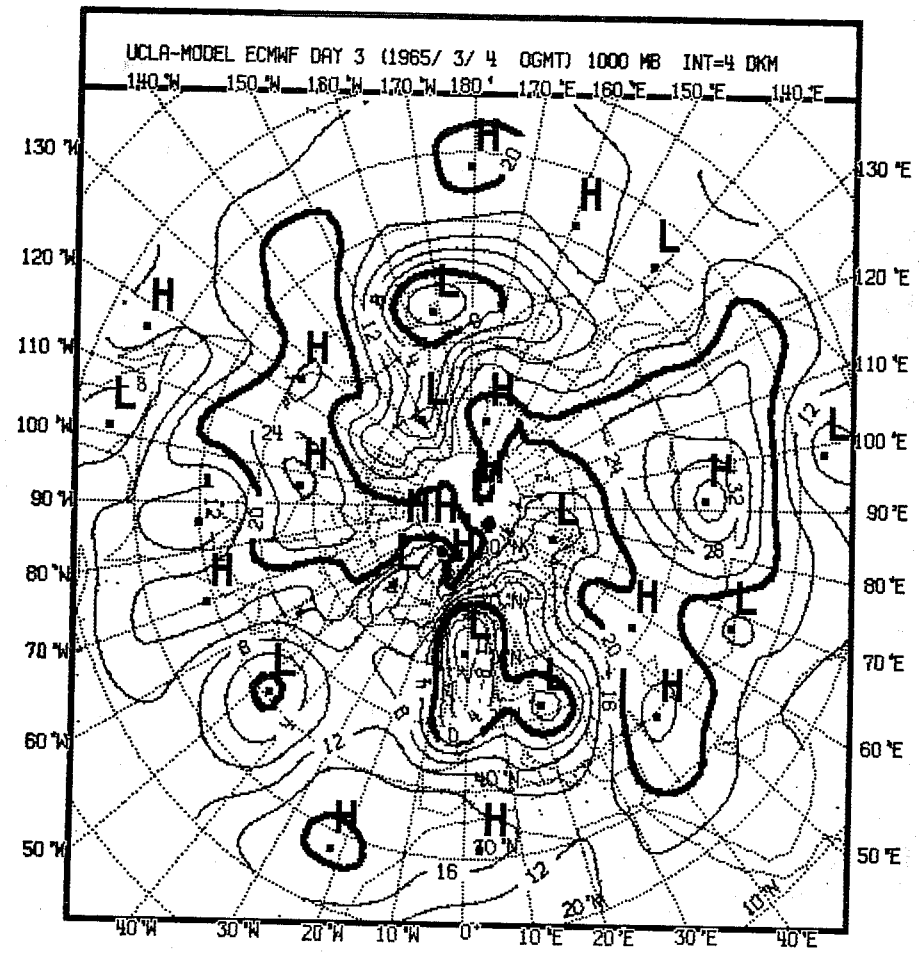
UCLA-MODEL ECMWF DAY 3 (1965/ 3/ 4 0GMT) 1000 MB INT=4 DKM
140°W 150°W 160°W 170°W 180° 170°E 160°E 150°E 140°E
130°W 120°W 110°W 100°W 90°W 80°W 70°W 60°W 50°W
130°E 120°E 110°E 100°E 90°E 80°E 70°E 60°E 50°E
40°W 30°W 20°W 10°W 0° 10°E 20°E 30°E 40°E
40°N
30°N
10°N

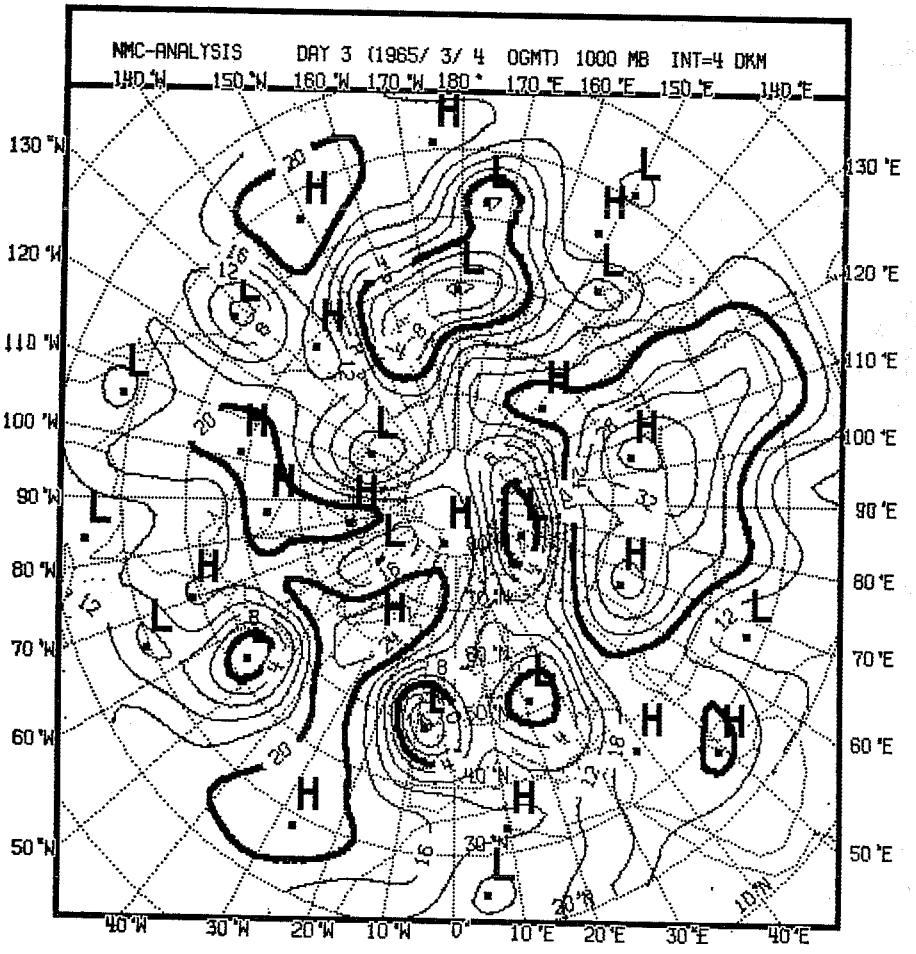
NMC-ANALYSIS DAY 3 (1965/ 3/ 4 0GMT) 1000 MB INT=4 DKM
140°W 150°W 160°W 170°W 180° 170°E 160°E 150°E 140°E
130°W 120°W 110°W 100°W 90°W 80°W 70°W 60°W 50°W
130°E 120°E 110°E 100°E 90°E 80°E 70°E 60°E 50°E
40°W 30°W 20°W 10°W 0° 10°E 20°E 30°E 40°E
40°N
30°N
10°N

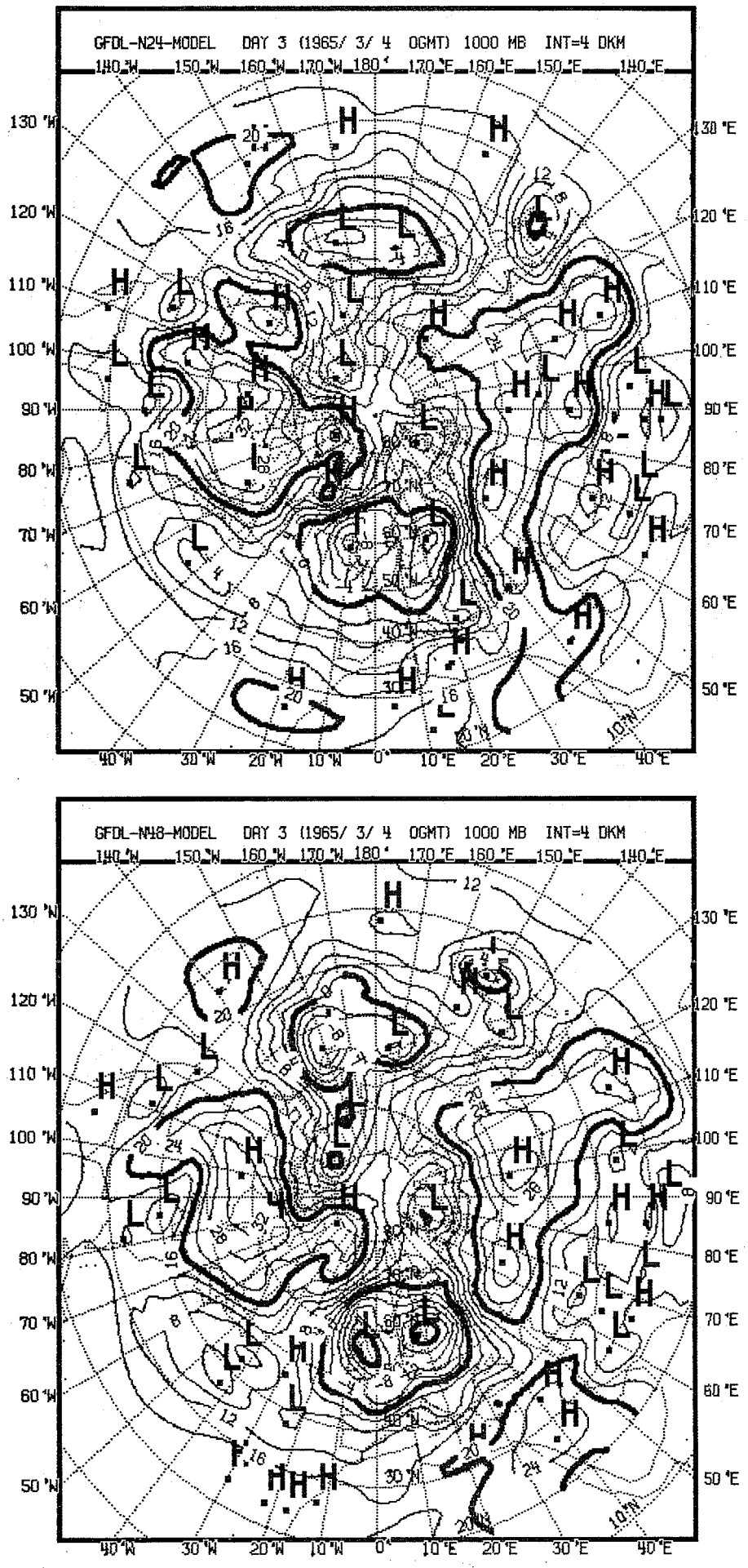

Fig. 4.2.14:Observed (bottom left) and predicted maps of 1000 mb geopotential height, day 3.

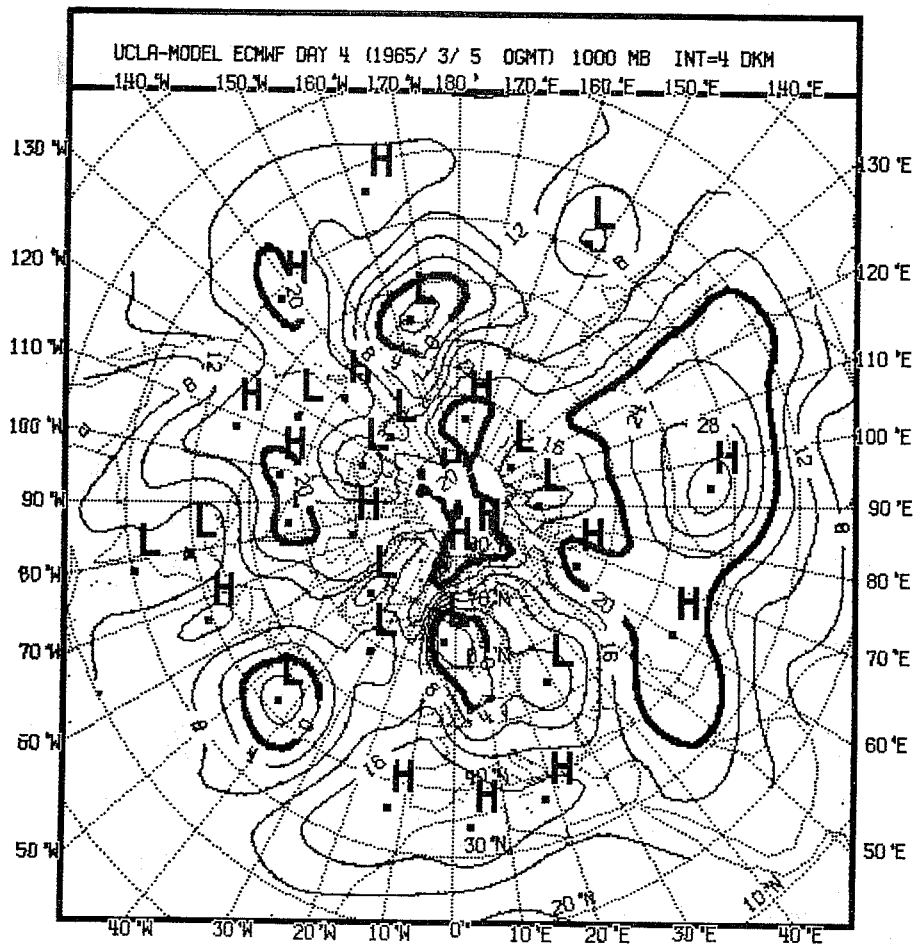
UCLA-MODEL ECMWF DAY 4 (1965/ 3/ 5 0GMT) 1000 MB INT=4 DKM
140 °W 150 °W 160 °W 170 °W 180 ° 170 °E 160 °E 150 °E 140 °E
130 °W 120 °W 110 °W 100 °W 90 °W 80 °W 70 °W 60 °W 50 °W
130 °E 120 °E 110 °E 100 °E 90 °E 80 °E 70 °E 60 °E 50 °E
40 °W 30 °W 20 °W 10 °W 0° 10 °E 20 °E 30 °E 40 °E
90 °N
60 °N
30 °N
10 °N

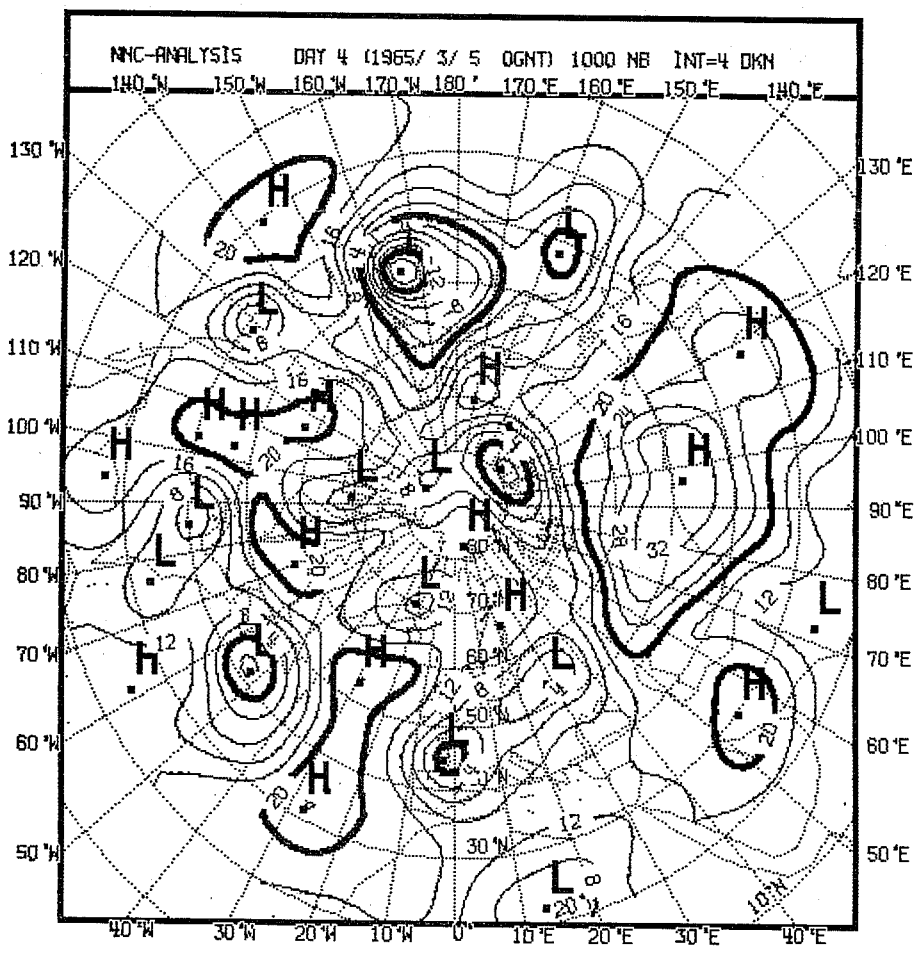
NMC-ANALYSIS DAY 4 (1965/ 3/ 5 0GMT) 1000 MB INT=4 DKM
140 °W 150 °W 160 °W 170 °W 180 ° 170 °E 160 °E 150 °E 140 °E
130 °W 120 °W 110 °W 100 °W 90 °W 80 °W 70 °W 60 °W 50 °W
130 °E 120 °E 110 °E 100 °E 90 °E 80 °E 70 °E 60 °E 50 °E
40 °W 30 °W 20 °W 10 °W 0° 10 °E 20 °E 30 °E 40 °E
90 °N
70 °N
60 °N
50 °N
30 °N
10 °N

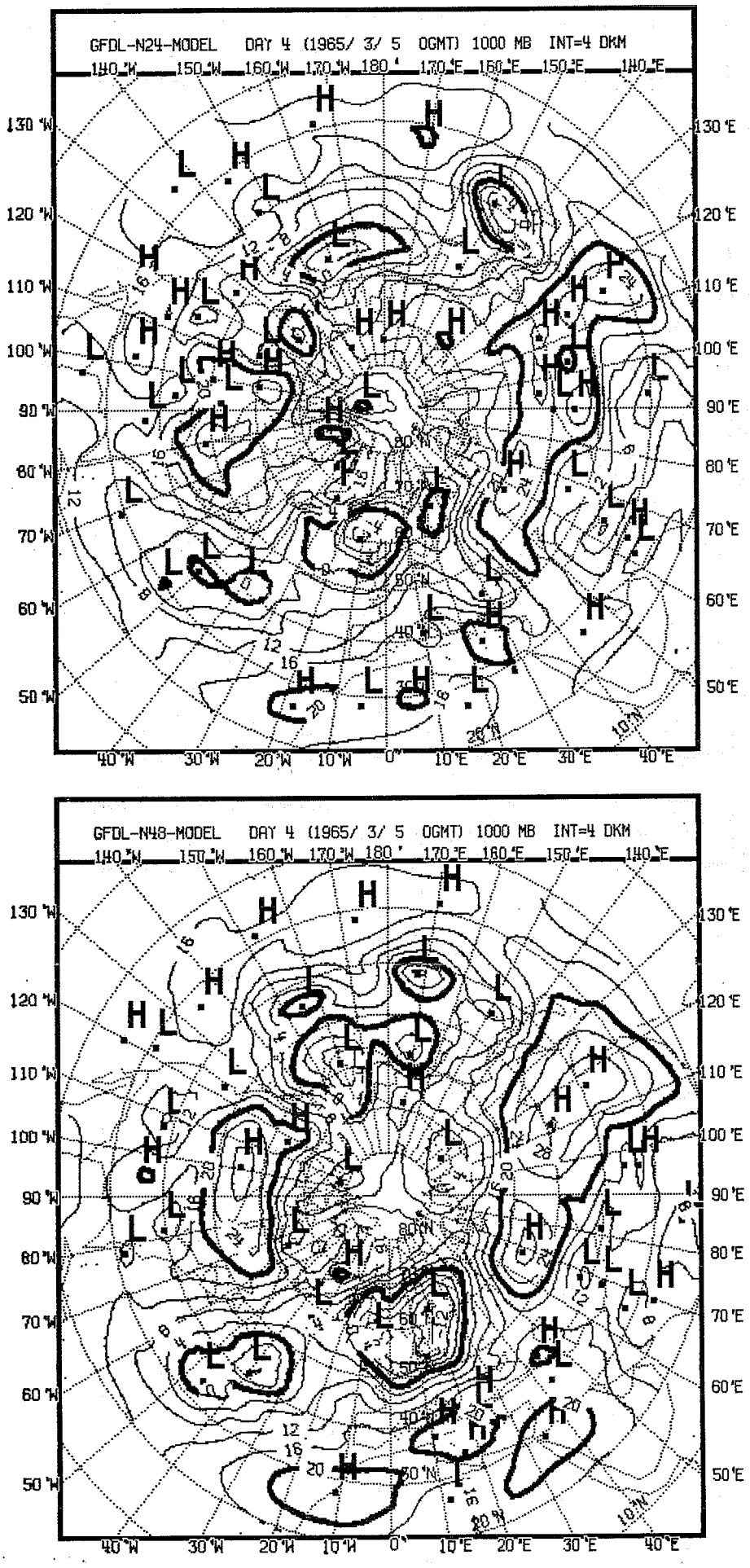

Fig. 4.2.15: Observed (bottom left) and predicted maps of 1000 mb geopotential height, day 4.

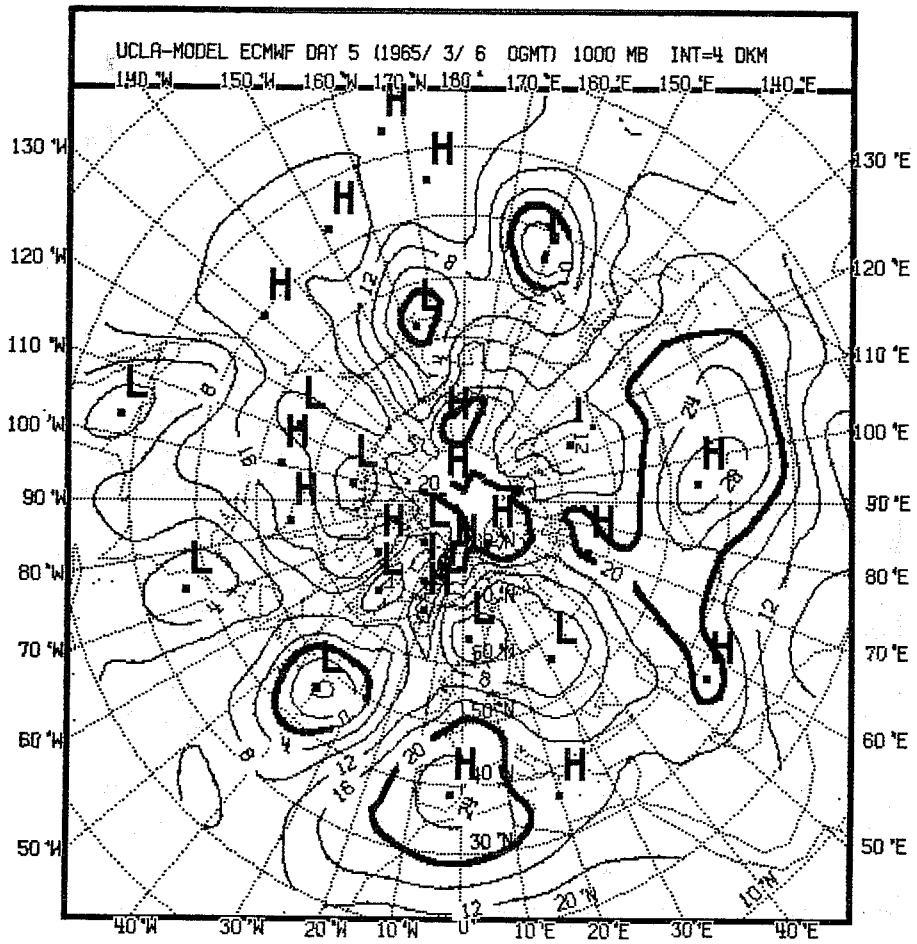
UCLA-MODEL ECMWF DAY 5 (1965/ 3/ 6 0GMT) 1000 MB INT=4 DKM
140 °W 150 °W 160 °W 170 °W 180 ° 170 °E 160 °E 150 °E 140 °E
130 °W 120 °W 110 °W 100 °W 90 °W 80 °W 70 °W 60 °W 50 °W
130 °E 120 °E 110 °E 100 °E 90 °E 80 °E 70 °E 60 °E 50 °E
40 °W 30 °W 20 °W 10 °W 0 10 °E 20 °E 30 °E 40 °E

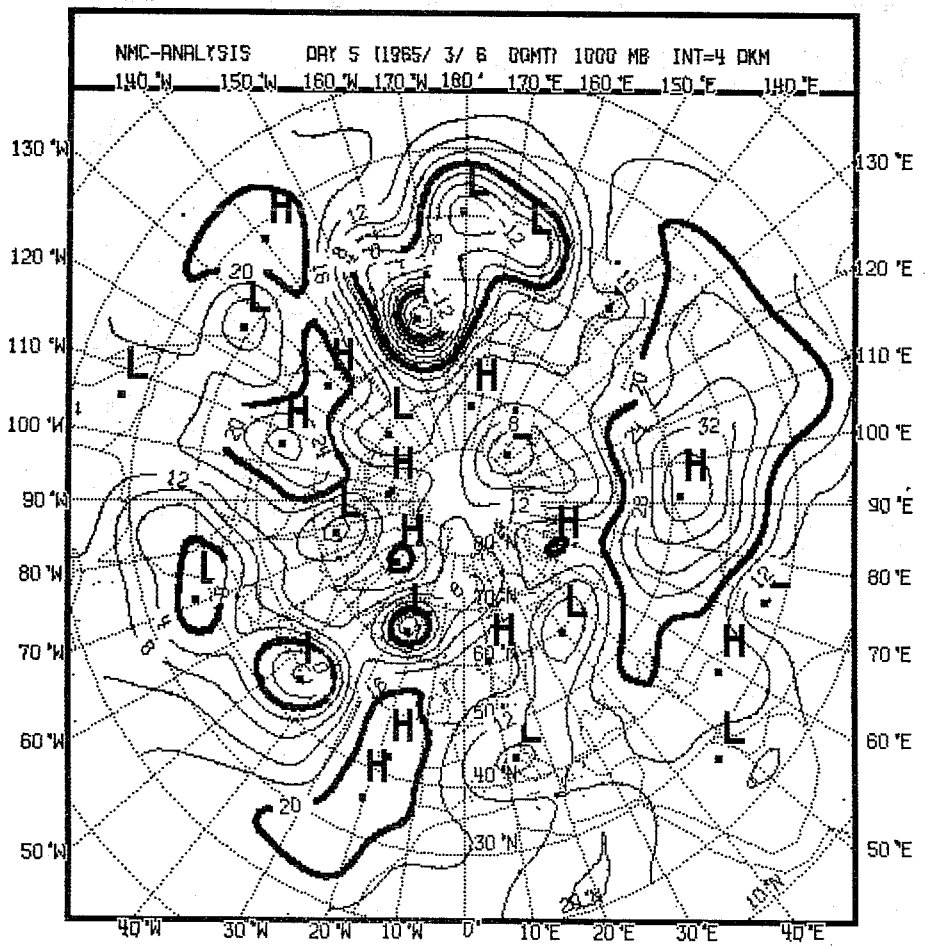
NMC-ANALYSIS DAY 5 (1965/ 3/ 6 0GMT) 1000 MB INT=4 DKM
140 °W 150 °W 160 °W 170 °W 180 ° 170 °E 160 °E 150 °E 140 °E
130 °W 120 °W 110 °W 100 °W 90 °W 80 °W 70 °W 60 °W 50 °W
130 °E 120 °E 110 °E 100 °E 90 °E 80 °E 70 °E 60 °E 50 °E
40 °W 30 °W 20 °W 10 °W 0 10 °E 20 °E 30 °E 40 °E

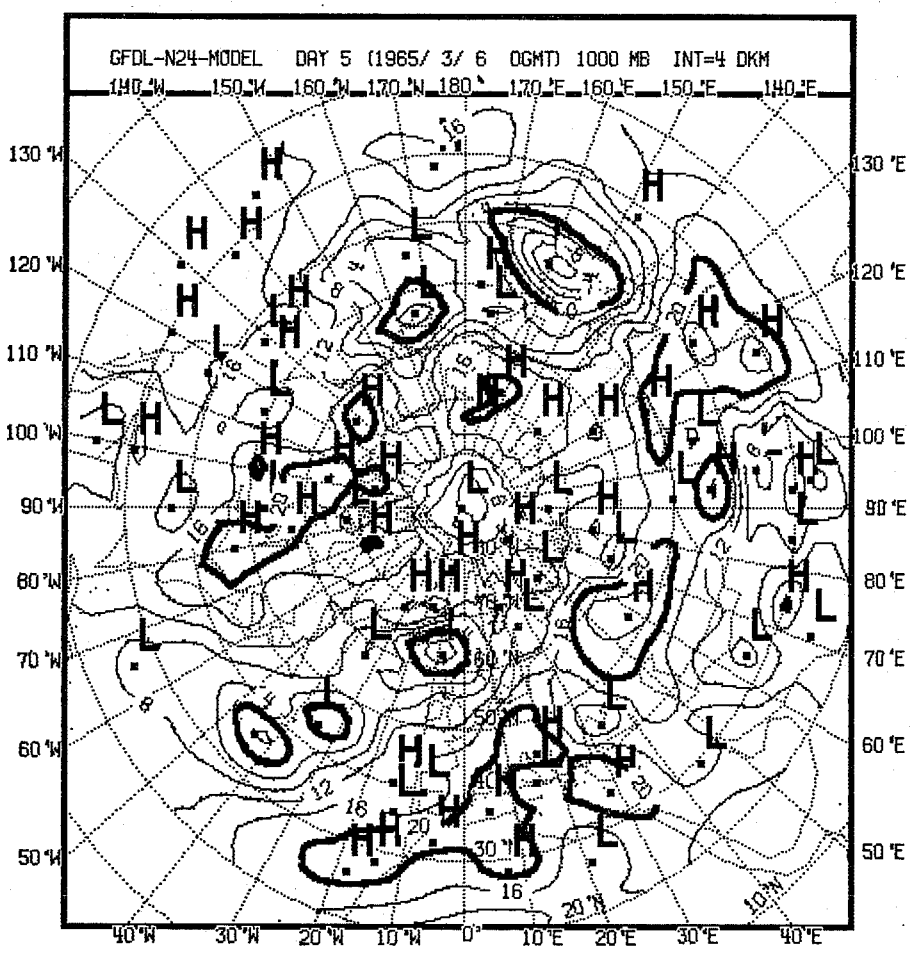

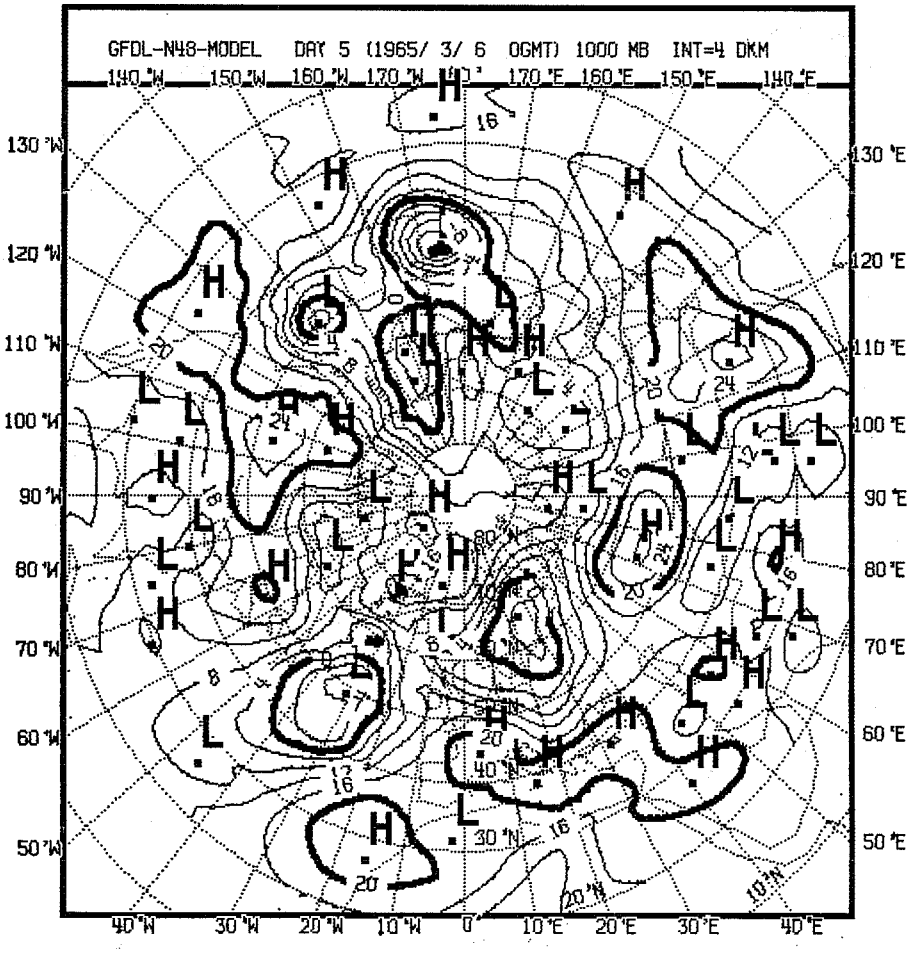

Fig. 4.2.16: Observed (bottom left) and predicted maps of 1000 mb geopotential height, day 5

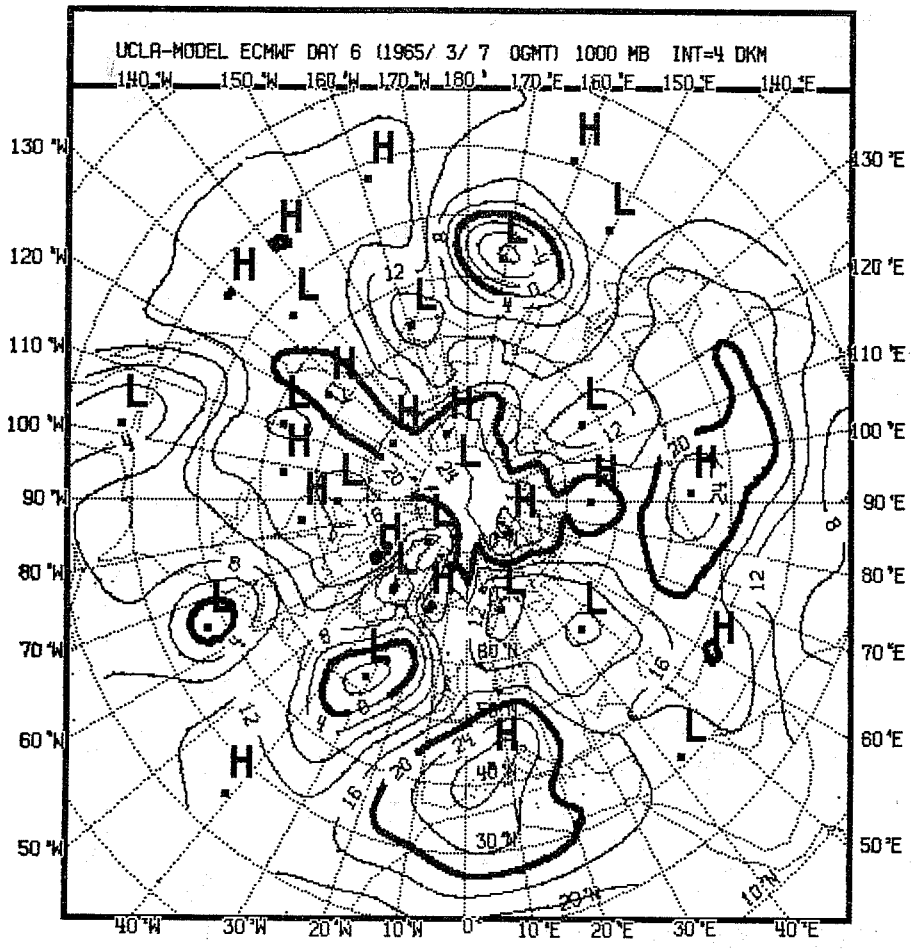
UCLA-MODEL ECMWF DAY 6 (1965/ 3/ 7 0GMT) 1000 MB INT=4 DKM
140°W 150°W 160°W 170°W 180° 170°E 160°E 150°E 140°E
130°W 120°W 110°W 100°W 90°W 80°W 70°W 60°W 50°W
130°E 120°E 110°E 100°E 90°E 80°E 70°E 60°E 50°E
40°W 30°W 20°W 10°W 0° 10°E 20°E 30°E 40°E
80°N
40°N
30°N
20°N
10°N

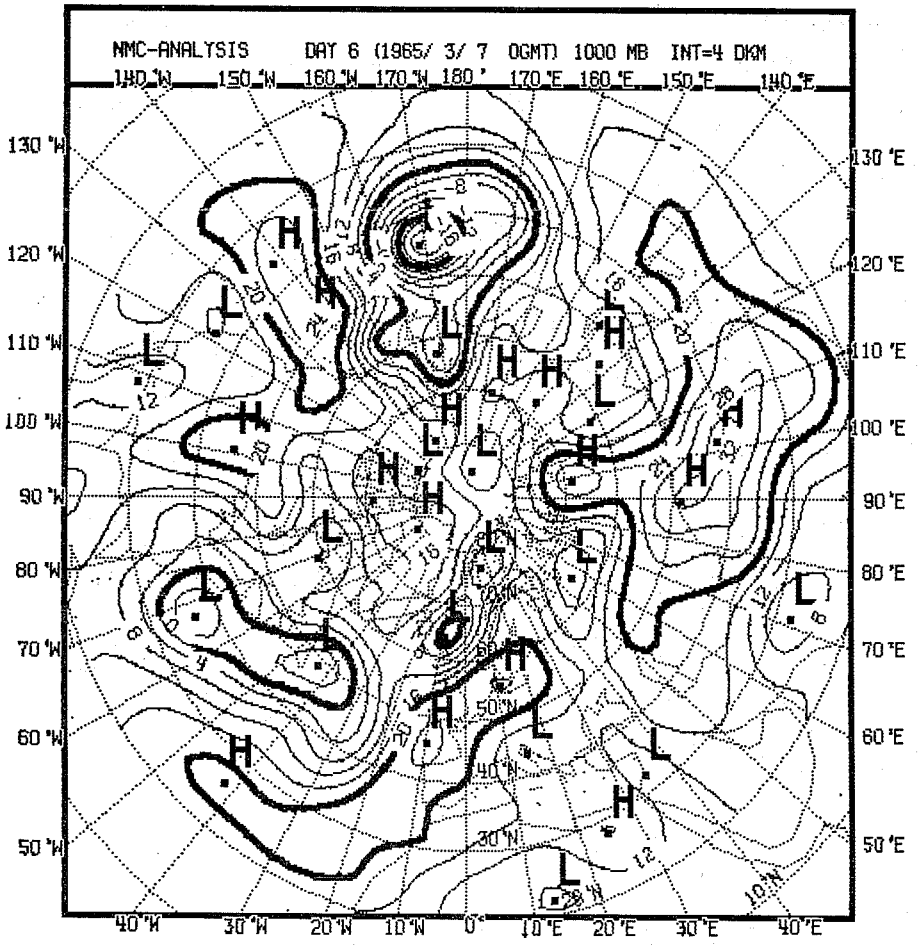
NMC-ANALYSIS DAY 6 (1965/ 3/ 7 0GMT) 1000 MB INT=4 DKM
140°W 150°W 160°W 170°W 180° 170°E 160°E 150°E 140°E
130°W 120°W 110°W 100°W 90°W 80°W 70°W 60°W 50°W
130°E 120°E 110°E 100°E 90°E 80°E 70°E 60°E 50°E
40°W 30°W 20°W 10°W 0° 10°E 20°E 30°E 40°E
80°N
70°N
60°N
50°N
40°N
30°N
20°N
10°N

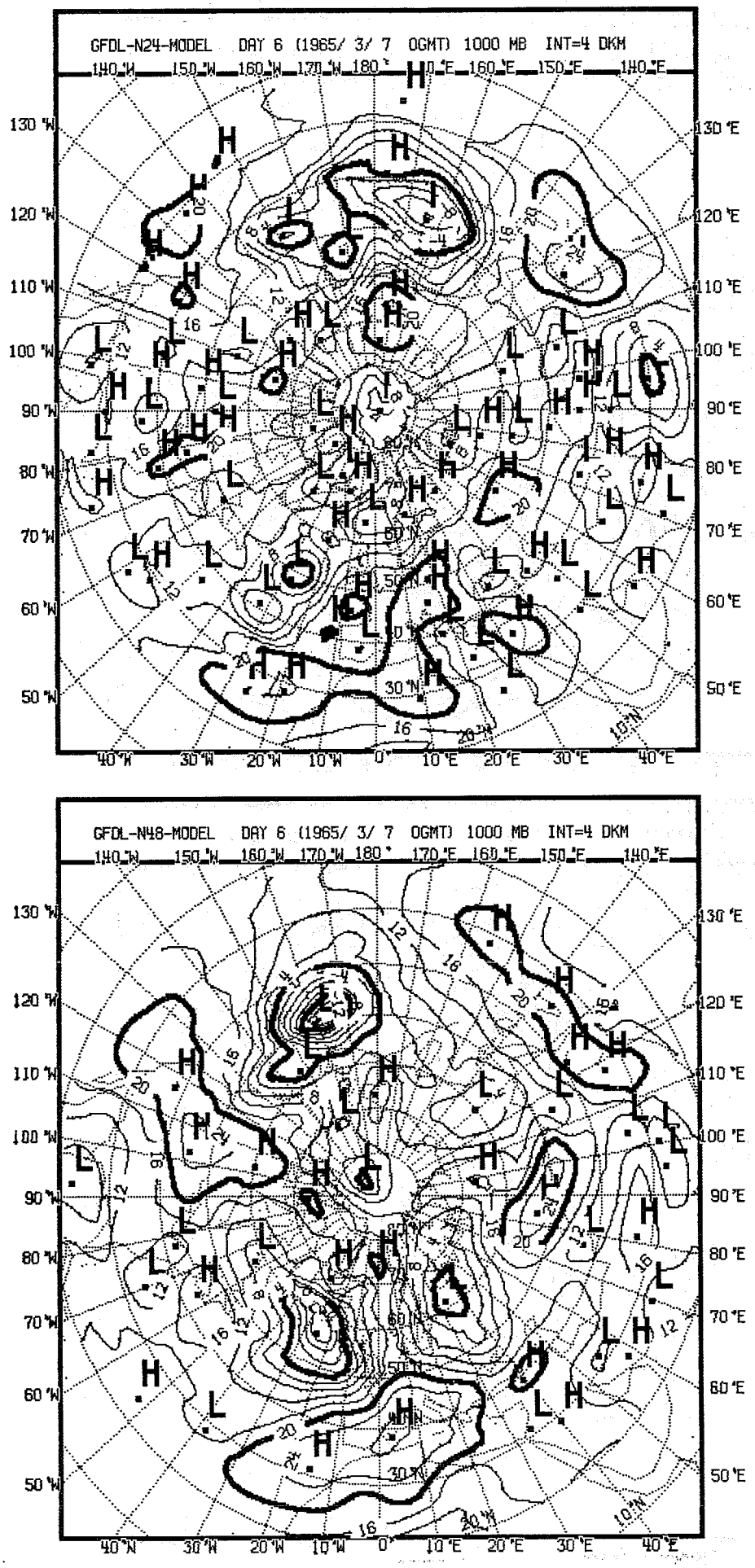

Fig. 4.2.17: Observed (bottom left) and predicted maps of 1000 mb geopotential height, day 6.

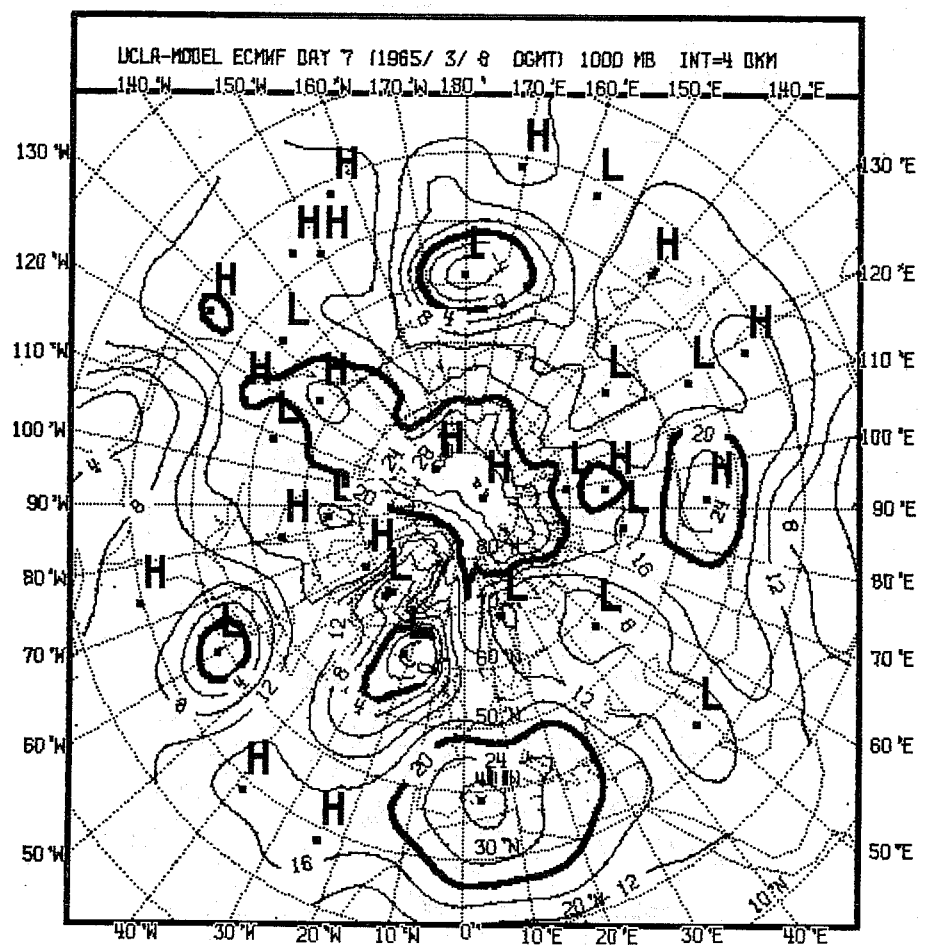
UCLA-MODEL ECMWF DAY 7 (1965/ 3/ 8 00GMT) 1000 MB INT=4 DKM
140°W 150°W 160°W 170°W 180° 170°E 160°E 150°E 140°E
130°W 120°W 110°W 100°W 90°W 80°W 70°W 60°W 50°W
130°E 120°E 110°E 100°E 90°E 80°E 70°E 60°E 50°E
40°W 30°W 20°W 10°W 0° 10°E 20°E 30°E 40°E
50°N
30°N
10°N

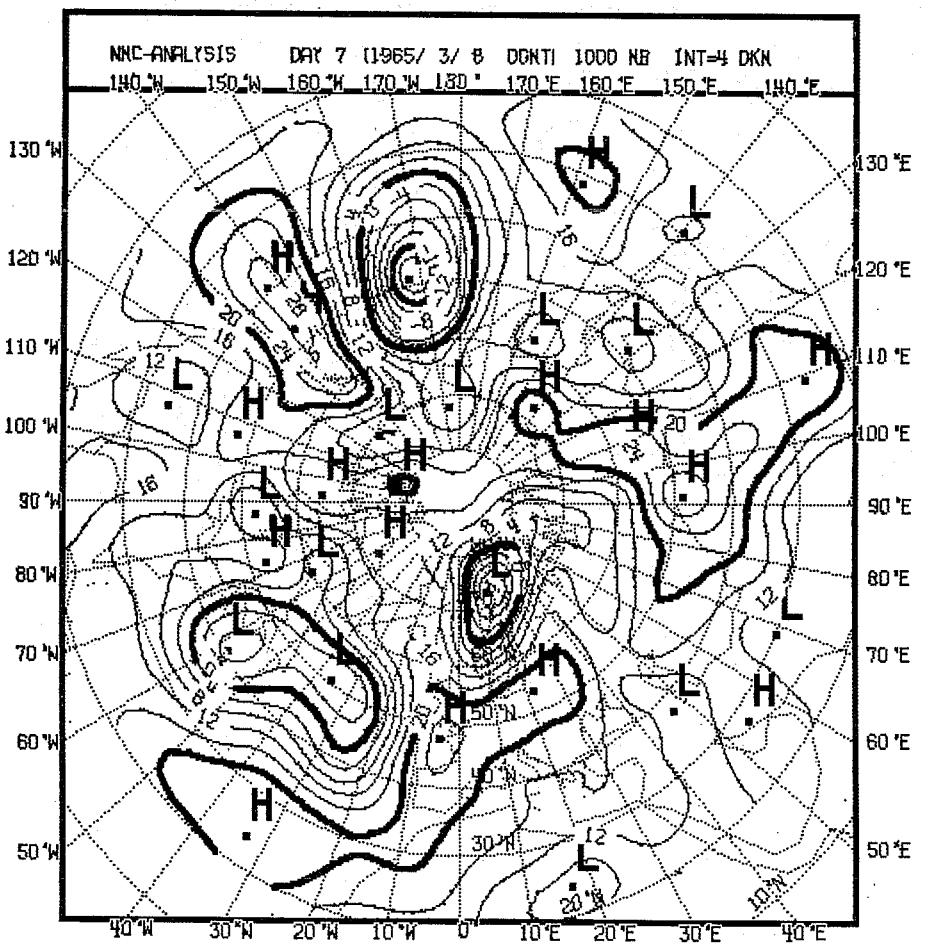
NMC-ANALYSIS DAY 7 (1965/ 3/ 8 00GMT) 1000 MB INT=4 DKM
140°W 150°W 160°W 170°W 180° 170°E 160°E 150°E 140°E
130°W 120°W 110°W 100°W 90°W 80°W 70°W 60°W 50°W
130°E 120°E 110°E 100°E 90°E 80°E 70°E 60°E 50°E
40°W 30°W 20°W 10°W 0° 10°E 20°E 30°E 40°E
50°N
30°N
10°N

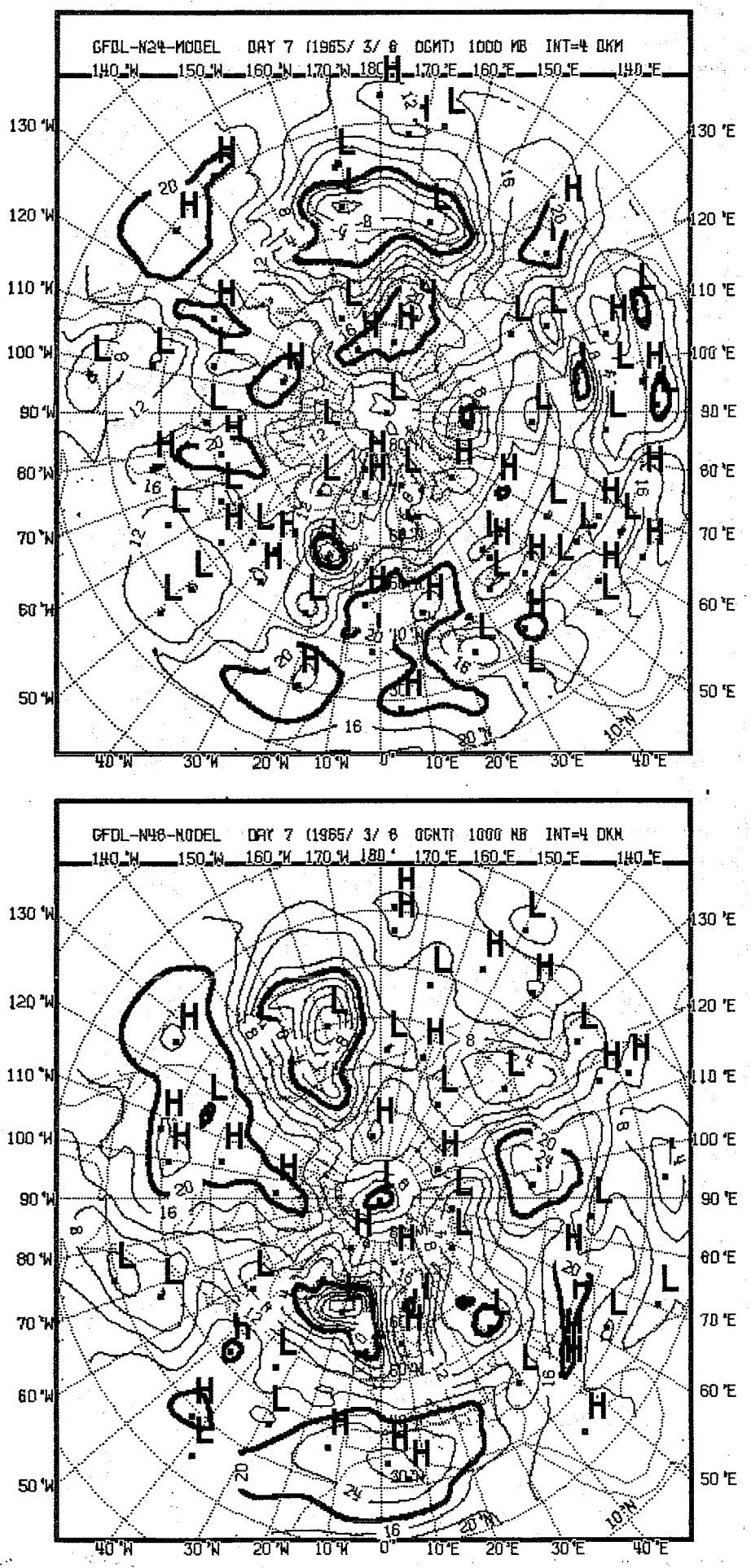

Fig. 4.2.18: Observed (bottom left) and predicted maps of 1000 mb geopotential height, day 7.

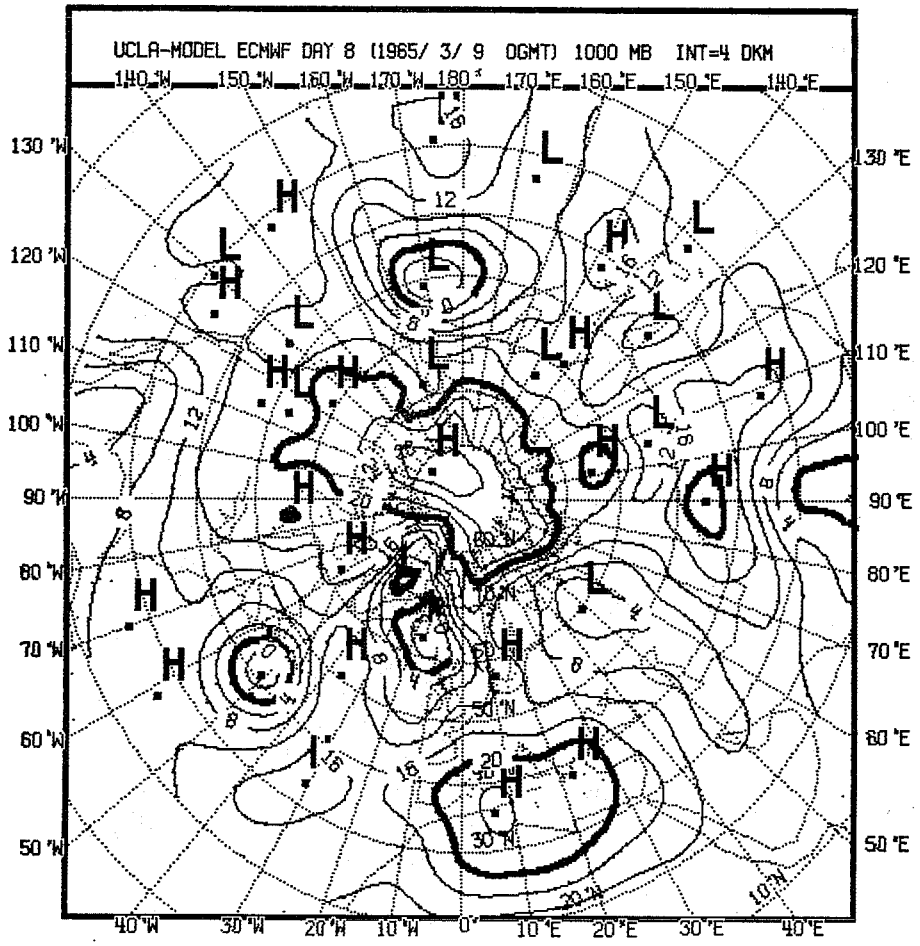
UCLA-MODEL ECMWF DAY 8 (1965/ 3/ 9 0GMT) 1000 MB INT=4 DKM
140°W 150°W 160°W 170°W 180° 170°E 160°E 150°E 140°E
130°W 120°W 110°W 100°W 90°W 80°W 70°W 60°W 50°W
130°E 120°E 110°E 100°E 90°E 80°E 70°E 60°E 50°E
40°W 30°W 20°W 10°W 0° 10°E 20°E 30°E 40°E
30°N
10°N

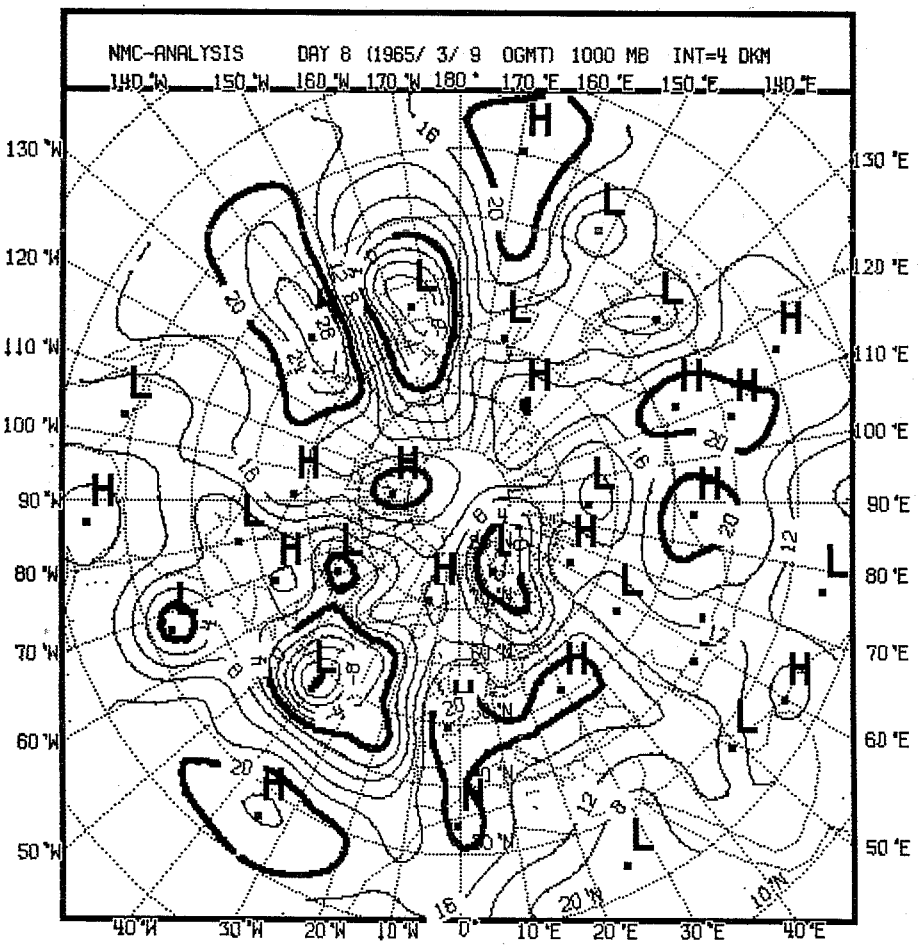
NMC-ANALYSIS DAY 8 (1965/ 3/ 9 0GMT) 1000 MB INT=4 DKM
140°W 150°W 160°W 170°W 180° 170°E 160°E 150°E 140°E
130°W 120°W 110°W 100°W 90°W 80°W 70°W 60°W 50°W
130°E 120°E 110°E 100°E 90°E 80°E 70°E 60°E 50°E
40°W 30°W 20°W 10°W 0° 10°E 20°E 30°E 40°E
30°N
10°N

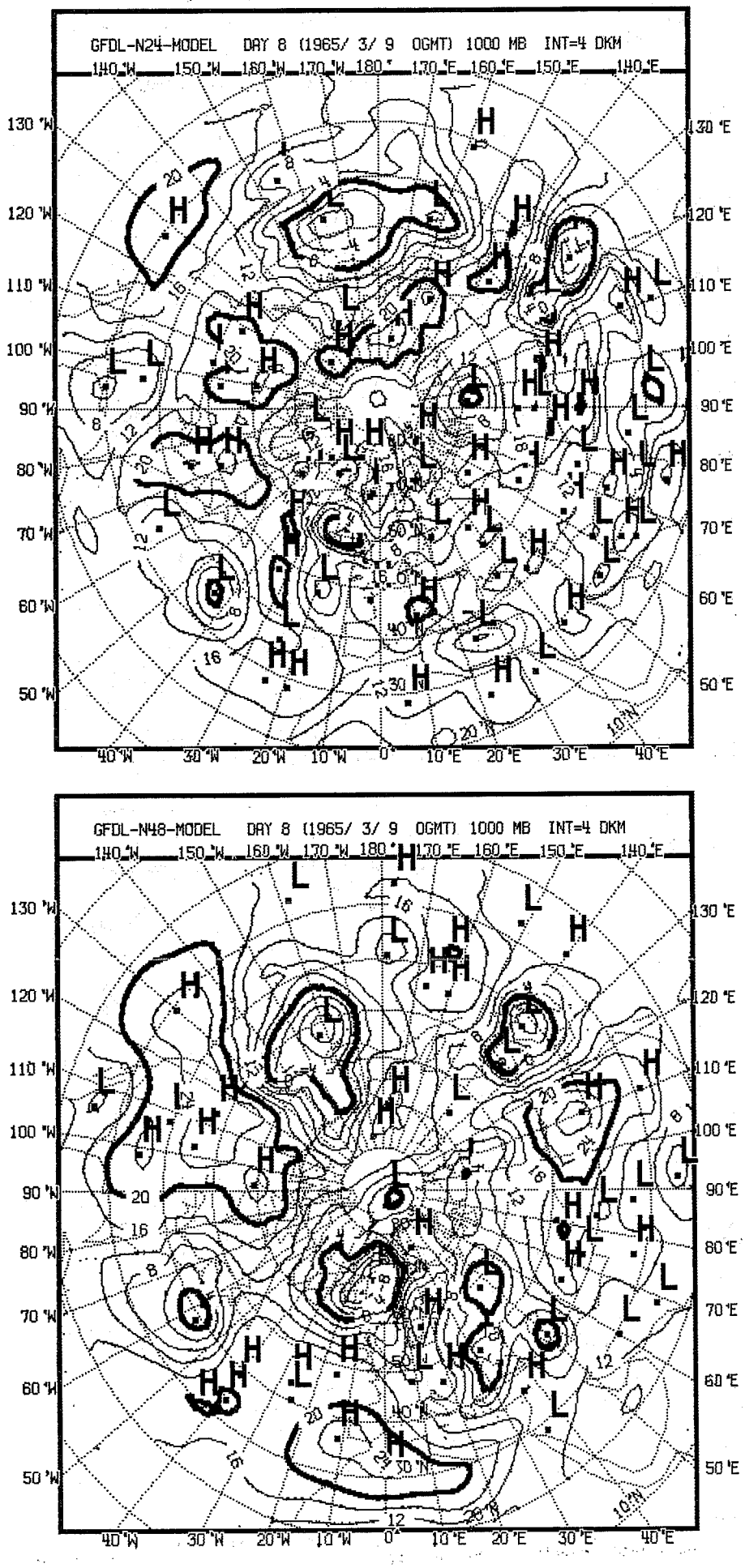

Fig. 4.2.19: Observed (bottom left) and predicted maps of 1000 mb geopotential height, day 8.

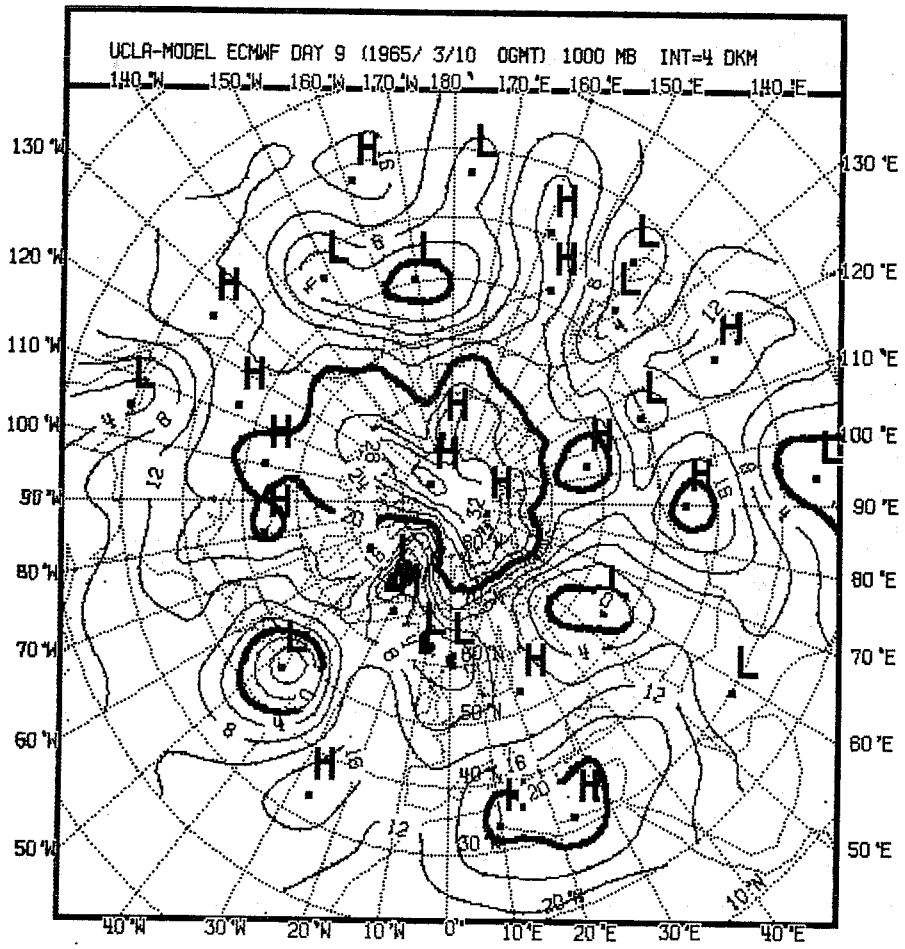
UCLA-MODEL ECMWF DAY 9 (1965/ 3/10 0GMT) 1000 MB INT=4 DKM
140 °W 150 °W 160 °W 170 °W 180 ° 170 °E 160 °E 150 °E 140 °E
130 °W 120 °W 110 °W 100 °W 90 °W 80 °W 70 °W 60 °W 50 °W
130 °E 120 °E 110 °E 100 °E 90 °E 80 °E 70 °E 60 °E 50 °E
40 °W 30 °W 20 °W 10 °W 0° 10 °E 20 °E 30 °E 40 °E

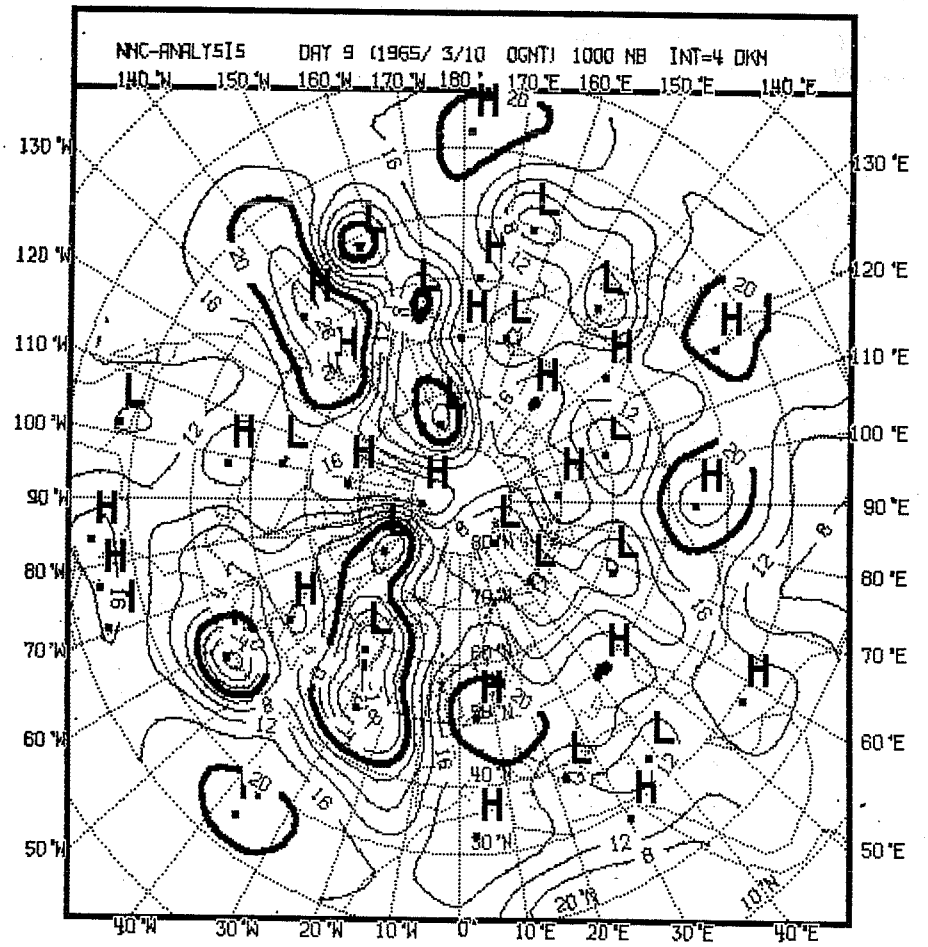
NMC-ANALYSIS DAY 9 (1965/ 3/10 0GMT) 1000 MB INT=4 DKM
140 °W 150 °W 160 °W 170 °W 180 ° 170 °E 160 °E 150 °E 140 °E
130 °W 120 °W 110 °W 100 °W 90 °W 80 °W 70 °W 60 °W 50 °W
130 °E 120 °E 110 °E 100 °E 90 °E 80 °E 70 °E 60 °E 50 °E
40 °W 30 °W 20 °W 10 °W 0° 10 °E 20 °E 30 °E 40 °E

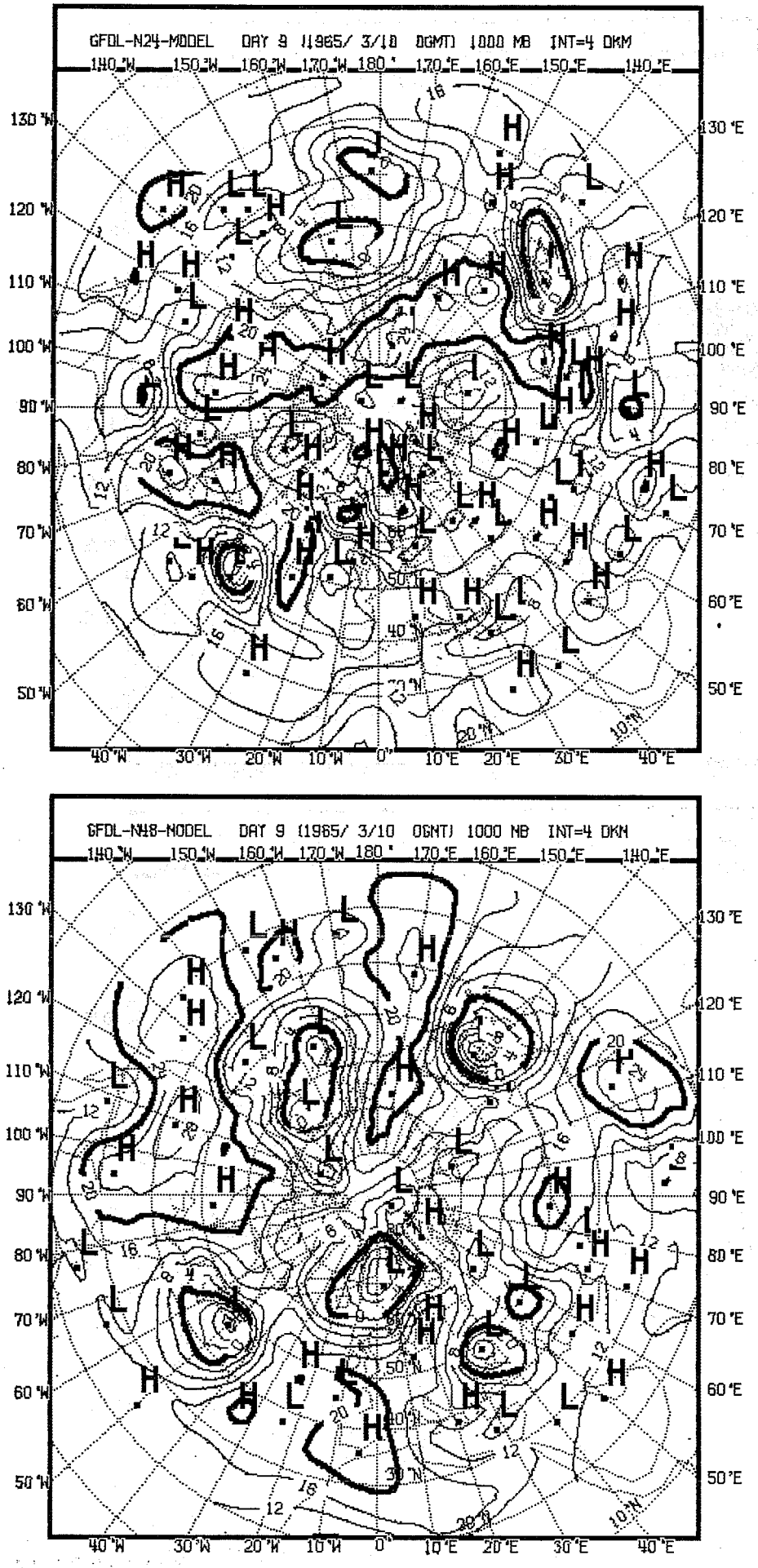

Fig. 4.2.20: Observed (bottom left) and predicted maps of

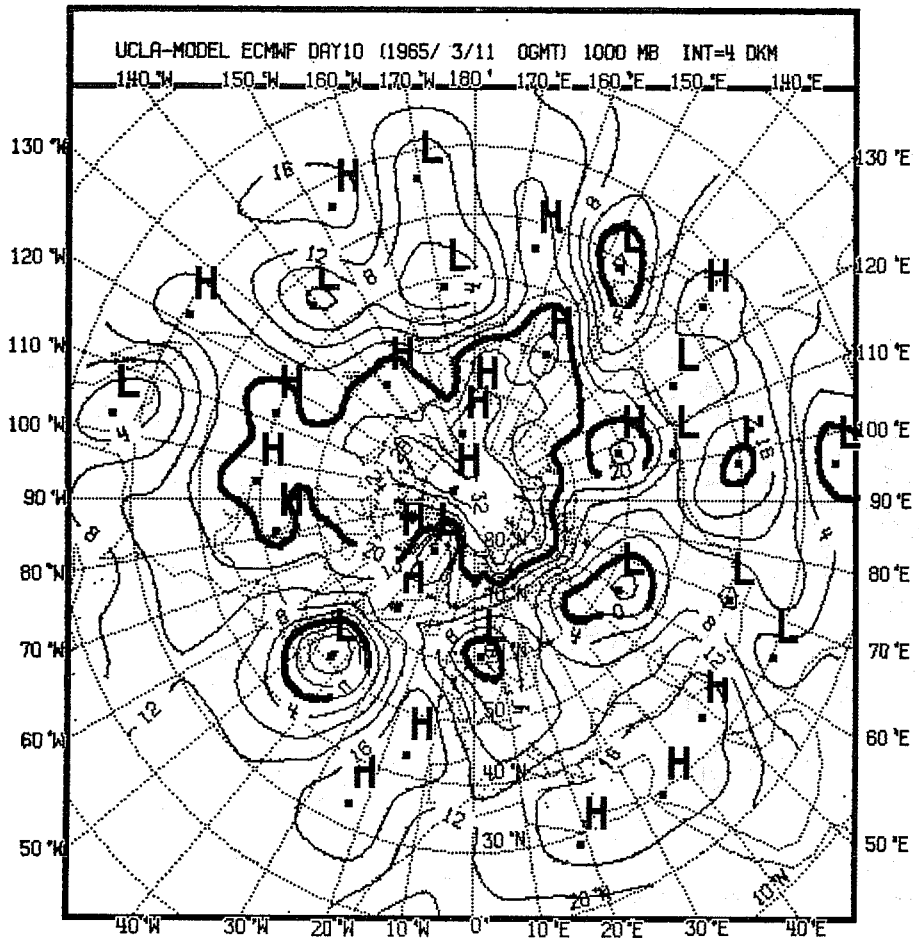
UCLA-MODEL ECMWF DAY10 (1965/ 3/11 0GMT) 1000 MB INT=4 DKM
140 °W 150 °W 160 °W 170 °W 180 ° 170 °E 160 °E 150 °E 140 °E
130 °W 120 °W 110 °W 100 °W 90 °W 80 °W 70 °W 60 °W 50 °W
130 °E 120 °E 110 °E 100 °E 90 °E 80 °E 70 °E 60 °E 50 °E
40 °W 30 °W 20 °W 10 °W 0° 10 °E 20 °E 30 °E 40 °E
80 °N 70 °N 60 °N 50 °N 40 °N 30 °N 20 °N 10 °N

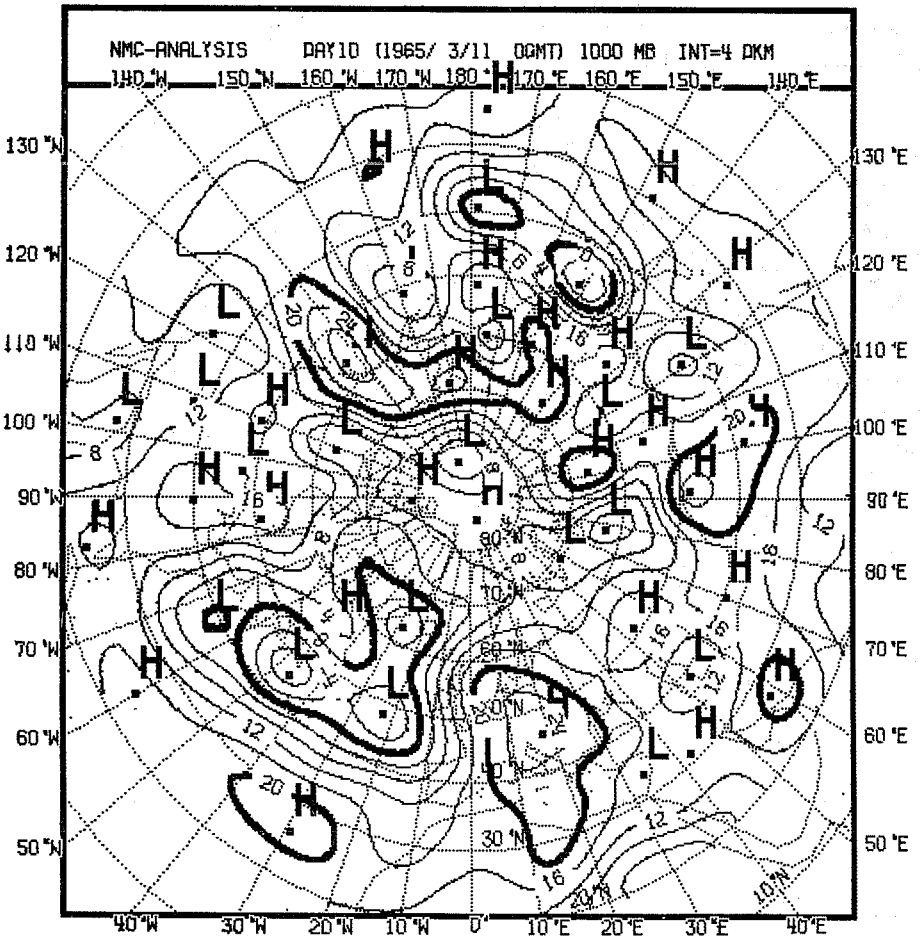
NMC-ANALYSIS DAY10 (1965/ 3/11 0GMT) 1000 MB INT=4 DKM
140 °W 150 °W 160 °W 170 °W 180 ° 170 °E 160 °E 150 °E 140 °E
130 °W 120 °W 110 °W 100 °W 90 °W 80 °W 70 °W 60 °W 50 °W
130 °E 120 °E 110 °E 100 °E 90 °E 80 °E 70 °E 60 °E 50 °E
40 °W 30 °W 20 °W 10 °W 0° 10 °E 20 °E 30 °E 40 °E
80 °N 70 °N 60 °N 50 °N 40 °N 30 °N 20 °N 10 °N

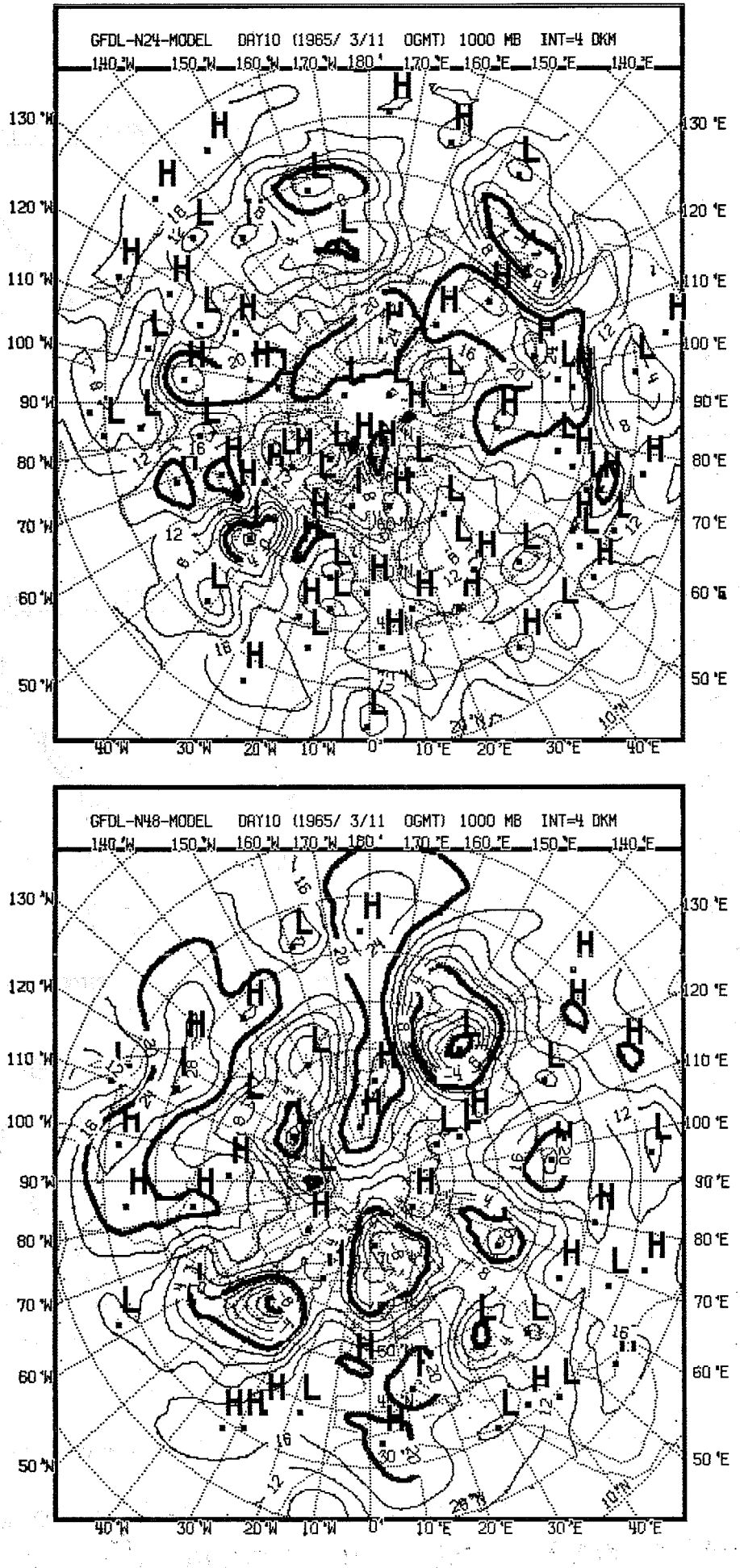

Fig. 4.2.21:Observed (bottom left) and predicted maps of 1000 mb geopotential height, day 10

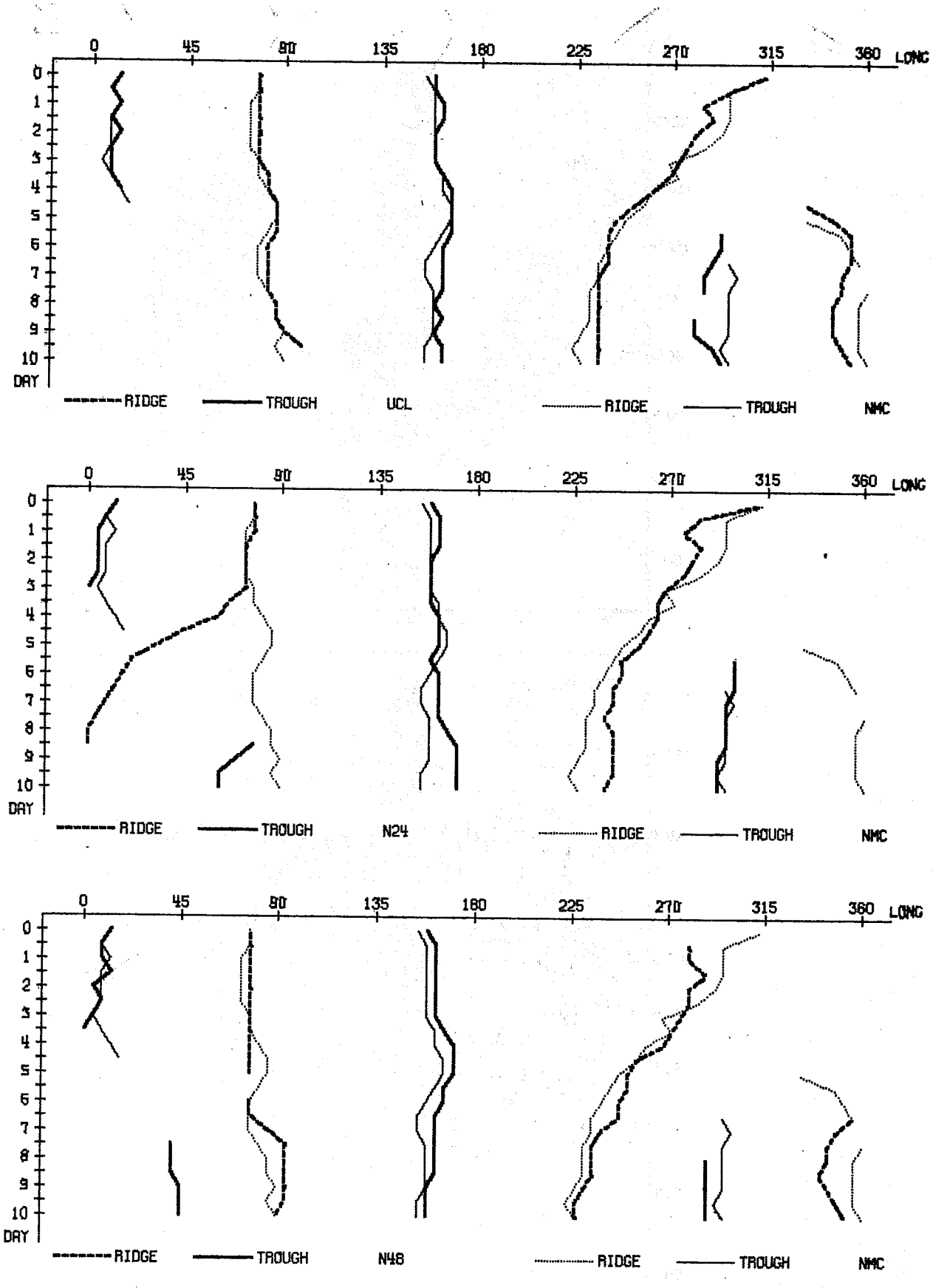

Fig. 4.2.22 :Hovmöller's trough-and-ridge diagrams

WAVENUMBER 1- 3 LATITUDE 50.0 N LEVEL 500 MB
GEOP. HEIGHT

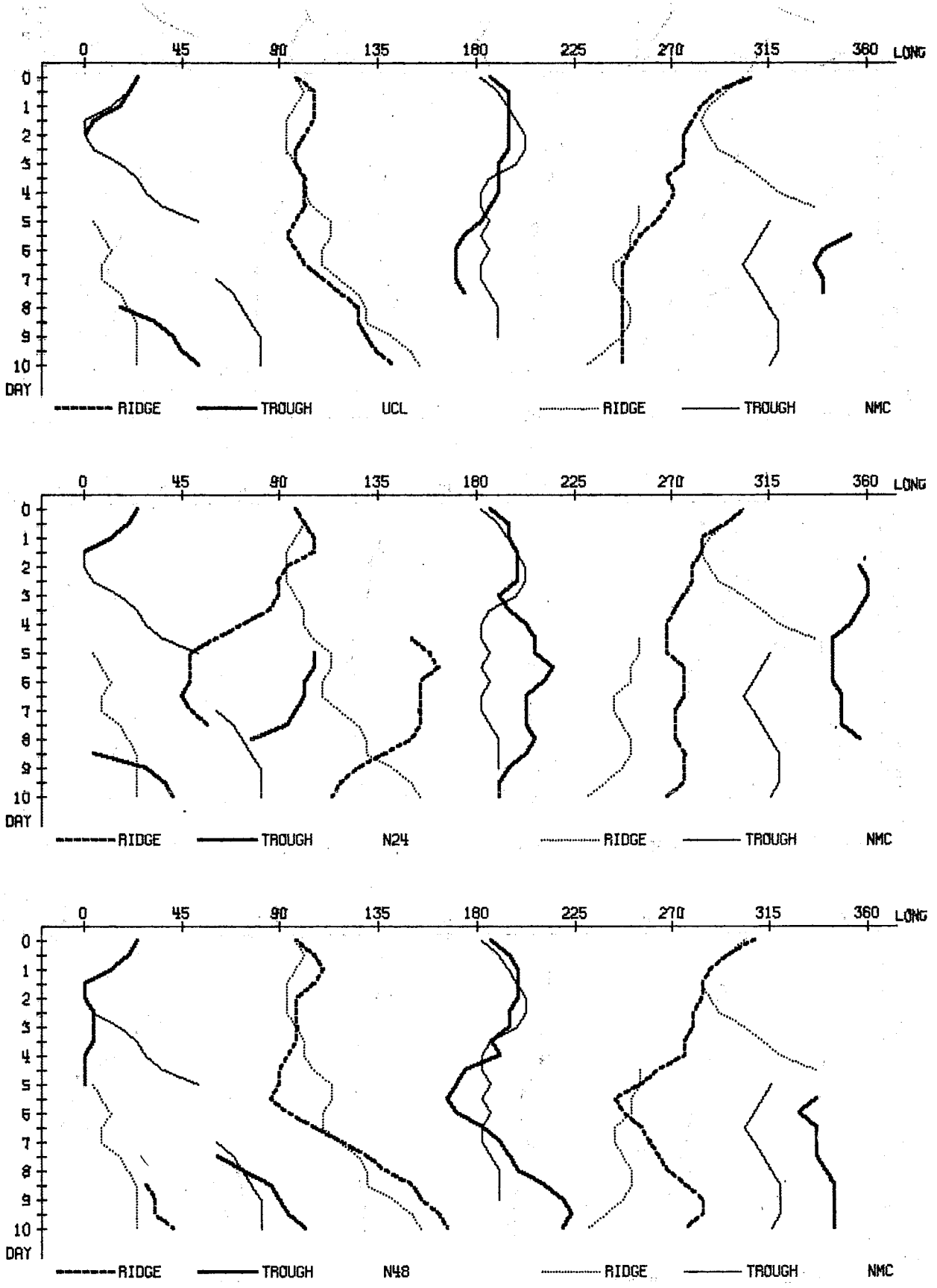

Fig. 4.2.23 : Same as 4.2.22

WAVENUMBER 1- 3 LATITUDE 60.0 N LEVEL1000 MB
GEOP. HEIGHT

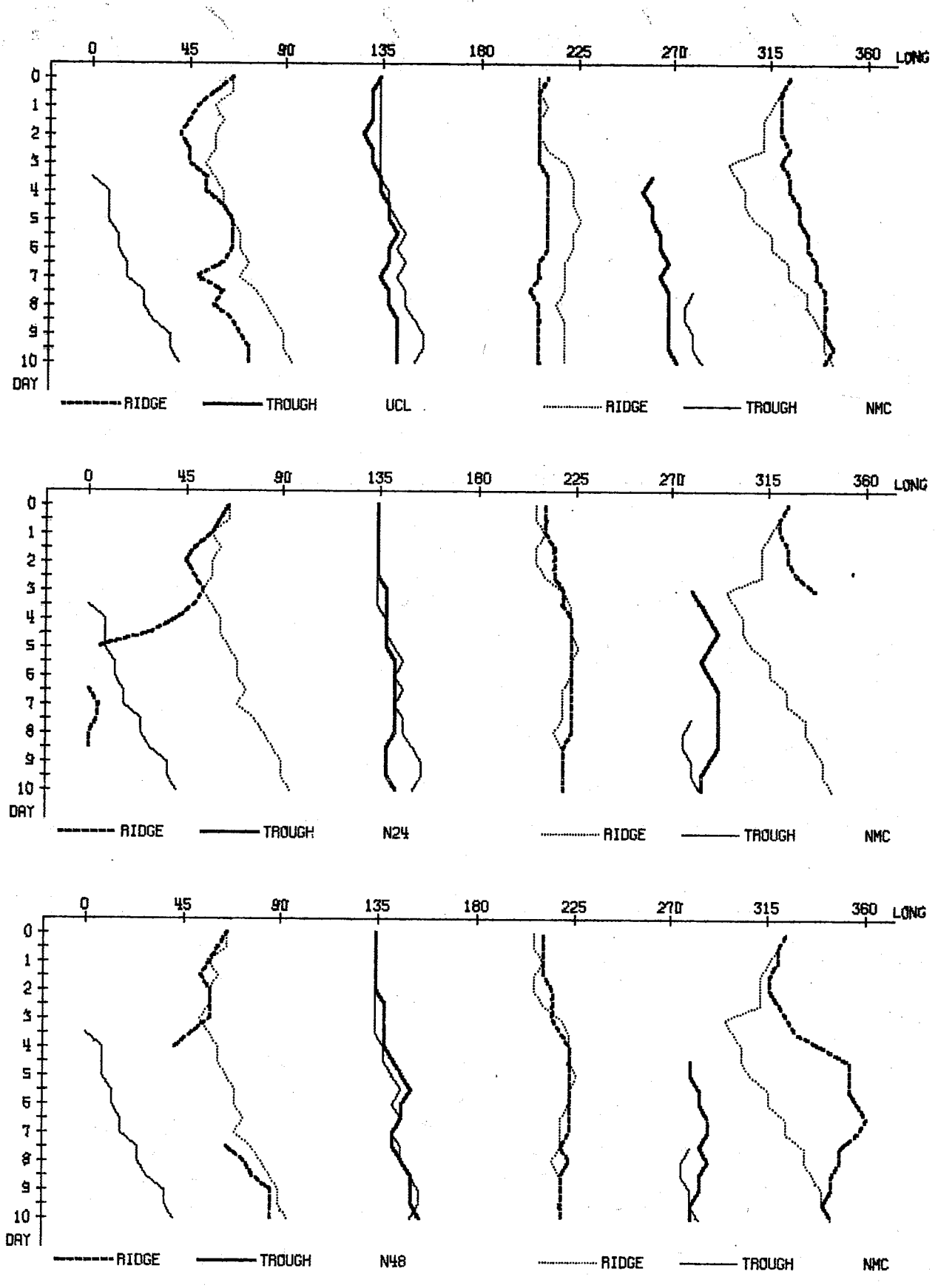

Fig. 4.2.24: Same as 4.2.22

WAVENUMBER 1- 3 LATITUDE 50.0 N LEVEL 850 MB

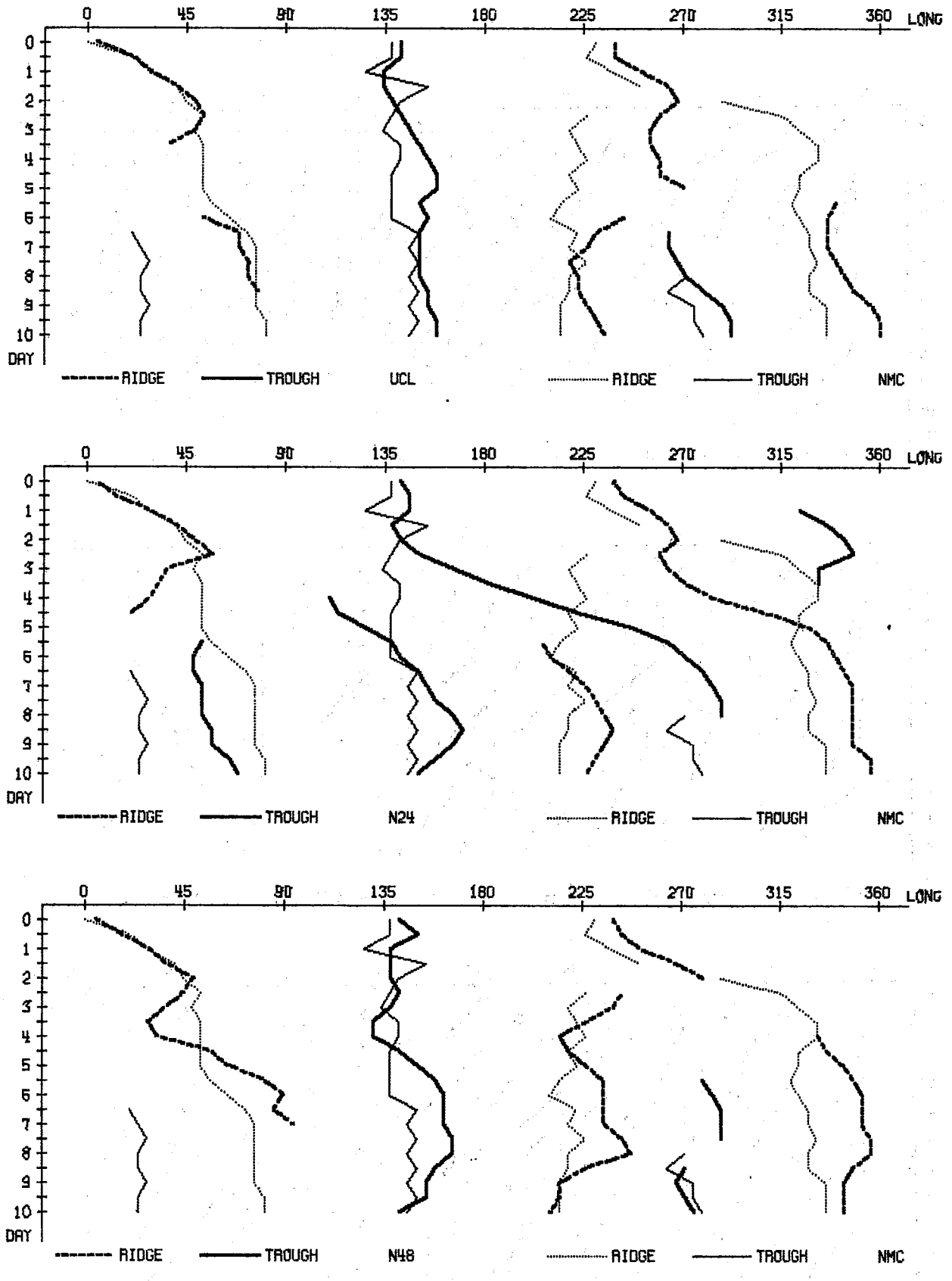

Fig. 4.2.25: Same as 4.2.22

WAVENUMBER 1- 3 LATITUDE 40.0 N LEVEL 500 MB TEMPERATURE

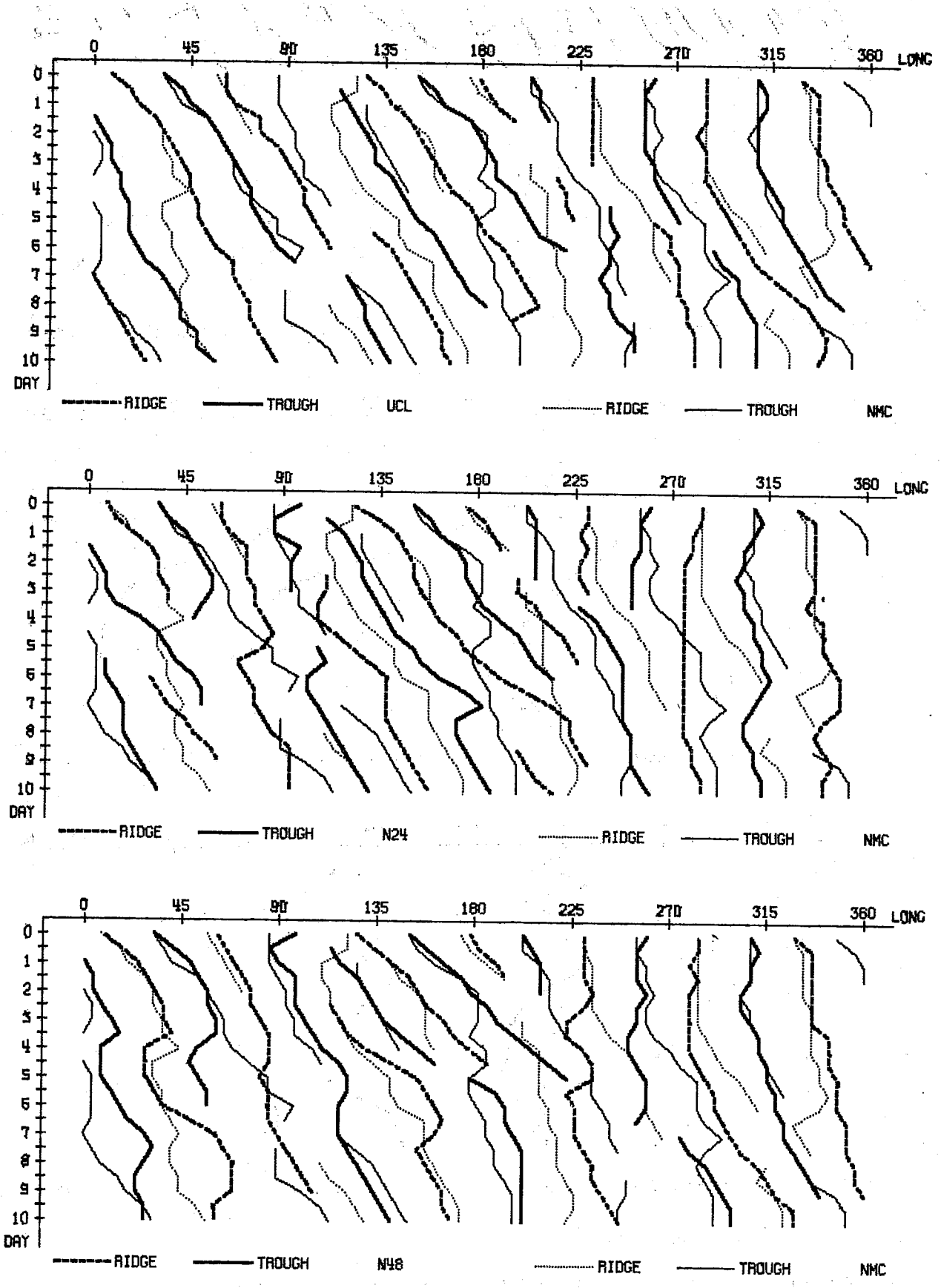

Fig. 4.2.26: Same as 4.2.22

WAVENUMBER 4- 9 LATITUDE 40.0 N LEVEL 500 MB
GEOP. HEIGHT

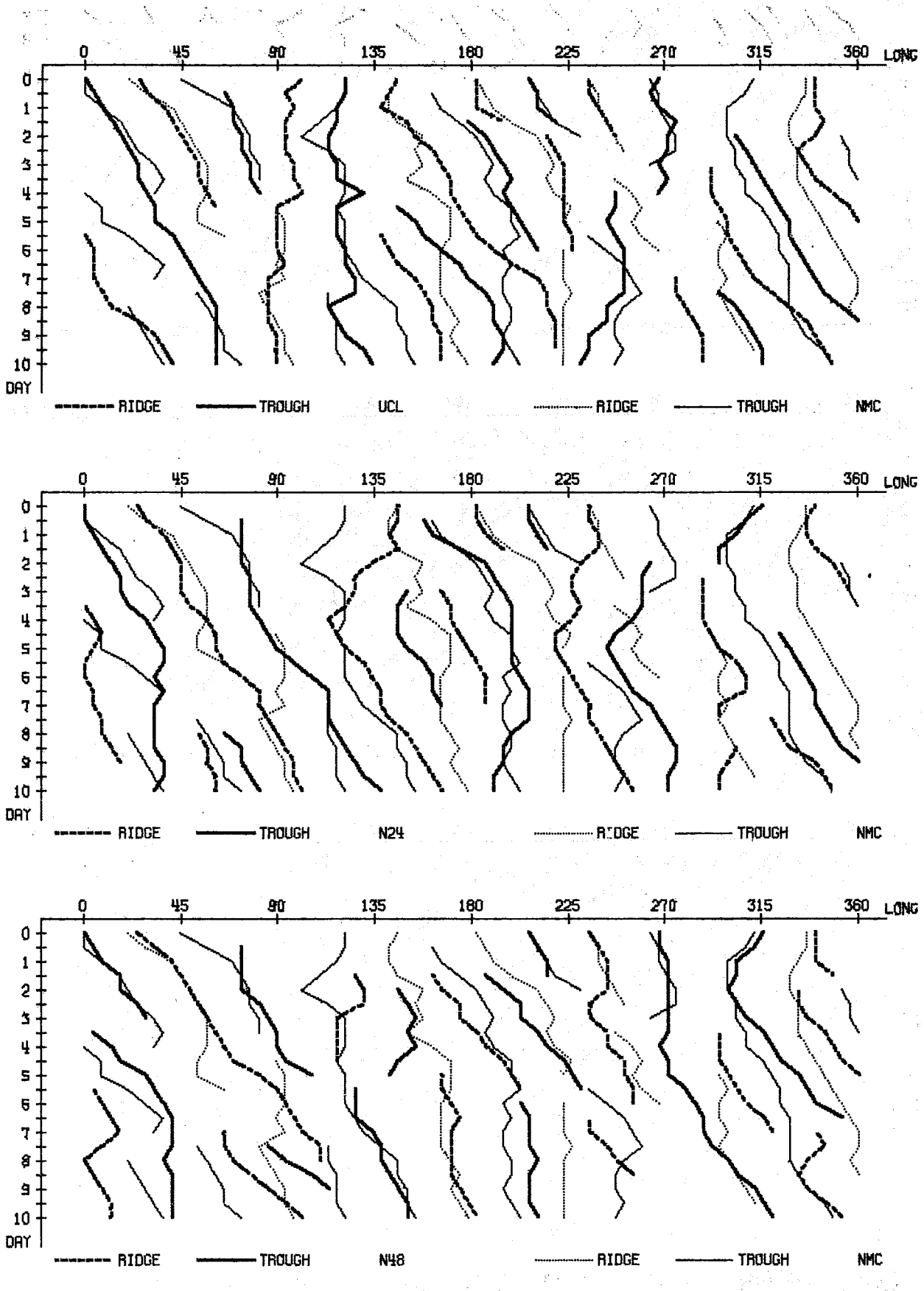

Fig. 4.2.27: Same as 4.2.22

WAVENUMBER 4- 9 LATITUDE 50.0 N LEVEL1000 MB
GEOP. HEIGHT

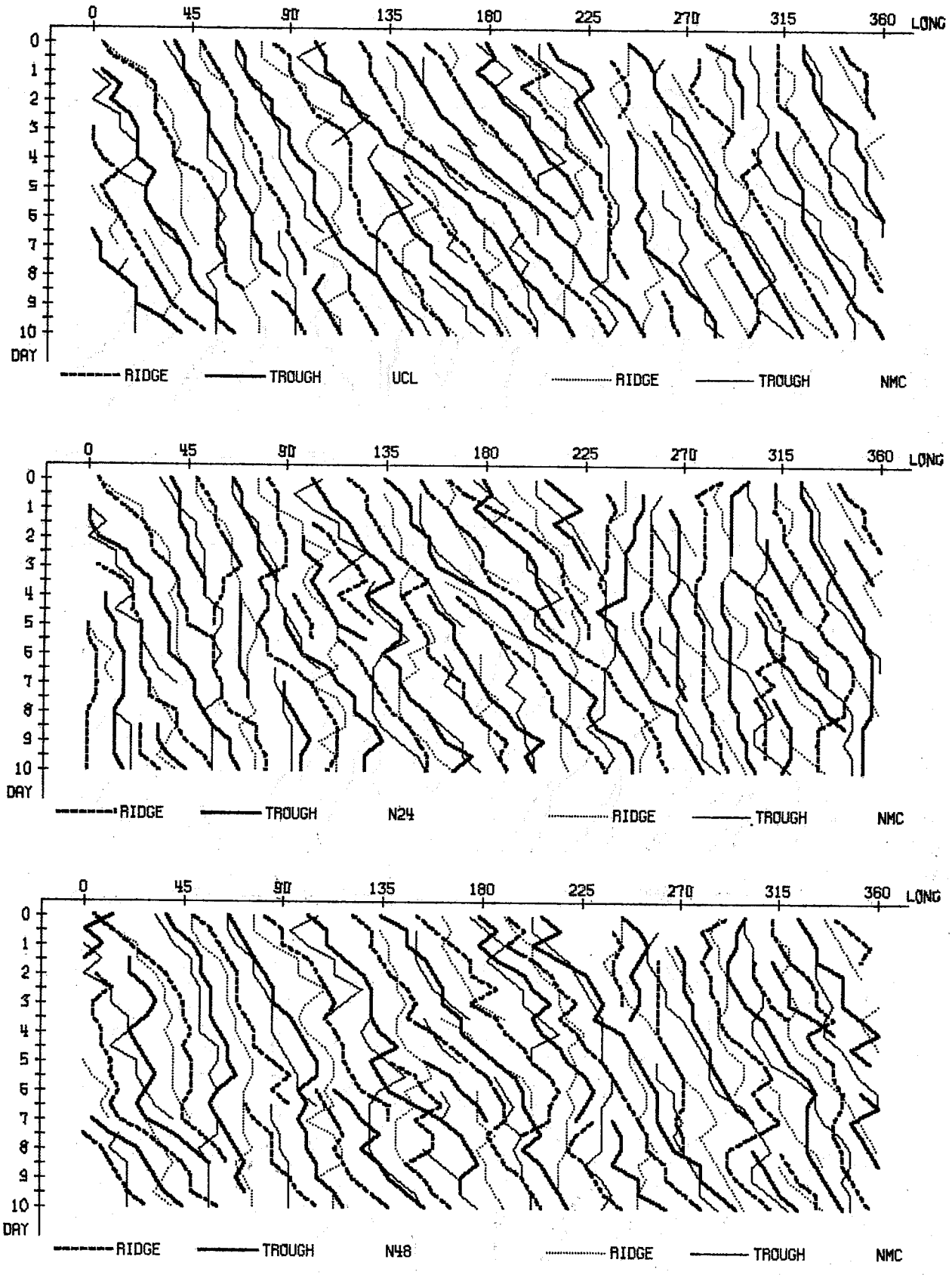

Fig. 4.2.28: Same as 4.2.22

WAVENUMBER 10-20 LATITUDE 40.0 N LEVEL 500 MB
GEOP. HEIGHT

The time variation of the mean RMS-error of the troposphere north of 20°N is shown in Fig. 4.3.1. It can easily be seen that for each of the wave number groups all forecasts are better than persistence. At the starting day the RMS-error is not zero for the forecasts, as it might be expected. This is due to different analyses, to initialisation, and to interpolation to sigma-coordinates and back. The shorter waves reach their maximum error values after 2 to 3 days. This probably means that the errors of the forecasts are smaller than persistence after 3 days only because they have less variance and not because they have higher skill.

The error of the zonal mean of the UCLA-forecast is worse than persistence. Looking into more details, it can be seen that this error comes mainly from the upper troposphere. It reflects the lack of two sharp jet streams or frontal zones in the forecasts, noted in the last sub-section.

It can be seen from figures 4.3.2 and 4.3.3 that the RMS-error of the long and medium waves starts to grow at the highest levels, spreading from there downwards. A corresponding growth at the lowest levels can also be seen. Figures 4.3.4 to 4.3.6 show the latitudinal differences in the RMS-errors. It is interesting to see in particular in figure 4.3.5 that there are two belts with higher values at about 40°N and about 60°N. These belts may indicate the positions of polar- and subtropic fronts, which naturally will cause large errors if their positions are not predicted precisely. A similar feature can be seen in corresponding figures for temperature.

Figure 4.3.6 shows a considerable growth of error of the zonal mean near the pole in the UCLA-forecast and in the persistence. A second maximum in all models and in the persistence can be seen at 50° to 60°N.

Figures 4.3.7 and 4.3.8 show the RMS-error for temperature. Only these two figures were selected, because all show in principle the same features as the RMS-errors of geopotential height. The only difference is an error minimum at about 300 mb, due to the minimum of temperature variance at this level.

Correlation coefficients

Correlation coefficients are often used as verification scores. The correlations for anomalies were chosen, so they will aymptotically approach zero as shown by MIYAKODA (1972). The formulation in wave number domain is the following:

$$CORR(M_1,M_2)=\frac{\int_{p_1}^{p_2}\int_{\psi_1}^{\psi_2}\sum_{M=M_1}^{M_2}\left[\left(\phi_F^c-\phi_C^c\right)\left(\phi_{Obs}^c-\phi_C^c\right)+\left(\phi_F^s-\phi_C^s\right)\left(\phi_{Obs}^s-\phi_C^s\right)\right]\cos\psi\,d\psi\,dp}{\left(\int_{p_1}^{p_2}\int_{\psi_1}^{\psi_2}\sum_{M=M_1}^{M_2}\left[\left(\phi_F^c-\phi_C^c\right)^2+\left(\phi_F^s-\phi_C^s\right)^2\right]\cos\psi\,d\psi\,dp\cdot\int_{p_1}^{p_2}\int_{\psi_1}^{\psi_2}\sum_{M=M_1}^{M_2}\left[\left(\phi_{Obs}^c-\phi_C^c\right)^2+\left(\phi_{Obs}^s-\phi_C^s\right)^2\right]\cos\psi\,d\psi\,dp\right)}$$

ϕ_F = forecast

ϕ_C = climate value (4.2)

ϕ_{obs} = observed

The climate data were taken from JENNE (1969).

For a first overview fig. 4.3.9 shows the correlation coefficients of geopotential height north of 20°N averaged over the whole troposphere. The correlation without separation into wave number groups (total) shows an almost linear decrease of all values with time and considerably higher values for the forecasts than for persistence. This advantage comes mainly from the long waves (1-3). The medium scale waves (4-9) show good correlation up to 4 days. For the short waves (10-20) already after one day persistence decreases to 0% and the forecasts decrease to 50 %. After about 4 days the forecast values are also down to 0%. The correlation of zonal means confirms the results of fig. 4.3.1 that in this regard only the GFDL-N24 model is better than persistence.

In fig. 4.3.10 and 4.3.11 the contributions of different levels to the correlation of geopotential heights are presented. In fig. 4.3.2 and 4.3.3 it was shown that the error propagated downward from the top of the atmosphere. In contrast, figure 4.3.10 shows the main error growth of the long waves originates near the earth's surface. Figure 4.3.11 gives almost no vertical differences for the medium wave length. (The RMS-error scores are not normalised whereas the correlation scores are).

It can be seen in fig. 4.3.12 that lowest correlations are at polar and tropical regions which may be connected with the small variances in this region.

As the corresponding figures for temperature look very similar to those already shown, only fig. 4.3.13 is presented to show the main differences with the height field. The low correlation at 300 mb due to the small variances at this level is illustrated.

4.4 Verification of energetics

The quantities which will be presented in this sub-section depend mostly on the wind field. As mentioned above, only geostrophic winds are used to get a simpler comparison to the observed data which do not include winds. We have therefore verified the geostrophic wind which may deviate substantially from the total wind field for the high wave number components.

Kinetic energy

The kinetic energy is computed in the wave number domain:

$$K(N_1,N_2)=\frac{1}{\int_{\psi_1}^{\psi_2}\cos\psi\,d\psi}\int_{p_1}^{p_2}\int_{\psi_1}^{\psi_2}\frac{\cos\psi}{4g}\sum_{N=N_1}^{N_2}\delta^N\left[U_c^2(N)+U_s^2(N)+V_c^2(N)+V_s^2(N)\right]d\psi\,dp \qquad (4.3)$$

$\delta^N = \begin{cases} 1 & \text{if } N>0 \\ 2 & \text{if } N=0 \end{cases}$

$U_c(N)$, $V_c(N)$ = cosine coeff. of Fourier series of winds

$U_s(N)$, $V_s(N)$ = sine coeff. of Fourier series of winds

This quantity will be represented by several figures, because they show significant differences between the three forecasts. For a survey, figure 4.4.1 shows a mean over the whole troposphere north of 20°N. The forecast values for the waves are for the most part considerably smaller than the observed values. This is to some extent caused by the extra smoothing of the forecast data due to many interpolations because even at the starting day big differences may be seen. The best result for the eddy kinetic energy is obtained by the GFDL-N48 model. The reason is probably related to the relatively higher resolution of this model.

In the vertical sections (figures 4.4.2 and 4.4.3) it can be seen that the main loss of energy, as compared with the observed data, is in the polar-jet-level of 300 mb where the energy is concentrated. This concentration cannot be found in the models and is generally poorest for the UCLA model, which has the lowest vertical resolution.

The patterns produced by all the models are very similar to the observations in figure 4.4.4, showing the latitudinal distribution of kinetic energy of the long waves during the first seven days. However, note that the forecast values are too low and that the subsequent increase of energy north of 50°N is badly predicted by the models.
In figure 4.4.5, the increase of kinetic energy of the medium waves (4-9) after the 8th day is predicted reasonably well by all the models, but the two lower resolution models underpredict the magnitude of this increase.

The latitudinal distribution of the zonal kinetic energy (fig. 4.4.6) shows that the subtropical jet stream is predicted slightly too far north during the first part of the period.

Available potential energy

The eddy available potential energy is a measure of temperature fluctuations around a latitudinal circle.

$$AE = A(N_1, N_2) = \frac{1}{\int_{\psi_1}^{\psi_2} \cos\psi \, d\psi} \int_{p_1}^{p_2} \frac{\gamma}{4} \int_{\psi_1}^{\psi_2} \sum_{N=N_1}^{N_2} \left[T_c^2(N) + T_s^2(N) \right] \cos\psi \, d\psi \, dp$$

$$AZ = \frac{1}{\int_{\psi_1}^{\psi_2} \cos\psi \, d\psi} \int_{p_1}^{p_2} \frac{\gamma}{2} \int_{\psi_1}^{\psi_2} \left[T_c(0) - \overline{T}^F \right]^2 \cos\psi \, d\psi \, dp$$

$$\gamma = \frac{-R}{g p \left(\frac{\partial \overline{T}}{\partial p} - \frac{R \overline{T}}{c_p p} \right)}$$

(4.4)

$T_c(N)$ = cosine coefficient of zonal Fourier series
$T_s(N)$ = sine coefficient of zonal Fourier series of temperature

$\overline{T} = T_c(0)$ = zonal mean of temperature

$\overline{T}^F$ = area mean of temperature north of $20^{\circ}N$

Figure 4.4.7 shows that the predicted zonal temperature variances are too small. On the other hand, in the meridional direction the variations are too strong after about 5 days, which is indicated by the zonal available potential energy. The high resolution GFDL-model agrees best with the observations.

Figure 4.4.8 and figure 4.4.9 indicate, like figure 4.4.2 and figure 4.4.3, that the models have weaker vertical contrasts than observed. It can best be seen by comparing the data at 500 mb and at 300 mb. This comparison agrees well with the previous results because smaller temperature variations in the lower troposphere mean smaller geopotential height variations in the higher troposphere.

In all of the models, as in the real atmosphere, a reduction of available potential energy can be found at the 300 mb level, due to the reduction of temperature contrasts at the tropopause.

In figure 4.4.10 it is interesting to see the variation of available potential energy with latitude for the long waves. It is best predicted by the GFDL-N48 model. However, the increase after seven days was either missed or was poorly predicted. All the models predict a second maximum at about 60^{o}N after three days, which was not observed.

Transfers between zonal and eddy energies

It would be interesting to examine all energy conversions and transports, but since only geostrophic winds from the observations are available, we have limited the study to the transfers between zonal and eddy kinetic and available potential energy respectively. The exact formulae for these transfers can be found e.g. in PAULIN (1968), here we have only what is relevant for this study.

Transfer from zonal to eddy kinetic energy :

$$CK(N_1,N_2) = \frac{-1}{2\int_{\psi_1}^{\psi_2}\cos\psi\,d\psi}\int_{p_1}^{p_2}\int_{\psi_1}^{\psi_2}\sum_{N=N_1}^{N_2}\left[U_C(N)V_C(N)+U_S(N)V_S(N)\right]\frac{\cos\psi}{a}\,\frac{\partial}{\partial\psi}\left(\frac{U_C(0)}{\cos\psi}\right)\cos\psi\,d\psi\,dp$$

(4.5)

Transfer from zonal to eddy available potential energy:

$$C_A(N_1,N_2) = \frac{-1}{\int_{\psi_1}^{\psi_2} \cos\psi \, d\psi} \int_{p_1}^{p_2} \frac{\gamma}{2} \int_{\psi_1}^{\psi_2} \sum_{N=N_1}^{N_2} \left[V_C(N)\, T_C(N) + V_S(N)\, T_S(N) \right] \frac{1}{a} \frac{\partial \bar{T}}{\partial \psi} \cos\psi \, d\psi \, dp$$

$$\gamma = \frac{-R}{g\,p\left(\frac{\partial \bar{T}}{\partial p} - \frac{R\bar{T}}{c_p\,p}\right)}$$

$\bar{T}$ = zonal mean of temperature

(4.6)

Figure 4.4.11 shows the mean over the northern hemisphere of CK. The transfers of wave number groups with long and medium wave lengths start with negative values. This means that the eddies are transferring energy to the mean flow. After about 12 hours the process changes. The dominance of positive values after this date is abnormal for this transfer.
For the long waves (1-3) the trend of CK was predicted well for 3 days ; for the medium scale waves (4-9) the prediction was only good for 2 days. After that there is almost no agreement between forecasts and observations.

More detailed information can be gained from figures 4.4.12 and 4.4.13, which confirm the above statements. In particular, the high values after 5 days in figure 4.4.12 are not forecast by any of the models.

In figure 4.4.14 it may be seen that the transfer from zonal to eddy available potential energy is positive for almost all wave number groups and all dates. That means that zonal available potential energy is transferred to the eddies. Here it is seen that the GFDL-models predict this transfer far better than the UCLA-N22 model, at least for the first 4 days. As this transferred energy will be mainly converted to eddy kinetic energy, it may be the reason why the UCLA-N22 model has the smallest amount of eddy kinetic energy, as was shown.

By the second day, the UCLA-N22 forecast of the value of this conversion for the long waves is only half of the observed value. Note, however, that only the predicted average transfer at this date by the GFDL-models is good. The forecasts with the GFDL-models in figure 4.4.15, are not better than the UCLA forecasts. The maximum of transfer with the GFDL-models on the second day, at about $70^{o}N$, was not observed.

The transfer in the medium wave lengths (4-9) is shown in a vertical cross-section (figure 4.4.16). It is clear that the models with low resolution cannot produce the strong gradients which are observed.

It is not clear yet how much of the large differences between observed and forecast data are due to the coarse method in computing them. But as the similarity is good for the first 36 hours, it is probable that the differences are due mainly to the inaccuracy of the forecasts.

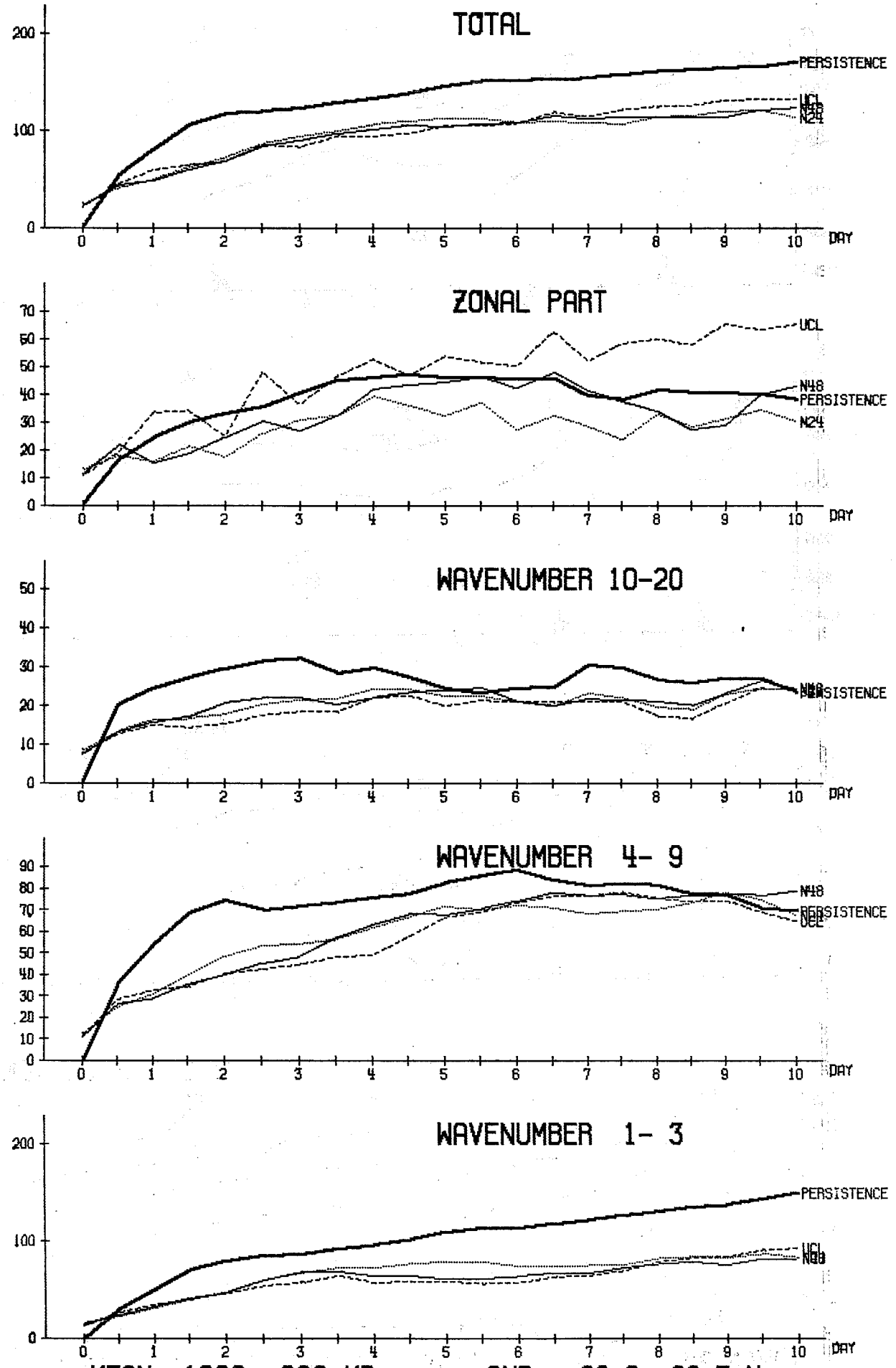
TOTAL
PERSISTENCE
UCL
N48
N24
DAY
ZONAL PART
UCL
N48
PERSISTENCE
N24
DAY
WAVENUMBER 10-20
PERSISTENCE
DAY
WAVENUMBER 4- 9
N48
PERSISTENCE
UCL
DAY
WAVENUMBER 1- 3
PERSISTENCE
UCL
N48
DAY
MEAN 1000- 200 MB AND 20.0- 82.5 N
RMS ERROR OF HEIGHT (M)

Fig. 4.2.1

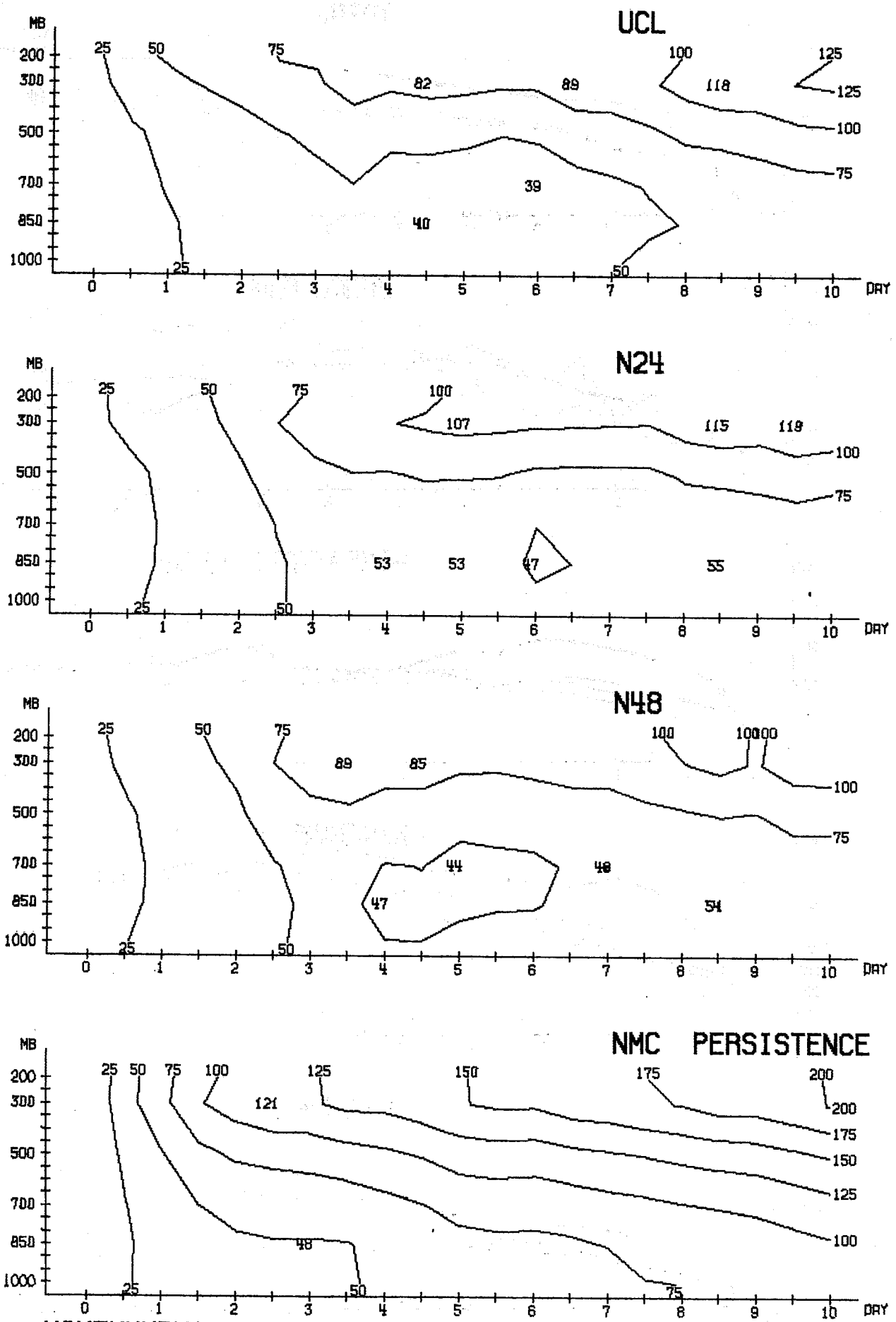

WAVENUMBER 1- 3 MEAN BETWEEN 20.0 AND 82.5 N
RMS ERROR OF HEIGHT (M)

Fig. 4.3.2

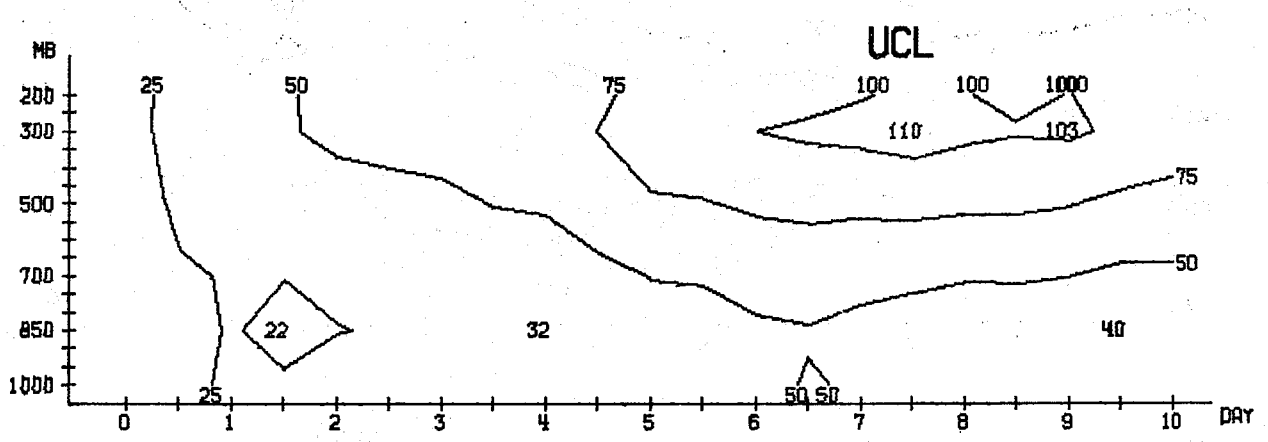

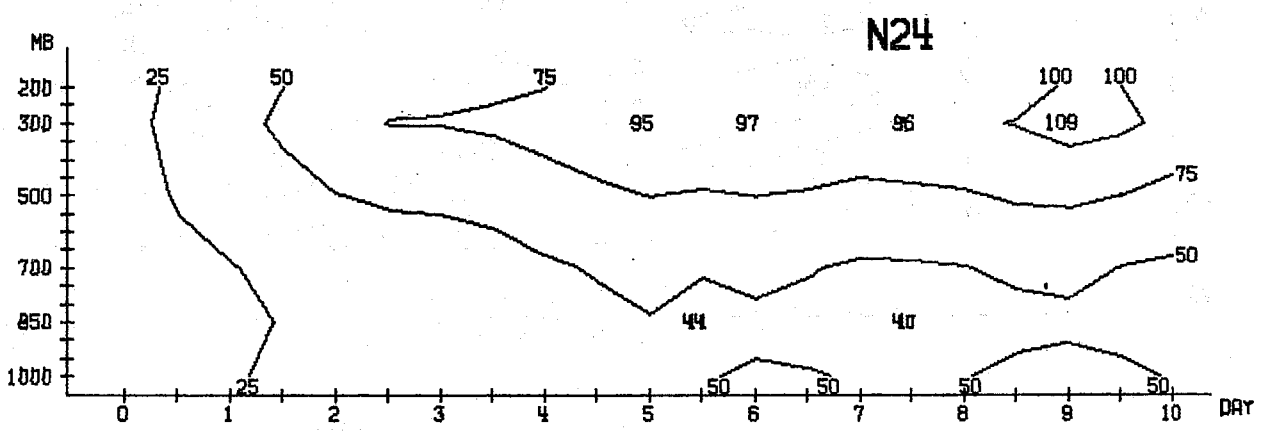

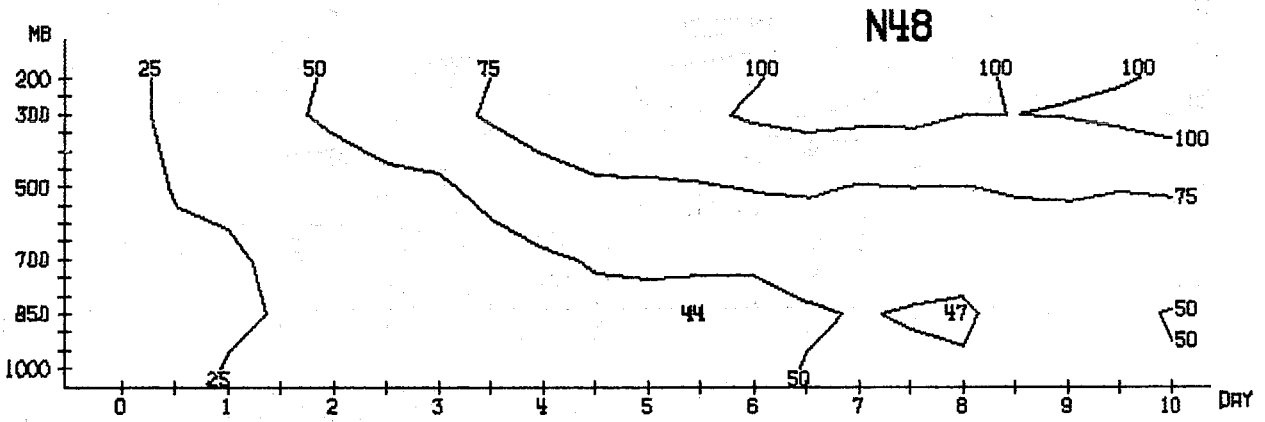

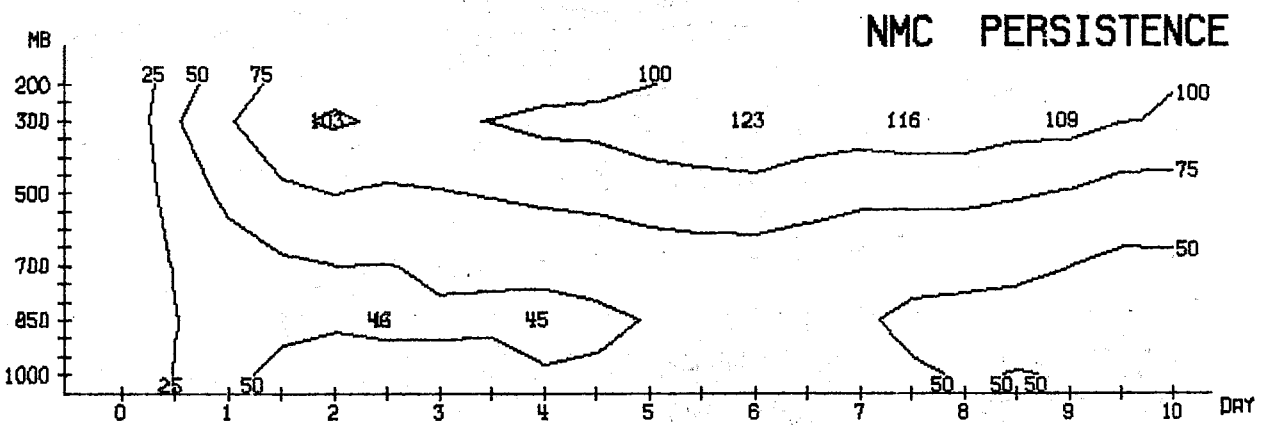

WAVENUMBER 4- 9 MEAN BETWEEN 20.0 AND 82.5 N

RMS ERROR OF HEIGHT (M)

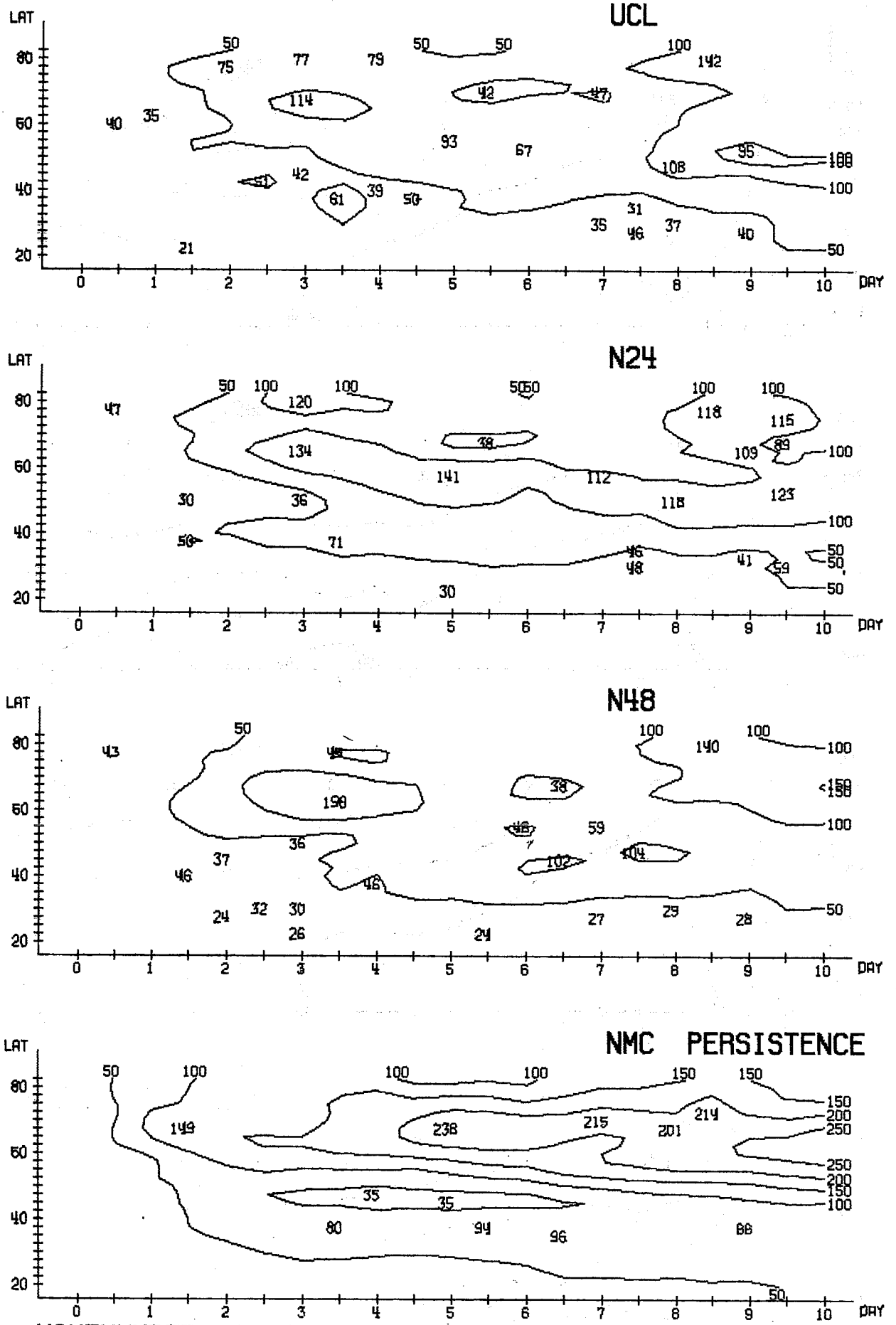

WAVENUMBER 1- 3 MEAN BETWEEN 1000 AND 200 MB
RMS ERROR OF HEIGHT (M)

Fig. 4.3.4

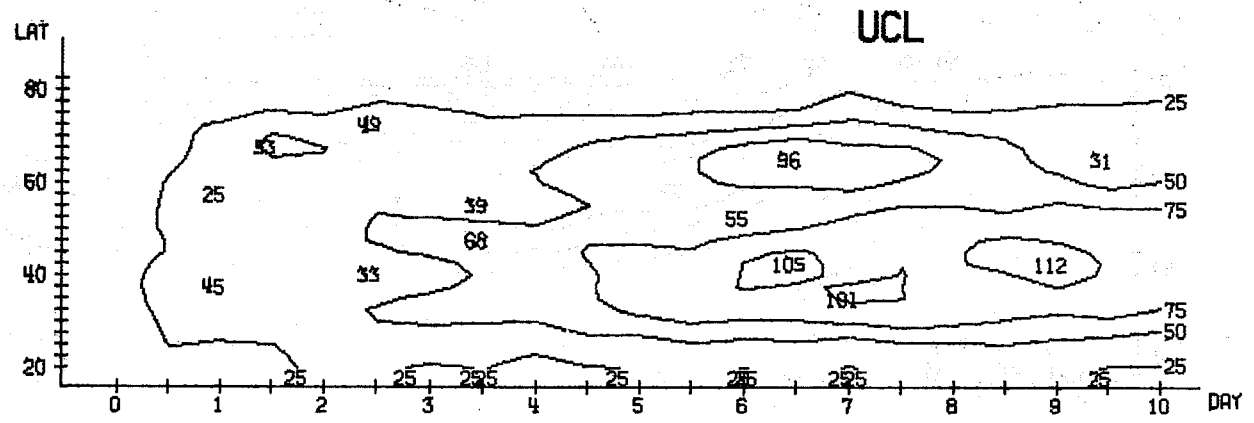

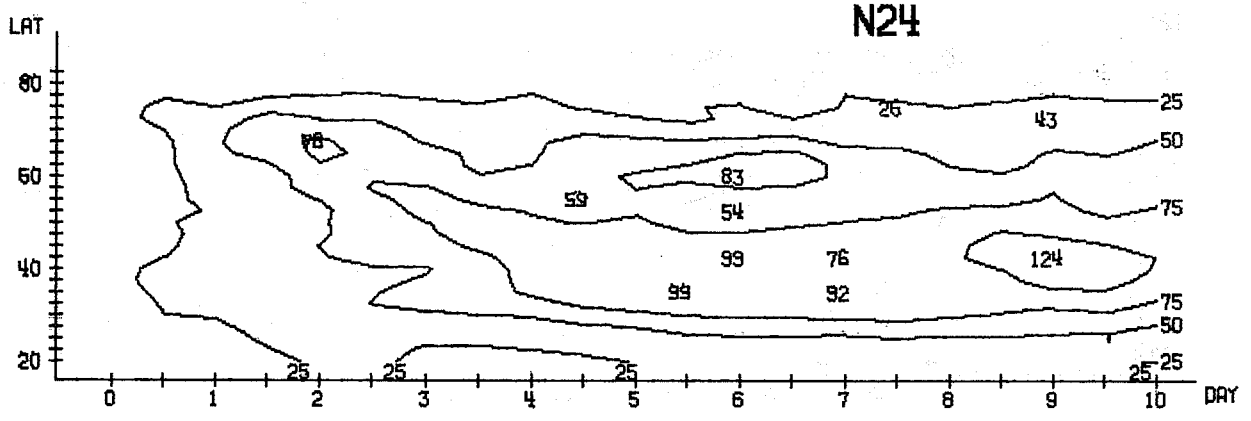

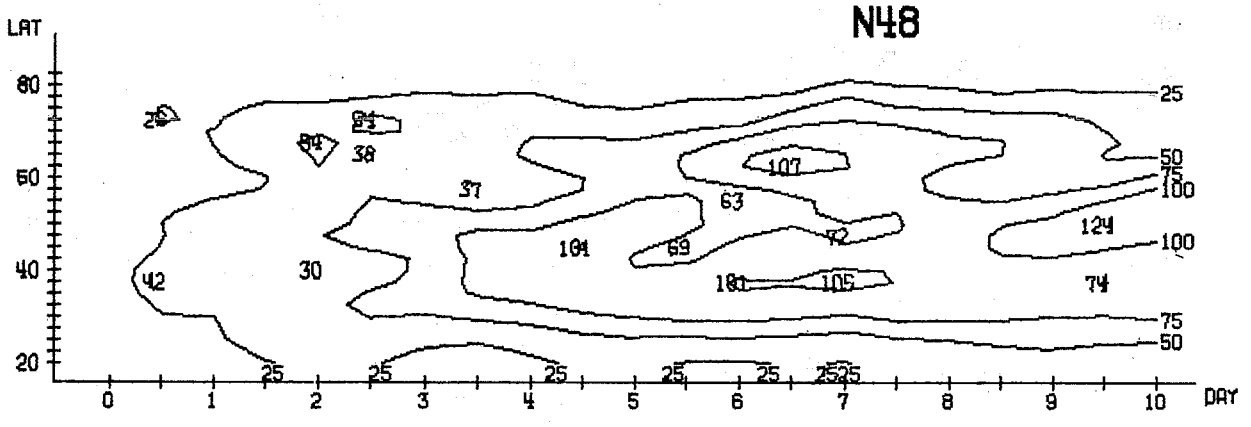

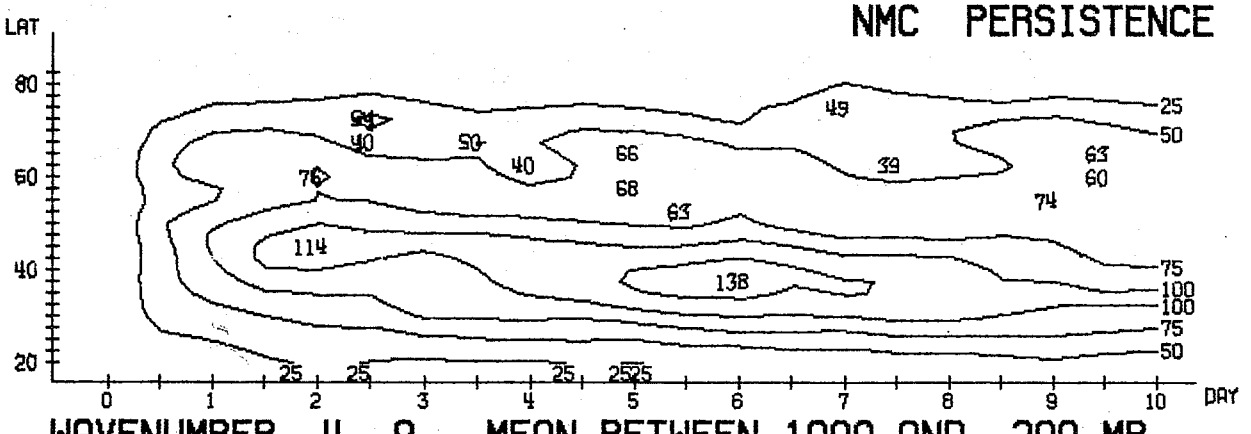

WAVENUMBER 4- 9 MEAN BETWEEN 1000 AND 200 MB

RMS ERROR OF HEIGHT (M)

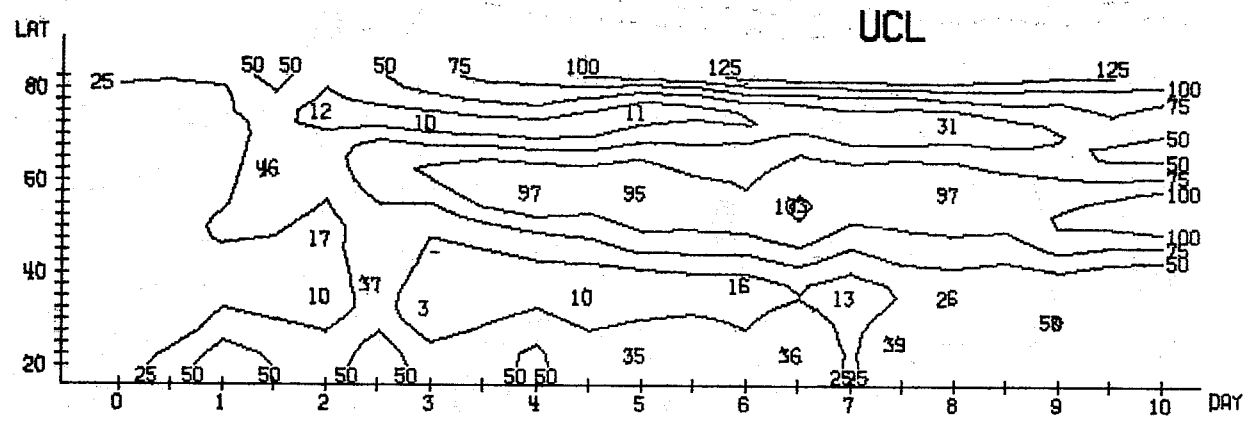

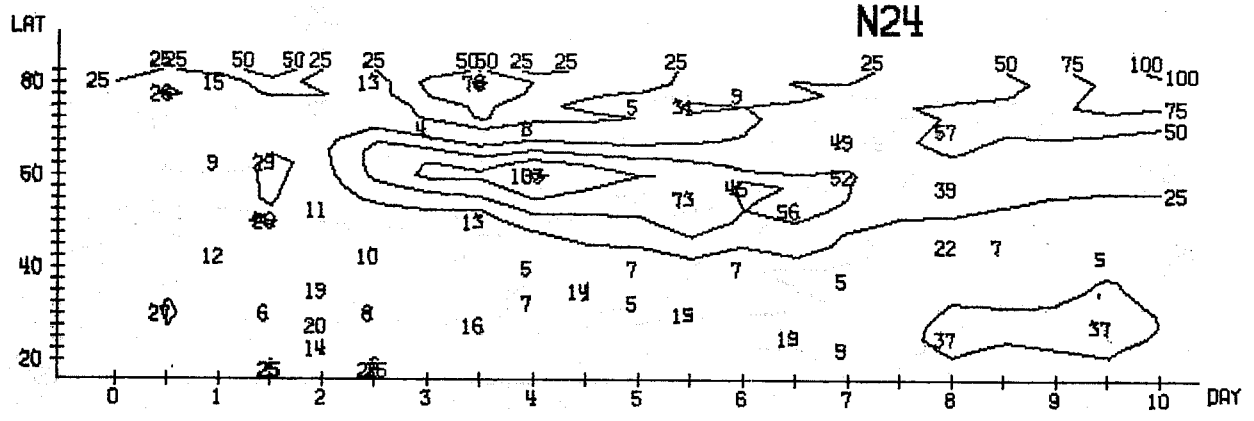

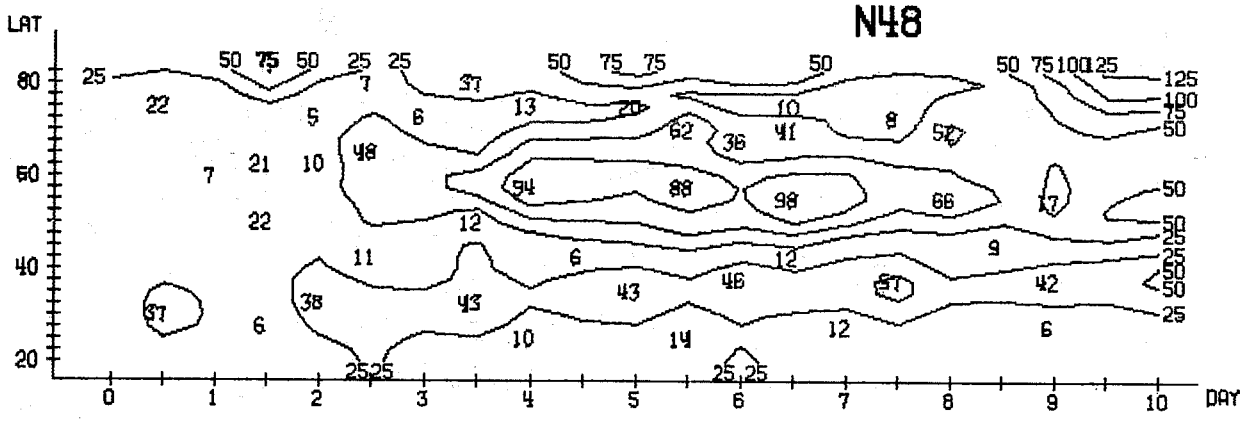

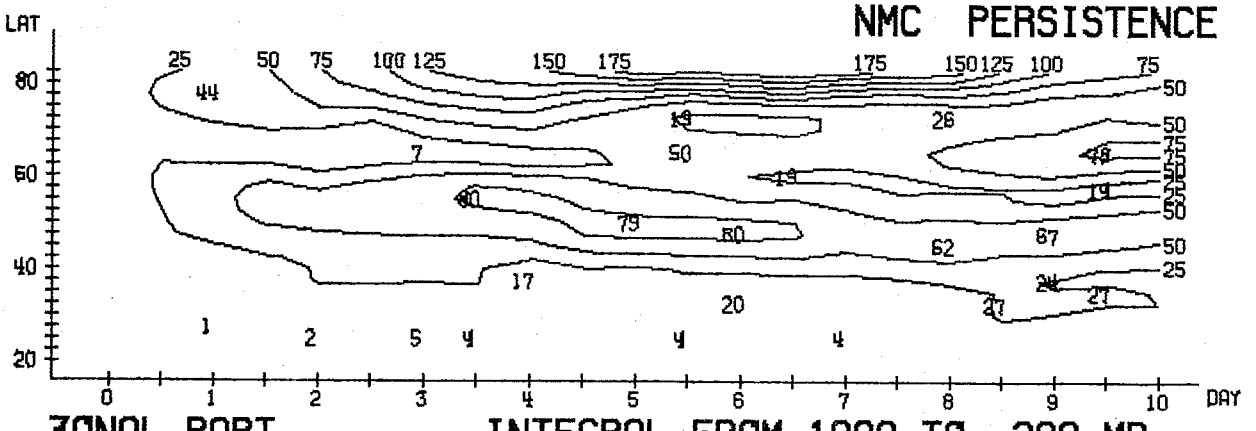

ZONAL PART INTEGRAL FROM 1000 TO 200 MB

RMS ERROR OF HEIGHT (M)

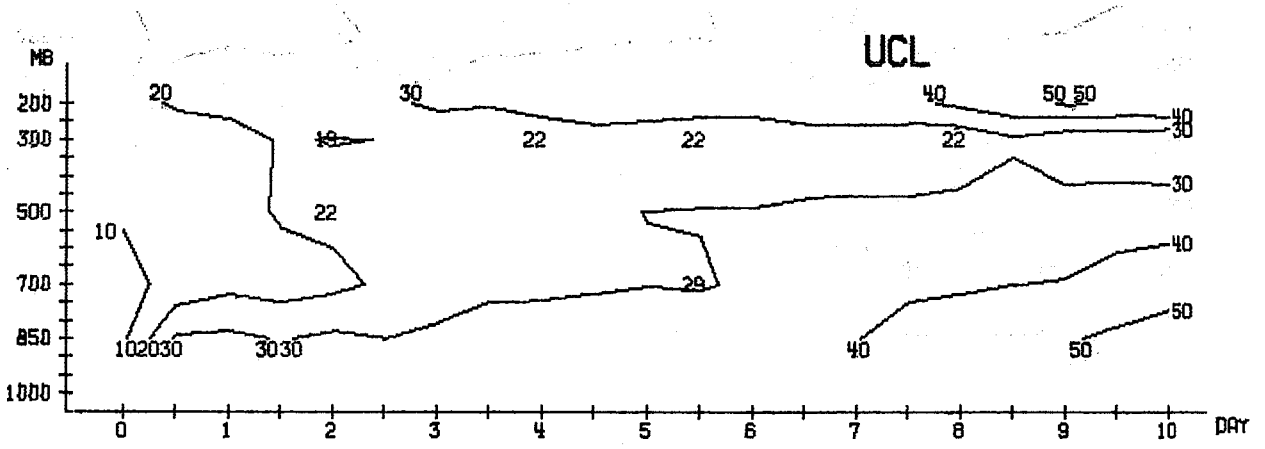

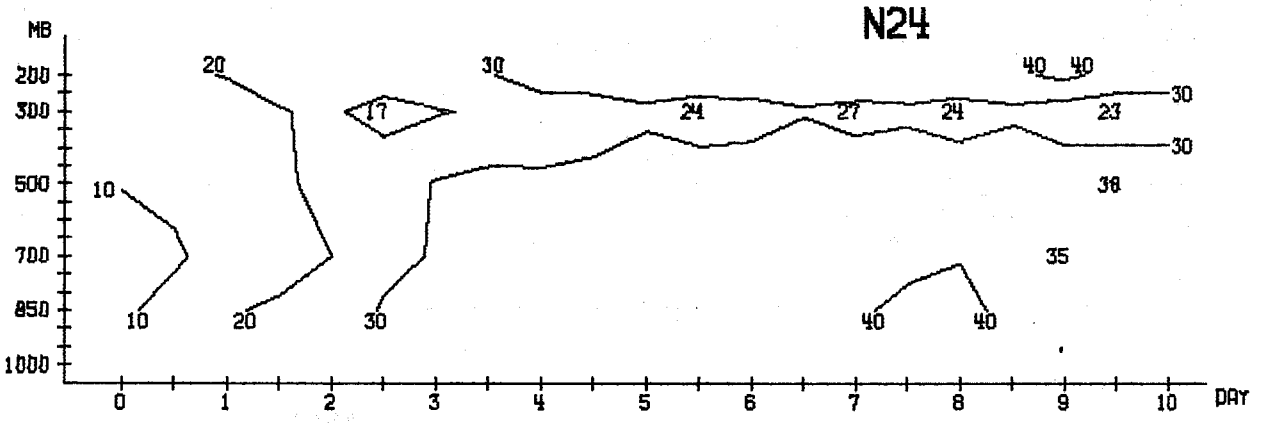

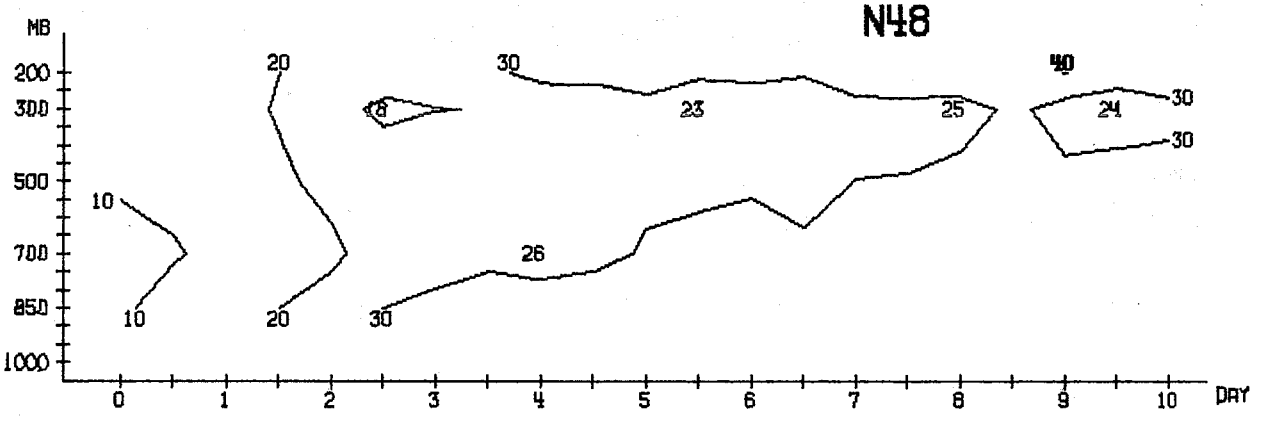

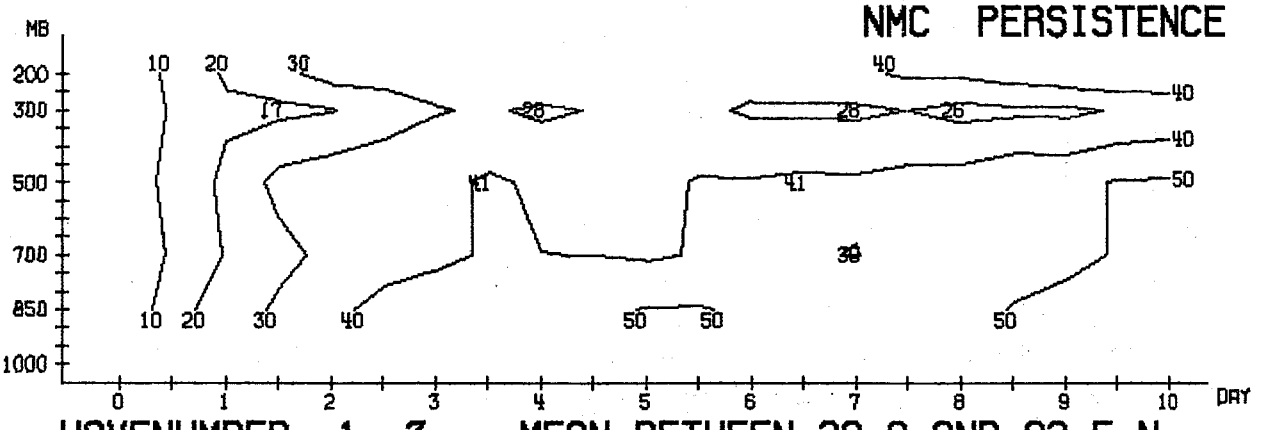

WAVENUMBER 1- 3 MEAN BETWEEN 20.0 AND 82.5 N

RMS ERROR OF TEMPERATURE (C/12)

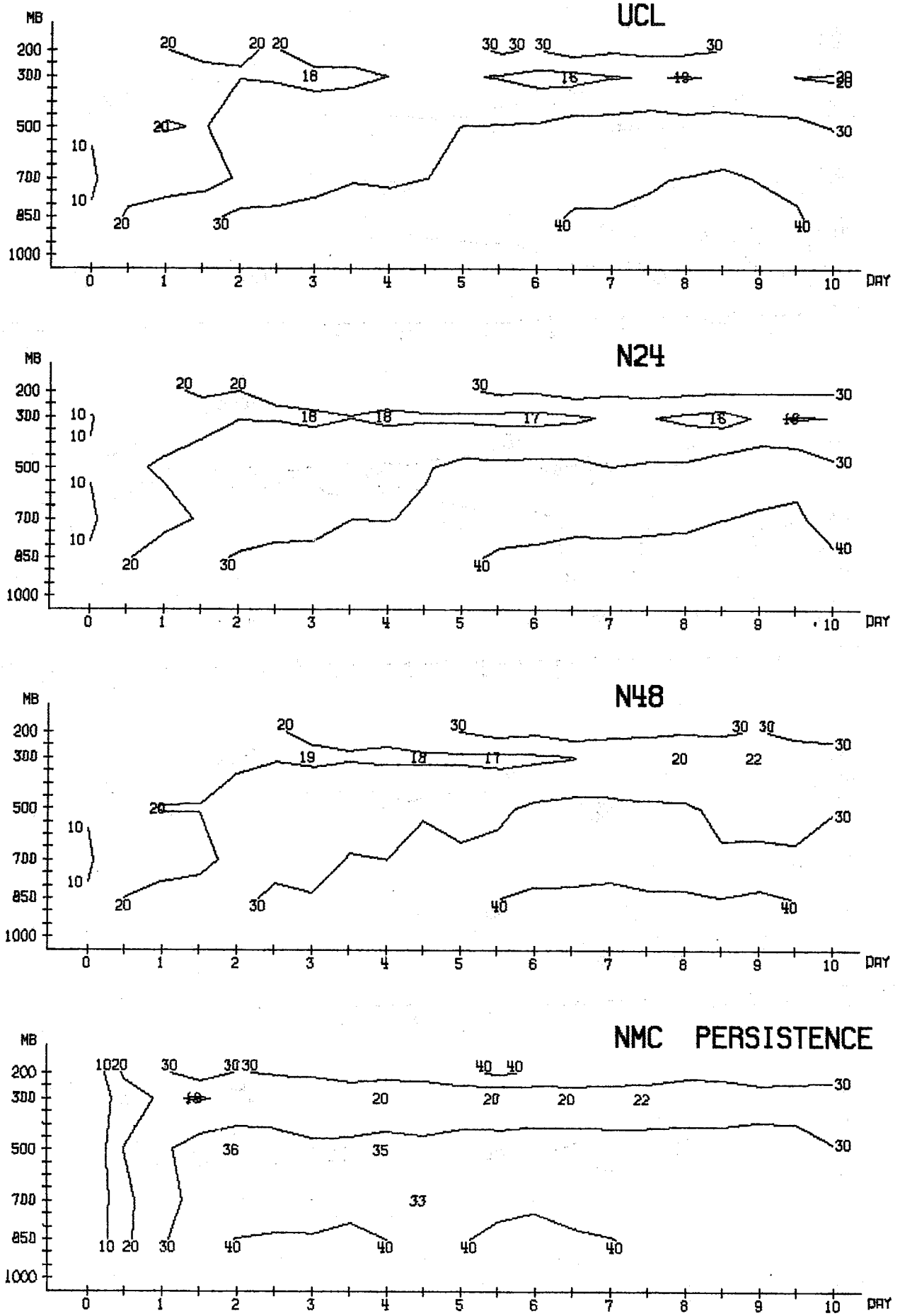
UCL
N24
N48
NMC PERSISTENCE
MB
DAY
WAVENUMBER 4- 9 MEAN BETWEEN 20.0 AND 82.5 N
RMS ERROR OF TEMPERATURE (C/10)

Fig. 4.3.8

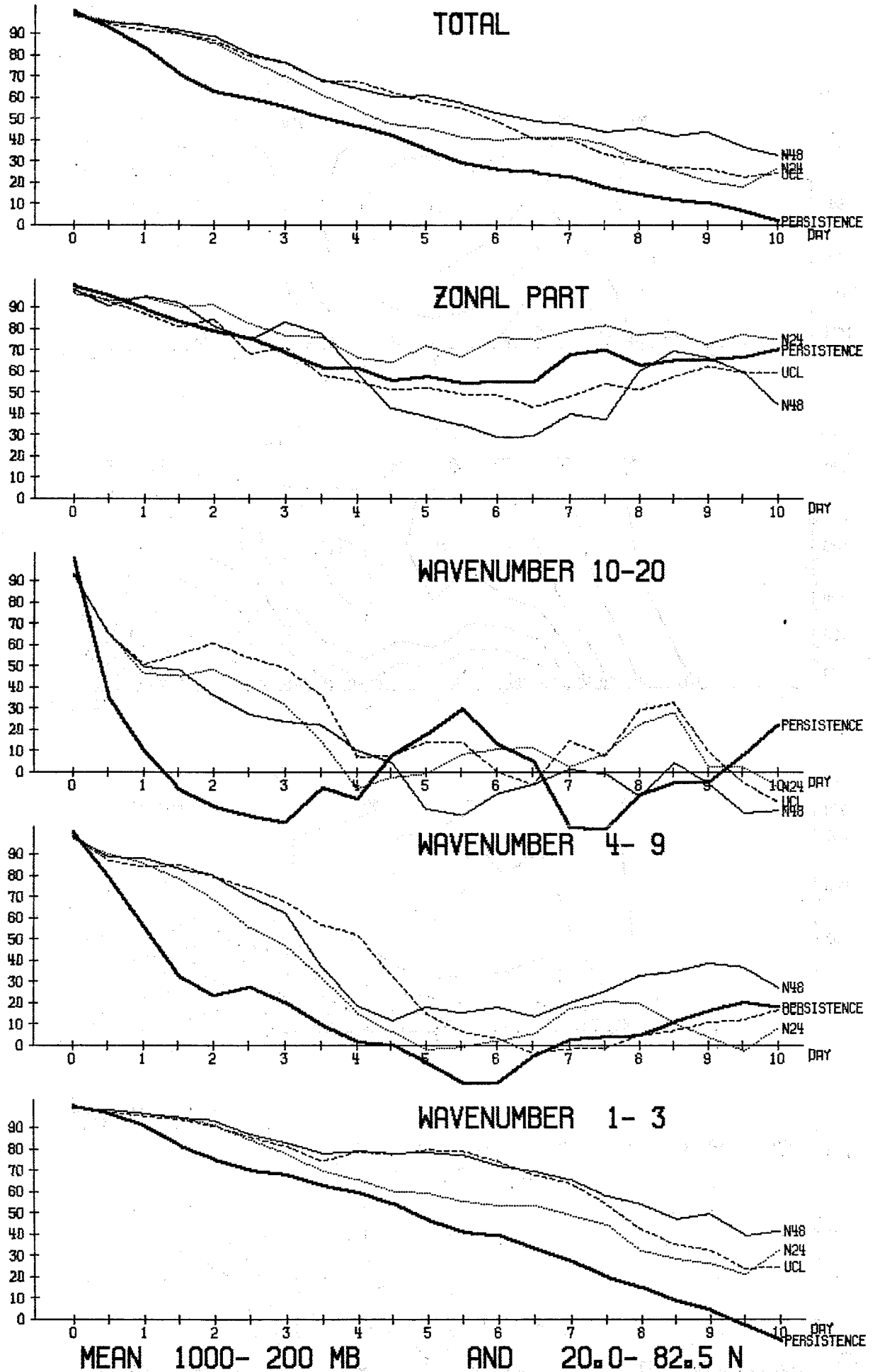

MEAN 1000- 200 MB AND 20.0- 82.5 N
CORRELATION OF HEIGHT %

Fig. 4.3.2

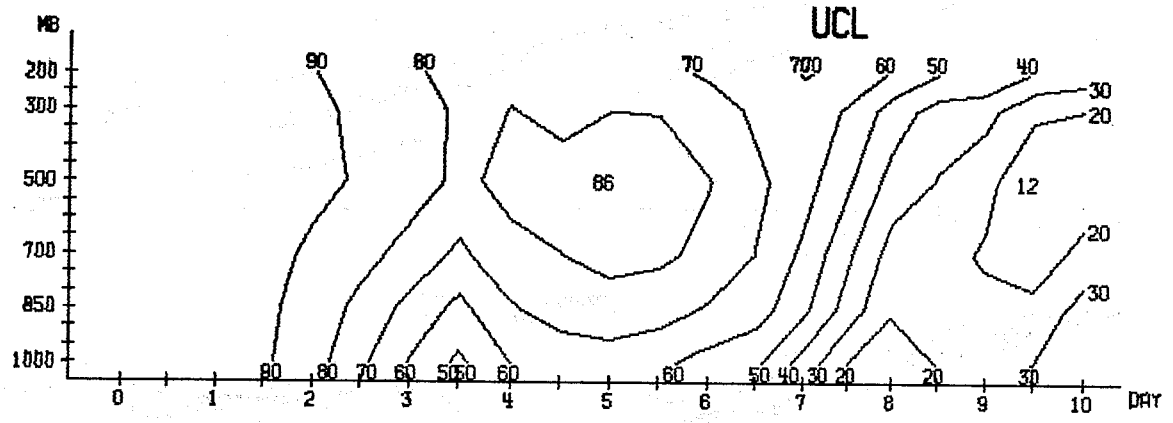

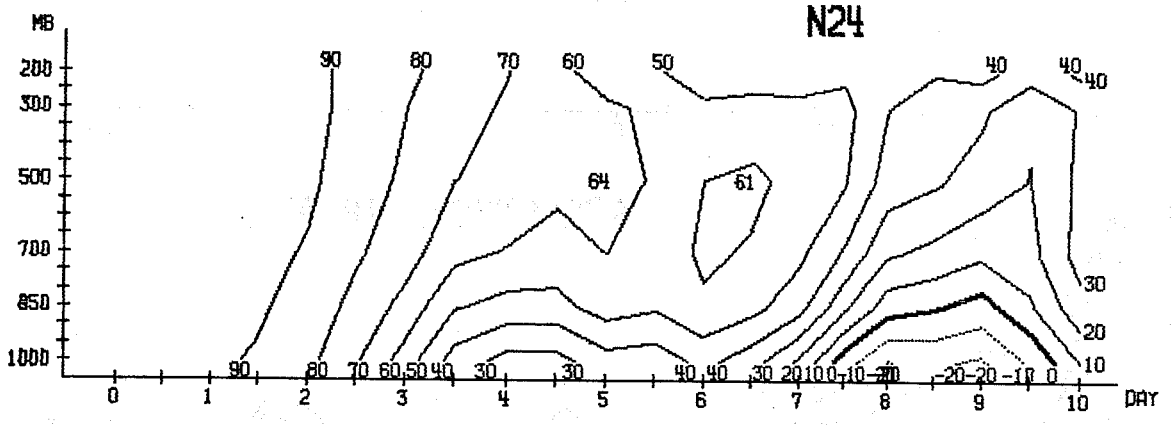

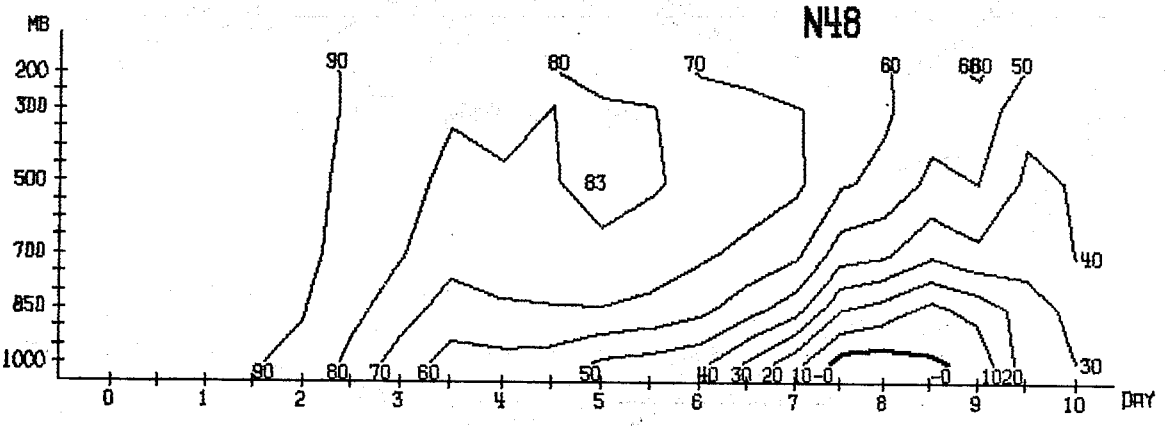

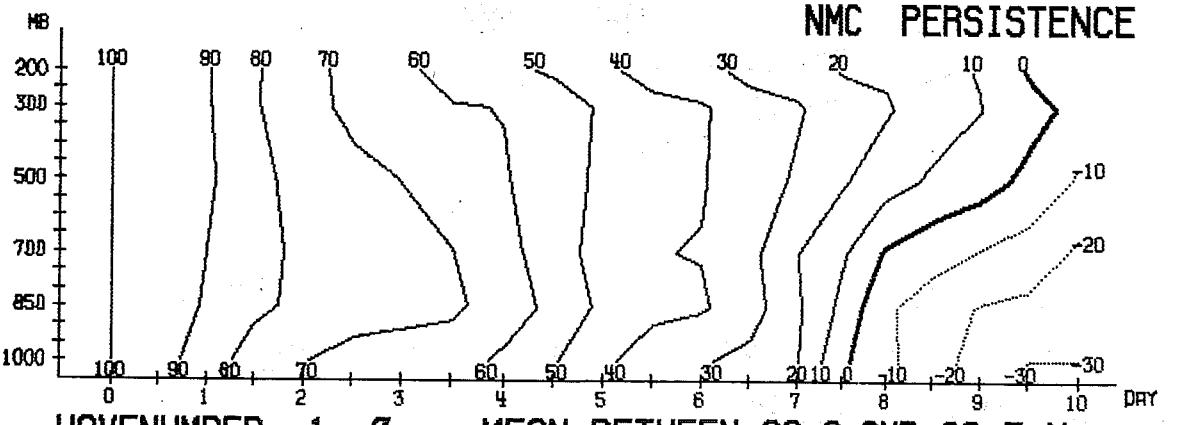

WAVENUMBER 1- 3 MEAN BETWEEN 20.0 AND 82.5 N

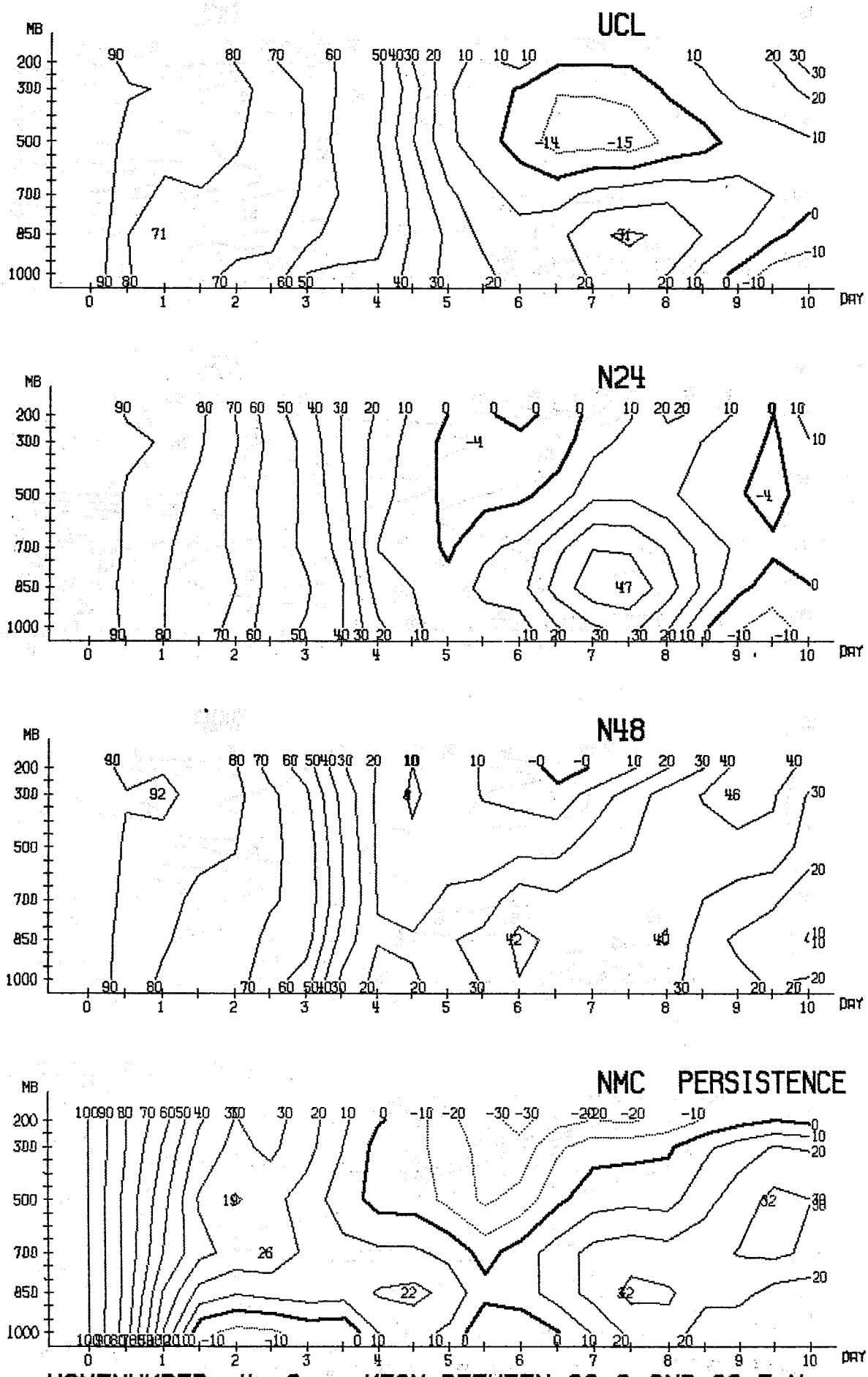
UCL
N24
N48
NMC PERSISTENCE
MB
DAY
WAVENUMBER 4- 9 MEAN BETWEEN 20.0 AND 82.5 N
CORRELATION OF HEIGHT %

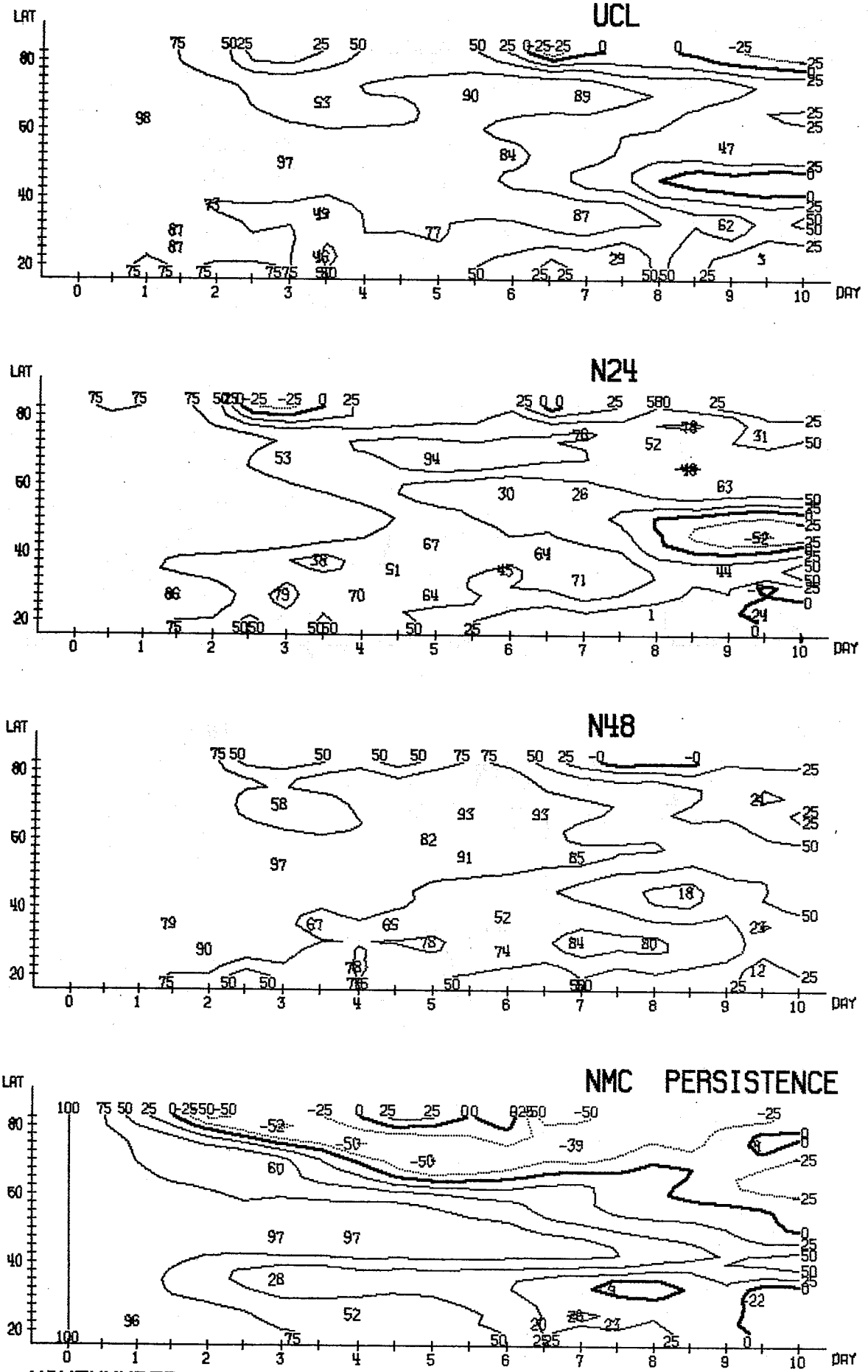
UCL
N24
N48
NMC PERSISTENCE
LAT
DAY
WAVENUMBER 1- 3 MEAN BETWEEN 1000 AND 200 MB
CORRELATION OF HEIGHT %

Fig. 4.3.12

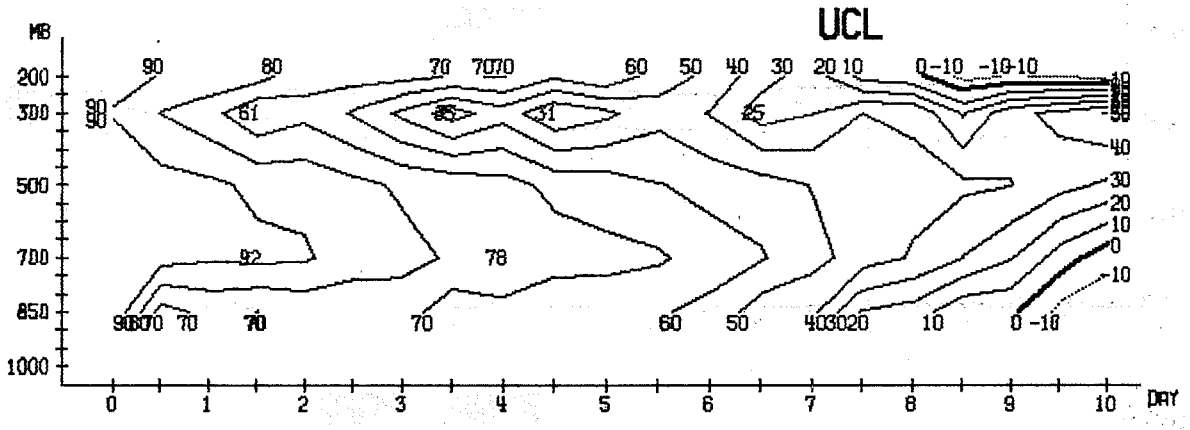

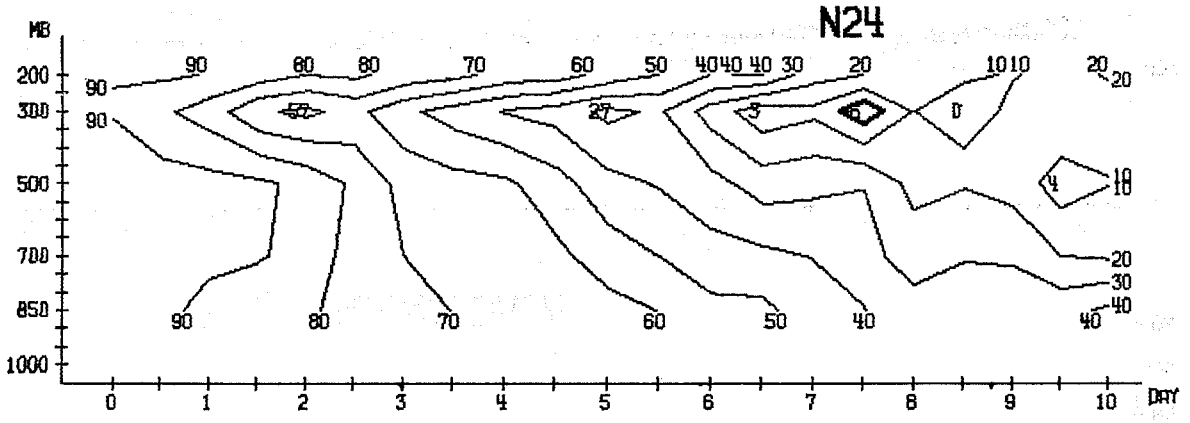

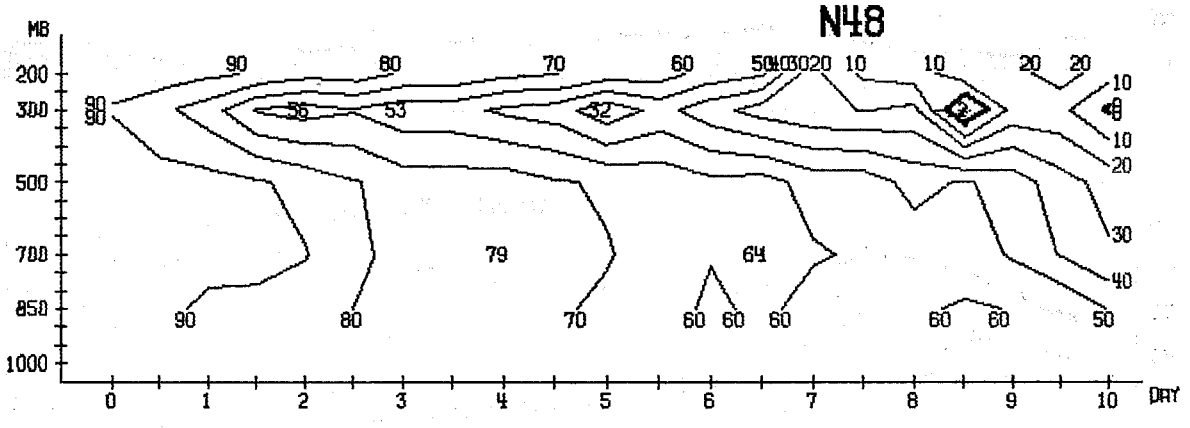

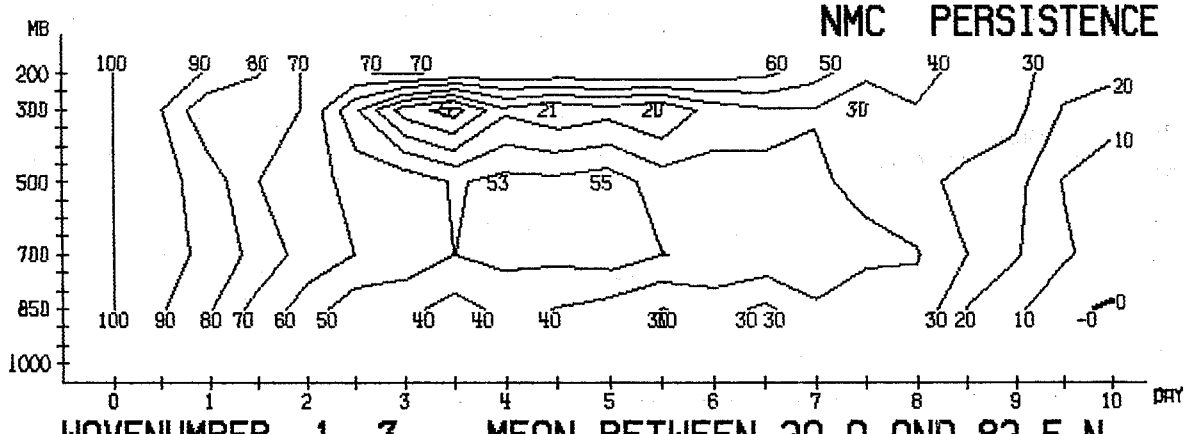

WAVENUMBER 1- 3 MEAN BETWEEN 20.0 AND 82.5 N
CORRELATION OF TEMPERATURE %

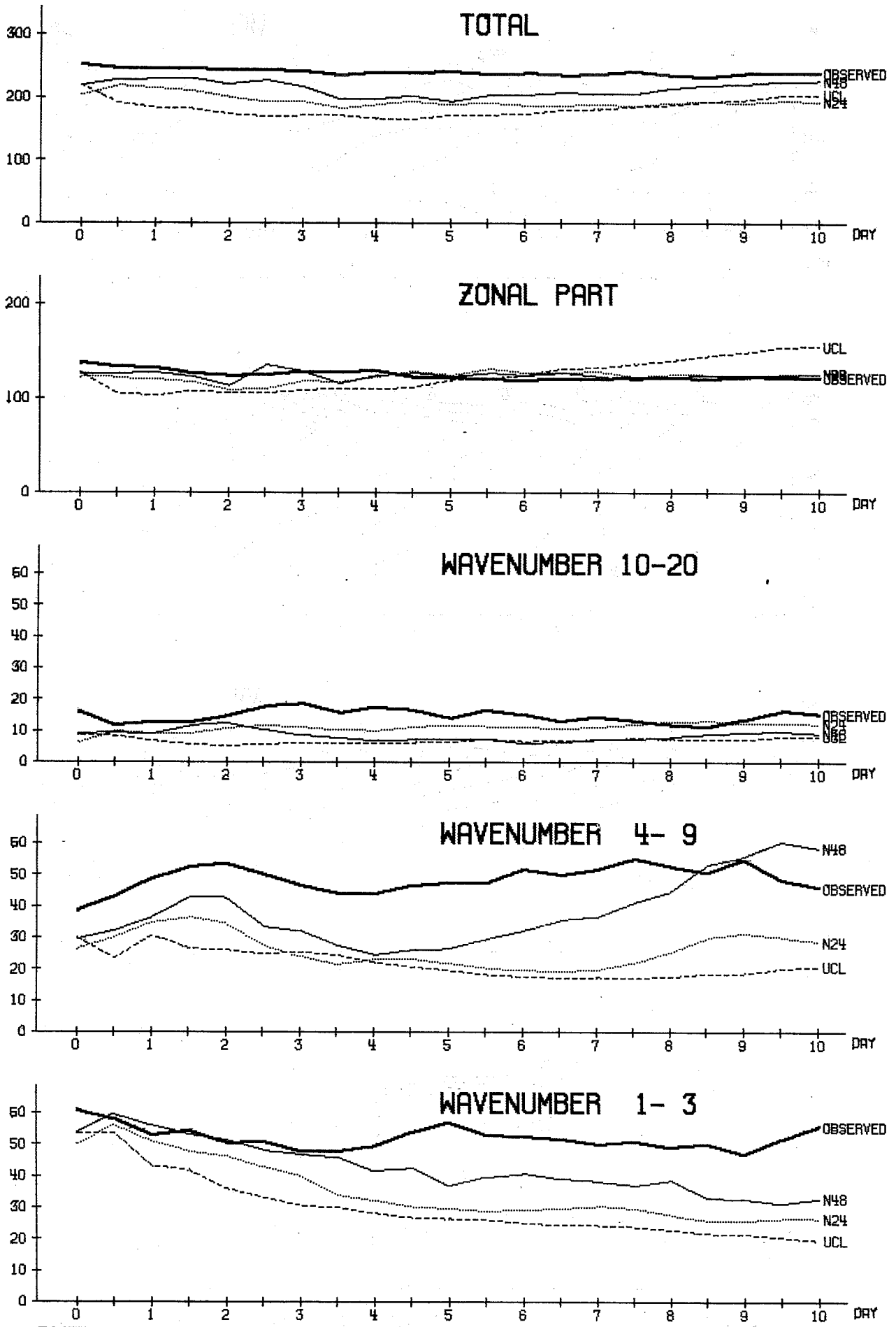

INTEGRAL 1000- 200 MB AREA MEAN 20.0- 82.5 N

KE (10 KJ/M2)

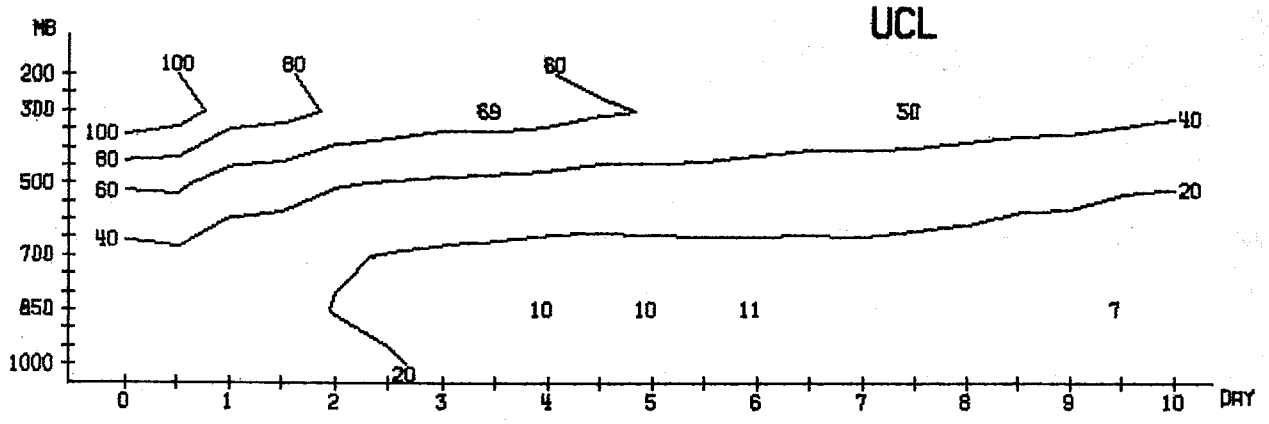

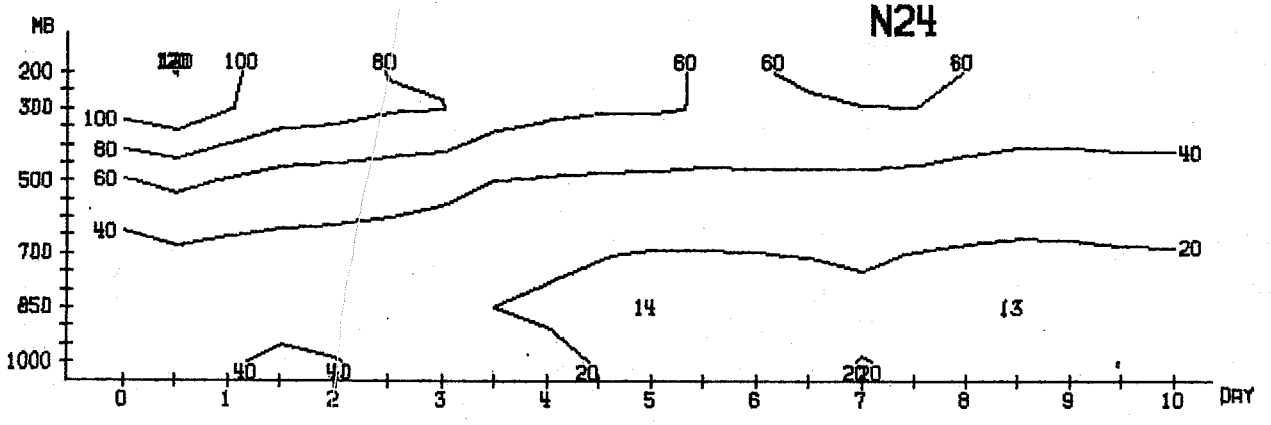

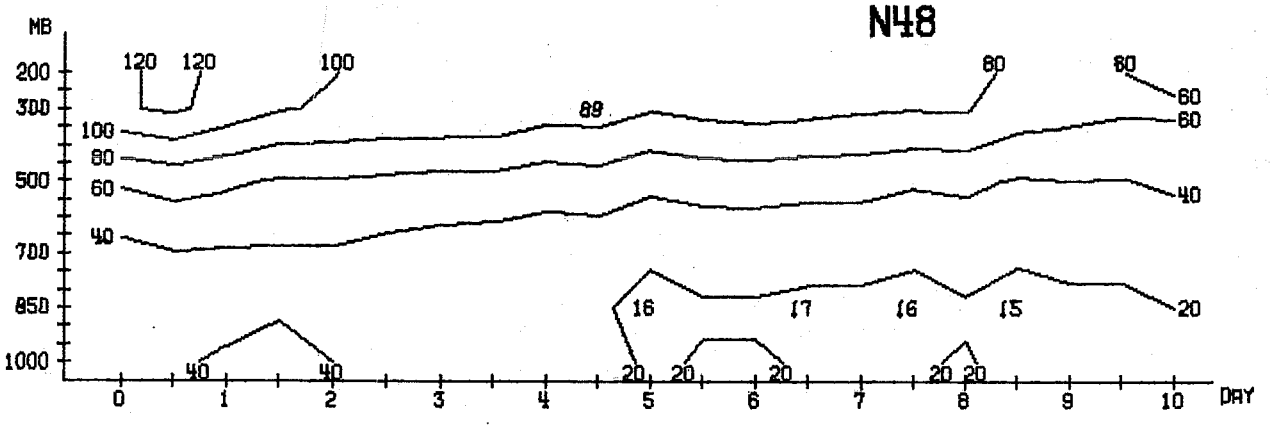

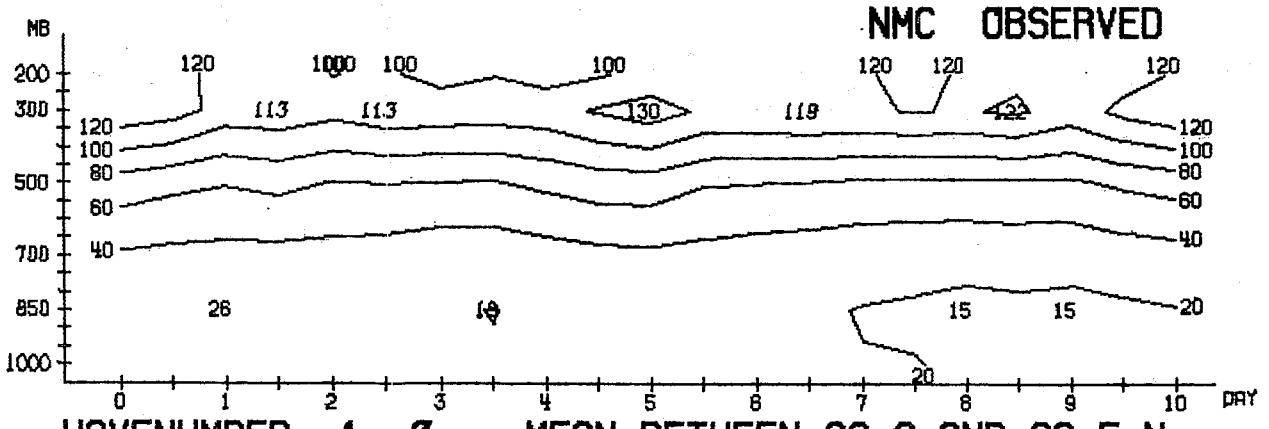

WAVENUMBER 1- 3 MEAN BETWEEN 20.0 AND 82.5 N
KE (10 KJ/M2/BAR)

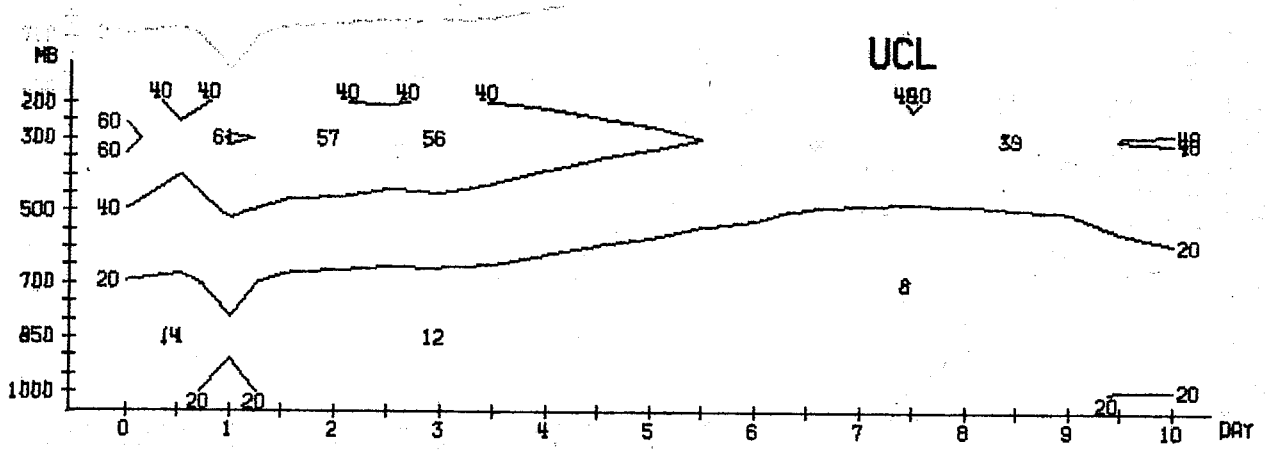

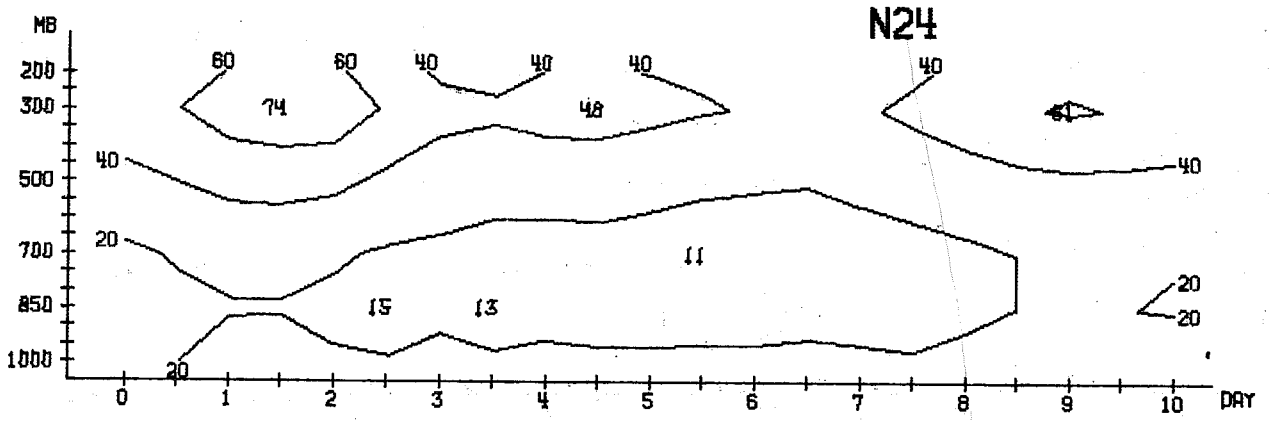

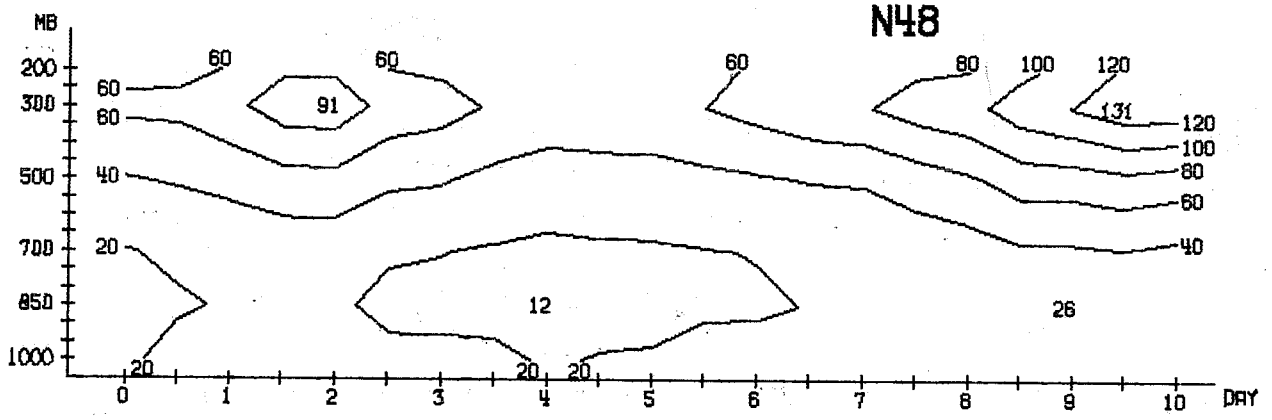

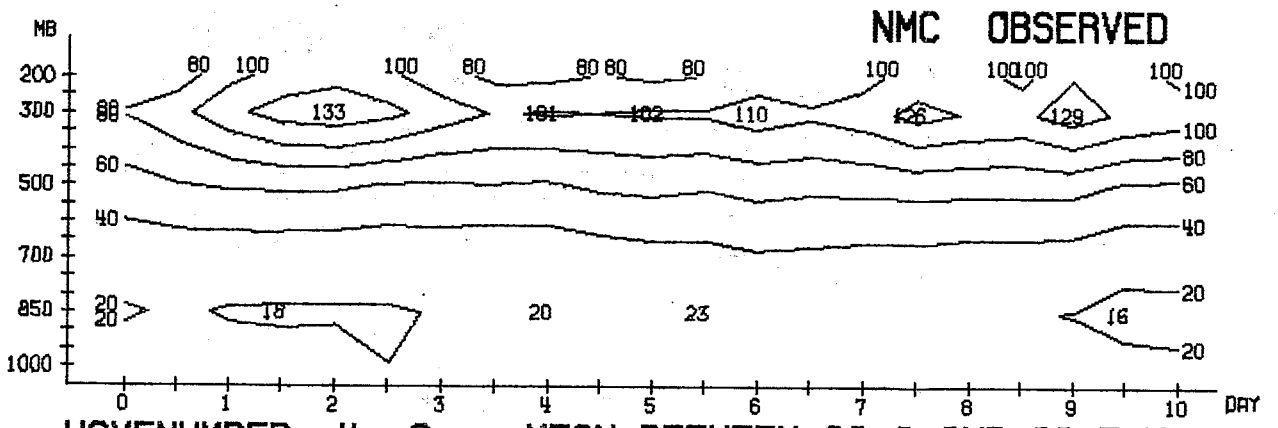

WAVENUMBER 4- 9 MEAN BETWEEN 20.0 AND 82.5 N
KE (10 KJ/M2/BAR)

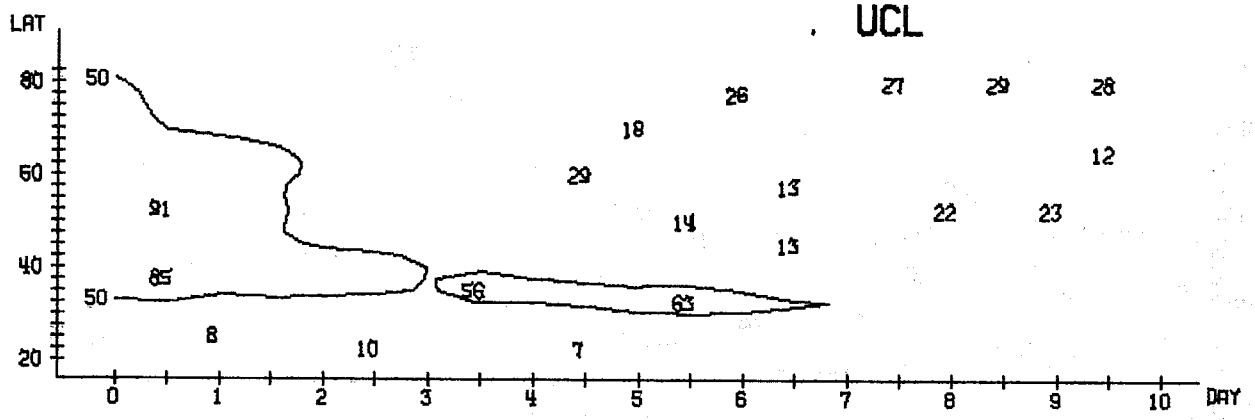

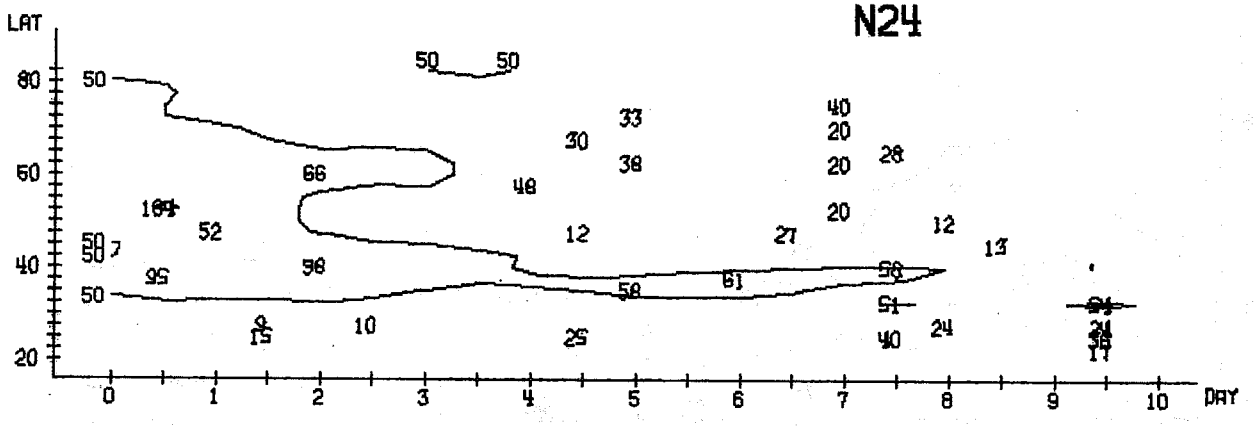

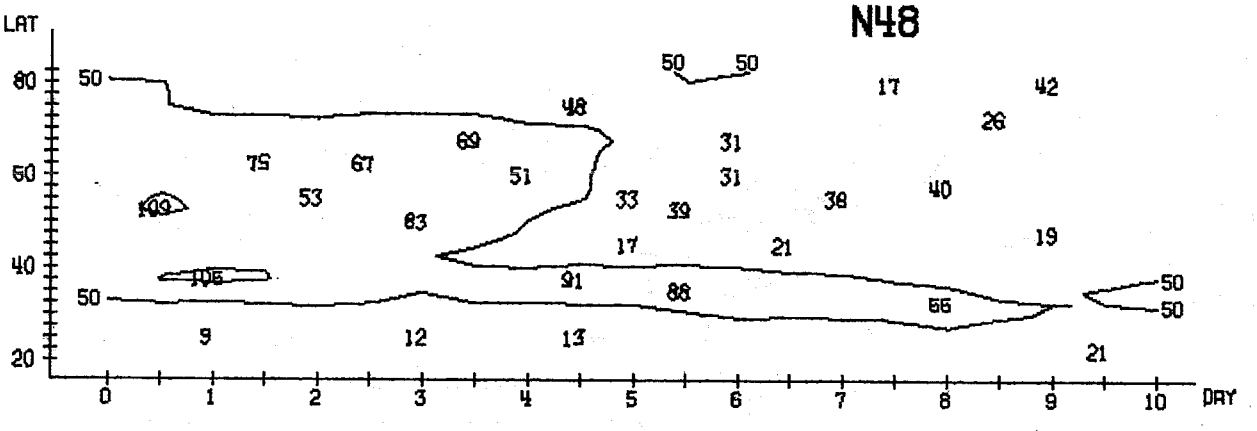

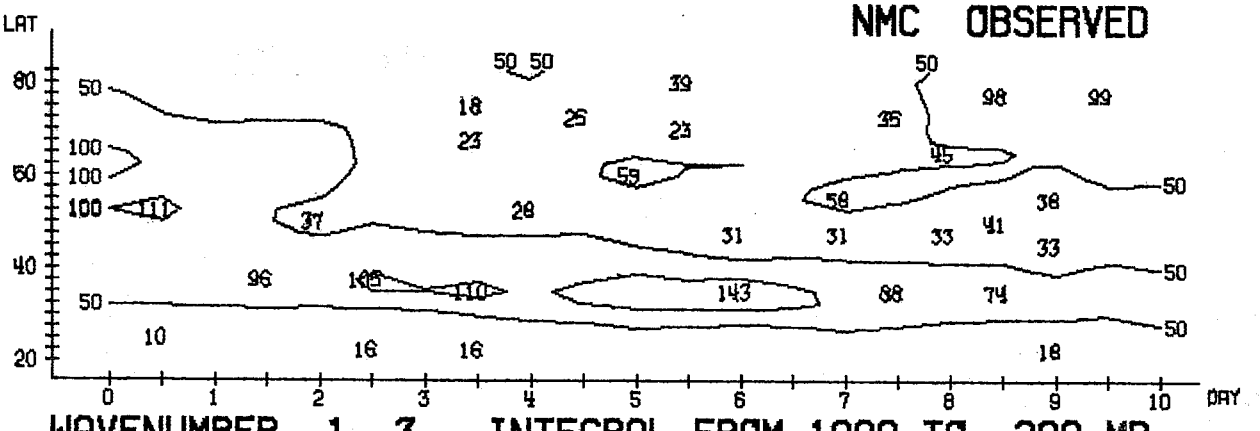

WAVENUMBER 1- 3 INTEGRAL FROM 1000 TO 200 MB
KE (10 KJ/M2)

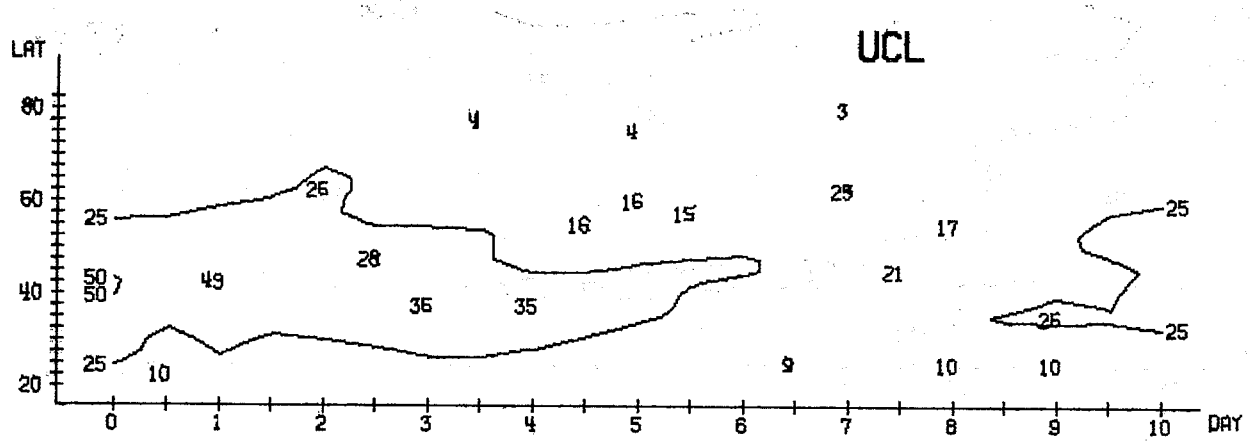

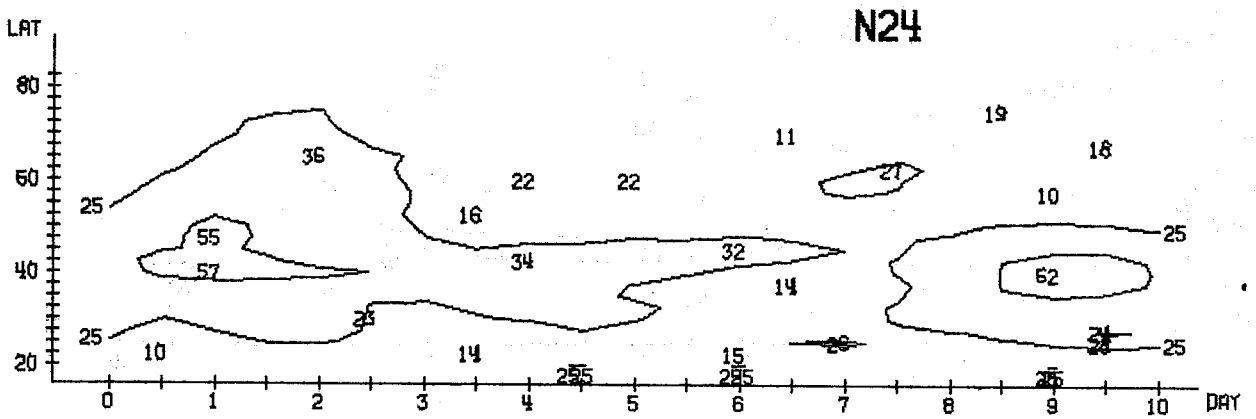

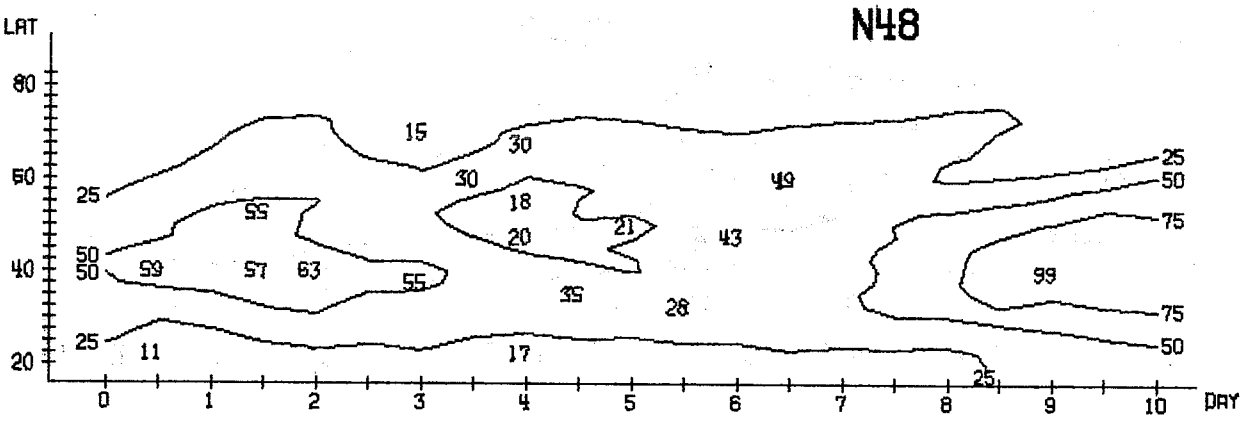

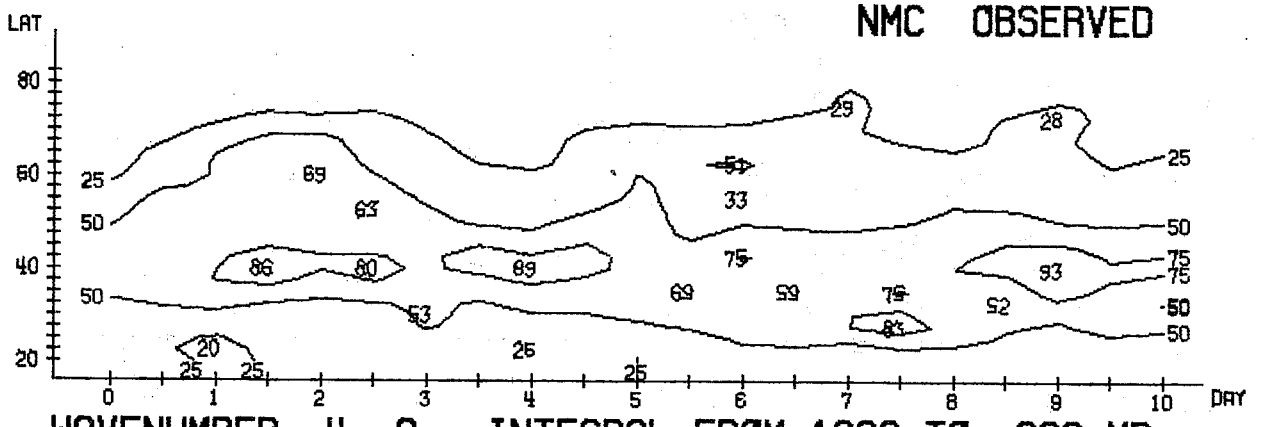

WAVENUMBER 4- 9 INTEGRAL FROM 1000 TO 200 MB
KE (10 K J/M2)

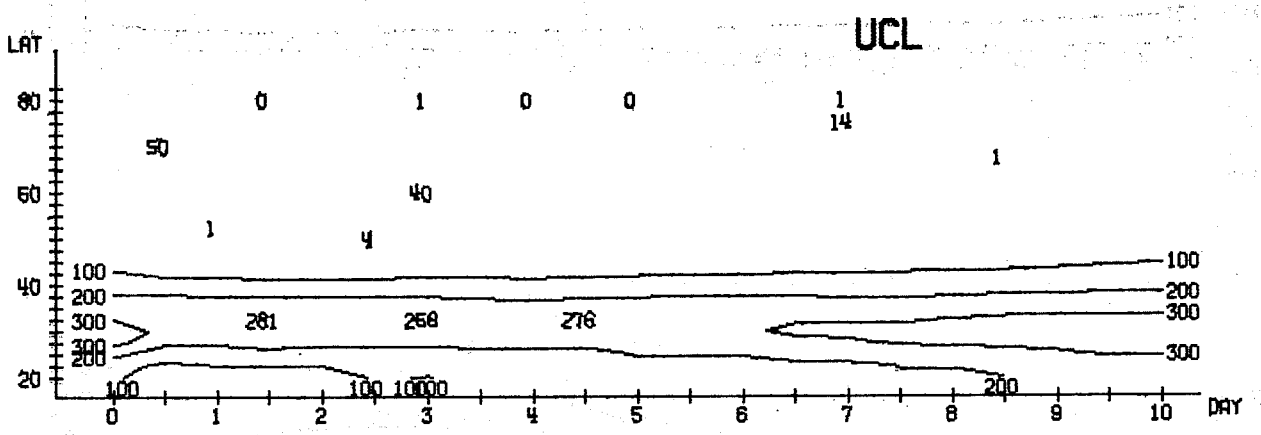

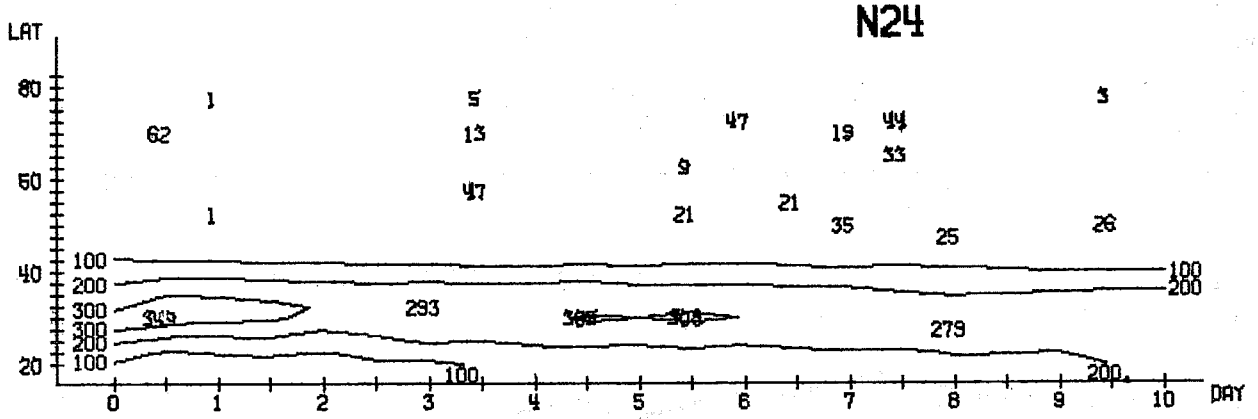

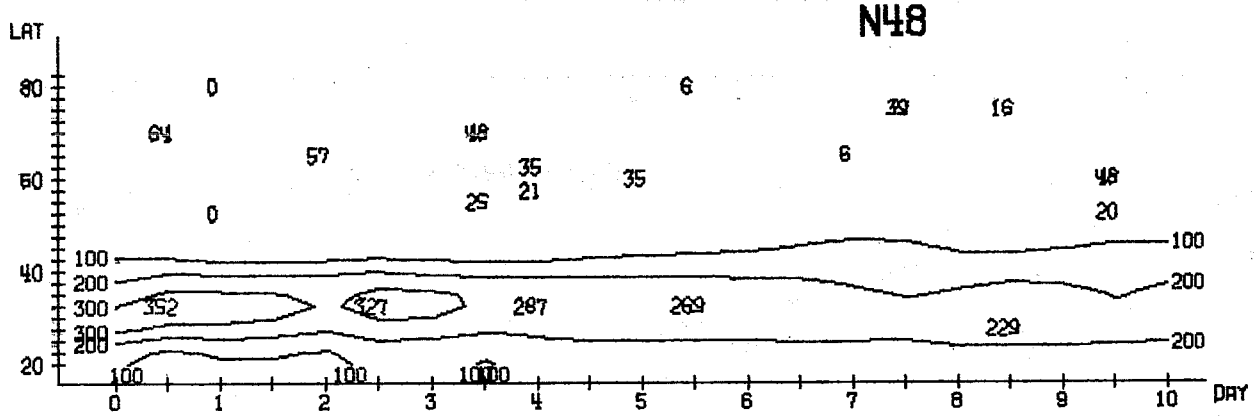

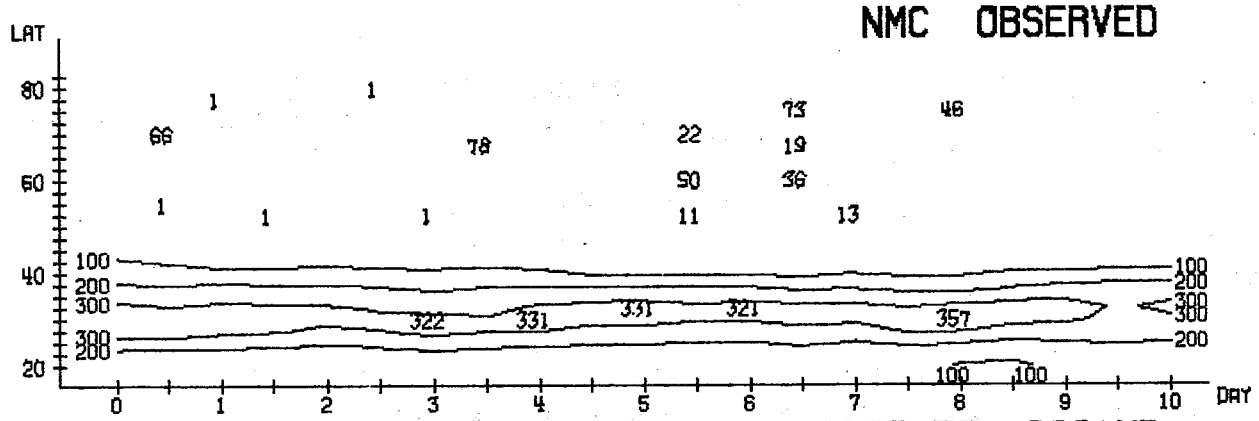

INTEGRAL FROM 1000 TO 200 MB

KZ (10 KJ/M2)

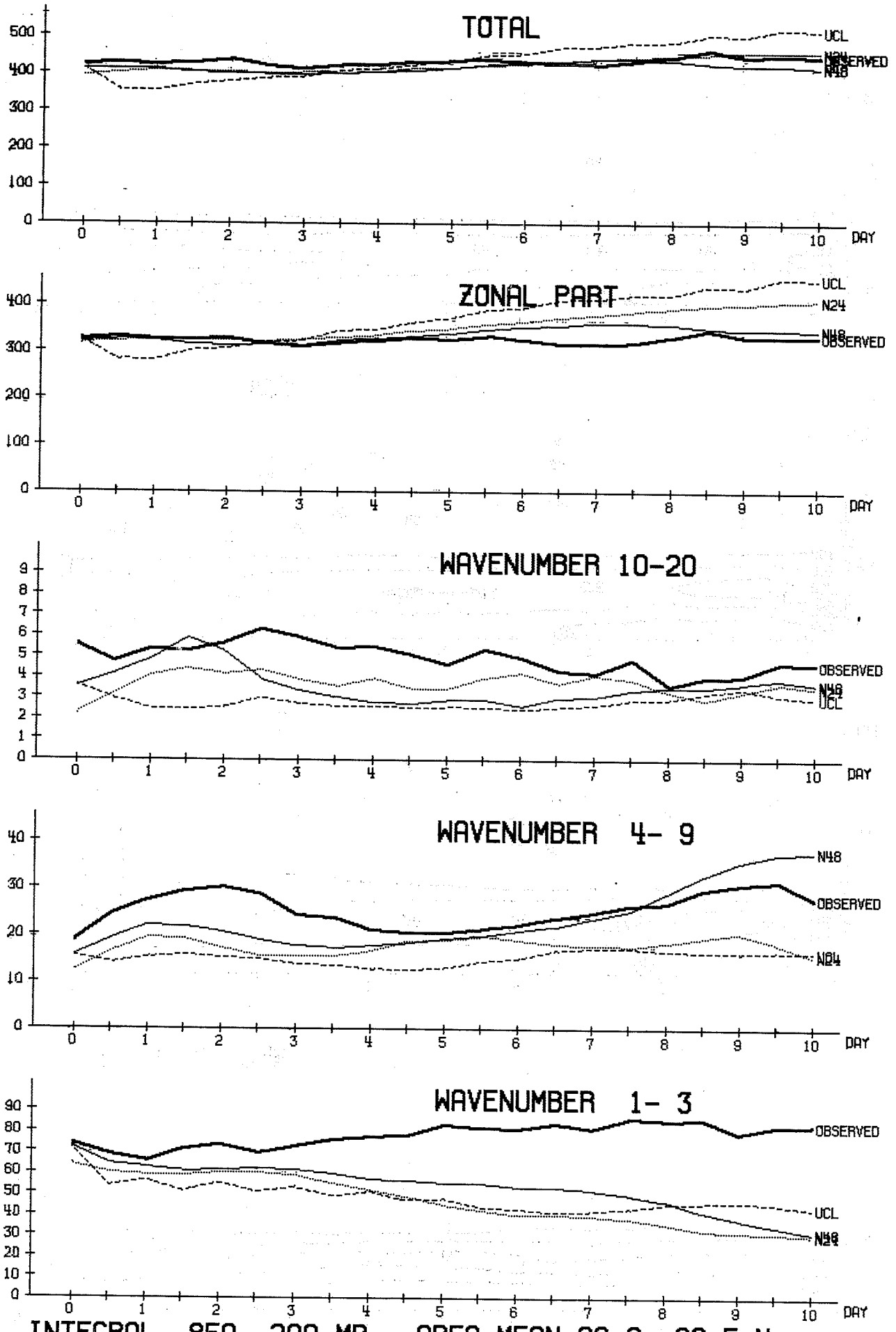

INTEGRAL 850- 200 MB AREA MEAN 20.0- 82.5 N

AE (10 KJ/M2)

Fig. 4.4.7

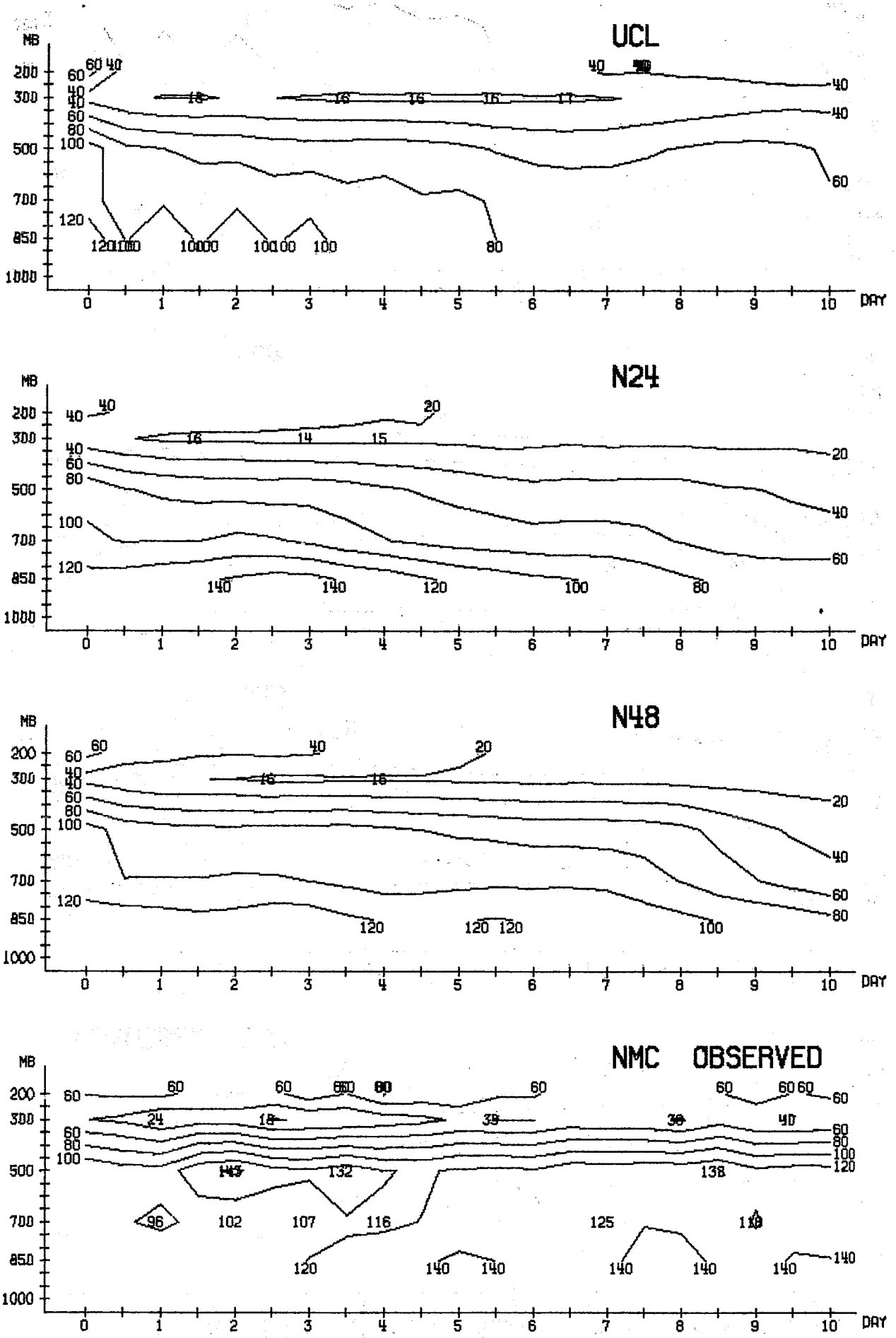
UCL
N24
N48
NMC OBSERVED
MB
DAY
WAVENUMBER 1- 3 MEAN BETWEEN 20.0 AND 82.5 N
AE (10 KJ/M2/BAR)

Fig. 4.4.8

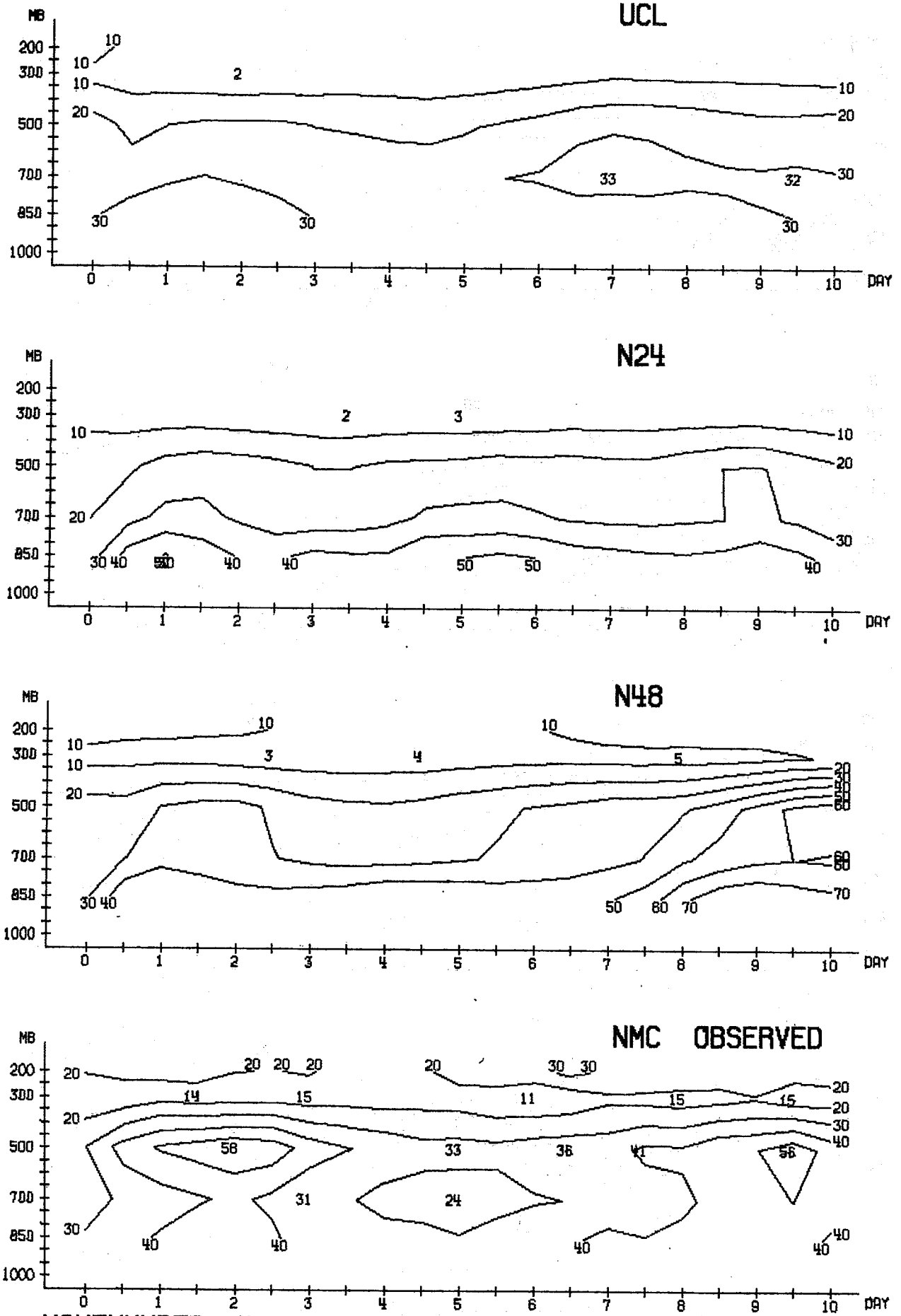
UCL
MB
200
300
500
700
850
1000
10
10
2
10
20
10
20
30
33
32
30
30
30
0
1
2
3
4
5
6
7
8
9
10
DAY
N24
MB
200
300
500
700
850
1000
2
3
10
10
20
20
30
30 40
40
40
50
50
40
0
1
2
3
4
5
6
7
8
9
10
DAY
N48
MB
200
300
500
700
850
1000
10
10
10
3
4
5
20
30 40
50
60
70
0
1
2
3
4
5
6
7
8
9
10
DAY
NMC OBSERVED
MB
200
300
500
700
850
1000
20
20 20 20
20
30 30
14
15
11
15
15
20
20
30
40
58
33
36
41
56
31
24
30
40
40
40
40
40
0
1
2
3
4
5
6
7
8
9
10
DAY
WAVENUMBER 4- 9 MEAN BETWEEN 20.0 AND 82.5 N
AE (10 KJ/M2/BAR)

Fig. 4.4.9

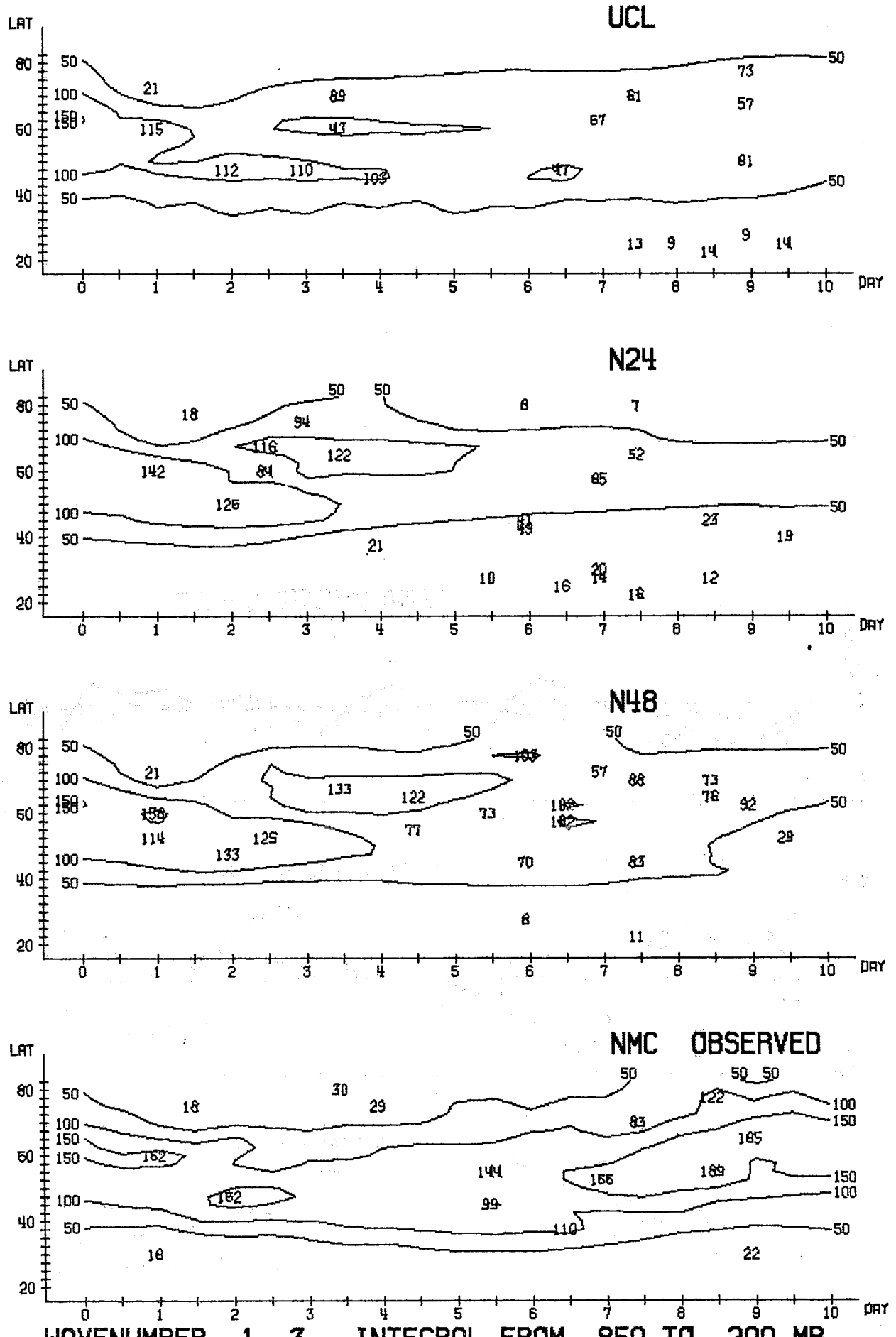
UCL
N24
N48
NMC OBSERVED
LAT
DAY
WAVENUMBER 1- 3 INTEGRAL FROM 850 TO 200 MB
AE (10 KJ/M2)

Fig. 4.4.10

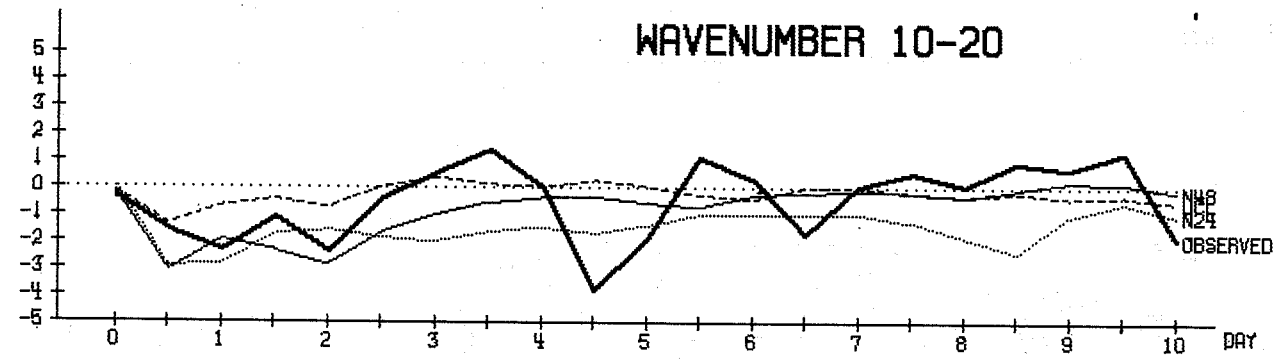

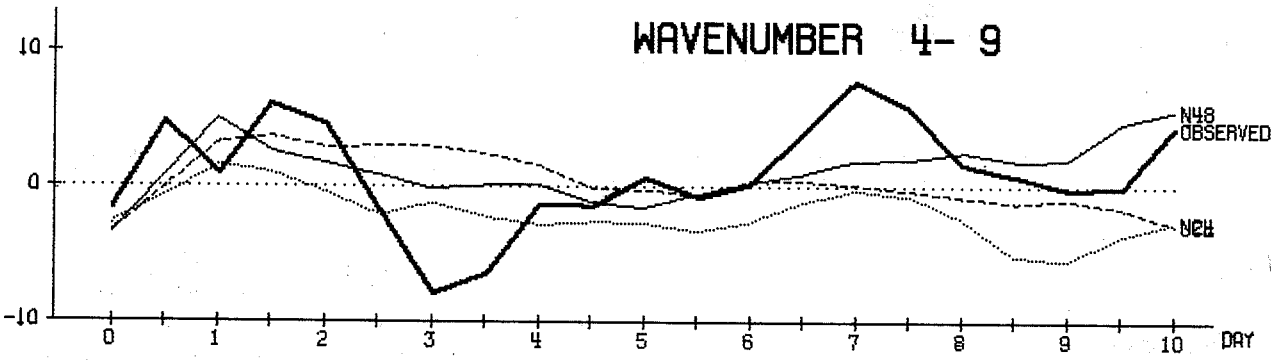

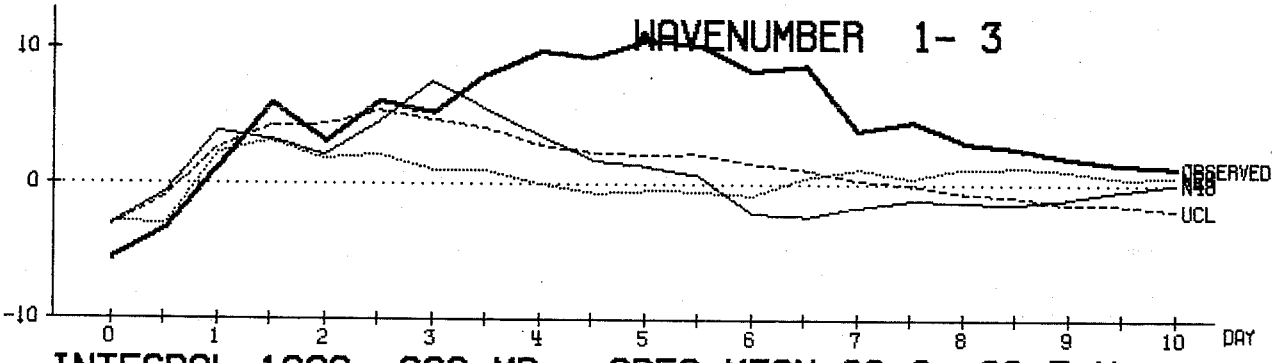

INTEGRAL 1000- 200 MB AREA MEAN 20.0- 82.5 N

CK (1/10 WATT/M2)

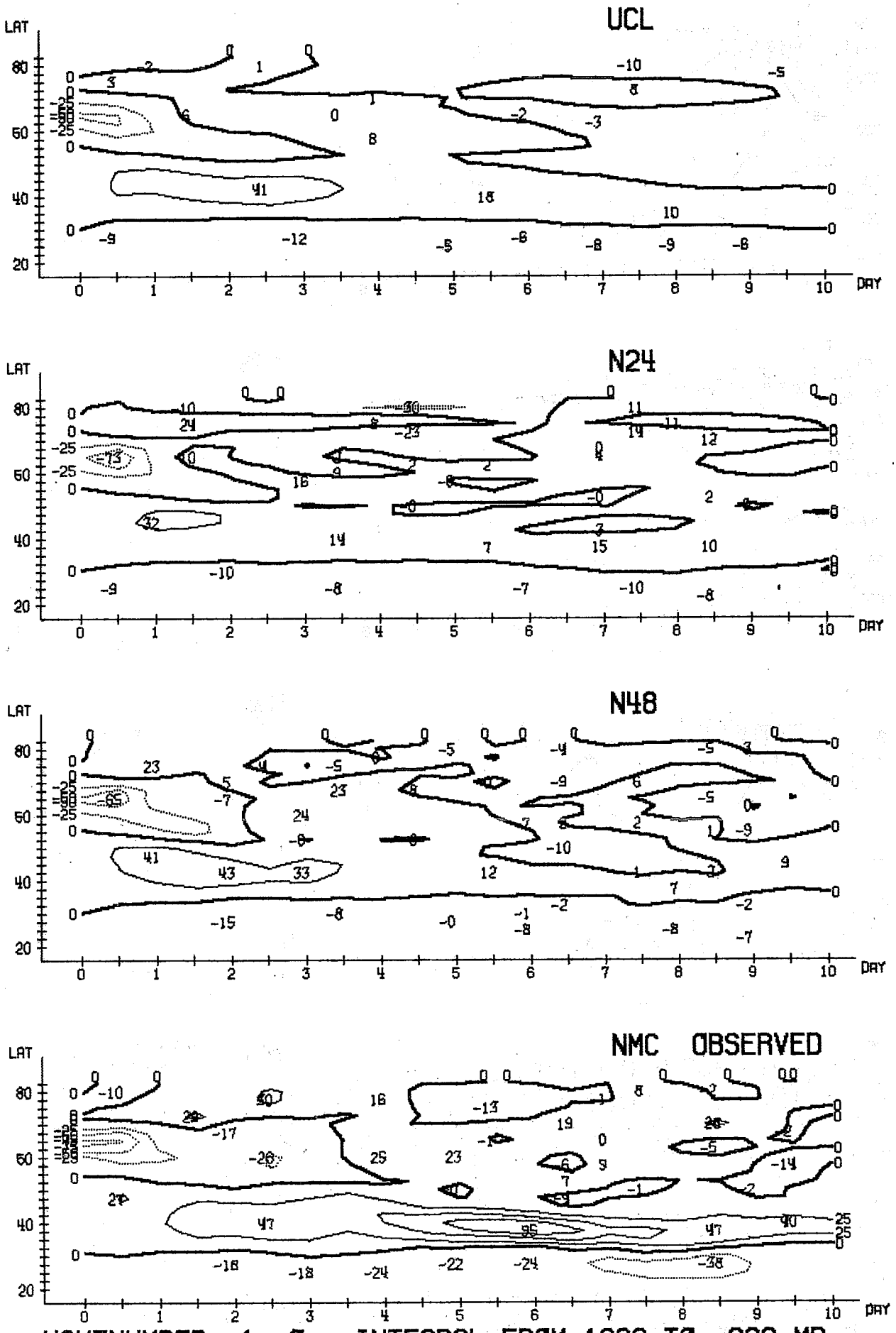
UCL
N24
N48
NMC OBSERVED
LAT
DAY
WAVENUMBER 1- 3 INTEGRAL FROM 1000 TO 200 MB
CK (1/10 WATT/M2)

Fig. 4.4.12

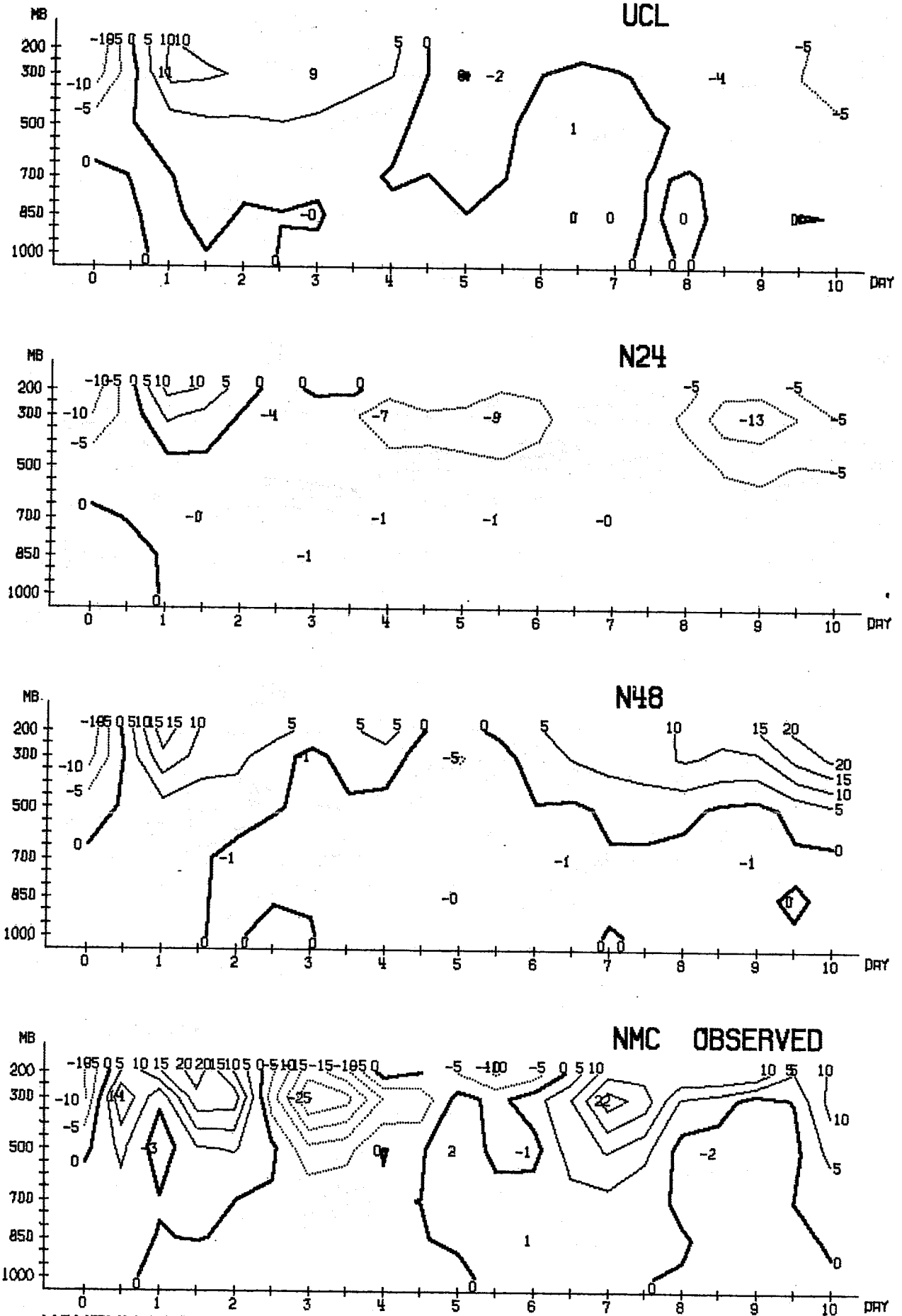

WAVENUMBER 4- 9 MEAN BETWEEN 20.0 AND 82.5 N
CK (1/10 WATT/M2/BAR)

Fig. 4.4.13

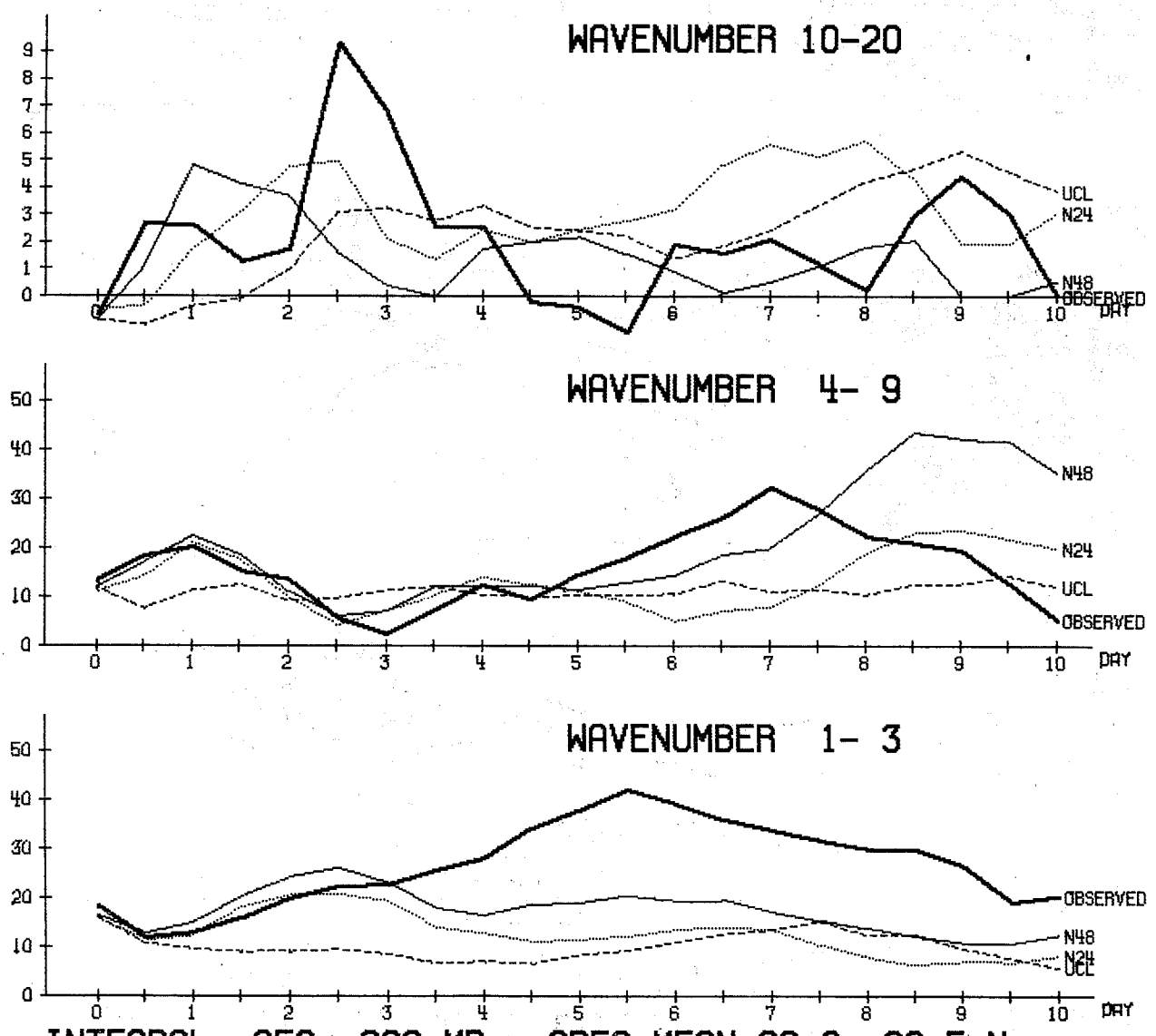
WAVENUMBER 10-20
UCL
N24
N48
OBSERVED
DAY
WAVENUMBER 4- 9
N48
N24
UCL
OBSERVED
DAY
WAVENUMBER 1- 3
OBSERVED
N48
N24
UCL
DAY
INTEGRAL 850- 200 MB AREA MEAN 20.0- 82.5 N
CA (1/10 WATT/M2)

Fig. 4.4.14

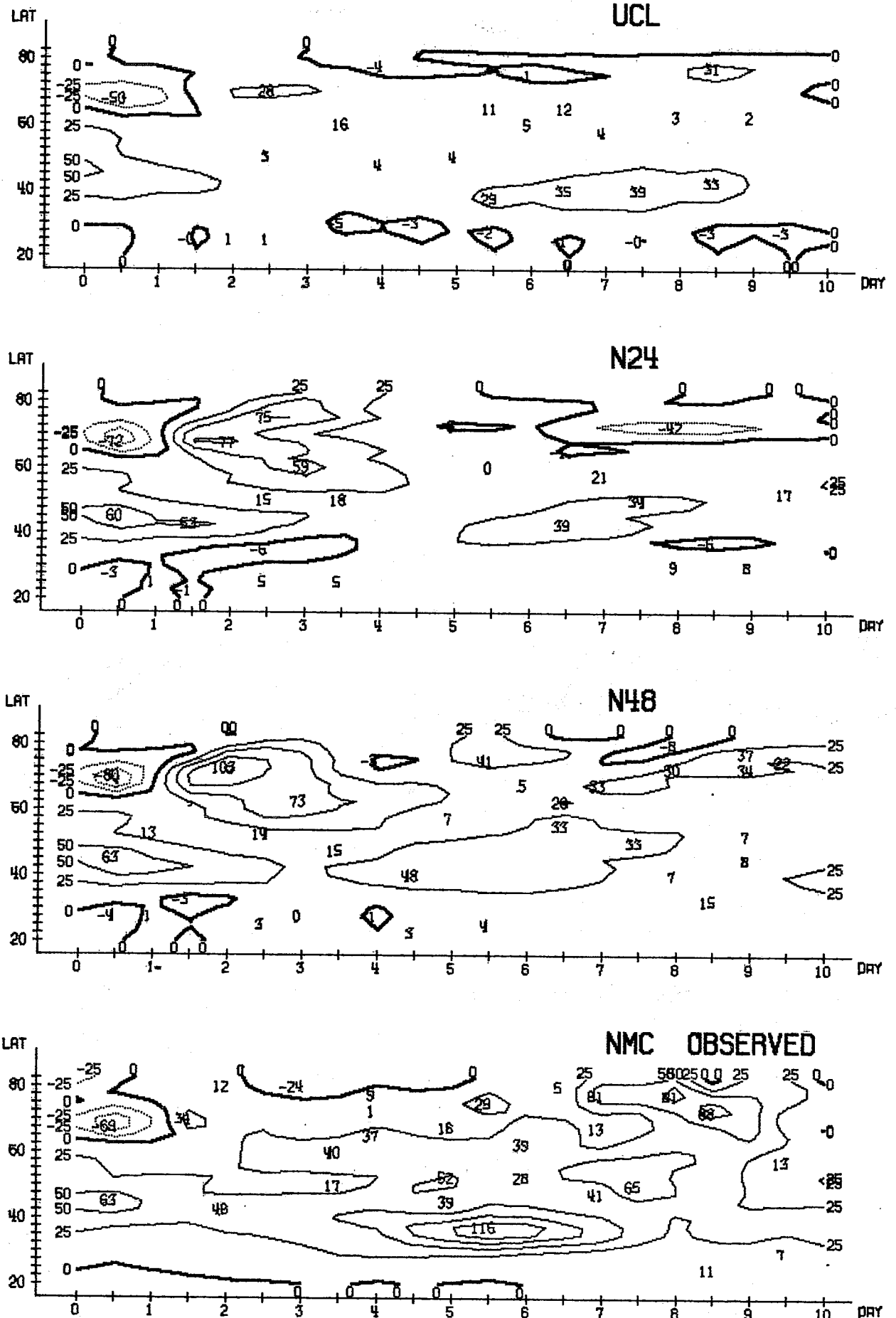

WAVENUMBER 1- 3 INTEGRAL FROM 850 TO 200 MB
CA (1/10 WATT/M2)

Fig. 4.4.15

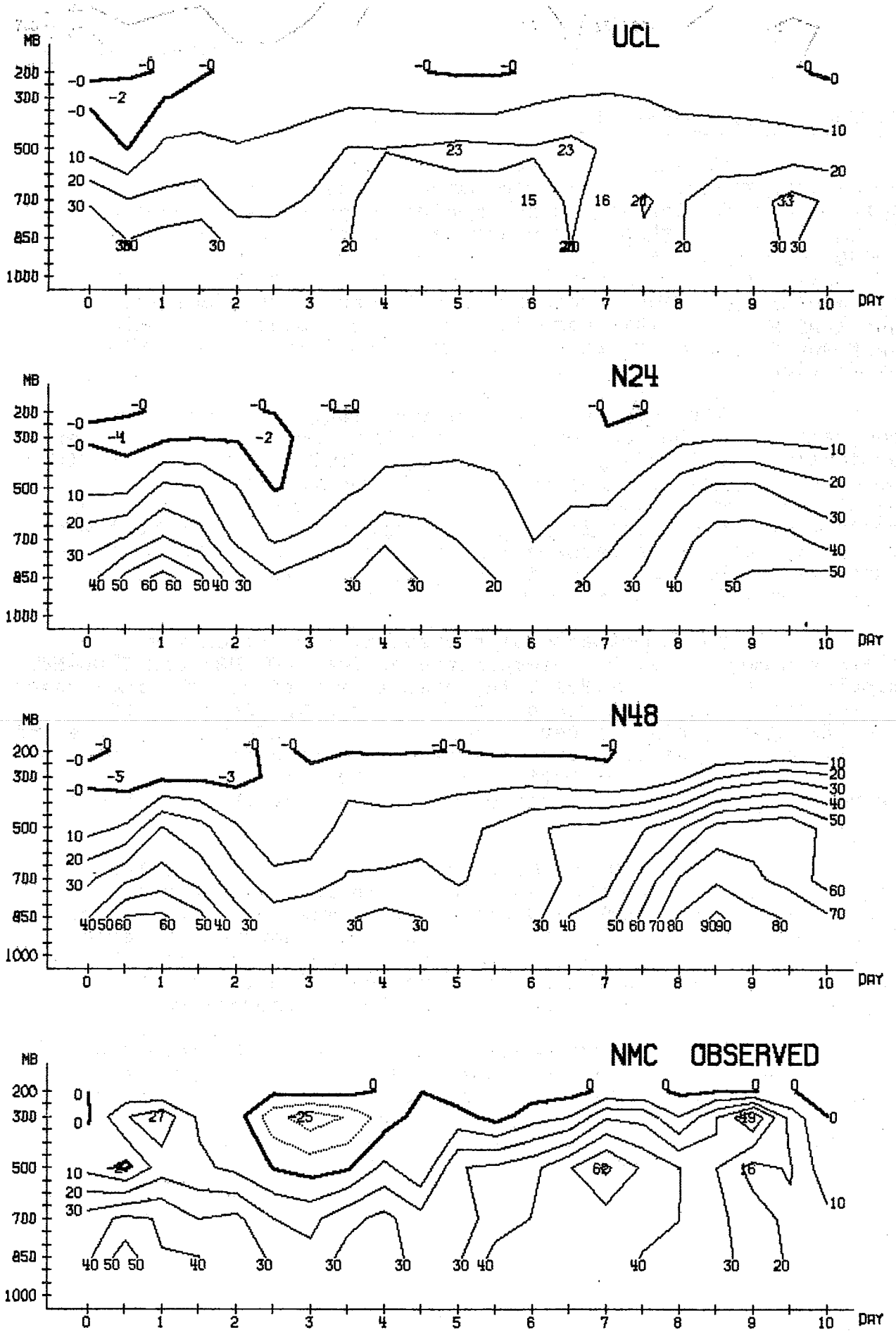
UCL
N24
N48
NMC OBSERVED
MB
DAY
WAVENUMBER 4- 9 MEAN BETWEEN 20.0 AND 82.5 N
CA (1/10 WATT/M2/BAR)

5. Summary and Conclusions

The main purpose of the present work was to obtain experience in the performance of some well established general circulation models for medium-range weather forecasts. It was found, in this particular case study, that a 10-day integration shows skill at least in the large scale flow as demonstrated by the verification of the phase velocities of the long waves. The successful prediction of the phases of the long waves in this case is interesting, since we usually have the opposite experience in operational numerical weather prediction.

The amplitudes of the very long waves are underestimated, and the coarser the resolution the greater the underestimation. Naturally, it is extremely difficult to draw definite conclusions from only one case study. The performance of a particular numerical model may vary from weather situation to weather situation and, in general, comparative integrations must be carried out for a large number of cases (perhaps the order of hundreds) before we can arrive at a firm conclusion about the relative performance of a numerical model.

The importance of horizontal resolution was clearly demonstrated by a comparison of the GFDL-N24 and GFDL-N48 models, with the N48 model being clearly superior. The importance of vertical resolution was not that clear-cut, since the UCLA and GFDL models also differ in their finite difference formulations and in the parameterisation of sub-grid scale processes. However, the higher vertical resolutions of the GFDL model may be responsible for producing better predictions of the eddy kinetic energy.

It was shown, by comparing the daily maps, that the UCLA-N22 model showed some superiority in forecasting the positions of the troughs and ridges; this was confirmed by the Hovmöller diagrams. The GFDL-N48 model was, however, superior in forecasting the intensities of the cyclones and anticyclones. This was seen also in the better agreement with the observed energy spectrum and with the distribution of energetics.

The UCLA-N22 model (which is more smoothed) shows slightly better verification scores (RMS-error and correlation coefficients), which indicates that these scores are more sensitive to the positions of the troughs and ridges than to their intensities. But the differences in these scores between the three forecasts are very small and not always in the same sense.

A major part of this study is devoted to verification. The stratification of the results in different spectral domains, as well as a verification of energetics, is found to be very instructive. Due to the strong model dependency of the vertical motions, only the transfers between the zonal and the eddy parts of the kinetic and available potential energies have been calculated. It was found that the energetics are very sensitive and give some indication of model performance. It was shown that the transfer from zonal to eddy available potential energy was too weak in the UCLA-N22 forecasts, and that this might be responsible for the excessive decay of the eddy kinetic energy. It was also shown that the vertical resolution of all models is not good enough to produce the observed strong vertical contrasts between the 500 mb and 300 mb eddy kinetic and eddy available potential energies. However, the energetics may be too sensitive an indicator of model performance, and disagreement with the observed energetics does not necessarily mean that the forecast is of little practical use.

Acknowledgements

The authors express gratitude to the Geophysical Fluid Dynamics Laboratory/NOAA for supplying the GFDL-general-circulation-models and the initial data for this study. Similarly they are also indebted to the Department of Meteorology, University of California Los Angeles, for making the UCLA-general-circulation-model available. We also wish to thank the ECMWF staff members for their support in carrying out the computations, offering helpful comments, and reviewing the report. In addition, we thank A. Dinshawe for typing the manuscript.

References:

Arakawa, A.	(1972)	Design of the UCLA Atmospheric General Circulation Model. Tech. Report No. 7, Dept. of Meteorology, University of California at Los Angeles.
Arakawa, A. and Lamb, V.	(1976)	Computational Design of the Basic Dynamical Processes of the UCLA General Circulation Model. To be published.
Arakawa, A. and Mintz, Y.	(1974)	The UCLA Atmospheric General Circulation Model. Dept. of Meteorology, University of California at Los Angeles.
Baede, A. and Hollingsworth, A.	(1976)	The effect of computer word length on meteorological integrations. Tech. Report No. 2, ECMWF, Bracknell.
Druyan, L.M., Somerville, C.J. and Quirk, W.J.	(1975)	Extended range forecasts with the GISS model of the global atmosphere. Tech. Note Inst. for Space Studies, Goddard Space Flight Centre, NASA, N.Y.
Jenne, L.R.	(1969)	Northern hemisphere climatological grid data tape. National Center for Atmospheric Research, Boulder, Colorado.
JOC WGNE	(1975)	Report on the twelfth session of the working group on numerical experimentation. Paris, November 1975.
Manabe, S., Holloway, J.L.Jr., and Spelman, M.J.	(1974)	GFDL Global 9-level Atmospheric Model. GARP Publication Series No. 14, 7 - 27.

Miyakoda, K. (1974) GFDL Global 18-level Atmospheric Model using modified Kurihara grid, GARP Publication Series, No. 14, 27 - 41.

Miyakoda, K., Hembree, G.D., Strickler, R.F. and Shulman, J. (1972) Cumulative Results of Extended Forecast Experiments. I. Model Performance for Winter Cases. Monthly Weather Review 100/12, 836 - 855.

Miyakoda, K., Moyer, R.W., Stambler, H., Clarke, R.H. and Strickler, R.F. (1971) A Prediction Experiment with a Global Model on the Kurihara Grid. Journal of Met. Soc. of Japan, 49, 521 - 536.

Miyakoda, K., Sadler, J.C. and Hembree, G.D. (1974) An Experimental Prediction of the Tropical Atmosphere for the Case of March 1965. Month. Wea. Rev. 102/8, 571 - 591.

Miyakoda, K., Strickler, R.F. and Hembree, G.D. (1970) Numerical Simulation of the Breakdown of a Polar-Night-Vortex in the Stratosphere. Journal of Atm. Sci., 27, 139 - 154.

Paulin, G. (1968) Spectral Atmospheric Energetics during January 1959. Publ. in Meteorology No. 91, McGill University, Montreal.

Smagorinsky, J. (1963) General Circulation Experiments with the Primitive Equations. Monthly Weather Rev., 91/3, 99 - 164.

Somerville, R.C.J. Stone, P.H., Halem, M., Hansen, J.E., Hogan, J.S., Duyan, L.M. Russel, G., Lacis, A.A., Quirk, W.J. and Tenenbaum, J. (1974) The GISS Model of the global atmosphere. J. Atmos. Sci. 31, 84 - 117.